Investigation of Sub-Granular Dynamics in Halide Perovskites via Atomic Force Microscopy

Dissertation

zur Erlangung des Grades

"Doktor der Naturwissenschaft"

Im Promotionsfach Chemie

am Fachbereich Chemie, Pharmazie, Geographie und Geowissenschaften

der Johannes Gutenberg-Universität Mainz

Mehmet Yenal Yalcinkaya
Mainz, 2023

The present work was carried out between March 2020 and November 2023 at the Max Planck Institute for Polymer Research in Mainz under the supervision of Prof. Dr. Hans-Jürgen Butt and Prof. Dr. Stefan A. L. Weber. To the best of my knowledge and conscience, I assure the reader that original research is presented, and no plagiarism has been committed. Sources are acknowledged to the best of my knowledge. Material originating from other publications has been reproduced with the corresponding permissions.

Mainz, 28. November 2023

Dekan:

1. Berichterstatter:

2. Berichterstatter:

Tag der mündlichen Prüfung:

I

II

https://www.youtube.com/watch?v=dQw4w9WgXcQ

„Bands bend but a band bends.“

Peter File, Reynholm Industries

Table of Contents

Abstract

Halide perovskites are considered as next generation solar cell absorbers due to their several advantages over conventional solar cell absorber materials such as adjustable bandgap, high photoluminescence (PL) quantum yield, low charge recombination rate, long charge diffusion length, and defect tolerance. However, perovskite photovoltaic devices suffer from power conversion losses at interfaces. Therefore, understanding the local features and charge carrier dynamics at interfaces is crucial, making macroscopic measurements inefficient for this purpose. Among the microscopic techniques, optical microscopy and its derivatives, such as PL microscopy, are the most common ones. However, they suffer from the diffraction limit, resulting in low-resolution imaging.

In this work, I focused on studying local features in halide perovskite films and devices at internal interfaces, such as grain boundaries and ferroelastic twin domains, or external interfaces in devices where two components of a perovskite-based device meet. Here, atomic force microscopy (AFM) comes into play. To understand the nanoscale properties of perovskite interfaces, I used electrical AFM modes such as piezoresponse force microscopy (PFM), conductive AFM (C-AFM), and Kelvin probe force microscopy (KPFM).

First, I investigated the strain properties in halide perovskites by monitoring ferroelastic twin domains via PFM and x-ray diffraction (XRD). I introduced strain to halide perovskite films by changing the precursor solution. PFM measurements showed altered twin domain patterns that are correlated with strain changes within films. I used XRD measurements to support my claim for a change in overall strain and twinning behavior in the films. My investigation revealed that any chemical gradient in halide perovskites leads to a strain gradient as well.

Furthermore, I investigated the local charge carrier dynamics and conductivity at halide perovskite grains and grain boundaries via time-resolved KPFM and C-AFM. Photoconductivity and photovoltage maps I obtained suggest that grain boundaries are high-defect areas that promote faster electron-hole recombination and ion migration. Furthermore, the behavior of charge carriers at grain boundaries changes when grain size changes.

Ultimately, this work shows how sub-granular features and device interfaces affect charge carrier dynamics in halide perovskite devices. Therefore, this work may contribute to the optimization of halide perovskite devices for commercialized use.

Zusammenfassung

Halogenidperowskite gelten als Absorber für Solarzellen der nächsten Generation, da sie gegenüber herkömmlichen Absorbermaterialien für Solarzellen mehrere Vorteile bieten, z. B. eine einstellbare Bandlücke, eine hohe Quantenausbeute bei der Photolumineszenz (PL), eine niedrige Ladungsrekombinationsrate, eine lange Ladungsdiffusionslänge und Defekttoleranz. Perowskit-Solarzellen weisen jedoch Energieumwandlungsverluste an den Grenzflächen auf. Daher ist das Verständnis der lokalen Eigenschaften und der Ladungsträgerdynamik an Grenzflächen von entscheidender Bedeutung, so dass makroskopische Messungen für diesen Zweck ineffizient sind. Unter den mikroskopischen Techniken sind die optische Mikroskopie und ihre Derivate, wie die PL-Mikroskopie, am weitesten verbreitet. Sie unterliegen jedoch dem Beugungslimit, was zu einer geringen Auflösung der Bildgebung führt.

In dieser Arbeit konzentrierte ich mich auf die Untersuchung lokaler Merkmale in Halogenid-Perowskit-Filmen und -Bauteilen an internen Grenzflächen, wie Korngrenzen und ferroelastischen Zwillingsdomänen, oder externen Grenzflächen in Bauteilen, an denen zwei Komponenten eines Perowskit-basierten Bauteils aufeinandertreffen. Hier kommt die Rasterkraftmikroskopie (AFM) ins Spiel. Um die Eigenschaften von Perowskit-Grenzflächen auf der Nanoskala zu verstehen, habe ich elektrische AFM-Modi wie Piezokraftmikroskopie (PFM), Leitfähigkeits-Rasterkraftmikroskopie (C-AFM) und Kelvinsondenkraftmikroskopie (KPFM) verwendet.

Zunächst untersuchte ich die Spannungseigenschaften in Halogenidperowskiten, indem ich ferroelastische Zwillingsdomänen mittels PFM und Röntgendiffraktometrie (XRD) beobachtete. Ich führte Spannungen in Halogenidperowskitfilme ein, indem ich die Präkursorlösung veränderte. PFM-Messungen ergaben veränderte Zwillingsdomänenmuster, die mit Spannungsänderungen in den Filmen korreliert sind. Ich habe XRD-Messungen verwendet, um zu belegen, dass sich die gesamte Spannung und das Zwillingsverhalten in den Filmen verändert haben. Meine Untersuchung ergab, dass jeder chemische Gradient in Halogenidperowskiten auch zu einem Spannungsgradienten führt.

Darüber hinaus untersuchte ich die lokale Ladungsträgerdynamik und Leitfähigkeit an Halogenidperowskit-Körnern und Korngrenzen mittels zeitaufgelöster KPFM und C-AFM. Die von mir erhobenen Abbildungen der Photoleitfähigkeit und Photospannung deuten darauf hin, dass Korngrenzen Bereiche mit hoher Anzahl an Defekten sind, die eine schnellere Elektron-Loch-Rekombination und Ionenmigration fördern. Außerdem ändert sich das Verhalten von Ladungsträgern an Korngrenzen, wenn sich die Korngröße ändert.

Letztlich zeigt diese Arbeit, wie subgranulare Merkmale und Bauteilgrenzflächen die Ladungsträgerdynamik in Halogenidperowskit-Bauteilen beeinflussen. Daher kann diese Arbeit zur Optimierung von Halogenidperowskit-Bauelementen für die kommerzielle Nutzung beitragen.

1 Basics and Theory

1.1 Introduction

The escalation of global climate change has instigated a multitude of natural disasters, encompassing heatwaves, severe storms, floods, and wildfires worldwide. Human-induced CO_2 emissions are the primary catalyst behind the escalating global temperatures, and the subsequent climate changes are projected to worsen in the near future. This poses a severe threat to all life forms inhabiting the planet, necessitating urgent resolution through the advancement of clean energy technology. Despite the historic signing of the Paris Agreement in 2016, global temperatures have already exceeded a 1 °C increase compared to preindustrial levels, and the critical threshold of 1.5°C, set forth by the Paris Agreement, could be surpassed as early as 2030. Consequently, it is imperative to expedite the implementation of renewable energy sources at the earliest opportunity[1]. However, the demand for electricity continues to increase steadily, while conventional energy sources contribute to pollution and are finite in supply. Therefore, there is a significant interest in the development of renewable energies. As a result, various photovoltaic technologies have been introduced, which can be categorized into four distinct generations[2].

At present, the predominant method of generating solar electricity involves the use of large-area silicon solar panels. Remarkable advancements in the fabrication process of silicon solar cells have led to a significant reduction in their manufacturing costs over the past five decades. In certain countries, the cost of power generation from silicon photovoltaics has even become lower than that of coal, natural gas, geothermal, and nuclear power plants[3]. However, to fulfill the ambitious goals set forth in the Paris Agreement, which aims to achieve zero CO_2 emissions by 2050, ongoing reductions in the cost of solar panels remain crucial. These cost reductions are essential in order to facilitate the transition towards a sustainable and carbon-neutral energy system[4]. As for the second generation, thin-film solar cells have emerged as cost-effective alternatives with promising performance compared to their predecessors. The third generation encompasses organic solar cell technologies, including dye sensitized solar cells, organic solar cells, and perovskite solar cells (PSC). Lastly, the fourth generation, known as hybrid technologies, incorporates multijunction cells, among other advancements.

PSCs, a rapidly emerging technology, hold tremendous potential and are widely regarded as the future of photovoltaics. The term "hybrid perovskite" refers to a unique material composition, combining organic and inorganic components in the form of perovskite crystals. This exceptional material has enabled the rapid development of high-efficiency devices, achieving milestones in solar cell history within a remarkably short timeframe. While it took half a century for silicon solar cells to reach 26.7% efficiency, hybrid PSCs have achieved a noteworthy efficiency of 25.73% in just 14 years[5]. One of the remarkable aspects of hybrid perovskite devices is their simple device structures, coupled with the ability to fabricate high-quality perovskite absorbers at low temperatures (around 100°C). These attributes make hybrid PSCs highly appealing. Consequently, the field of hybrid perovskite research has emerged as the most captivating and dynamic domain in solar cell research, evident from the significant number of research papers submitted in this field. Starting from 2014, PSCs have showcased their remarkable compatibility as sub-cells in tandem

solar cell configurations when compared to other technologies. This inherent compatibility due to the tunable bandgap of perovskites has led to substantial efficiency enhancements in these tandem solar cells, with perovskite-silicon combinations achieving an impressive record efficiency of 33.2%[6]. Ongoing research endeavors aim to push the boundaries even further, continuously seeking new breakthroughs and innovations to advance efficiency records in the field of PSCs.

Since the first report of their performance, lots of researchers in solar cell, spectroscopy, and microscopy fields focus on improving and understanding the properties of halide perovskites. The typical assessment method for perovskite quality is to measure the efficiency of perovskite devices. Further typical characterizations to understand the quality and the perfromance of halide perovskites include methods such as photoluminescence (PL) spectroscopy, transient PL (tr-PL), and PL quantum yield measurements. These methods characterize the free charge carrier behaviour within the perovskite layer or the whole device. As it will be discussed later, PL is one of the possible results of recombination of electrons and holes in halide perovskites without the effect of the defects. The other possibility is the defect-assisted recombination of the electrons and holes. Therefore, the PL spectroscopy can give information about the defect density based on the PL intensity obtained by the perovskite film. Similarly, the PL quantum yield measurement which measures the emitted-to-absorbed photon ratio can also give information about defect density in the perovskite structure. Moreover, defect-assisted recombination typically occurs faster than defect-free recombination which effects the overall free charge carrier lifetime. Here, tr-PL can be useful since it is a method to measure the recombination times of the electrons and holes. Considering the fact that a solar cell relies on free electrons and holes, longer the recombination time would correspond to better solar cell efficiency. However, the bottleneck of semiconductor devices such as solar cells are the interfaces between different layers or structures. A device that does not show uniform quality is not considered reliable and is a problem for mass production. This fact makes local charge carrier, recombination, and defect properties within the perovskite layer crucial. However, the methods that were listed above either do not give information about the localized properties or localized dynamics within the halide perovskites. Therefore, in my thesis I focused on atomic force microscopy (AFM) techniques on halide perovskite thin films. By implementing electric modes of AFM such as piezoresponse force microscopy (PFM), conductive AFM (C-AFM), and Kelving Probe Force Microscopy (KPFM), I investigated the subgranular structures and dynamics within halide perovskites. I studied the strain behavior within methylammonium lead iodide (MAPbI$_3$) via tracking the ferroelastic twin domains via PFM. I used C-AFM to study the changes at the grain boundaries of triple cation perovskite films before and after methylamine gas treatment which lead to larger perovskite grains. Lastly, I investigated the charge carrier dynamics behavior based on perovskite layer and interface between perovskite and charge transport layer in perovskite half-cells.

1.1.1 Semiconductor Materials

In this part, I give a brief introduction to semiconductor physics to be able to explain the photovoltaic effect. This part includes Bloch theorem, energy bands, and electron-hole recombination.

Since the components of a perfect crystals (atoms and ions) form a periodic order, it is safe to

assume an electron in a crystal lattice will be affected by this periodicity of the lattice[7],

$$U(r + R) = U(r) \tag{1.1}$$

where R corresponds to all lattice vectors.

For a single electron, the Schrödinger equation goes as[7]

$$H\psi = \left(\frac{-h^2}{2m} \nabla^2 + U(r) \right) \psi = E\psi \tag{1.2}$$

Here, the term U is given for the periodicity potential. Free single electrons that obeys the Schrödinger equation in a periodic potential are referred as "Bloch electrons" as oppose to free electrons for which the periodic potential is zero.

Bloch's Theorem

The electrons in metals are assumed to be free. However, this is an approximation of an ideal free behavior. Some differences from the ideal free behavior is to be expected due to the presence of periodic potential caused by the crystal lattice that electrons must undergo. Therefore, we must include this periodic potential into the eigenfunctions for the Hamiltonian of the electrons. These functions are called Bloch functions and they are generated by lattice periodicity function and a free electron wave function.

The presence of energy gaps can be explained through the fact that the electrons undergo Bragg reflection from the periodic planes of the lattice. The incapacity of an electron, which is assumed as a wave, of suitable energy is similar to the emergence of forbidden gaps in a continuous energy spectrum. Furthermore, the broadening of the discrete energy states into energy bands can be explained by the fact that the electrons cannot possibly distinguish which atoms they belong. Combining this with the Pauli exclusion principle that requires individual electrons to localize at unique quantum states would lead to the broadening of the otherwise discrete energy states into energy bands.

Bloch proposed that electron in a periodic potential due to the crystal lattice can be written as a wave function in a form given in Equation (1.3)[7].

$$\psi_k(r) = u_k(r)e^{ik.r} \tag{1.3}$$

where u_k(r) represents the periodicity of the crystal lattice and when a translation vector, R_j takes the lattice into itself, we would get Equation (1.4)[7].

$$\psi_k(r + R_j) = u_k(r) \tag{1.4}$$

$$\psi(r + R) = e^{ik.R}\psi(r) \tag{1.5}$$

Even though the k based descriptions are limited to a single primitive lattice, it is useful to allow k into a range of all k-space. Since the all wave functions and energy levels for two k values are
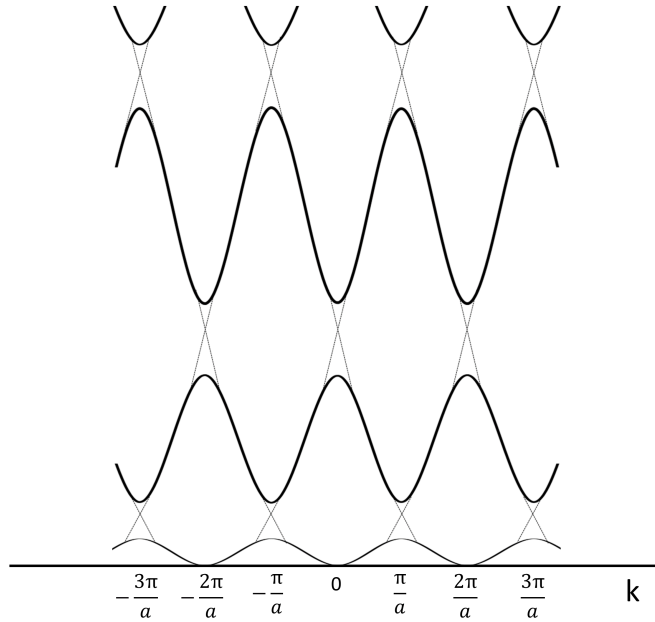
Figure 1.1: Repeated zone scheme showing the energy gaps.

differed by a reciprocal lattice vector must be identical, we can assign the n indices to the energy levels in a way that the eigenstates and eigenvalues are periodic functions of k in the reciprocal lattice[7]:

$$\psi_{n,k+K}(r) = \psi_{nk}(r),$$
$$\varepsilon_{n,k+K} = \varepsilon_{nk} \tag{1.6}$$

Thus, the energy levels of an electron in a periodic potential can be described as continuous functions ε_{nk} (or $\varepsilon_n(\mathrm{k})$), each with the periodicity of the reciprocal lattice. This gives rise to the band structure in solids. For each n value, the electronic energy levels specified by $\varepsilon_n(\mathrm{k})$ are called energy bands.

Energy Bands

When there is no interaction, the energy levels appear as a parabola in k. However, when the k-points are close to a Bragg plane in the lattice the continuity of this parabola is ceased by a bandgap. When we apply this for all Bragg planes at each $\pi/2$, we have the energy gaps of the free electrons in a solid as given in Figure 1.1[7].

These energy levels where electrons are able to localize are called energy bands. Thus, it can be said that energy bands are filled with electrons. Each solid has their specific band structure where the fullness of the band may differ. Here, the term 'Fermi level' is an important concept. The Fermi level (E_F) is referred as the highest energy that an electron can occupy in a solid at absolute zero temperature. Therefore, filling of an energy band by electrons is determined by Fermi level at 0 K. Fermi level in solids may lie within the energy bands or bandgaps. When Fermi level lies within a band, the electrons can only occupy energy levels below Fermi level at 0 K and these

bands are referred as partially filled bands. Electrons in a completely filled band do not carry any current without any external energy input because there is no other state available for electrons to move. This is the main distinction between the metals and the insulators according to the independent electron model. Therefore, the ground state of an insulator is either completely filled or completely empty whereas the ground state of a metal has at least one partially filled band. The insulators can be characterized based on the energy gap or bandgap, E_g which is the gap between the bottom of the lowest empty band and the top of the highest filled band. The filled bands in an insulator form so-called valence band whereas the empty bands form so-called conduction band. An insulator with an energy gap will not be conducting at T = 0 K. However, if the insulator is thermally excited above T = 0 K, some electrons could move to the conduction band and act as free electrons according to the Fermi-Dirac statistics. Fermi-Dirac statistics determines the energy level occupation probabilities of electrons in an insulator solid. When the temperature exceeds 0 K, the electrons can occupy energy levels higher than Fermi level of the solid. At a random temperature T, the electrons and holes are distributed within an energy range. The occupation probability of an electron (f_e) with an energy E_e is given in Equation (1.7)[8]

$$f_e(E_e) = \frac{1}{exp[(E_e - E_{F_e})/k_B T] + 1} \tag{1.7}$$

where k_B is the Boltzmann constant and T is the temperature. During this process the excited electrons leave unoccupied states within the valence band which are referred to as holes. Both of these electrons and holes can contribute to the conduction within a material.

The insulators whose energy gaps allow the electron conduction at higher temperatures below the melting point are called semiconductors. Even though the distinction between insulators and semiconductors is not particularly certain, typically the insulators with a bandgap below 3 eV are considered as semiconductors due to relatively low energy needed to generate free electrons. The excitation of electrons to the conduction band from the valence band can occur thermally as shown by Fermi-Dirac statistics, as well as upon photon absorption by electrons. Once a semiconductor is excited with a light with an energy exceeding the bandgap, the electrons can be excited to the conduction band. This makes the semiconductors useful type of materials for optical applications such as solar cells and photodetectors[8].

1.1.1.1 Doping of Semiconductors

In semiconductor physics, doping is the process where an impurity is introduced to an pure or intrinsic semiconductor in order to modify its structural, electrical, and optical properties. As opposed to intrinsic semiconductors, doped semiconductors are named extrinsic semiconductors. Doping in semiconductors is separated into two: (i) n-type doping and (ii) p-type doping. The type of doping is determined by the respective numbers of valence electrons of the dopant and the intrinsic semiconductor. In n-type doping, the semiconductor is doped with a dopant with more valence electrons and the dopant takes places in the crystal lattice. This will lead to the presence of an additional electron in the semiconductor, resulting in a so-called donor state in the bandgap which is close to the conduction band. In p-type doping, a dopant with fewer valence electrons is

introduced to the semiconductor and the presence of the dopant in the crystal lattice will result in additional holes as positive charge carrier. As a result, a so-called acceptor state forms close to the valence band. These additional donor and acceptor states also affect the Fermi level of the semiconductor. Fermi level increases and decreases as results of n-type and p-type doping, respectively[9, 10].

Doping in semiconductors may still occur even in the absence of any external dopants. This happens due to the crystal defects which are the discontinuities within the crystal lattice. The defects can be formed as point defects where an atom leaves the lattice and leaves a vacancy behind, grain boundaries where the grains with different orientations meet, or surfaces where dangling bonds mostly located[10]. The donor or acceptor states caused by the presence of defects are typically referred as defect states or trap-states.

1.1.1.2 Recombination Mechanisms

After electrons got excited to the conduction band from the valence band, they may give up their energy and recombine with the hole in the valence band. This process in semiconductors is referred as recombination process. There are three types of recombination that occur in a semiconductor solid depending on the energy emission: (i) radiative recombination where photons are emitted, (ii) non-radiative recombination where phonons are emitted, and (iii) Auger recombination where the energy of another free charge carrier increases. Although, I will be describing radiative and non-radiative recombinations since they are the most common ones in solar cells[11].

(i) Radiative Recombination

In a radiative or band-to-band recombination process, the electron in the conduction band directly transitions to the valence band and interacts with a free hole. This process is referred to as recombination due to the fact that the electron-hole interaction as a result of a band-to-band transition results in a photon emission that has the same energy as the bandgap. The density dependence of the radiative recombination is given by Equation (1.8)[11],

$$U_{np} = Bnp \tag{1.8}$$

where n is the number of free electrons, p is the number of free holes, and B is a recombination coefficient which depends on temperature and other conditions. The radiative recombination for silicon and Gallium Arsenide at 300K are $B \approx 1 \cdot 10^{-14} cm^3 s^{-1}$ and $B \approx 7.2 \cdot 10^{-10} cm^3 s^{-1}$, respectively[12–15]. Equation (1.8) can be written in a way that it shows the dependence of the recombination rate on voltage applied to the solid is given by Equation (1.9)[11]

$$U_{np} = Bn_i^2 e^{qV/k_B T} \tag{1.9}$$

The recombination rate is usually associated with the free electron lifetime. The higher recombination rate would mean lower electron lifetime. For a linear recombination rate, this relation is given by Equation (1.10).

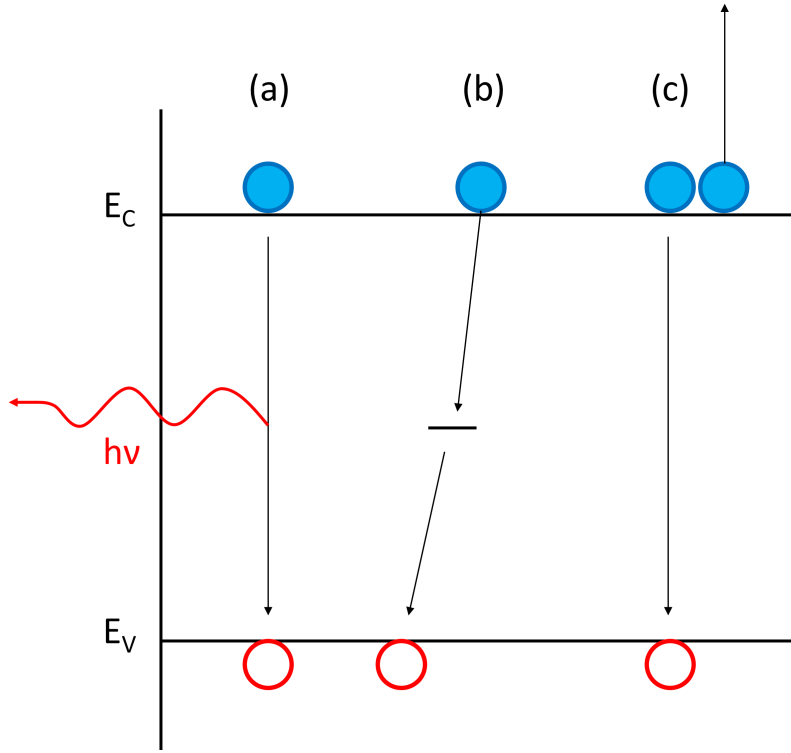$$\tau = \frac{1}{k_{rec}} \tag{1.10}$$

Figure 1.2: Illustration of recombination mechanisms in semiconductors. (a) Radiative, (b) non-radiative, and (c) Auger.

Based on this relation, we can quantitatively estimate the recombination rate by measuring the free electron lifetime. For example tr-PL measurements track the PL from a sample over time to estimate when the PL diminishes, which gives the free electron lifetime.

(ii) Non-radiative Recombination

The recombination process must always yield an energy emission due to the energy conservation law. For non-radiative recombination, the energy mainly is either taken by electrons or holes as in Auger recombination or phonons in defect related recombination.

Recombination can also take place through the presence of trap levels within the bandgap. Consequently, when an electron descends from the conduction band to midgap state, it can lead to the emission of a photon, which is subsequently redshifted relative to the bandgap photons. In cases where recombination occurs via a midgap state, it more frequently involves a multiphonon process in which the energy of the bandgap is transferred to a multitude of phonons, rather than being emitted as photons. This type of recombination is referred to as nonradiative recombination. Nonradiative recombination is often linked to defects found within the bulk or on the surface of the semiconductor. The semiconductor's surface, particularly in proximity to contact points, often harbors defects and recombination sites, which are termed surface recombination[11].

A typical model for recombination is the Shockley-Read-Hall (SRH) recombination model. It takes place at a localized state within the bandgap which takes both electrons and holes from conduction and valence bands, respectively. The recombination rate of excess charge carries is given by Equation (1.11)[11]

$$U_{SRH} = \frac{np - n_i^2}{\tau_p(n + n_1) + \tau_n(p + p_1)} \tag{1.11}$$

where τ_n is the electron lifetime for a large density of holes, τ_p is the hole lifetime for a large density of electrons, and $n_1, p_1 = n_i^2/n_1$ are the electron and hole densities when the Fermi level overlaps with the trap state energy that is the recombination center[11]:

$$n_1 = N_c exp((E_t - Ec)/k_B T) p_1 = N_v exp((E_v - Et)/k_B T) \tag{1.12}$$

1.2 Photovoltaics and Solar Cells

The photovoltaic effect occurs when a semiconductor, with two electrodes at its ends, is exposed to photons with sufficient energy to excite electrons to the conduction band while leaving holes in the valence band which leads to a potential due to charge asymmetry. Photovoltaic effect is the main working mechanism of solar cells. The subsequent flow of the free electrons and holes through the whole structure is the photocurrent. The absorber material is the main component of a solar cell and must be chosen carefully in order to have a functioning solar cell. Therefore, the bandgap of the absorber layer must allow the absorption of the wide range of the solar photons and the diffusion of the free charge carriers[11].

1.2.1 Working Principle of Solar Cells

A solar cell is an electronic device that absorbs incident photons and converts them to electricity. During this process, the photo-generated charge carriers are extracted due to an external load[16]. When the semiconductor material is exposed to super-bandgap radiation, it shifts into a different the steady state of recombination and generation equilibrium with excess electron-hole pairs that causes the splitting of the Fermi levels as shown in Figure 1.3. This difference in electrochemical potentials of electrons and holes, μ_{np} is called the quasi-Fermi level splitting and expressed as in Equation (1.13)[11].

$$\mu_{np} = \eta_n + \eta_p = \mu_n + \mu_p = E_{F_n} - E_{F_p} \tag{1.13}$$

Once the photons are absorbed by the semiconductor and the respective electrochemical potential for electrons and holes are generated, further steps are still required for the conversion to electrical energy. The efficiency of this process is all about the interplay between the free charge carrier density and the electrochemical potential difference of electrons and holes. Therefore, the bandgap of the semiconductor is extremely important for the efficiency. A low bandgap of the semiconductor would lead to higher number of free charge carriers in expense of lower electrochemical potential difference and vice versa. Furthermore, since the existance of free charge carrier is the
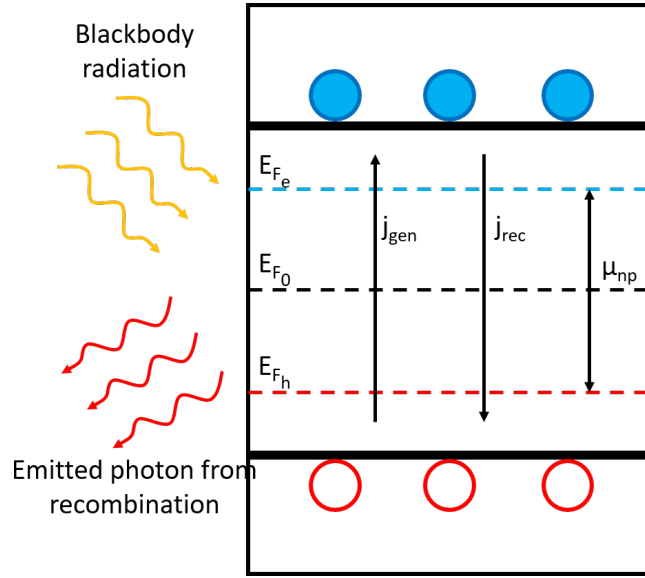
Figure 1.3: Illustration of the processes in a solar cell absorber. j_{gen}, j_{rec}, and μ_{np} are charge generation flux, charge recombination flux, and internal chemical potential, respectively.

main mechanism for these devices, recombination of electrons and holes are not desired. Considering the effect of defects on electron-hole recombination, a defect free semiconductor is required for the conversion process. For this kind of devices, charge carriers are required to transform into a voltage. This can be achieved via p-n junction which uses external contacts to the semiconductor to separate the direction of the charge carrier flows[11].
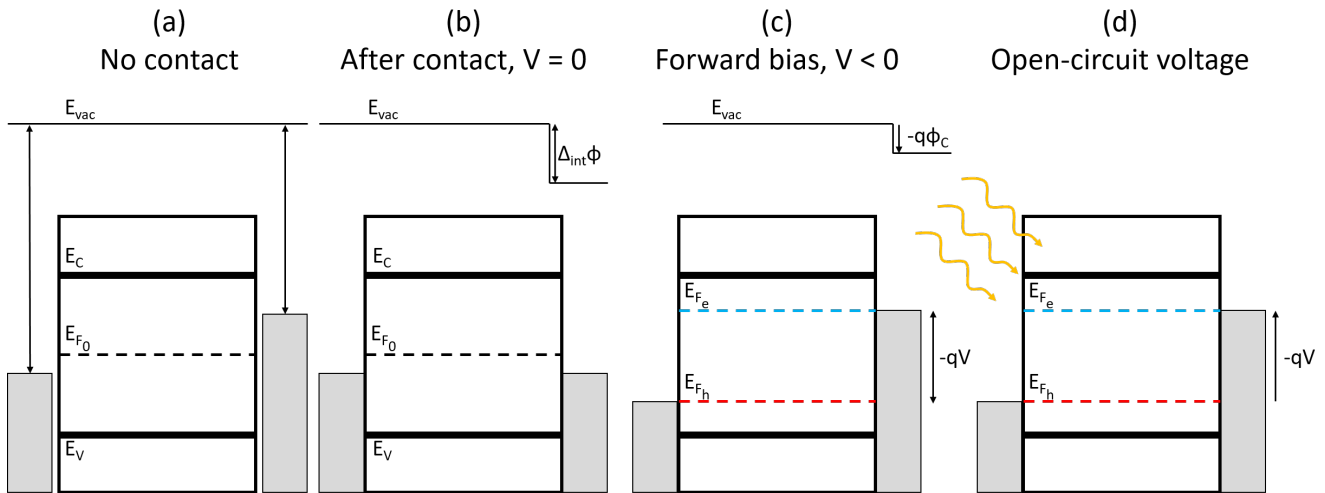
Figure 1.4: Illustration of the effect of contact layers in a solar cell.

One important aspect of contact layers is the work function. Work function defines the minimum thermodynamic energy needed in order to remove an electron from a solid to the vacuum level which is the energy level of an electron outside of any solid. In other words, work function is the energy difference between the Fermi level and the vacuum level. Figure 1.4 gives an illustration of

9

a diode with contact layers with different work functions. After putting all the materials in contact (Figure 1.4b), we see an equalization of the materials on a identical Fermi level. This equalization process can occur via band bending in the absorber layer or the modification of the vacuum level, E_{vac}. Any potential drop (vacuum level change) related to an applied voltage appears just at this interface, as shown for the forward bias in Figure 1.4c. The internal chemical potential μ_{np} is extracted and a voltage V is obtained which has the relation given in Equation (1.14)[11].

$$qV = E_{F_n} - E_{F_p} \tag{1.14}$$

1.2.1.1 Charge Selective Contacts in Solar Cells

In order to build functioning solar cells, segregation of charge carriers is required. This can be carried out by p-n junctions or charge selective contacts at each side of the absorber layer[17]. A p-n junction consists of two components of the same type of intrinsic semiconductor. The p-part is the p-type semiconductor whereas the n-part is the n-type semiconductor. In between there is a depletion zone due to n- and p-regions being in contact. The free electrons will be moving through the n-part to reach the electrode while the free holes are moving through the p-part to reach the other electrode. A setup with charge selective contacts can be considered as a p-i-n structure where i is the intrinsic semiconductor. A good charge selective contact should consist of a material that allows one charge type to pass while blocking the other charge type[11].

Charge selective contacts in a solar cell have two main functions. They cause charge extraction and injection asymmetry within the cell to maintain a diode structure. This way, the electrons can be extracted from one contact layer and retrieved at the other layer with a lower electrochemical potential. The second objective of the charge selective contact layers is to generate equilibrium quasi-Fermi levels under light illumination, while light illumination can only cause non-equilibrium quasi-Fermi levels. Therefore charge selective contact layers enable converting the energy difference of these levels into a voltage[11].

In order to maintain charge selectivity of the layers regarding electrons and holes, charge selective contact layers must have a work function offset with regard to the absorber layer. This difference in work functions generates an initial built-in potential within the solar cell. Figure 1.5a shows an illustration of an p-i-n type solar cell where the absorber layer is put in between a p-type hole transfer layer and a n-type electron transfer contact layer. The contact layers here slants the absorber bands at zero bias. Furthermore, as the names suggest, the electron transfer layer and hole transfer layers enables selective conduction of the charge carriers due to their available states for the electrons at lower energy levels compared the absorber layer.. An applied voltage affects the band structure of the device and results in flat bands (Figure 1.5b), thus the charge collection influenced by an electric field. The function of the contact layers here is mainly characterized by how much slant they cause in the absorber layer which affects the charge selection. The open-circuit condition under light illumination is achieved when the bands flatten and the charge extraction stops (Figure 1.5b)[11].
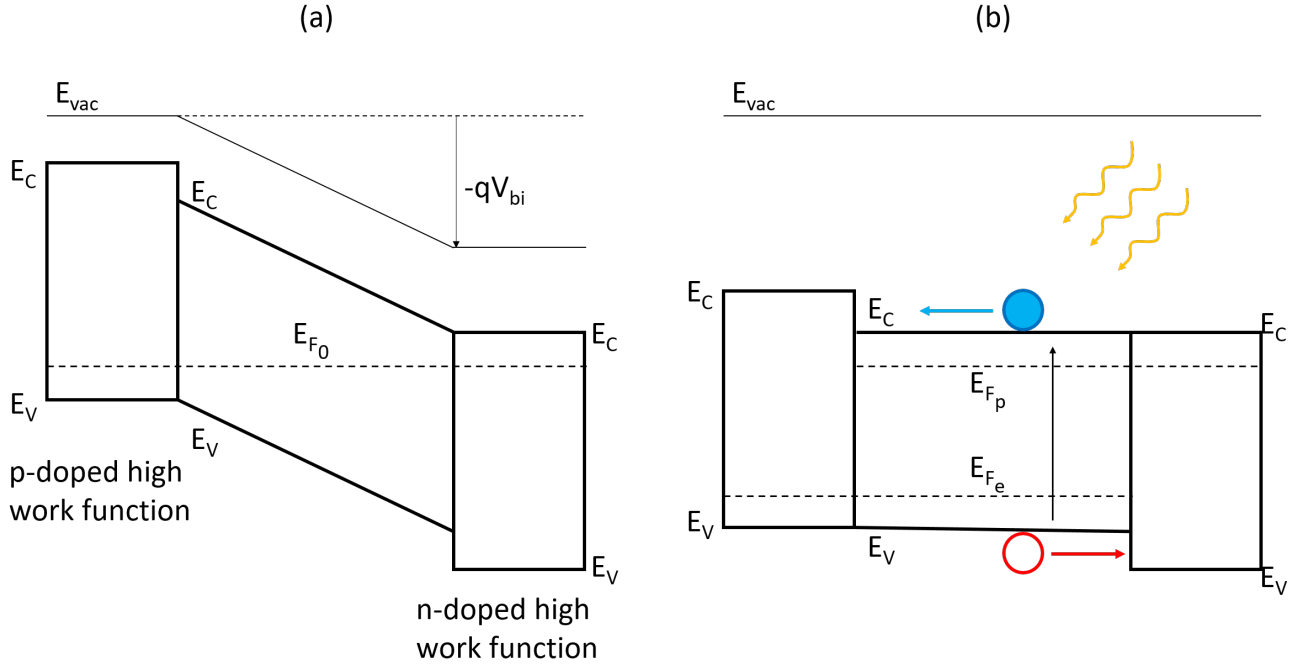
Figure 1.5: Illustration of a p-i-n solar cell (a) in equilibrium and (b) when bands flatten under light illumination, in open-circuit condition.

1.2.2 Solar Cell Parameters

The performance of a solar cell is characterized by power conversion efficiency (PCE); that is the ratio of the output electrical power to the input solar power as in Equation (1.15)[10]

$$PCE = \frac{P_{el}}{P_{sol}} \tag{1.15}$$

where P_{sol} is the solar power while P_{el} is the electrical power which is defined by photocurrent (I) and photovoltage (V) in Equation (1.16)

$$P_{el} = I * V \tag{1.16}$$

Comparison of different solar cells is generally performed via current density-voltage (J-V) curves that is given in Figure 1.6. A J-V curve is obtained through an external voltage sweep over the cell under dark or illuminated conditions. From a J-V curve, the main solar cell parameters short-circuit current density J_{SC}, open-circuit voltage (V_{OC}), fill factor (FF), and PCE can be obtained.

J_{SC} describes the current density provided by a solar cell at short-circuit conditions. J_{SC} mainly depends on photo-generated charge carrier population and their transfer via charge selective contact layers. The higher the number of free charge carriers, the higher the J_{SC}. Therfore, J_{SC} increases with decreasing bandgap since the number of photo-generated charge carriers will increase under same illumination conditions. Similarly, J_{SC} will also increase when the absorber layer of
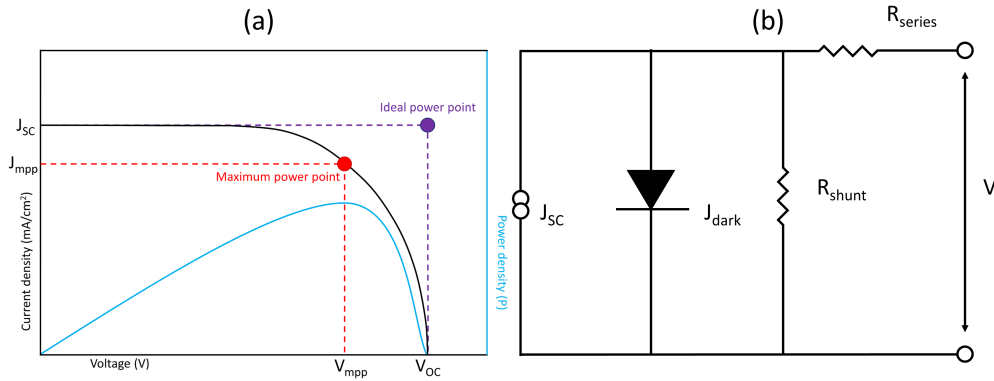
11

Figure 1.6: (a) Illustration of a typical J-V curve of a solar cell. (b) Illustration of a solar cell circuit with current density (J_{SC}), dark current density (J_{dark}), and series and shunt resistances (R_{series} and R_{shunt}, respectively).

the solar cell is thicker so it would absorb more of the incident photons. It reaches its maximum value in short-circuit condition when the voltage is zero.

V_{OC} is defined by the maximum potential difference between the electrodes of the solar cell during light illumination. The potential difference reaches to a maximum at open-circuit condition when the current density is at zero. V_{OC} is affected by the bandgap of the absorber layer of the solar cell. The higher bandgap will lead to a higher potential difference between the electrodes and the resulting V_{OC} will be higher. Since V_{OC} is the potential difference for the whole device, it is also affected by the contact layers as well. V_{OC} is limited by the conduction band minimum and valence band maximum of the charge selective contact layers in a solar cell constructed similar to the one illustrated in Figure 1.5. Last factor affects the V_{OC} is the defect density within the absorber layer of the solar cell. The V_{OC} is originated from splitting quasi-Fermi levels of electrons and holes in the photoexcited abosrber layer. Defects in the absorber layer lead to faster recombination of electrons and holes, leading to diminished quasi-Fermi level splitting. As a result, the V_{OC} will decrease[18].

The FF defines the maximum power output of a solar cell by estimating the ratio of the measured solar cell power output against an ideal solar cell with the maximum possible power output[19]. The power outputs of the measured solar cell and an ideal solar cell are given by the maximum power point (the point where the maximum power output is obtained) in Figure 1.6. The FF is calculated via the formula given in Equation (1.17).

$$FF = \frac{V_{MP}J_{MP}}{V_{OC}J_{SC}} \tag{1.17}$$

The FF is affected by the power losses within the solar cell. There are two internal mechanisms that cause power losses in the solar cell: shunt resistance and series resistance[10,20]. The shunt resistance is related to the leakage in the solar cell layers that creates alternative pathways for the photo-generated charge carriers. It can originate from pinholes within the film layers or lower

12

charge selectivity of the contact layers. The series resistance is the resistance in the solar cell layers against the photo-generated charge carriers. Therefore, it is affected by the absorber/contact layer interfaces as well as the conductivity of each layer. Therefore, layers with high thickness may result in higher series resistance ergo lower J_{SC}.

By using all these parameters mentioned above, we can estimate the PCE of a solar cell. If we convert the formula in Equation (1.15) to the mentioned solar cell parameters in a J-V curve as $P_{el} = P_{max} = V_{mpp} * J_{mpp}$, we would get the PCE formula given in Equation (1.18).

$$PCE = \frac{J_{SC} * V_{OC} * FF}{P_{sol}} \tag{1.18}$$

1.3 Halide Perovskites and Perovskite Solar Cells

This type of solar cells get their name from the perovskite absorber layer. Since then, the efficincies of PSCs increased significantly, reaching 25.5% as of 2022[21]. The high potential of halide perovskites as ideal solar absorbers come from their unique optoelectronic properties such as high absorption coefficient[22], low electron-hole binding energies[23], long charge carrier diffusion lengths[24], direct and tunable bandgaps[25], and indifferent electronic properties in presence of bulk defects, namely defect tolerance[26]. On top of these properties, easy thin film production from solution makes this material group ideal for mass production.

Despite their good optoelectronic properties and significant improvements they showed, halide perovskites still suffer from instability under ambient conditions[27]. Also high defect density at layer interfaces[28] and grain boundaries[29] and ion migration[30] during the device operations hinders their performances in practical applications.

1.3.1 Crystal Structure of Perovskites

The perovskite structure gets its name from the mineral calcium titanate ($CaTiO_3$) that was first discovered by Gustav Rose on Ural Mountains and named after Lev Perovski[31]. Generally, the class of perovsktie crystals is defined by a ABX_3 structure and consists of $[BX]^{-2}$ octahedras surrounded by A^{2+} cations (Figure 1.7). After the discovery of the perovskite mineral, any crystalline solid that obtains the similar crystal structure is referred as perovskite such as oxide perovskites including $BaTiO_3$ or $PbTiO_3$[32]. Similar to the oxide perovskites, other perovskite structures can be formed with different oxidation states as it occurs in halide perovskites. The most commonly used halide perovskite $MAPbI_3$ consists of $[PbI_6]^-$ octahedras surrounded by MA^+ cations[33].

Perovskites in general abide by the Goldschmidt tolerance factor which estimates the possible formation of a perovskite structure depending on the ionic radii of the components. Equation (1.19) gives the Goldschmidt tolerance factor[34].

$$\tau = \frac{r_A + r_X}{\sqrt{2}(r_B + r_X)} \tag{1.19}$$

where τ is the tolerance factor and r_A, r_B, and r_X stand for the ionic radii of A, B, and X ions, respectively. The value of τ determines the formation possibility of a perovskite structure. If τ lies between 0.8 and 1, the perovskite structure formation is favoured[34]. Moreover, τ values between 0.9 and 1 yield a cubic perovskite structure whereas values between 0.8 and 0.9 range yields distorted perovskite crystals[35].

According to the τ values, the ions in a perovskite structure can be substituted. The most common B^{2+} cation Pb^{2+} can be changed with Sn^{2+}, Mn^{2+}, or Ge^{2+}. Halogen ions (Cl^-, Br^-, I^-) can be used as X^- anions. Lastly, the A^+ cations can be an element such as Cs^+ or larger organic cations such as or formamidinium. The size of the A^+ may lead to unstable or metastable perovskite phases due to the τ value[36].

Cubic	Tetragonal	Orthorhombic
a = b = c	a = b ≠ c	a ≠ b ≠ c
α = β = γ	α = β = γ	α = β = γ

A — A
X — X
B — B
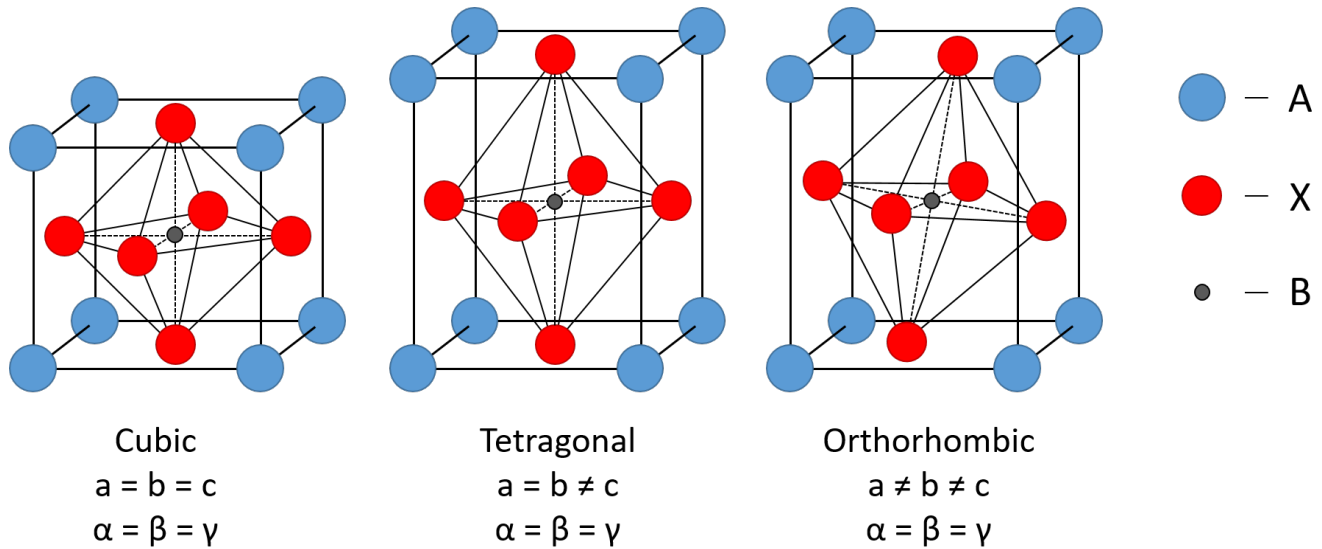
Figure 1.7: Illustration of ABX_3 perovskite crystal structure.

1.3.2 Electronic Structure of Halide Perovskites

Halide perovskites are direct bandgap semiconductors that have strong absorption in the visible or near-infrared part of the electromagnetic spectrum[37,38]. They have high optical absorption coefficients that enable efficient light absorption even in thin active layers, making them excellent candidates for use as an active layer in solar cells or photodetectors. The valence band of halide perovskites formed by anti-bonding of s-orbital from B^{2+} cation and p-orbital from X^- halide. The conduction band is consists of anti-bonding p-orbitals from B^{2+} cation and X^- halide[39,40].

The band structure of halide perovskites is also suitable for modification via ion substitution. Substitution of B^{2+} cation or X^- halide directly affects the band structure. As the halide changes from Cl^- to Br^- to I^-, the energy of the p-ortbital increases which results in increased valence band maximum, i.e. bandgap reduction[41]. In a similar fashion, substitution of Pb^{2+} with Sn^{2+}

leads to increase of the s-orbital, which results in bandgap decrease[42]. The ability to engineer the composition of metal halide perovskites has a direct impact on their bandgap, which can be tuned to cover a broad spectral range. For instance, the wide bandgap of $MAPbCl_3$ (3.11 eV) can be narrowed down to 2.35 eV for $MAPbBr_3$, and further to 1.55 eV for $MAPbI_3$ by partial substitution, allowing the bandgap of the material to be tuned between these values and cover almost the entire visible spectrum[43–45].

1.3.3 Defects in Halide Perovskites

Defect state formation in a semiconductor material can be a limiting problem for some applications due to resulting trapping of excited charge carriers. Therefore, the energy level of the trap states can determine the trapping behavior of the free charge carriers. If the defect state lies within or close to the bands, the trapped charge carriers can be thermally excited before recombination. These type of defect states are called shallow trap states. On the contrary, if the defect state is close to the middle of the bandgap, the trapped charge carriers are less likely to thermally excited to be free. These type of defect states are called deep trap states. The shallow trap states are typically benign to the performance of the semiconductor where deep traps are responsible for non-radiative recombination[46,47].

In halide perovskites, even though deep traps can occur due to interstitials (atoms occupying an interstitial site in the crystal lattice) and anti-sites (atoms occupying the position of another ion of a different type), the most common defect type is the point defect which leads to formation of shallow traps due to their low formation energy[18]. These type of defects usually do not affect the performance of perovskite based devices. Even though the bulk of the halide perovskite are defect tolerant, the surfaces of halide perovskite are more prone to have deep traps due to surface defects[48]. Therefore, high defect areas such as grain boundaries are known to contribute to trap-assisted recombination[49,50] and ion migration[51–53].

1.3.4 Ferroelastic Twin Domains in MAPbI$_3$

Crystal twinning is a phenomenon where two or more crystal domains are formed within a single crystal structure, where each domain has a different orientation but the same lattice structure. These domains, known as twin domains, are related to each other by a mirror or rotation symmetry operation. Crystal twinning can occur during crystal growth due to variations in the growth conditions, or during deformation of a crystal due to applied stress. Twinning can affect the physical and mechanical properties of a crystal, including its hardness, cleavage, and optical properties[54].

Ferroelasticity is a property of materials in which reversible deformations occur in response to an applied stress or external field. This deformation is due to the rearrangement of domains within the crystal structure, leading to changes in the shape or size of the crystal[55]. Ferroelastic materials may exhibit a reversible phase transformation between two or more crystal structures with different symmetries. This transformation is accompanied by the formation of domain walls

or twin boundaries, which separate the different domains within the crystal structure. Ferroelasticity is a common property of many materials, including ceramics, metals, and polymers, and is important for many technological applications, such as actuators, sensors, and memory devices.

The formation of ferroelastic twin domains in $MAPbI_3$ is due to crystallographic symmetry. $MAPbI_3$ has a perovskite crystal structure with a tetragonal symmetry. The tetragonal unit cell can be described by the lattice parameters a, b, and c, where a = b $\neq$ c. The tetragonal symmetry of $MAPbI_3$ allows for the formation of twin domains along the c-axis, which is the axis of lower symmetry. Typically, ferroelastic twin domains show 90° angle with each other[56]. However, it was also reported that the increased stress on $MAPbI_3$ crystal may lead to non-90°domain angles[57]. Various techniques have been used to characterize the ferroelastic twin domains in $MAPbI_3$. They were first discovered via PFM[56]. Other than that, they can be observed via X-ray diffraction (XRD)[57,58], scanning electron microscopy (SEM)[59], transmission electron microscopy (TEM)[60], or polarized optical microscopy (POM)[61].

1.3.5   Perovskite Solar Cells

PSCs are typically based on three device architecture type. These are p-i-n, n-i-p mesoporous, and n-i-p planar solar cells. The n, i, and p names assigned to the layers represent n-type, intrinsic, and p-type semiconductors. A typical n-i-p PSC illustration is given in Figure 1.8a. Here, electron transport layer (ETL) is coated on top of indium tin oxide (ITO) or fluorine doped tin oxide (FTO). The most common ETL materials for n-i-p PSCs are TiO_2 and SnO_2[62]. The perovskte absorber layer is coated on an ETL and then a hole transport layer (HTL) is coated on top of perovskite. The typical HTL materials for n-i-p PSCs are Spiro-OMeTAD and Poly[bis(4-phenyl)(2,4,6-trimethylphenyl)amine (PTAA)[63]. Lastly, a metal layer (gold, silver, aluminium, copper etc.) is evaporated on top of the PSC as an electrode[64]. When the ETL in a n-i-p PSC includes a mesoporous component to improve the contact and charge extraction from the perovskite layer, the device architecture is named mesoporous n-i-p PSC. Usually TiO_2 based PSCs are built as mesoporous n-i-p PSCs which consists of a compact TiO_2 and on top a mesoporous TiO_2 layer[65]. On the other hand, SnO_2 based PSCs are usually built as planar n-i-p PSCs[66]. If an HTL is coated on top of ITO or FTO to be further coated by the perovskite layer, then the device is called a p-i-n PSC. The common HTLs for p-i-n PSCs are NiO_x[67] or PTAA[68] whereas common ETLs for p-i-n PSCs are C60/BCP or PCBM[69].

As discussed before, the charge selective contacts can affect the photo-generated electron-hole population due to respective extraction of electrons and holes, non-radiative recombination due to interfacial defects, and charge accumulation in the semiconductor they are in contact with. Figure 1.8b shows the band alignment of the contact layers with the perovskite layer. The band alignment in such way allows electrons to relax to the conduction band of the ETL instead of the valence band of perovskite, which enhances electron extraction and charge carrier lifetime. Similarly, the the bands of HTL stand at a higher energy level compared to the that of perovskite layer. Therefore, the photo-generated holes move towards to HTL. The ETL / perovskite and perovskite / HTL interfaces are extremely important regarding the efficiency of a PSC. The defects at the devices interfaces can act as non-radiative recombination sites and decrease the efficiency of
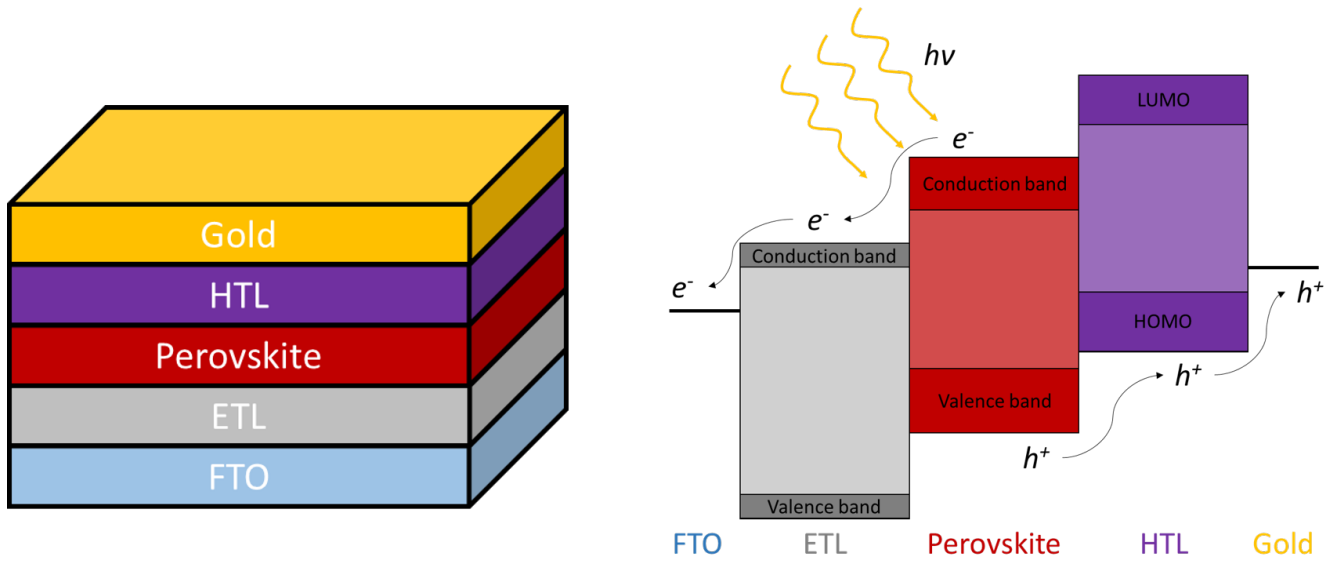
Figure 1.8: PSC architecture and the band alignment

the device. To counter this issue, the contact layers can be improved[70] or thin interlayers between perovskite and the contact layers can be formed[21].

The performance and stability of PSCs can be affected by the movement of ions within the perovskite crystal lattice, known as ion migration[71]. The mechanisms of ion migration in PSCs can involve both intrinsic and extrinsic factors. Intrinsic factors include the presence of defects in the perovskite crystal lattice, such as vacancies or interstitials, which can create a gradient of ion concentration and lead to ion migration[18]. Extrinsic factors include the presence of external electric fields, thermal gradients, or light irradiation, which can also induce ion migration in PSCs[72]. Ion migration can have a significant impact on the performance of PSCs, particularly in terms of efficiency and stability. For example, the migration of organic cations can contribute to degradation of the perovskite material over time, leading to decreased efficiency and stability of the solar cell[71]. Additionally, ion migration can affect the charge carrier recombination dynamics and the transport properties of the perovskite material, further impacting device performance. Controlling ion migration is crucial for improving the performance and stability of PSCs. Various strategies have been proposed to mitigate ion migration, including the use of different types of cations or the addition of other materials to the perovskite to improve ion dynamics. Additionally, surface passivation, the use of interface layers, and the optimization of device fabrication conditions have been shown to reduce ion migration and improve device performance and stability.

1.4 Characterization Techniques

Understanding the characterization methods for perovskite materials in PSCs is crucial for unlocking the full potential of this promising technology. These methods provide insights into the structural, chemical, and electronic properties of perovskite layers, enabling researchers to optimize their composition and performance. By delving into the intricate details of perovskite

17

characterization, we can overcome challenges, enhance efficiency, and ultimately pave the way for a cleaner, more sustainable energy future. Characterization is the key to unraveling the mysteries of PSCs and harnessing their incredible potential for renewable energy generation.

1.4.1 Atomic Force Microscopy

AFM simply is a device consisting of a sharp tip mounted on a lever that moves over the surface of the sample. The illustration of a standard AFM measurement is given in Figure 1.9. The tip on the lever is referred as a cantilever and typically made out of silicon-based substances. During the scanning, the tip acts as a detector to measure the topography and several types of interactions may occur between the tip and the sample, such as van der Waals interactions, electrostatic interactions, chemical interactions, and magnetic interactions. Measuring these interactions between the tip and the sample provides additional information about the surface. The the tip deflection caused by the interaction forces are detected by the laser beam pointed towards a photo-diode after being reflected on the back side of the cantilever[73].

During an AFM measurement, the sample movement for the scanning is controlled by x-, y-, and z- scanners while the relative tip-sample position is controlled by a z-piezo element to which the cantilever is connected[74]. When the tip is away from the with a considerable distance, no force acts on the cantilever. When the distance reduces to a few nanometers, the cantilever enters to the force field of attractive van der Waals[75] and electrostatic forces[76] which leads to the cantilever to deflect downwards. Further approach of the tip causes the cantilever to return to its rest position until Pauli repulsion causes the upwards deflection[77]. Additional adhesive forces take part when the tip is being retracted, leading to a delayed withdrawal of the cantilever from the surface.

The AFM has several modes which indicates the way how the AFM cantilever is driven[78]. The three most common AFM modes are contact mode, non-contact mode, and tapping mode. Non-contact mode is usually considered under ultra-high vacuum conditions. In contact mode, the cantilever is constantly in contact with the sample during the whole measurement. In tapping mode, the cantilever is tapped at the surface at a certain frequency which is typically the first resonance frequency of the cantilever while scanning across the surface at a distance. Since the tip is not constantly touching the surface, the effect of the measurement on the damage applied to the sample is compared to contact mode.

There are several different modulation types that can be used in AFM, including most common methods amplitude modulation and frequency modulation . Amplitude modulated AFM (AM-AFM) involves modulating the amplitude of the cantilever oscillation, while freqeuency modulated AFM (FM-AFM) involves modulating the frequency of the oscillation. Each of these modulation types has its own advantages and disadvantages, and the choice of modulation type depends on the specific application and the properties of the sample being studied[79]. Although, it has been shown that electrical AM-AFM modes are more prone to topographical cross-talks compared to FM-AFM modes, therefore less reliable to use in applications like KPFM[80].

During tapping mode AFM operation, the cantilever is regarded as a driven harmonic oscillator

which is damped by the interaction between the tip and the sample. The optical beam deflection setup constantly measures the amplitude of the cantilever and the sample is moved in the x and y planes during the scan. The changes in the amplitude during the scan will be detected by the feedback system and the amplitude will be reset back to the setpoint amplitude. Finally, the topographical image is generated by the z-piezo signal[81].

Any interaction that gives rise to a sufficiently strong tip sample force can be measured by AFM. Therefore on top of the topography, AFM can be used to detect other properties of a surface such as Young's modulus, electrical properties, and magnetic properties. Therefore, AFM system can be used as a circuit on nanoscale to characterize the electrical properties of semiconductor material and devices. For perovskite research we will be focusing on 2 electrical AFM modes: PFM and Kelvin probe force microscopy (KPFM).
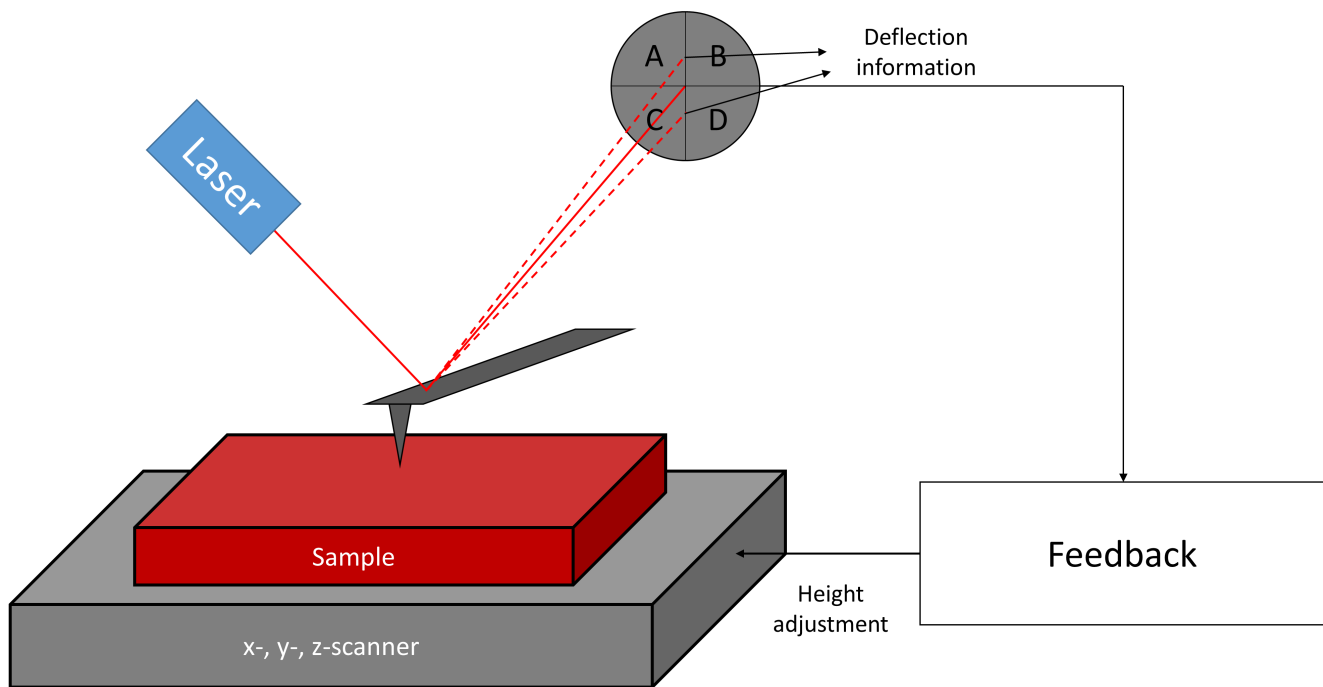
Figure 1.9: The configuration of a contact mode AFM setup. A force-sensing tip mounted on a cantilever scans the sample surface in the x and y directions, while changes in the cantilever's z-displacement (deflection) due to surface topography are detected using optical beam deflection. In this method, a laser beam is directed onto the backside of the cantilever and then reflected onto a four-quadrant photodiode at an angle determined by the cantilever's deflection. The movement of the reflected beam is sent to a feedback control system that compares the measured deflection to a predefined deflection setpoint. This system adjusts the tip-sample distance through the z-scanner height to maintain a constant tip-sample force. Both the topography and feedback error channels provide valuable information about the surface structure.

19

1.4.1.1 Conductive Atomic Force Microscopy

With a C-AFM, it is possible to probe the local electric, ionic or capacitive conductivity of the sample. In C-AFM, a voltage is applied between the sample and a conductive probe. A sensitive current amplifier, which is usually integrated into the cantilever holder, detects the tip-sample current. Depending on the conductivity and the applied voltage, currents are on the order of pA up to μA. The most common operation mode of C-AFM is contact mode, where the probe tip and the sample are in constant mechanical contact. However, high shear forces during the scanning motion of the tip make this method unsuitable for soft materials such as organic materials or nanorods. Moreover, C-AFM can be used to measure photoconductivity of photo-active materials by measuring the current under light illumination[82,83].

1.4.1.2 Piezoresponse Force Microscopy

PFM is a electrical AFM measurement that is performed in contact mode and it is used to measure the electromechanical properties of samples (Figure 1.10). It utilizes an AC voltage applied to the sample via a conductive AFM tip and the inverse piezoelectric effect from the sample. Under AC voltage, the sample undergoes a displacement which is detected by the AFM tip. This process continues as the scan carries on. The mechanical oscillation generated on the tip by the applied AC voltage is detected as periodic defclection of the cantilever by a lock-in-amplifier. The piezoelectric coefficient is revealed by the amplitude of the sample oscillation. Any changes on the sample surface like domain changes is detected by the changes in the oscillation amplitude and phase. These information, especially the phase, can be used to examine the angle between alternating domains[84]. PFM can be conducted vertically to detect out-of-plane domains and laterally to observe in-plane domains as shown in Figure 1.10.
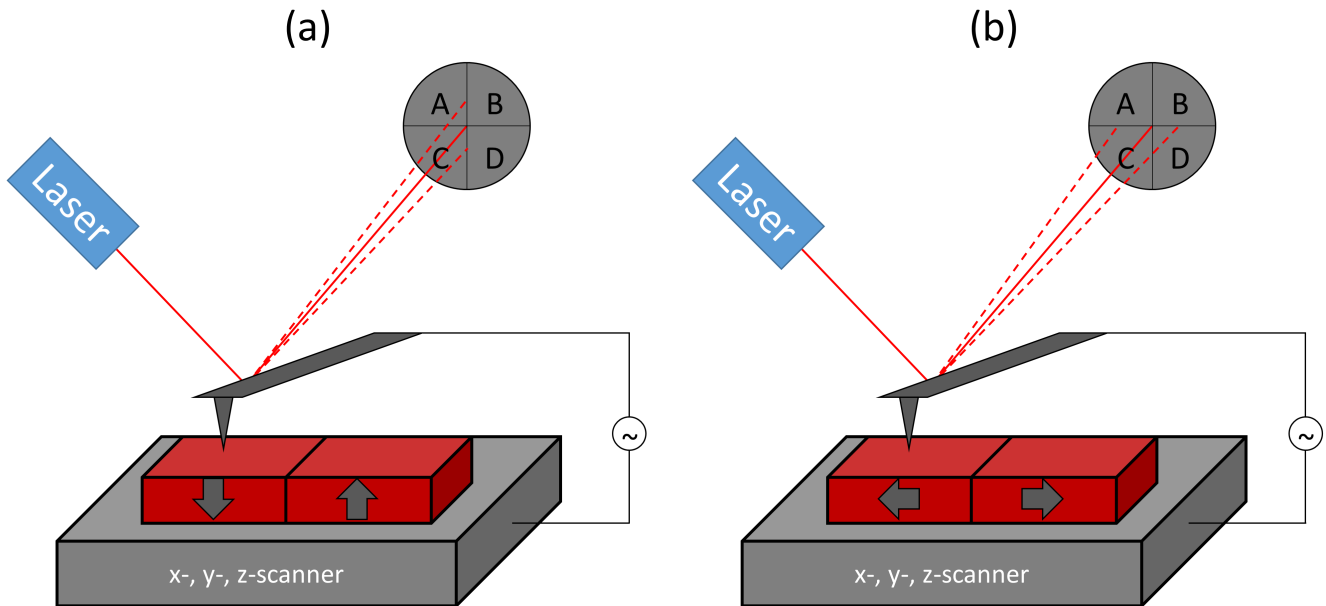
Figure 1.10: Illustration of the (a) vertical and (b) lateral PFM scanning.

Since piezoelectric displacement for an applied voltage is within the range of pm/V, the piezoresponse detection is difficult via PFM. In order to increase the signal intensity, the frequency of applied AC voltage is around the contact resonance of the cantilever. The resonance of an AFM cantilever changes when it is in contact with a sample, therefore the contact resonance is not equal to the free resonance of the cantilever. Although, performing PFM measurements around the contact resonance is not so straightforward. Significant topographical changes on the sample during the scan may shift the contact resonance and may cause a PFM contrast since the signal is boosted by applying AC voltage around the contact resonance. Nevertheless, during a scan in which the tip-sample contact area remains unchanged, contact area and subsequent PFM contrast may originate from a physical feature of the sample[84,85].

1.4.1.3 Kelvin Probe Force Microscopy

If two materials (or one tip and one sample) with different work functions Φ_1 and Φ_2 are electrically connected as in Figure 1.11a, their Fermi levels align, generating an electric field E. The contact potential difference (CPD or V_{CPD}) between the this electric field will lead to an attractive force between tip and sample Equation (1.20). During a KPFM measurement, V_{CPD} is detected and nullified by a DC bias, V_{DC} and the value of V_{CPD} is determined by the value of V_{DC}[86,87].
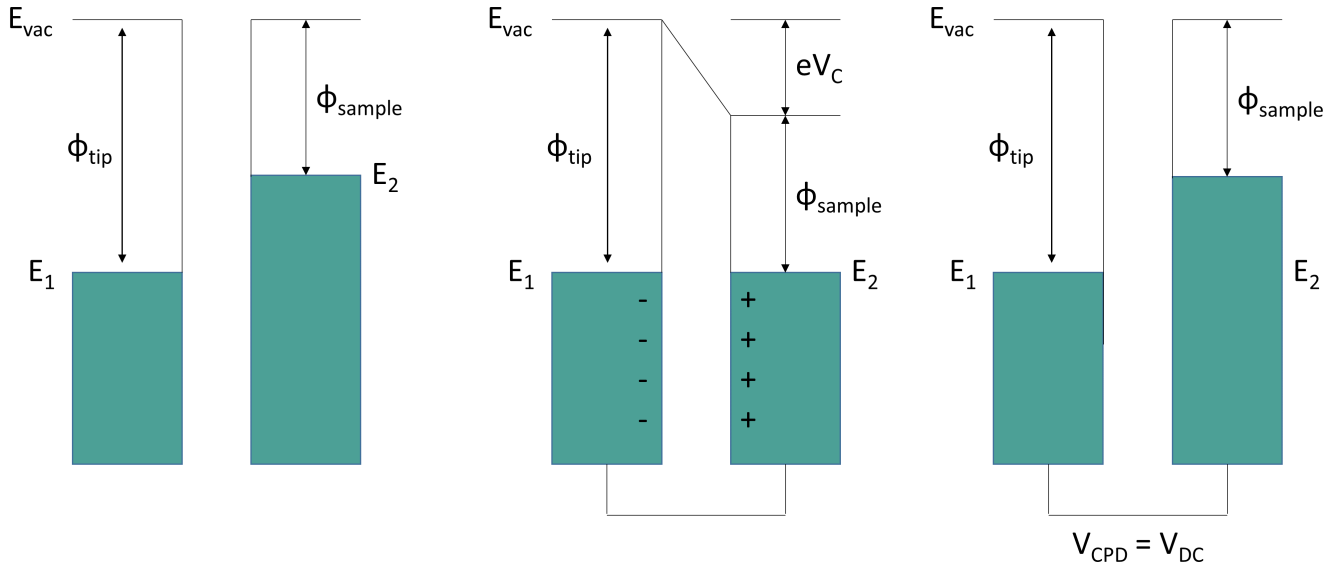
Figure 1.11: Illustration of the KPFM working principle.

$$V_{\mathrm{CPD}} = \frac{E_F^{\mathrm{tip}} - E_F^{\mathrm{sample}}}{e} \tag{1.20}$$

On insulating surfaces, such as polymers and ceramics, electrostatic fields can arise from uncompensated static charges close to the surface[88,89]. These charges will generate image charges in a metallic tip, leading to an attractive force. Here, we will focus on the case of metallic and semiconducting surfaces, as they are more relevant to energy materials.

An AC bias, V_{AC} is applied to a conductive cantilever during a KPFM measurement to enhance the electrostatic field between the tip and the sample. KPFM system can be considered as a capacitor with capacitance C and we can get the electrostatic force given in Equation (1.21)[87].

$$E = \frac{1}{2}\frac{\partial C}{\partial z}(\Delta V)^2 \tag{1.21}$$

where z and $\Delta V = V_{ext} - V_{CPD}$ are the distance and potential difference between the tip and the sample, respectively, while V_{ext} being the all external voltages to the tip or the sample. When the sample is grounded and external AC and DC voltages are applied ($V_{ext} = V_{DC} + V_{AC}sin(\omega_E t)$, the electrostatic force would be the sum of three following components that describes static deflection of the cantilever (Equation (1.22)), force component at frequency ω_E (Equation (1.23)), and the capacitance relation at frequency $2\omega_E$ (Equation (1.24))[90]:

$$F_{\text{stat}} = \frac{1}{2}\frac{\partial C}{\partial z}\left[(V_{DC} - V_{CPD})^2 + \frac{V_{AC}^2}{2}\right] \tag{1.22}$$

$$F_{\omega_E} = \frac{\partial C}{\partial z}(V_{DC} - V_{CPD})V_{AC}sin(\omega_E t) \tag{1.23}$$

$$F_{2\omega_E} = -\frac{1}{4}\frac{\partial C}{\partial z}V_{AC}^2cos(2\omega_E t) \tag{1.24}$$

The second component is eliminated when $V_{CPD} = V_{DC}$ is satisfied and V_{CPD} can be obtained.

1.4.1.3.1 KPFM Methods

Before going into the KFPM modes, one needs to understand the resonance frequencies of the cantilever during a KPFM measurement. The eigenmodes of the cantilever is given in Figure 1.12.

In amplitude modulated KPFM (AM-KPFM), the amplitude of the cantilever frequency at ω_E is tracked during the measurement. The resonance frequencies shift due to the forces on the cantilever. Since topographical features may also shift the first resonance frequency, topographical cross-talk cannot be avoided during AM-KPFM[80,86].

In frequency modulated KPFM (FM-KPFM), the applied AC voltage, V_{AC} causes a modulation of the electrostatic force and this force is detected by the osilaction an frequency, ω_E of the frequency variation of f_1. The measurement range of frequency, ω must be chosen carefully. The chosen lower limit determines the cross-talk from the topographical signal. When higher freqcuencies are selected, the coupling between the topography and CPD. On the other hand, even though the cross-talk between topography and CPD decreases with increasing frequency, ω_E, the signal intensity of the electrostatic force also decreases due to the limited bandwidth of the frequency demodulator, which is a limitation independent of the cantilever type. Furthermore, an AC voltage of minimum 2V is required to obtain sufficient sensitivity, which may affect the topography signal or cause enhanced band bending in semiconductor samples[91]. Therefore, AC voltages during FM-KPFM must be minimized.
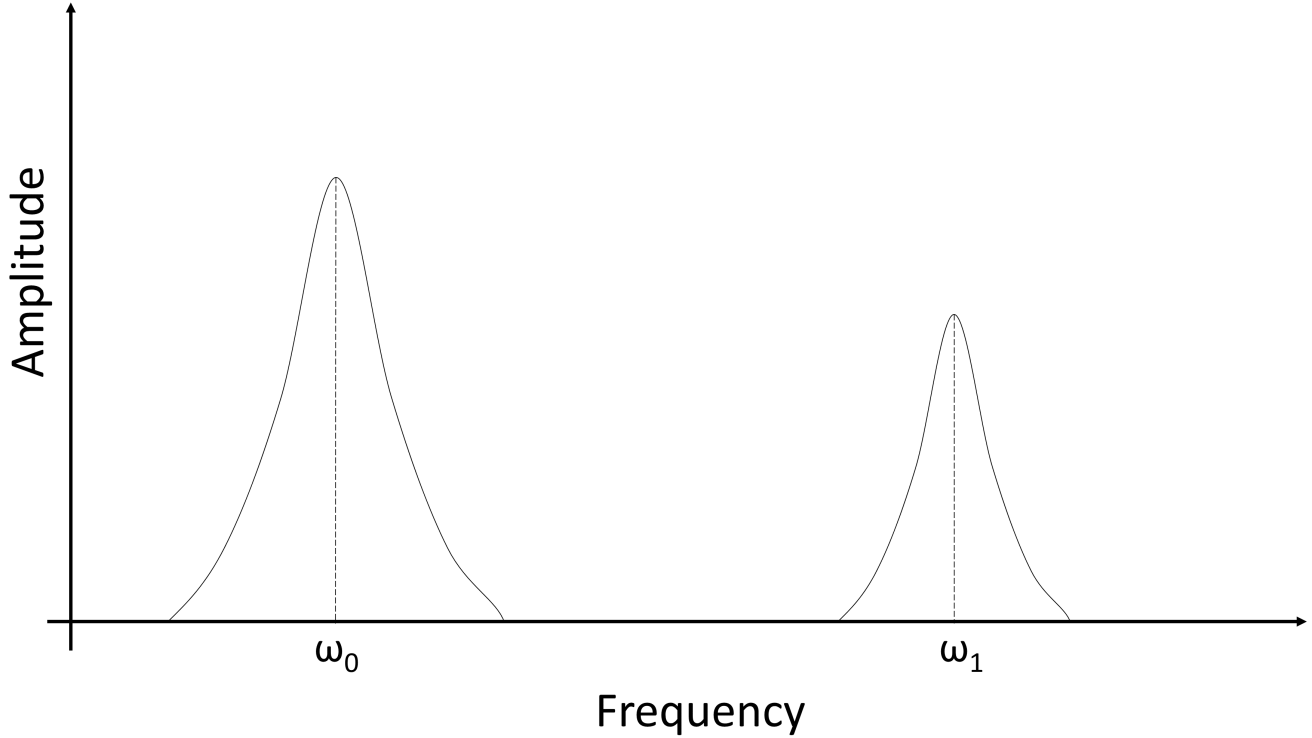
Figure 1.12: Cantilever frequency eigenmodes.

In FM heterodyne KPFM, different frequencies to measure the topography and V_{CPD} are used during the same scan. Applying the AC voltage at different frequencies than ω_0 causes a frequency mixing and additional signals form at $\omega_0 \pm \omega_{AC}$ in the frequency spectrum of the cantilever. Choosing the AC voltage frequency with $\omega_{AC} = \omega_1 - \omega_0$ leads to appearance of an additional peak that overlaps with ω_1 and higher signal-to-noise ratio. The KPFM feedback to nullify V_{CPD} with V_{DC} takes place at ω_1 while topography measurement is carried out at ω_0. Therefore, FM heterodyne KPFM enables KFPM measurements with higher resolution than AM-KPFM with lower topographical cross-talk while maintaining higher scan rates compared to FM-KPFM[87].

1.4.1.3.2   Contributions to the Local Contact Potential Difference

The CPD maps of a sample can be obtained after a KPFM measurement which can be used to characterize the electronic properties of the sample on the nanoscale. However, great care needs to be taken when interpreting CPD maps. Therefore, possible contributions to CPD during KPFM measurement should be addressed. The first possible contribution to CPD image is the cross-talk between the topography image and the CPD image. Even when FM mode is utilized during KPFM measurement, this effect can not be fully eliminated. Especially, when the topography takes extremely sharp edges the effect of the tip geometry can be also seen on the CPD map. Moreover, any phase jumps of the oscillation of the cantilever will be reflected to the CPD images[92].

The CPD values can also change on the chemical features within the sample. Two different phases within the same sample that have different work functions will be showing different CPD

values[93] on the map as well as the different facets[94] of the same phase can exhibit different CPD signals. Therefore KPFM can be used to detect any segregated phases or the orientation of the grains within the films.
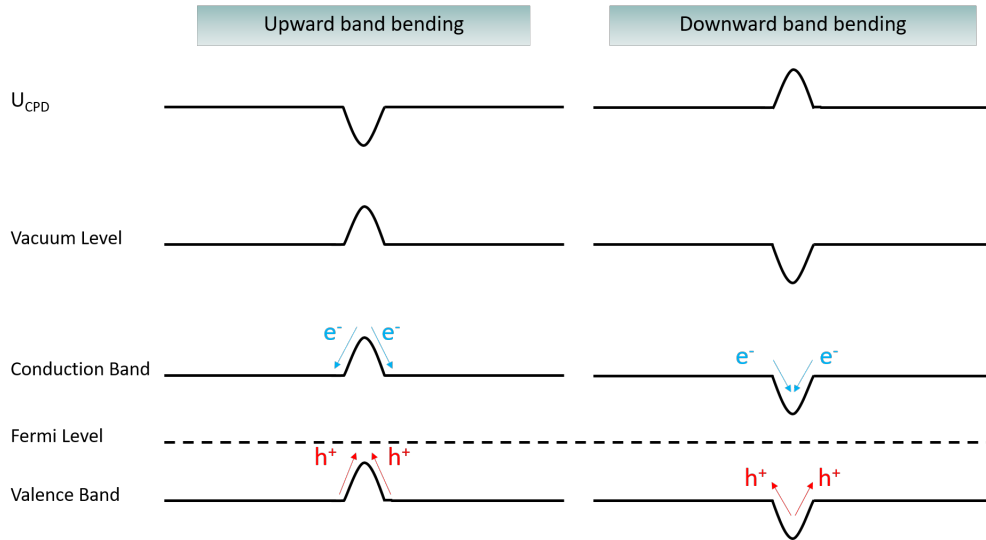
Figure 1.13: The band bending contribution to CPD signal.

The CPD of the sample will also be affected by the local changes within the band structure such as band bending[80, 95]. Band bending is caused by the charge accumulation caused by defect states within the material. The band bending is a result of charge accumulation and can occur in two ways as upward band bending and downward band bending (Figure 1.13). The type of band bending depends on the type of defect present in the structure which affect the type of charge that accumulates. Downward band bending occurs due to donor type defect states which results in electron accumulation and increase in V_{CPD}. On the contrary, upward band bending occurs due to acceptor type defect states which leads to hole accumulation and it decreases V_{CPD}. Since the CPD changes can be tracked via CPD maps, KPFM stands as a useful tool to localize defects in the halide perovskite films.

1.4.2 Supporting Techniques

Through the AFM-based methods, local information about the conductivity, defect density, band bending, domains in halide perovskite structures and devices can be obtained. Nonetheless, further characterization of the perovskites is still required to assign the results we can obtain via AFM to the occurrences within the perovskite films. To this end, methods such as XRD to assign the crystal lattice and the strain within the crystal lattice of the sample, UV-Vis spectroscopy to monitor the bandgap of the sample, PL spectroscopy to gain information about the electron-hole recombination dynamics and defect density within the sample, and time-of-flight secondary ion mass spectroscopy (ToF-SIMS) to map the chemical component profiles in the sample.

1.4.2.1 X-ray Diffraction

The interaction of periodically stacked structures with waves results in diffraction if the periodicity of the stacks and the wavelength are of similar magnitude. To this end, x-rays can be generated to correspond to the unit cell parameters of crystal lattices. Therefore, XRD can be used to characterize the stacking of the atoms and ions in a crystal structure which allows researchers to identify the crystal structure. Also, since XRD is greatly affected by the diffraction which depends on the periodicity of the crystal structure, any deviations or differences from the reference crystal lattice such as phase change, twinning, and strain can be monitored via XRD.[96].

Once the x-ray beam is pointed at a sample, the x-rays scatter from the lattice planes within the sample. When the path of the wave scattered off the lower two planes is longer by an integer number (n) of wavelength (λ) than that of the wave scattered off the upper plane, constructive interference occurs. The reflection off of the plane will follow the Bragg equation[97]:

$$n\lambda = 2dsin\theta \tag{1.25}$$

where θ is the angle between the lattice planes and the incident X-ray beam and d is the interplanar distance within the crystal lattice[98].
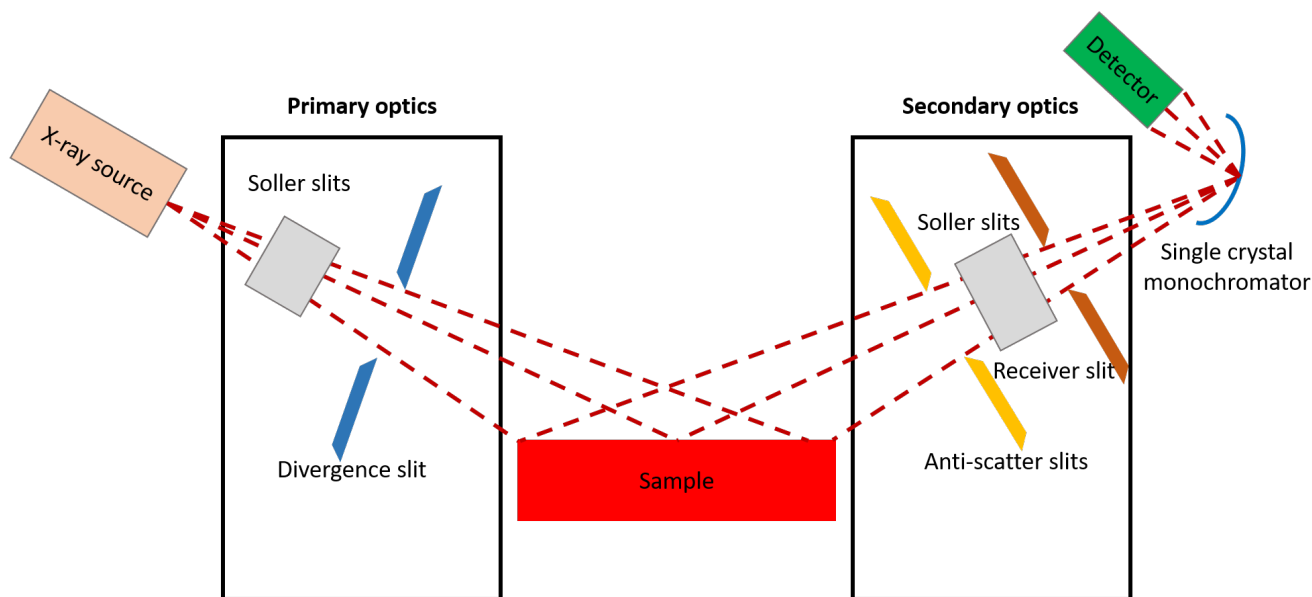
Figure 1.14: The schematics of a standard XRD measurement.

Figure Figure 1.14 shows the schematics of a standard XRD measurement. The monochromatic incident X-ray beam is generated by a cathode ray tube and aimed towards to the sample. The periodicity of the crystal lattice leads to the diffraction of the X-ray beams which follows Bragg's law (Equation (1.25)). Finally, the X-ray beams that were reflected off of the sample are collected

by the detector. The diffraction pattern which consists of diffraction peaks at different 2θ angles obtained in the end are used for identifying the crystal structure.

1.4.2.2 UV-Vis Spectroscopy

Characterizing the optical properties is a good way to estimate the band structure in semiconductors. Only photons with energy equal to or higher than semiconductor's bandgap can be absorbed and excite electrons from valence band to the conduction band. Therefore, measuring absorption properties of a semiconductor by exposing to photons with varying wavelengths would give the bandgap energy. UV-Vis spectroscopy is the typical method to measure the absorption capabilities of semiconductors within the UV and visible light range. This technique relies on the Beer-Lambert law[99].

$$A = log\frac{I_0}{I} \tag{1.26}$$

where A is the absorbance, I_0 is the incident light intensity, and I is the transmitted light intensity.
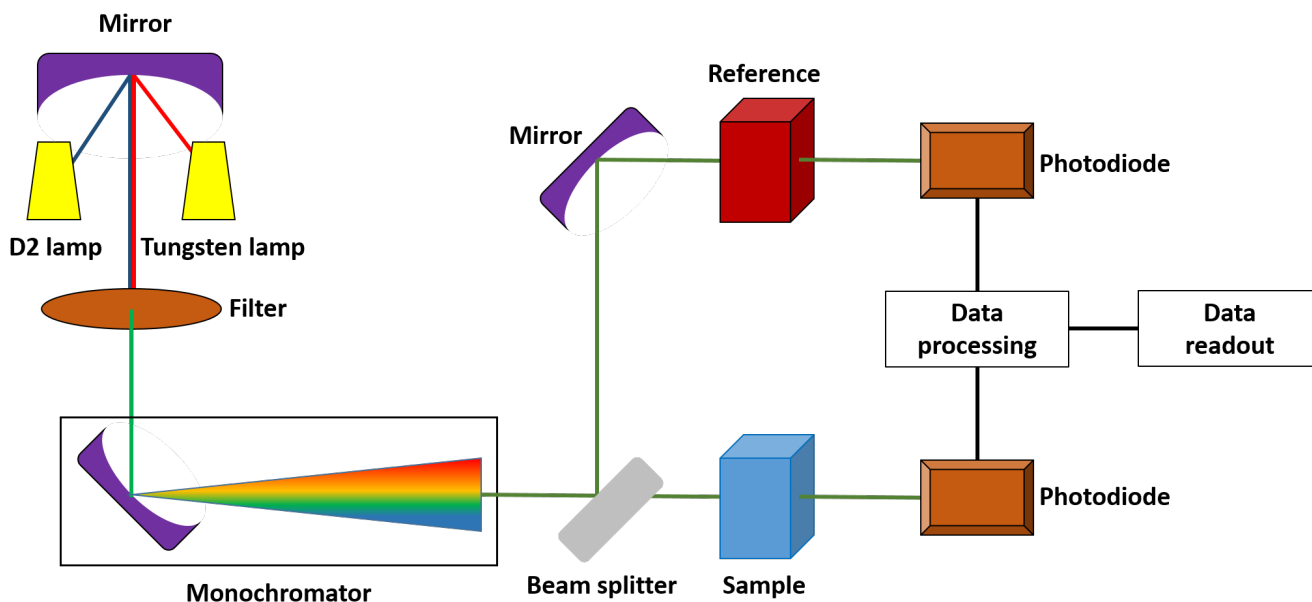
Figure 1.15: The schematics of a standard UV-Vis spectroscopy measurement. The beam splitting is sometimes used to measure the reference sample and the sample at the same time.

The operation of a UV-Vis spectrophotometer works as illustrated in Figure 1.15. The measurement starts when the lamp emits photons in UV or visible light range. The deuterium lamp is the source for the UV light whereas the tungsten lamp emits the visible light. The light then reaches to the monochromator in which two slits separated by a prism or a diffraction grating is used. The monochromator produces a light beam with a narrow bandwidth or a wavelength

range. The first slit of the monochromator lets the initial light beam pass through and refracted into the prism, leading to generation of photons with varying wavelengths. Among these, only a single wavelength passes through the second slit. The beam splitter divides the light beam into two with the same intensity to compare the measurements of the reference and the sample. In order to avoid interpreting scattering of light as absorption of the sample, a spherical contraption that reflects all scattered light into the detector named integrating sphere can be used.

1.4.2.3 Photoluminescence Spectroscopy

As mentioned in previous chapters, PL is the energy emission caused by a radiative recombination process. Therefore, PL spectroscopy can give information about band structure and defect density of a measured semiconductor material[100]. The most common PL spectroscopy measurements are steady-state and tr-PL spectroscopy methods. Figure 1.16 shows an illustration of a typical PL spectroscopy setup. The setup for both of these measurements are similar with minor changes in the components[101].

As mentioned previously, PL is the result of the radiative recombination in a direct bandgap semiconductor. Therefore, PL based methods can give information about the band structure and defect density within the semiconductor sample. By exploiting the PL properties of the sample, two types of PL spectroscopy measurements can be performed: Steady-state PL spectroscopy and tr-PL spectroscopy. Figure 1.16 shows the illustration of a typical PL spectroscopy setup. The setup for both of these measurements are similar with minor changes in the components. The steady-state PL technique shares a similar arrangement with tr-PL, but with the addition of a charge-coupled device detector placed behind the monochromator. This allows for the simultaneous capture of the entire spectrum. Solid-state laser diodes are the most popular excitation sources in modern instruments due to their availability in various wavelengths and laser power options. The excitation and detection process can either be performed in a con-focal arrangement or with separate beam paths[101]. Since, PL quantum yield is practically the ratio of emitted photons to the absorbed photons and non-radiative recombination of electrons-holes are indicators of defects within the semiconductors, steady-state PL can be used to compare the defect density of two semiconductors with similar absorption properties. Furthermore, charge extraction process would decrease the PL intensity from a solar cell. Therefore, steady-state PL can give information about the charge extraction efficiency in a solar cell[102, 103].

The time-correlated single photon counting technique is commonly used to measure tr-PL signals. A typical setup (Figure 1.16) involves a single-photon sensitive detector such as an avalanche photodiode or a photomultiplier tube, coupled with time-measuring electronics. The detection unit records the time between the excitation laser pulse and the first photon emitted and detected by the unit. A high repetition rate (kHz–MHz) is necessary to generate a histogram of photon emission times that resembles the luminescence decay observed for the sample since photon emission is statistical. A monochromator can be placed before the photon detection unit to obtain spectral information. The time resolution of the method ranges from about 50 ps to several ns. To prevent state-filling effects, it is important to ensure that the repetition rate is smaller than the inverse PL decay time when using high-frequency pulsed lasers. The excitation flux and density should be
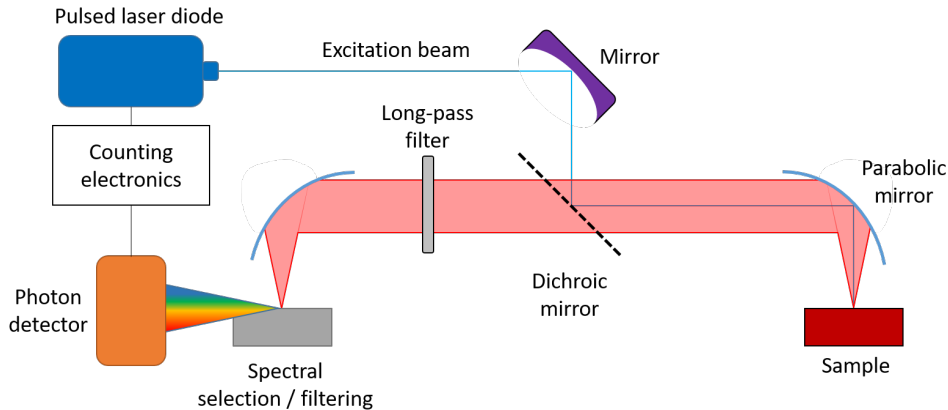
Figure 1.16: The schematics of a steady-state and tr-PL spectroscopy measurement.

recorded and reported since they can strongly affect the luminescence data and completely change the dominating recombination path. The excitation spot size and luminescence collection area are determined by the numerical aperture of the excitation and collection optics and can be adjusted. When using conducting layers in experiments, partial illumination may cause distortions such as lateral currents and a reduction in luminescence intensity. Additionally, the repetition rate of the pulsed laser system should be adjusted to prevent unpredictable additional recombination losses. For lead-halide perovskite samples, repetition rates below 100 kHz should be used to obtain consistent data. It is also advisable to check different excitation wavelengths to avoid complications such as bi-exponential decay. Using long wavelength excitation on perovskites with a gap of 1.6 eV has been observed to lead to single-exponential decay behavior at low fluences[101,104]. Defect-assisted or non-radiative recombination of electrons and holes typically happens faster compared to band-to-band or radiative recombination. Therefore, by measuring the lifetime of free electrons and holes by tr-PL, we can estimate the defect density within a semiconductor sample via tr-PL[66].

1.4.2.4   Time-of-Flight Secondary Ion Mass Spectroscopy

ToF-SIMS is an chemical analysis method that relies on secondary ions after a surface bombardment. The bombardment results in emission of particles, neutral atoms, electrons, and secondary ions. The ions extracted from the surface are segregated in a field-free drift tube. A multi-stage detector system is used for ion detection[105].

Figure 1.17 shows the schematics of a basic ToF-SIMS setup. The primary ions for surface bombardment are generated in the ion gun. Then, the ions are focused on the target. The rastering unit is used to guide the ions to a certain position on the sample. After the surface bombardment with the primary ions, secondary ions from the sample are generated and these ions enter the drift tube through transport optics. After the mass separation in the drift tube and the reduction of the influence of kinetic energy spread on flight time in the reflectron, the detection of secondary ions becomes easier. An electron flood gun, along with a sophisticated beam timing scheme, is utilized to supply low energy electrons to the sample surface for charge compensation[106].
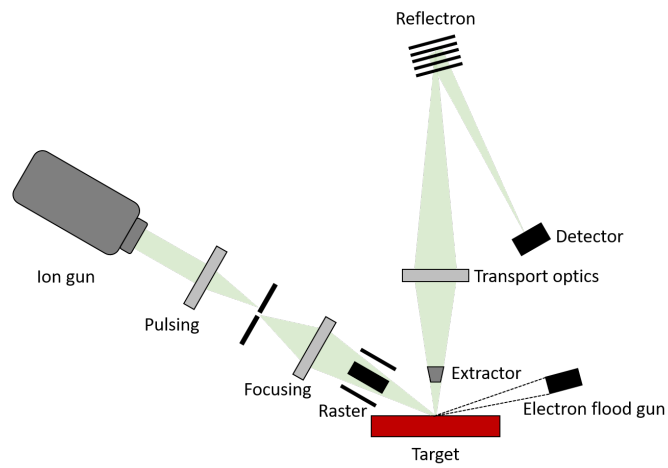
Figure 1.17: The illustration that represents the ToF-SIMS setup.

1.5   References

[1] Front Matter, pages i–xix. John Wiley Sons, Ltd, 2021.

[2] Saida Laalioui. Perovskite-Based Solar Cells. De Gruyter, Berlin, Boston, 2022.

[3] Moses Jeremiah Barasa Kabeyi and Oludolapo Akanni Olanrewaju. The levelized cost of energy and modifications for use in electricity generation planning. Energy Reports, 9:495–534, 2023.

[4] Hiroyuki Fujiwara. Hybrid Perovskite Solar Cells: Characteristics and Operation. John Wiley & Sons, 2021.

[5] Jaewang Park, Jongbeom Kim, Hyun-Sung Yun, Min Jae Paik, Eunseo Noh, Hyun Jung Mun, Min Gyu Kim, Tae Joo Shin, and Sang Il Seok. Controlled growth of perovskite layers with volatile alkylammonium chlorides. Nature, 616(7958):724–730, 2023.

[6] Silvia Mariotti, Eike Köhnen, Florian Scheler, Kári Sveinbjörnsson, Lea Zimmermann, Manuel Piot, Fengjiu Yang, Bor Li, Jonathan Warby, Artem Musiienko, et al. Interface engineering for high-performance, triple-halide perovskite–silicon tandem solar cells. Science, 381(6653):63–69, 2023.

[7] Neil W Ashcroft and N David Mermin. Solid state physics. Cengage Learning, 2022.

[8] Govind P Agrawal and Niloy K Dutta. Semiconductor lasers. Springer Science & Business Media, 2013.

[9] Wolfgang Demtröder. Experimentalphysik 3: Atome, Moleküle und Festkörper. Springer-Verlag, 2010.

[10] Jenny A Nelson. The physics of solar cells. World Scientific Publishing Company, 2003.

[11] Juan Bisquert. The physics of solar cells: perovskites, organics, and photovoltaic fundamentals. CRC press, 2017.

[12] W Gerlach, H Schlangenotto, and H Maeder. On the radiative recombination rate in silicon. physica status solidi (a), 13(1):277–283, 1972.

[13] T Trupke, Mr A Green, P Würfel, PP Altermatt, A Wang, J Zhao, and R Corkish. Temperature dependence of the radiative recombination coefficient of intrinsic crystalline silicon. Journal of Applied Physics, 94(8):4930–4937, 2003.

[14] W Michaelis and MH Pilkuhn. Radiative recombination in silicon p-n junctions. physica status solidi (b), 36(1):311–319, 1969.

[15] Yatendra Pal Varshni. Temperature dependence of the energy gap in semiconductors. physica, 34(1):149–154, 1967.

[16] Gerardo L Araújo and Antonio Martí. Absolute limiting efficiencies for photovoltaic energy conversion. Solar energy materials and solar cells, 33(2):213–240, 1994.

[17] Juan Bisquert, David Cahen, Gary Hodes, Sven Rühle, and Arie Zaban. Physical chemical principles of photovoltaic conversion with nanoparticulate, mesoporous dye-sensitized solar cells. The Journal of Physical Chemistry B, 108(24):8106–8118, 2004.

[18] Mahdi Malekshahi Byranvand and Michael Saliba. Defect passivation of perovskite films for highly efficient and stable solar cells. Solar RRL, 5(8):2100295, 2021.

[19] Hongwei Qu and Xingcan Li. Temperature dependency of the fill factor in pv modules between 6 and 40 c. Journal of Mechanical Science and Technology, 33(4):1981–1986, 2019.

[20] Thomas Dittrich. Materials concepts for solar cells. World Scientific, 2015.

[21] Hanul Min, Do Yoon Lee, Junu Kim, Gwisu Kim, Kyoung Su Lee, Jongbeom Kim, Min Jae Paik, Young Ki Kim, Kwang S Kim, Min Gyu Kim, et al. Perovskite solar cells with atomically coherent interlayers on sno2 electrodes. Nature, 598(7881):444–450, 2021.

[22] Stefaan De Wolf, Jakub Holovsky, Soo-Jin Moon, Philipp Loper, Bjoern Niesen, Martin Ledinsky, Franz-Josef Haug, Jun-Ho Yum, and Christophe Ballif. Organometallic halide perovskites: sharp optical absorption edge and its relation to photovoltaic performance. The journal of physical chemistry letters, 5(6):1035–1039, 2014.

[23] Paolo Umari, Edoardo Mosconi, and Filippo De Angelis. Infrared dielectric screening determines the low exciton binding energy of metal-halide perovskites. The journal of physical chemistry letters, 9(3):620–627, 2018.

[24] Samuel D Stranks, Giles E Eperon, Giulia Grancini, Christopher Menelaou, Marcelo JP Alcocer, Tomas Leijtens, Laura M Herz, Annamaria Petrozza, and Henry J Snaith. Electron-hole diffusion lengths exceeding 1 micrometer in an organometal trihalide perovskite absorber. Science, 342(6156):341–344, 2013.

[25] EL Unger, Lukas Kegelmann, K Suchan, D Sörell, Lars Korte, and Susanne Albrecht. Roadmap and roadblocks for the band gap tunability of metal halide perovskites. Journal of Materials Chemistry A, 5(23):11401–11409, 2017.

[26] Guan-Woo Kim and Annamaria Petrozza. Defect tolerance and intolerance in metal-halide perovskites. Advanced Energy Materials, 10(37):2001959, 2020.

[27] Byung-wook Park and Sang Il Seok. Intrinsic instability of inorganic–organic hybrid halide perovskite materials. Advanced Materials, 31(20):1805337, 2019.

[28] Jinane Haddad, Benedikt Krogmeier, Benjamin Klingebiel, Lisa Krückemeier, Stephanie Melhem, Zhifa Liu, Jürgen Hüpkes, Sanjay Mathur, and Thomas Kirchartz. Analyzing interface recombination in lead-halide perovskite solar cells with organic and inorganic hole-transport layers. Advanced materials interfaces, 7(16):2000366, 2020.

[29] Gede WP Adhyaksa, Sarah Brittman, Haralds Āboliņš, Andries Lof, Xueying Li, Joel D Keelor, Yanqi Luo, Teodor Duevski, Ron MA Heeren, Shane R Ellis, et al. Understanding detrimental and beneficial grain boundary effects in halide perovskites. Advanced Materials, 30(52):1804792, 2018.

[30] Stefan AL Weber, Ilka M Hermes, Silver-Hamill Turren-Cruz, Christopher Gort, Victor W Bergmann, Laurent Gilson, Anders Hagfeldt, Michael Graetzel, Wolfgang Tress, and Rüdiger Berger. How the formation of interfacial charge causes hysteresis in perovskite solar cells. Energy & environmental science, 11(9):2404–2413, 2018.

[31] Alexandra Navrotsky and Donald J Weidner. Perovskite: a structure of great interest to geophysics and materials science. Washington DC American Geophysical Union Geophysical Monograph Series, 45, 1989.

[32] Ronald E Cohen and Henry Krakauer. Electronic structure studies of the differences in ferroelectric behavior of batio3 and pbtio3. Ferroelectrics, 136(1):65–83, 1992.

[33] Khuong P Ong, Teck Wee Goh, Qiang Xu, and Alfred Huan. Structural evolution in methylammonium lead iodide ch3nh3pbi3. The Journal of Physical Chemistry A, 119(44):11033–11038, 2015.

[34] Victor Moritz Goldschmidt. Die gesetze der krystallochemie. Naturwissenschaften, 14(21):477–485, 1926.

[35] Gregor Kieslich, Shijing Sun, and Anthony K Cheetham. Solid-state principles applied to organic–inorganic perovskites: new tricks for an old dog. Chemical Science, 5(12):4712–4715, 2014.

[36] Matteo Pitaro, Eelco Kinsa Tekelenburg, Shuyan Shao, and Maria Antonietta Loi. Tin halide perovskites: from fundamental properties to solar cells. Advanced Materials, 34(1):2105844, 2022.

[37] Lata Chouhan, Sushant Ghimire, Challapalli Subrahmanyam, Tsutomu Miyasaka, and Vasudevanpillai Biju. Synthesis, optoelectronic properties and applications of halide perovskites. Chemical Society Reviews, 49(10):2869–2885, 2020.

[38] Ioannis B Koutselas, Laurent Ducasse, and George C Papavassiliou. Electronic properties of three-and low-dimensional semiconducting materials with pb halide and sn halide units. Journal of Physics: Condensed Matter, 8(9):1217, 1996.

[39] Douglas H Fabini, Ram Seshadri, and Mercouri G Kanatzidis. The underappreciated lone pair in halide perovskites underpins their unusual properties. MRS Bulletin, 45(6):467–477, 2020.

[40] Anuj Goyal, Scott McKechnie, Dimitar Pashov, William Tumas, Mark Van Schilfgaarde, and Vladan Stevanovic. Origin of pronounced nonlinear band gap behavior in lead–tin hybrid perovskite alloys. Chemistry of Materials, 30(11):3920–3928, 2018.

[41] Jiwei Liang, Cong Chen, Xuzhi Hu, Zhiliang Chen, Xiaolu Zheng, Jing Li, Haibing Wang, Feihong Ye, Meng Xiao, Zhengyi Lu, et al. Suppressing the phase segregation with potassium for highly efficient and photostable inverted wide-band gap halide perovskite solar cells. ACS Applied Materials & Interfaces, 12(43):48458–48466, 2020.

[42] Maarten G Goesten and Roald Hoffmann. Mirrors of bonding in metal halide perovskites. Journal of the American Chemical Society, 140(40):12996–13010, 2018.

[43] Loredana Protesescu, Sergii Yakunin, Maryna I Bodnarchuk, Franziska Krieg, Riccarda Caputo, Christopher H Hendon, Ruo Xi Yang, Aron Walsh, and Maksym V Kovalenko. Nanocrystals of cesium lead halide perovskites (cspbx3, x= cl, br, and i): novel optoelectronic materials showing bright emission with wide color gamut. Nano letters, 15(6):3692–3696, 2015.

[44] Constantinos C Stoumpos, Christos D Malliakas, and Mercouri G Kanatzidis. Semiconducting tin and lead iodide perovskites with organic cations: phase transitions, high mobilities, and near-infrared photoluminescent properties. Inorganic chemistry, 52(15):9019–9038, 2013.

[45] Nobuaki Kitazawa, Y Watanabe, and Y Nakamura. Optical properties of ch 3 nh 3 pbx 3 (x= halogen) and their mixed-halide crystals. Journal of materials science, 37:3585–3587, 2002.

[46] Handong Jin, Elke Debroye, Masoumeh Keshavarz, Ivan G Scheblykin, Maarten BJ Roeffaers, Johan Hofkens, and Julian A Steele. It's a trap! on the nature of localised states and charge trapping in lead halide perovskites. Materials Horizons, 7(2):397–410, 2020.

[47] Samuel D Stranks, Victor M Burlakov, Tomas Leijtens, James M Ball, Alain Goriely, and Henry J Snaith. Recombination kinetics in organic-inorganic perovskites: excitons, free charge, and subgap states. Physical Review Applied, 2(3):034007, 2014.

[48] Hiroki Uratani and Koichi Yamashita. Charge carrier trapping at surface defects of perovskite solar cell absorbers: a first-principles study. The journal of physical chemistry letters, 8(4):742–746, 2017.

[49] Dane W de Quilettes, Sarah M Vorpahl, Samuel D Stranks, Hirokazu Nagaoka, Giles E Eperon, Mark E Ziffer, Henry J Snaith, and David S Ginger. Impact of microstructure on local carrier lifetime in perovskite solar cells. Science, 348(6235):683–686, 2015.

[50] Ji-Sang Park, Joaquín Calbo, Young-Kwang Jung, Lucy D Whalley, and Aron Walsh. Accumulation of deep traps at grain boundaries in halide perovskites. ACS Energy Letters, 4(6):1321–1327, 2019.

[51] Wolfgang Tress, Nevena Marinova, Thomas Moehl, Shaik Mohammad Zakeeruddin, Mohammad Khaja Nazeeruddin, and Michael Grätzel. Understanding the rate-dependent j-v hysteresis, slow time component, and aging in ch 3 nh 3 pbi 3 perovskite solar cells: the role of a compensated electric field. Energy & Environmental Science, 8(3):995–1004, 2015.

[52] DJ Slotcavage, HI Karunadasa, and MD McGehee. Acs energy lett. 1, 1199 (2016).

[53] Yuichi Kato, Luis K Ono, Michael V Lee, Shenghao Wang, Sonia R Raga, and Yabing Qi. Silver iodide formation in methyl ammonium lead iodide perovskite solar cells with silver top electrodes. Advanced Materials Interfaces, 2(13):1500195, 2015.

[54] Marina Viktorovna Klassen-Neklyudova. Mechanical twinning of crystals. Springer Science & Business Media, 2012.

[55] Vinod K Wadhawan. Ferroelasticity and related properties of crystals. Phase Transitions: A Multinational Journal, 3(1):3–103, 1982.

[56] Ilka M Hermes, Simon A Bretschneider, Victor W Bergmann, Dan Li, Alexander Klasen, Julian Mars, Wolfgang Tremel, Frédéric Laquai, Hans-Jürgen Butt, Markus Mezger, Rudiger Berger, Brian J. Rodriguez, and Stefan A. L. Weber. Ferroelastic fingerprints in methylammonium lead iodide perovskite. The Journal of Physical Chemistry C, 120(10):5724–5731, 2016.

[57] Yenal Yalcinkaya, Ilka M Hermes, Tobias Seewald, Katrin Amann-Winkel, Lothar Veith, Lukas Schmidt-Mende, and Stefan AL Weber. Chemical strain engineering of mapbi3 perovskite films. Advanced Energy Materials, page 2202442, 2022.

[58] Asma Aicha Medjahed, Pia Dally, Tao Zhou, Noëlla Lemaitre, David Djurado, Peter Reiss, and Stéphanie Pouget. Unraveling the formation mechanism and ferroelastic behavior of mapbi3 perovskite thin films prepared in the presence of chloride. Chemistry of Materials, 32(8):3346–3357, 2020.

[59] Yongtao Liu, Liam Collins, Roger Proksch, Songkil Kim, Brianna R Watson, Benjamin Doughty, Tessa R Calhoun, Mahshid Ahmadi, Anton V Ievlev, Stephen Jesse, Scott T. Retterer, Alex Belianinov, Kai Xiao, Huang, Bobby G. Sumpter, Sergei V. Kalinin, Bin Hu, and Olga S. Ovchinnikova. Chemical nature of ferroelastic twin domains in ch 3 nh 3 pbi 3 perovskite. Nature materials, 17(11):1013–1019, 2018.

[60] Mathias Uller Rothmann, Wei Li, Ye Zhu, Udo Bach, Leone Spiccia, Joanne Etheridge, and Yi-Bing Cheng. Direct observation of intrinsic twin domains in tetragonal ch 3 nh 3 pbi 3. Nature communications, 8(1):1–8, 2017.

[61] Evgheni Strelcov, Qingfeng Dong, Tao Li, Jungseok Chae, Yuchuan Shao, Yehao Deng, Alexei Gruverman, Jinsong Huang, and Andrea Centrone. Ch3nh3pbi3 perovskites: Ferroelasticity revealed. Science advances, 3(4):e1602165, 2017.

[62] Min Jae Paik, Jin Wook Yoo, Jaewang Park, Eunseo Noh, Hyeonwoo Kim, Sang-Geun Ji, Yu Young Kim, and Sang Il Seok. Sno2–tio2 hybrid electron transport layer for efficient and flexible perovskite solar cells. ACS Energy Letters, 7(5):1864–1870, 2022.

[63] Florine M Rombach, Saif A Haque, and Thomas J Macdonald. Lessons learned from spiro-ometad and ptaa in perovskite solar cells. Energy & Environmental Science, 14(10):5161–5190, 2021.

[64] Lusheng Liang, Yu Cai, Xin Li, Mohammad Khaja Nazeeruddin, and Peng Gao. All that glitters is not gold: Recent progress of alternative counter electrodes for perovskite solar cells. Nano Energy, 52:211–238, 2018.

[65] Mojtaba Abdi-Jalebi, M Ibrahim Dar, Aditya Sadhanala, Satyaprasad P Senanayak, Fabrizio Giordano, Shaik Mohammed Zakeeruddin, Michael Gratzel, and Richard H Friend. Impact of a mesoporous titania–perovskite interface on the performance of hybrid organic–inorganic perovskite solar cells. The journal of physical chemistry letters, 7(16):3264–3269, 2016.

[66] Chunqing Ma and Nam-Gyu Park. Paradoxical approach with a hydrophilic passivation layer for moisture-stable, 23% efficient perovskite solar cells. ACS Energy Letters, 5(10):3268–3275, 2020.

[67] Sajid Sajid, Ahmed Mourtada Elseman, Hao Huang, Jun Ji, Shangyi Dou, Haoran Jiang, Xin Liu, Dong Wei, Peng Cui, and Meicheng Li. Breakthroughs in niox-htms towards stable, low-cost and efficient perovskite solar cells. Nano Energy, 51:408–424, 2018.

[68] Jie Xu, Jinfei Dai, Hua Dong, Peizhou Li, Jinbo Chen, Xinyi Zhu, Zhenxiao Wang, Bo Jiao, Xun Hou, Jingrui Li, et al. Surface-tension release in ptaa-based inverted perovskite solar cells. Organic Electronics, 100:106378, 2022.

[69] Hyun-Jung Lee and Seok-In Na. Investigation of pcbm/zno and c60/bcp-based electron transport layer for high-performance pin perovskite solar cells. Journal of Alloys and Compounds, 921:166007, 2022.

[70] Alexander Klasen, Philipp Baumli, Qu Sheng, Ewald Johannes, Simon A Bretschneider, Ilka M Hermes, Victor W Bergmann, Christopher Gort, Amelie Axt, Stefan AL Weber, et al. Removal of surface oxygen vacancies increases conductance through tio2 thin films for perovskite solar cells. The Journal of Physical Chemistry C, 123(22):13458–13466, 2019.

[71] Yongbo Yuan and Jinsong Huang. Ion migration in organometal trihalide perovskite and its impact on photovoltaic efficiency and stability. Accounts of chemical research, 49(2):286–293, 2016.

[72] Weike Zhu, Shurong Wang, Xin Zhang, Aili Wang, Cheng Wu, and Feng Hao. Ion migration in organic–inorganic hybrid perovskite solar cells: current understanding and perspectives. Small, 18(15):2105783, 2022.

[73] Tim J Senden and Calum J Drummond. Surface chemistry and tip-sample interactions in atomic force microscopy. Colloids and Surfaces A: Physicochemical and Engineering Aspects, 94(1):29–51, 1995.

[74] Paul K Hansma, VB Elings, O Marti, and CE Bracker. Scanning tunneling microscopy and atomic force microscopy: application to biology and technology. Science, 242(4876):209–216, 1988.

[75] Jeffrey L Hutter and John Bechhoefer. Measurement and manipulation of van der waals forces in atomic-force microscopy. Journal of Vacuum Science & Technology B: Microelectronics and Nanometer Structures Processing, Measurement, and Phenomena, 12(3):2251–2253, 1994.

[76] BM Law and Francois Rieutord. Electrostatic forces in atomic force microscopy. physical Review B, 66(3):035402, 2002.

[77] Nikolaj Moll, Leo Gross, Fabian Mohn, Alessandro Curioni, and Gerhard Meyer. A simple model of molecular imaging with noncontact atomic force microscopy. New Journal of Physics, 14(8):083023, 2012.

[78] Greg Haugstad. Atomic force microscopy: understanding basic modes and advanced applications. John Wiley & Sons, 2012.

[79] Franz J Giessibl. Advances in atomic force microscopy. Reviews of modern physics, 75(3):949, 2003.

[80] Evandro Martin Lanzoni, Thibaut Gallet, Conrad Spindler, Omar Ramirez, Christian Kameni Boumenou, Susanne Siebentritt, and Alex Redinger. The impact of kelvin probe force microscopy operation modes and environment on grain boundary band bending in perovskite and cu (in, ga) se2 solar cells. Nano Energy, 88:106270, 2021.

[81] Bert Voigtländer. Atomic force microscopy. Springer, 2019.

[82] Sascha Sadewasser and Clemens Barth. Electrostatic force microscopy and kelvin probe force microscopy. Characterization of Materials, pages 1–12, 2002.

[83] Mario Lanza. Conductive atomic force microscopy: applications in nanomaterials. John Wiley & Sons, 2017.

[84] Sergei V Kalinin, Andrei Rar, and Stephen Jesse. A decade of piezoresponse force microscopy: progress, challenges, and opportunities. IEEE transactions on ultrasonics, ferroelectrics, and frequency control, 53(12):2226–2252, 2006.

[85] Alexei Gruverman, Marin Alexe, and Dennis Meier. Piezoresponse force microscopy and nano-ferroic phenomena. Nature communications, 10(1):1661, 2019.

[86] Sascha Sadewasser and Thilo Glatzel. Kelvin probe force microscopy, volume 48. Springer, 2012.

[87] Amelie Axt, Ilka M Hermes, Victor W Bergmann, Niklas Tausendpfund, and Stefan AL Weber. Know your full potential: Quantitative kelvin probe force microscopy on nanoscale electrical devices. Beilstein journal of nanotechnology, 9(1):1809–1819, 2018.

[88] Tingting Xu, Swaminathan Venkatesan, David Galipeau, and Qiquan Qiao. Study of polymer/zno nanostructure interfaces by kelvin probe force microscopy. Solar energy materials and solar cells, 108:246–251, 2013.

[89] Andrea Liscio, Vincenzo Palermo, and Paolo Samori. Nanoscale quantitative measurement of the potential of charged nanostructures by electrostatic and kelvin probe force microscopy: unraveling electronic processes in complex materials. Accounts of chemical research, 43(4):541–550, 2010.

[90] S Hudlet, M Saint Jean, B Roulet, J Berger, and C Guthmann. Electrostatic forces between metallic tip and semiconductor surfaces. Journal of applied physics, 77(7):3308–3314, 1995.

[91] Ch Sommerhalter, Th Glatzel, Th W Matthes, A Jäger-Waldau, and M Ch Lux-Steiner. Kelvin probe force microscopy in ultra high vacuum using amplitude modulation detection of the electrostatic forces. Applied surface science, 157(4):263–268, 2000.

[92] Sophie Barbet, Michka Popoff, Heinrich Diesinger, Dominique Deresmes, Didier Theron, and Thierry Melin. Cross-talk artefacts in kelvin probe force microscopy imaging: a comprehensive study. Journal of Applied Physics, 115(14), 2014.

[93] Martin Jönsson, Dominique Thierry, and Nathalie LeBozec. The influence of microstructure on the corrosion behaviour of az91d studied by scanning kelvin probe force microscopy and scanning kelvin probe. Corrosion Science, 48(5):1193–1208, 2006.

[94] MH Abdellatif, M Salerno, Anatolii Polovitsyn, Sergio Marras, and Francesco De Angelis. Sensing the facet orientation in silver nano-plates using scanning kelvin probe microscopy in air. Applied Surface Science, 403:371–377, 2017.

[95] Y Rosenwaks, R Shikler, Th Glatzel, and S Sadewasser. Kelvin probe force microscopy of semiconductor surface defects. Physical Review B, 70(8):085320, 2004.

[96] H Stanjek and WJHI Häusler. Basics of x-ray diffraction. Hyperfine interactions, 154:107–119, 2004.

[97] William Henry Bragg and William Lawrence Bragg. The reflection of x-rays by crystals. Proceedings of the Royal Society of London. Series A, Containing Papers of a Mathematical and Physical Character, 88(605):428–438, 1913.

[98] Myeongkyu Lee. X-Ray diffraction for materials research: from fundamentals to applications. CRC Press, 2017.

[99] Huaiyu Wang and Paul K Chu. Surface characterization of biomaterials. In Characterization of biomaterials, pages 105–174. Elsevier, 2013.

[100] GD Gilliland. Photoluminescence spectroscopy of crystalline semiconductors. Materials Science and Engineering: R: Reports, 18(3-6):99–399, 1997.

[101] Thomas Kirchartz, José A Márquez, Martin Stolterfoht, and Thomas Unold. Photoluminescence-based characterization of halide perovskites for photovoltaics. Advanced energy materials, 10(26):1904134, 2020.

[102] Sreekanth Mandati, Easwaramoorthi Ramasamy, S Mallick, TN Rao, Ganapathy Veerappan, et al. Rapid assessment of photovoltaic activity of perovskite solar cells by photoluminescence spectroscopy. Materials Letters, 299:130056, 2021.

[103] E Regalado-Pérez, Evelyn B Díaz-Cruz, J Landa-Bautista, NR Mathews, and X Mathew. Impact of vertical inhomogeneity on the charge extraction in perovskite solar cells: a study by depth-dependent photoluminescence. ACS Applied Materials & Interfaces, 13(10):11833–11844, 2021.

[104] Martin Stolterfoht, Pietro Caprioglio, Christian M Wolff, José A Márquez, Joleik Nordmann, Shanshan Zhang, Daniel Rothhardt, Ulrich Hörmann, Yohai Amir, Alex Redinger, et al. The impact of energy alignment and interfacial recombination on the internal and external open-circuit voltage of perovskite solar cells. Energy & environmental science, 12(9):2778–2788, 2019.

[105] John C Vickerman. Tof-sims—an overview. ToF-SIMS: surface analysis by mass spectrometry, pages 1–40, 2001.

[106] Anastasia Georgantzopoulou, Yekkuni L Balachandran, Philipp Rosenkranz, Maria Dusinska, Anna Lankoff, Maria Wojewodzka, Marcin Kruszewski, Cédric Guignard, Jean-Nicolas Audinot, Shanmugam Girija, et al. Ag nanoparticles: size-and surface-dependent effects on model aquatic organisms and uptake evaluation with nanosims. Nanotoxicology, 7(7):1168–1178, 2013.

2 Motivation

Halide perovskites are potential materials that are to be used in photonic applications such as solar cells, LEDs, and photodetectors[2]. The common factor in all these applications is the charge carrier dynamics inside the perovskite layer and the whole device. Interfacial, surface, and interior defects in perovskite limit the performance of perovskite-based devices by causing recombination of the free electrons and holes[1]. Furthermore, migrating ions from the perovskite also affect the device performance and lifetime. An understanding of sub-structures and their effects on free charge carriers are needed to maximize the device performance that is mainly limited by defects and ion migration in perovskite-based devices[3]. In this work, my main objective was to investigate the nature or origin of the sub-structures such as ferroelastic twin domains or grain boundaries in halide perovskites. My second objective was to understand the effect of these sub-structures on charge carrier dynamics in halide perovskite devices.

In Chapter 3, I present my work on the chemical strain engineering in halide perovskites. This study introduces a new chemical method for controlling the strain in $MAPbI_3$ perovskite crystals by varying the ratio of lead acetate ($Pb(Ac)_2$) and lead chloride ($PbCl_2$) in the precursor solution. To observe the effect on crystal strain, a combination of PFM and XRD is used. The PFM images show an increase in the average size of ferroelastic twin domains upon increasing the $PbCl_2$ content, indicating an increase in crystal strain. The XRD spectra support this observation with strong crystal twinning features that appear in the spectra. This behaviour is caused by a strain gradient during the crystallization due to different evaporation rates of methylammonium acetate (MA(Ac)) and methylammonium chloride (MACl) as revealed by ToF-SIMS and grazing incidence XRD (GIXRD) measurements. Additional tr-PL show an increased carrier lifetime in the $MAPbI_3$ films prepared with higher $PbCl_2$ content, suggesting a decreased trap density in films with larger twin domain structures. The results demonstrate the potential of chemical strain engineering as an easy method for controlling strain-related effects in lead halide perovskites.

In Chapter 4, I investigated the local defect behavior and charge carrier dynamics within the halide perovskite via KPFM. In this study, I investigate the spatial defect distribution in the vicinity of grain boundaries. To this end, I introduce local photovoltage, photovoltage decay, and defect mapping via time-resolved KPFM. By measuring the photovoltage decay on perovskite samples with small and large grains, I am able to detect and localize areas of increased charge carrier recombination, ion migration, and defects. Furthermore, I demonstrate our new method on light ideality factor mapping within the perovskite films to deduce which mechanisms dominate the charge recombination process. Our results show a significant increase in free electron-hole lifetimes and suppressed ion migration in large grained perovskite films. The ideality factor mapping revealed grain boundary - grain interior contrast in the films. Furthermore, the ideality factor became lower and more uniform after the perovskite film was passivated.

In Chapter 5, I introduce a method utilizing methylamine gas for the controlled recrystallization of perovskite layers, resulting in millimeter-sized domains, irrespective of the initial quality. The application of methylamine substantially enhances crystallinity, leading to crystal growth with a preferred orientation. PL and space-charge limited current measurements reveal a significant

reduction in trap density post-recrystallization. C-AFM measurements demonstrate increased surface conductivity and improved spatial homogeneity following methylamine treatment. When incorporated into photodetectors, the enhanced film quality of the recrystallized films yields higher detectivities of approximately 4×10^{11} Jones compared to the 3×10^9 Jones observed in a reference device. Additionally, the response time decreases from 0.1 to 10^{-5} s after methylamine treatment. Thus, our work presents a promising approach for producing reproducible, high-quality perovskite films through controlled recrystallization.

2.1 References

[1] Mahdi Malekshahi Byranvand and Michael Saliba. Defect passivation of perovskite films for highly efficient and stable solar cells. Solar RRL, 5(8):2100295, 2021.

[2] Soumyadipta Rakshit, Piotr Piatkowski, Iván Mora-Seró, and Abderrazzak Douhal. Combining perovskites and quantum dots: synthesis, characterization, and applications in solar cells, leds, and photodetectors. Advanced Optical Materials, 10(14):2102566, 2022.

[3] Weike Zhu, Shurong Wang, Xin Zhang, Aili Wang, Cheng Wu, and Feng Hao. Ion migration in organic–inorganic hybrid perovskite solar cells: current understanding and perspectives. Small, 18(15):2105783, 2022.

3   Chemical Strain Engineering of MAPbI$_3$ Perovskite Films

Summary & Author Contributions

In this paper, we showed a chemical route to adjust the strain within MAPbI$_3$ thin films by adjusting the ratio of precursors namely, PbCl$_2$ and Pb(Ac)$_2$. We traced the strain behavior by monitoring the structure of ferroelastic twin domains in MAPbI$_3$ films via PFM and XRD. We then showed via ToF-SIMS and GIXRD that the vertical chemical gradient in the films causes a strain gradient. Lastly, we measured the optical properties of MAPbI$_3$ films with different strains to see the structure-property relations.

Mehmet Yenal Yalcinkaya fabricated MAPbI$_3$ films, performed PFM measurements, analyzed and visualized the XRD data, estimated free electron lifetimes, and estimated the bandgaps of the samples.

Chemical Strain Engineering of MAPbI₃ Perovskite Films

*Yenal Yalcinkaya, Ilka M. Hermes, Tobias Seewald, Katrin Amann-Winkel, Lothar Veith, Lukas Schmidt-Mende, and Stefan A.L. Weber**

This study introduces a new chemical method for controlling the strain in methylammonium lead iodide (MAPbI₃) perovskite crystals by varying the ratio of Pb(Ac)₂ and PbCl₂ in the precursor solution. To observe the effect on crystal strain, a combination of piezoresponse force microscopy (PFM) and X-ray diffraction (XRD) is used. The PFM images show an increase in the average size of ferroelastic twin domains upon increasing the PbCl₂ content, indicating an increase in crystal strain. The XRD spectra support this observation with strong crystal twinning features that appear in the spectra. This behavior is caused by a strain gradient during the crystallization due to different evaporation rates of methylammonium acetate and methylammonium chloride as revealed by time-of-flight secondary ion mass spectroscopy and grazing incidence X-ray diffraction measurements. Additional time-resolved photoluminescence shows an increased carrier lifetime in the MAPbI₃ films prepared with higher PbCl₂ content, suggesting a decreased trap density in films with larger twin domain structures. The results demonstrate the potential of chemical strain engineering as a simple method for controlling strain-related effects in lead halide perovskites.

1. Introduction

Hybrid lead halide perovskites[1–6] show remarkable properties such as a direct adjustable bandgap,[7–9] high defect tolerance,[10] and long charge carrier lifetimes[11–13] that make them ideally suited as absorber materials for photovoltaic applications. An interesting effect that has been observed in many hybrid lead halide perovskite materials is that the optoelectronic properties can be strongly influenced by external or internal strain. Thus, strain engineering can be a useful method to control and tune the optoelectronic properties or structural stability of perovskite materials.[14,15] For example, Zhu et al. showed improved charge extraction at the perovskite-hole transport layer interface by eliminating the strain gradient and thereby flattening the valence band.[16] Kim et. al. used strain engineering to relax the crystal lattice of formamidinium lead iodide (FAPbI₃), enabling improved solar cell performance.[17] In addition, strain engineering had also been used by various groups to increase the stability of perovskite structures. Zhao et al. demonstrated that strain engineering of MAPbI₃ by mechanically bending the substrate increased the stability.[18] Strain engineering was also used to stabilize metastable phases such as CsPbI₃ and FAPbI₃ by the introduction of biaxial strain via cooling a perovskite crystal clamped to a ceramic substrate[19] or applying strain by heteroepitaxially growing the perovskite on another perovskite material.[20]

Another important strain-related effect observed in methylammonium lead iodide (MAPbI₃) crystals is the formation of sub-granular ferroelastic twin domains. Ferroelastic twin domains in tetragonal MAPbI₃ were first observed via piezoresponse force microscopy (PFM) by our group,[21] followed by many others.[22–25] The domains form due to the strain resulting from the cubic to tetragonal phase change at 57 °C. Strelcov et al. observed via polarized optical microscopy (POM) that mechanical stress leads to a rearrangement of the twin domains in MAPbI₃, supporting the conclusion that the domains are ferroelastic.[26] Since our first report in 2016, ferroelastic twins have been observed by many other techniques, including transmission electron microscopy (TEM),[24] X-ray diffraction (XRD),[27] and neutron scattering.[28]

The existence of a sub-granular domain structure raises the question whether these domains have an influence on the electronic transport properties. Recently, Xiao et al.[29] concluded

Y. Yalcinkaya, K. Amann-Winkel, L. Veith, S. A. L. Weber
Max Planck Institute for Polymer Research
Ackermannweg 10, 55128 Mainz, Germany
E-mail: webers@mpip-mainz.mpg.de
Y. Yalcinkaya, K. Amann-Winkel, S. A.L. Weber
Institute of Physics
Johannes Gutenberg University Mainz
Duesbergweg 10-14, 55128 Mainz, Germany
I. M. Hermes
Leibniz Institute for Polymer Research Dresden e.V.
Institute of Physical Chemistry and Polymer Physics
Department Polymer Interfaces
Hohe Str. 6, 01069 Dresden, Germany
T. Seewald, L. Schmidt-Mende
Department of Physics
University of Konstanz
Universitätsstr. 10, 78464 Konstanz, Germany

**ADVANCED
SCIENCE NEWS**

www.advancedsciencenews.com

**ADVANCED
ENERGY
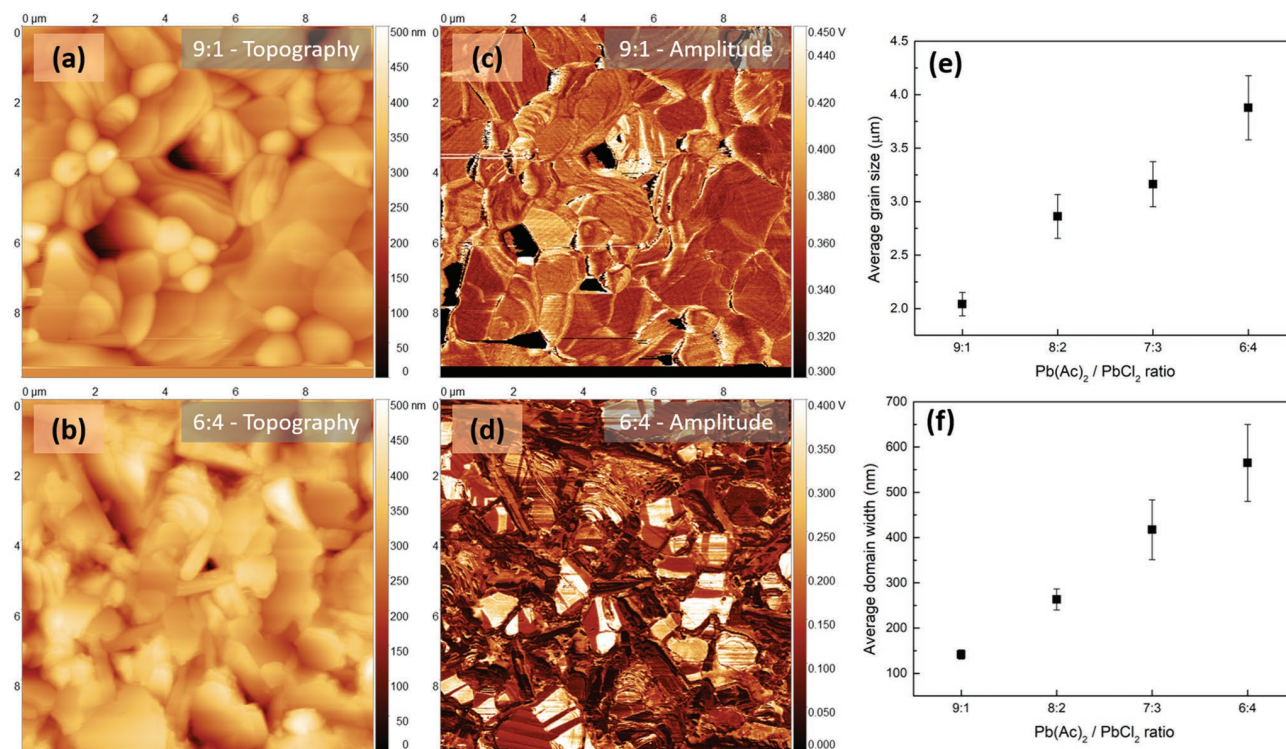MATERIALS**

www.advenergymat.de

Figure 1. Topography and PFM amplitude images of MAPbI$_3$ thin films with Pb(Ac)$_2$/PbCl$_2$ ratios of a,c) 9:1, and b,d) 6:4. e) Average grain size and f) domain width profiles of MAPbI$_3$ thin films with different Pb(Ac)$_2$/PbCl$_2$ ratios.

from PL and lifetime mapping experiments that the ferroelastic twin domains are benign to recombination kinetics. To separate potential grain boundary effects, our group recently investigated large isolated MAPbI$_3$ grains. Using time-resolved PL microscopy, we found an anisotropic charge transport that was correlated to the ferroelastic twin domain structure in the crystal.[30] In particular, the charge diffusion perpendicular to the ferroelastic domains was slower compared to the charge diffusion parallel to the domains.

Such an anisotropic diffusion would be interesting for guiding charge carriers, e.g., to the electrodes of an optoelectronic device. Thus, a targeted manipulation or engineering of the twin domain structure would be desirable. Next to domain manipulation through mechanical straining,[26] we showed that the ferroelastic twin domain structure changes when using different cooling rates after annealing.[30,31] Here, a slower cooling rate resulted in a more dense and ordered domain structure whereas a higher cooling rate lead to disordered and less dense twin domains. Lastly, Röhm et al. demonstrated the domain manipulation via a lateral electric field.[32] However, all the domain manipulation methods mentioned above are not easy to scale up for mass production.

In this study, we introduce a new method for controlling the mechanical strain during the crystal growth via the composition of the precursor solution. In particular, we use different ratios of Pb(Ac)$_2$ and PbCl$_2$ to synthesize MAPbI$_3$ thin films on glass substrates in order to adjust the overall crystallization of MAPbI$_3$ films. Acetate and chloride anions were chosen because they require similar annealing temperatures for evaporation/sublimation while iodide-based synthesis requires higher annealing temperatures.[33] Using a combination of PFM and XRD, we

observed an increase in crystal strain connected to an increase in the average twin domain size upon increasing the PbCl$_2$ content. Additionally, we observed a change from stripe-like to rectangular domains, an effect that has been connected to increased crystal strain.[26] Based on time-of-flight secondary ion mass spectroscopy (ToF-SIMS) experiments, where we found an accumulation of chloride at the substrate interface, we suggest that the strain during crystal growth is caused by the combined effect of low temperature crystallization and ion exchange during annealing. This chloride accumulation is most likely caused by different evaporation rate of the methylammonium acetate (MA(Ac)) and sublimation rate of methylammonium chloride (MACl). Additional time-resolved photoluminescence (TRPL) showed an increased carrier lifetime in the MAPbI$_3$ films prepared with higher PbCl$_2$ content, suggesting a decreased trap density in films with larger twin domain structures.

2. Results and Discussion

2.1. Piezoresponse Force Microscopy (PFM)

We prepared several batches of MAPbI$_3$ films on glass with precuror ratios between 9:1 and 6:4 and investigated the topography and the lateral piezoresponse using AFM/PFM (**Figure 1**a–d; Figure S2, Supporting Information; details on the working mechanism of PFM are given in the Experimental Section). Figure 1e shows the average grain sizes obtained from several areas of the films with changing Pb(Ac)$_2$/PbCl$_2$ ratios. The most obvious effect of the the precursor ratio change is an increase in average grain size (<d>) from 2.04 ± 0.11 μm for the 9:1 Pb(Ac)$_2$/PbCl$_2$

2202442 (2 of 8)
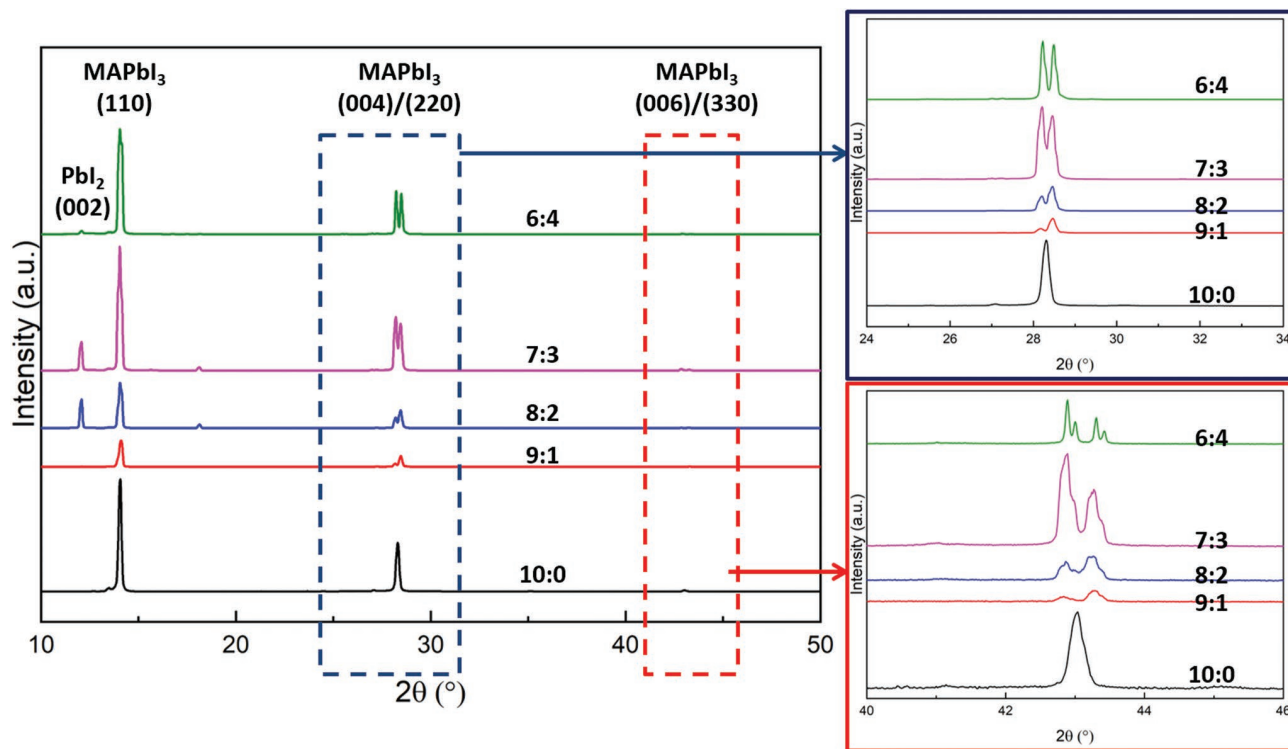
Figure 2. XRD patterns of MAPbI$_3$ thin films with Pb(Ac)$_2$/PbCl$_2$ ratios of 10:0, 9:1, 8:2, 7:3, and 6:4. Intensities were shifted for clarity, the data are not normalized.

ratio to 3.9 ± 0.3 μm for the 6:4 Pb(Ac)$_2$/PbCl$_2$ ratio (Figure 1e). A MAPbI$_3$ film prepared from pure Pb(Ac)$_2$ precursor had an even smaller average grain size of 0.85 ± 0.31 μm (Figure S1, Supporting Information). The decrease in grain size upon lowering the PbCl$_2$ content comes from the decreased Cl or MACl content which speeds up the crystallization of perovskite and leads to smaller grains.[33] Furthermore, the combined effect of MACl and DMF annealing seems to be causing a significant increase in grain size compared to MAPbI$_3$ film prepared from pure Pb(Ac)$_2$ precursor. In addition to the grain size, the general grain morphology also changed upon decreasing Pb(Ac)$_2$/PbCl$_2$ ratio. In between the perovskite grains we observed more pinholes and undefined structures (Figure 1b). On average, the density of pinholes and undefined structures increases with decreasing Pb(Ac)$_2$/PbCl$_2$ ratio (Figure S2, Supporting Information), suggesting these structures could be caused by residual PbI$_2$ or MAPbCl$_3$ that forms after the spin coating.[27] The reason for this effect could again be a slower crystallization in the MAPbI$_3$ film due to the lower volatility of MACl compared to MA(Ac). Later on, we will show that this interpretation is also supported by XRD (**Figure 2**), ToF-SIMS (**Figure 3**), and UV-Vis absorption (Figure S12, Supporting Information) results.

The lateral PFM amplitude images show the familiar striped ferroelastic domain structure[21] (Figure 1c,d). Compared to MAPbI$_3$ films with 9:1 Pb(Ac)$_2$/PbCl$_2$ ratio (Figure 1c), films prepared from the 6:4 precursor ratio show a less dense domain structure (Figure 1d). In particular, we observed an increase in the width of the ferroelastic twin domains with increasing PbCl$_2$ content. Figure 1f shows average ferroelastic twin domain width values gathered from various areas of the samples. The distances between the high amplitude and low amplitude areas

revealed an average domain width (<w>) of 137 ± 10 nm for the MAPbI$_3$ film with 9:1 and 560 ± 90 nm and 6:4 Pb(Ac)$_2$/PbCl$_2$ ratio, respectively (Figure 1f).

As twin domains are purely strain related, it seems obvious from the changing domain pattern that the strain in the films is influenced by different Pb(Ac)$_2$/PbCl$_2$ ratios. The work by Strelcov et al.[26] has demonstrated that external stress can alter the domain structure. Their results show that upon increasing the strain within the MAPbI$_3$ films the stripe-shaped domains evolve into larger areas. Furthermore, the emergence of non-90° domain angles were observed upon increased external stress.[26] We also observed such domain shapes (Figure 1), suggesting that the precursor mixing with Pb(Ac)$_2$/PbCl$_2$ or MA(Ac) and MACl increases the strain within the Pb(Ac)$_2$/PbCl$_2$ structure.

2.2. X-Ray Diffraction

To support the hypothesis of precursor-induced strain adjustment in our MAPbI$_3$ films with different Pb(Ac)$_2$/PbCl$_2$ ratios, we performed XRD measurements. In the XRD, all mixed precursor samples showed the typical reflections for MAPbI$_3$ with addition of PbI$_2$ (Figure 2; Figure S3, Supporting Information) and some unidentified weak peaks around 18° that may belong to intermediates or a Lewis acid-base adduct due to retarded crystallization caused by increased PbCl$_2$.[34] As the PbCl$_2$ amount increases, the intensity ratio of MAPbI$_3$ (110)/PbI$_2$ (002) peaks also increases and reaches to a maximum value for 6:4 Pb(Ac)$_2$/PbCl$_2$ ratio, resulting in quenched PbI$_2$ (002) signal in Figure 2. We also observed a peak splitting around 28° due to {00l}/{hk0} twinning in MAPbI$_3$ films[27] (Figure 2, blue box) in MAPbI$_3$
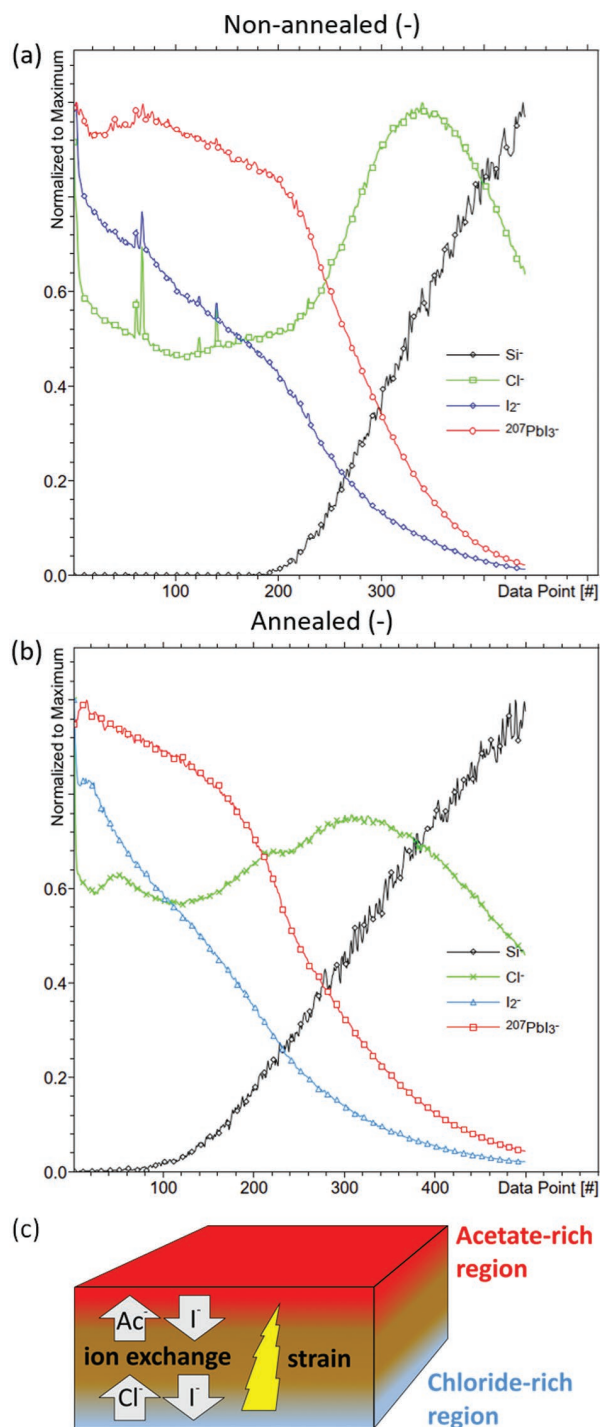
Figure 3. Chemical depth profiles of a) non-annealed and b) annealed MAPbI₃ film made with 6:4 Pb(Ac)₂/PbCl₂ ratio and c) Illustration of strain mechanism.

films with Pb(Ac)₂/PbCl₂. The intensity ratio of the (004) peaks to the (220) peaks ≈28° increased when the Pb(Ac)₂/PbCl₂ ratio was decreased. The lower inset of Figure 2 (red box) shows the XRD signal in the range between 40° and 46°. Again, as the Pb(Ac)₂/PbCl₂ ratio was decreased, the (006)/(330) peak inten-

sity ratios increased. Interestingly, we found a further splitting of the split peaks in samples prepared from a 6:4 Pb(Ac)₂/PbCl₂ ratio, resulting in four peaks ≈43°. Based on the work by Dang et al.,[35] these additional peaks may belong to the (134) and (402) planes. Such further peak splitting in the XRD could be related to lower symmetry for smaller Pb(Ac)₂/PbCl₂ ratios as a result from the formation of non-90° domains. A similar observation in XRD pattern of MAPbI₃ was observed by Leonhard et al.[36] where the emerging peaks disappeared upon further annealing, indicating strain relaxation. These results suggest that the larger domain areas in the PFM images in Figure 1b belong to {00l} facets and that their XRD intensity increases due to increased area. Furthermore, the observation of a second peak splitting may indicate an increased residual strain resulted by different Pb(Ac)₂/PbCl₂.

To learn more about the overall strain behavior within the MAPbI₃ films, we analyzed the XRD peak shifts as a function of Pb(Ac)₂/PbCl₂ ratio. The position for MAPbI₃ (110) peak for 10:0, 9:1, 8:2, 7:3, and 6:4 Pb(Ac)₂/PbCl₂ ratios were observed at ≈14°. One important observation in MAPbI₃ (110) plane for 6:4 Pb(Ac)₂/PbCl₂ ratio is the emerging shoulder at 14.14° (Figure 2). This splitting of the (110) plane suggests that another twinning starts to take place in these samples, likely caused by a higher strain. The peak splitting trends of (004)/(220) and (006)/(330) suggest that the peak at the higher scattering angles belongs to {hk0} planes while the peak at the lower scattering angles belongs to the {00l} planes, possibly (002). Furthermore, the positions of split MAPbI₃ (004)/(220) peaks were observed at 28.32° (only (220)), 28.18/28.47°, 28.2/28.46°, 28.21/28.45°, and 28.23/28.49° for 10:0, 9:1, 8:2, 7:3, and 6:4 Pb(Ac)₂/PbCl₂ ratios, respectively. It is safe to assume that strain controls the trends observed in the XRD measurements since the enlarged domains were also observed in PFM as a result of increased strain. Here, a shift to lower scattering angles in MAPbI₃ (110) plane for Pb(Ac)₂/PbCl₂ ratios lower than 9:1 that may indicate the emergence of another peak from the (002) plane. Alternatively, this shift may indicate lattice expansion based on Bragg's law and interplanar distance formulas (Equations S1 and S2, Supporting Information). Moreover, a shift to the higher scattering angles for MAPbI₃ (004) plane and a shift to lower scattering angles for MAPbI₃ (220) was observed with decreasing Pb(Ac)₂/PbCl₂ ratio that may indicate lattice shrinking and lattice expansion, respectively (Equations S1 and S2, Supporting Information).

Lastly, we have also performed an XRD measurement on a MAPbI₃ film made from a precursor solution containing only MAI and Pb(Ac)₂. This sample in particular was not annealed but only dried at room temperature in the glovebox since MA(Ac) is much more volatile compared to MACl and MAPbI₃ can form without any heat treatment. The resulting films had a very small grain structure, which made PFM experiments impossible. Therefore, the twinning was only monitored via XRD for this sample (Figure S4a, Supporting Information). The resulting XRD pattern exhibited larger peak splitting, even more distinct then MAPbI₃ with 6:4 Pb(Ac)₂/PbCl₂ ratio. This result supports the notion of room temperature twinning in MAPbI₃.[28] Also, the stronger (004) signal in non-annealed MAPbI₃ film made from only MAI and Pb(Ac)₂ compared to annealed samples in Figure 2 is because of strain relaxation upon annealing.

**ADVANCED
SCIENCE NEWS**

www.advancedsciencenews.com

**ADVANCED
ENERGY
MATERIALS**

www.advenergymat.de
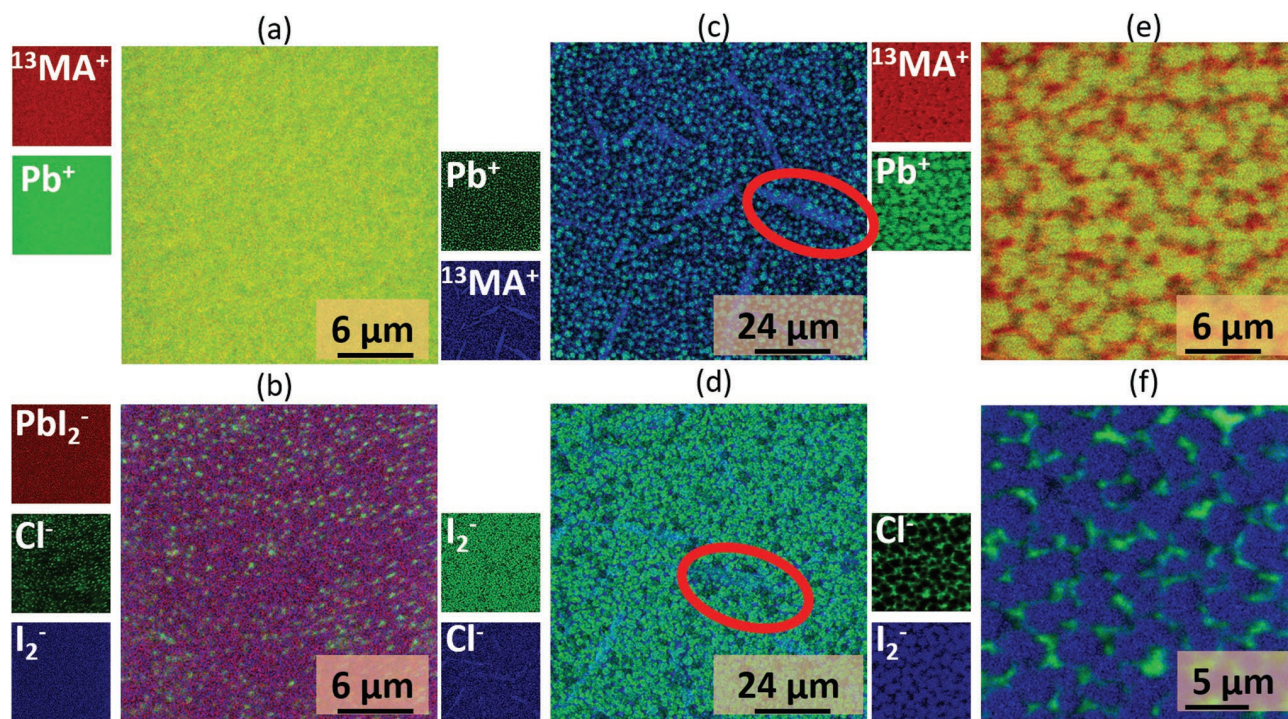
Figure 4. Lateral ion distributions in a,b) non-annealed and c,d,e,f) annealed MAPbI$_3$ films made from 6:4 Pb(Ac)$_2$/PbCl$_2$ ratio.

2.3. Chemical Gradients and Strain Mechanism

To synthesize the MAPbI$_3$, methylammonium iodide (MAI), lead acetate (Pb(Ac)$_2$), and lead chloride (PbCl$_2$) precursors were utilized. In this synthesis, the molar ratio of MA precursor to Pb precursor is 3:1 as can given in Equation (1):

$$3MAI + PbX_2 \rightarrow MAPbI_3 + 2MAX \tag{1}$$

where X can be Ac, Cl, or I. The MAX compound is volatile and evaporates during the annealing of the film. The volatility and thus the evaporation rate of MAX depends on the X anion used in the precursor solution. Therefore, the crystallization kinetics in the MAPbI$_3$ film is controlled by the evaporation rate of the MAX compound.

The observed changes in the ferroelastic twin domain structure in PFM and the peak splitting behavior in the XRD spectra suggest a correlation between the strain in the MAPbI$_3$ films and the Pb(Ac)$_2$/PbCl$_2$ ratio in the precursor solution. A recent study by Medjahed et al.[27] has investigated the strain in MAPbI$_3$ films prepared from a 3MAI/PbCl$_2$ solution by monitoring the twinning via XRD. According to this study, MAPbCl$_3$ forms within the film prior to annealing and I$^-$/Cl$^-$ ion exchange occurs during annealing. This process gives rise to strain formation within the MAPbI$_3$ film and eventually results in twin formation.

To investigate chemical kinetics within the perovskite film, we carried out ToF-SIMS. The profiles for both PbI$_3^-$ and Cl$^-$ show a pronounced chemical gradient within the film (Figure 3a,b). In the non-annealed film, we observed elevated levels of Cl$^-$ at the bottom of the film compared to static/cen-

tral part of the profile line. As suggested previously, there might be volatile compounds on the surface involving Cl$^-$ that could be the reason for high Cl$^-$ concentration on the surface. The high Cl$^-$ concentration in the depths of the film on the other hand shows that Cl$^-$ ions tend to localize closer to the substrate in the mixed precursor MAPbI$_3$ film. A similar behaviour has been reported for pure MAI/PbCl$_2$ films.[37] A similar trend was also observed for Cl$^-$ in the annealed MAPbI$_3$ film, as well, however with an increased uniformity through the film. This can be an indication of I$^-$/Cl$^-$ ion exchange that leads to the formation of MAPbI$_3$.

The depth profiles in both pristine and annealed MAPbI$_3$ films show I$_2^-$ and PbI$_3^-$ signals with the opposite trend of Cl$^-$. After the precursor deposition, MAPbI$_3$ grains form closer to the surface while Cl-rich species stay at the bottom of the film. Upon annealing, MACl reaches the surface through the ion exchange. This ion exchange reaction of MAPbCl$_3$ is expected give rise to a vertical strain gradient. An illustration of this vertical ion exchange reaction is given in Figure 3c.

The depth profiles for positive ions (Figure S7, Supporting Information) show a uniform Pb$^+$ ion distribution and a slight gradient in MA$^+$ ion distribution. The non-uniform distribution of MA$^+$ ion could also be contributing to the vertical strain gradient as observed before.[38]

To investigate a potential strain gradient along the vertical direction of the film, we employed grazing incidence X-ray diffraction (GIXRD). GIXRD enables to change the X-ray penetration into the film by changing the incidence angle, providing depth-dependent crystal structure information. The GIXRD spectra of a MAPbI$_3$ film with 6:4 Pb(Ac)$_2$/PbCl$_2$ ratio shows a change in XRD reflection around 14° (Figure S6a,

**ADVANCED
SCIENCE NEWS**
www.advancedsciencenews.com

**ADVANCED
ENERGY
MATERIALS**
www.advenergymat.de
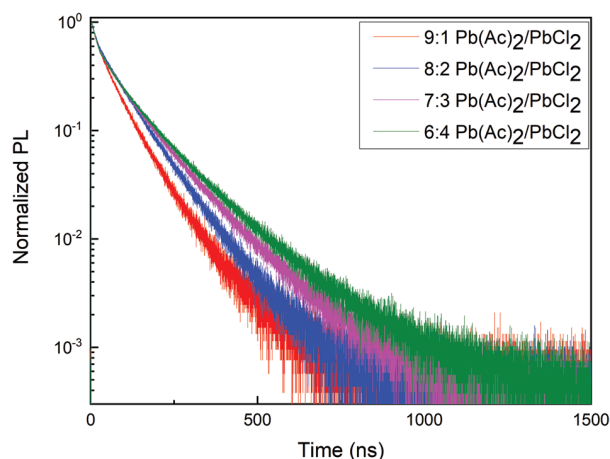
Figure 5. PL lifetimes of MAPbI$_3$ thin films with Pb(Ac)$_2$/PbCl$_2$ ratios of 9:1, 8:2, 7:3, and 6:4.

Supporting Information). Deconvolution of the signal reveals a clear shift in the lattice parameters as the X-ray penetration into the perovskite film changes (Figure S6b, Supporting Information). These shifts are a clear signature of a vertical strain gradient.

The lateral chemical distribution was also determined using ToF-SIMS on non-annealed and annealed MAPbI$_3$ films with 6:4 Pb(Ac)$_2$/PbCl$_2$ ratio (**Figure 4**). The ion distribution in the non-annealed MAPbI$_3$ film reveals uniform distribution of MA$^+$, Pb$^+$, and I$_2^-$ ions after spin coating, whereas The Cl-ions show a distribution pattern (Figure 4a,b). Based on the information we obtained from XRD measurements on non-annealed samples (Figure S5, Supporting Information), perovskite films at this stage should be consisting of MAPbI$_3$ and MAPbCl$_3$. Therefore, we suggest the Cl-rich areas in the film are mostly MAPbCl$_3$ areas where the acetate-rich areas quickly transform into MAPbI$_3$. Upon annealing, some morphological and chemical changes occured within the perovskite film: MA- and Cl-rich needle-like structures are prominent in the ToF-SIMS images (blue images in Figure 4c,d, marked with red), similar to the needle structures that we observed in the AFM images (Figure 1b). In contrast, the Pb$^+$ distribution was much more homogeneous (Figure 4c), whereas the I$_2^-$ concentration was reduced in the needle-like structures (Figure 4d), suggesting these structures could be MACl that forms after I$^-$/Cl$^-$ ion exchange. At larger magnification (Figure 4e,d), we see that grain interiors are rich in MA$^+$, Pb$^+$, and I$_2^-$, whereas the exterior of the grains is rich in Cl$^-$. However, there are small areas where the MA$^+$ and Pb$^+$ maps do not exactly match. These map mismatches suggest that the structures outside of MAPbI$_3$ grains could belong to structures such as PbI$_2$ and MACl that is not sublimated yet. In addition, we observed small amounts of Cl$^-$ inside of the MAPbI$_3$ grains, suggesting a minor Cl$^-$ doping could be taking place during fabrication. The ion maps show that next to a vertical chemical gradient there is also a lateral chemical gradient within the perovskite films (Figures 3 and 4). Since the correlation between the vertical chemical gradient and the strain gradient in the perovskite film is well established through our GIXRD results (Figure S6a,b, Supporting Information) and

supported by other studies,[27,38] we conclude that lateral strain will be present within the films, as well.

2.4. Optical Measurements

Ferroelastic domain walls distort the local crystalline order and might form energetic barriers.[30,39] In our earlier study, we found an alternating polarization at the domain walls that could act as shallow traps states or scattering centres, affecting the charge carrier dynamics.[30] To study the effect of different domain morphologies on charge carrier lifetimes, we conducted TRPL measurements on our MAPbI$_3$ films with different Pb(Ac)$_2$/PbCl$_2$ ratios (**Figure 5**). We fitted the results bi-exponentially to obtain lifetime parameters. We found that the carrier lifetime increased from 68.47 ± 0.23 ns for the film with 9:1 ratio to 104.35 ± 0.24 ns for the 6:4 Pb(Ac)$_2$/PbCl$_2$ ratio (all values are given in Table S1, Supporting Information). This trend suggests the charged carriers move more freely in case of lower Pb(Ac)$_2$/PbCl$_2$ ratios where the density of ferroelastic domain walls is decreased since the low energy barriers caused by the domain walls are eliminated. This result is in an agreement with our previous findings and the previously proposed energetic barriers theory. Furthermore Zhang et al. discovered that the charge carrier mobility in MAPbI$_3$ is plane dependent, i.e., anisotropic,[40] offering an explanation for the energy barriers caused by ferroelastic twin domains.

To monitor the presence of additional phases and the optical properties, we performed UV–vis spectroscopy on the MAPbI$_3$ films with all the different Pb(Ac)$_2$/PbCl$_2$ ratios (Figure S12, Supporting Information) where all samples showed an absorption band edge ≈780 nm. The absorption edge ≈600 nm that is visible in all spectra comes from PbI$_2$ which is in an agreement with the PbI$_2$ signal that we observed in XRD measurements. Furthermore, a new peak at 390 nm emerged belonging to MAPbCl$_3$ at any Pb(Ac)$_2$/PbCl$_2$ ratio below 8:2 . This matches with the expectation since MAPbCl$_3$ forms when PbCl$_2$ is used or increased in the precursor solution,[27] which was also supported by ToF-SIMS results (Figure 3) and non-annealed XRD results (Figure S5, Supporting Information). Furthermore, the absorption decreased with decreasing Pb(Ac)$_2$/PbCl$_2$ ratio due to decreasing amount of MAPbI$_3$ in the obtained film. This is possibly a result of the slow crystallization of MAPbI$_3$ due to the presence of PbCl$_2$. Nevertheless, the MAPbCl$_3$ phase could not be detected by the XRD measurements in Figure 2, most likely due to the low MAPbCl$_3$ content in the films. In addition, we calculated Tauc plots (Figure S13, Supporting Information) from the absorption data from UV–vis results (Figure S12, Supporting Information). The bandgap of MAPbI$_3$ films slightly decreased with decreasing Pb(Ac)$_2$/PbCl$_2$ ratio (Figures S13 and S14, Supporting Information). Since the bandgap of MAPbI$_3$ is the same for (110) and (001) planes,[40] the bandgap change can be attributed to increased strain as suggested elsewhere.[16]

3. Conclusion

In this work, we have shown a chemical route to control the strain in MAPbI$_3$ thin films by using different Pb(Ac)$_2$/PbCl$_2$

ratios in the precursor solution. Using PFM and XRD, we monitored the internal structure; in particular, the formation of ferroelastic twin domains—a signature of internal strain. The PFM results showed an increase in the average ferroelastic twin domain areas as the $Pb(Ac)_2/PbCl_2$ ratio decreased. The XRD results confirmed that this increase was accompanied by an increase in lattice strain. We suggest that this strain increase is caused by the volatility difference of MA(Ac) and MACl that eventually leads to crystallization rate differences in various regions in the film. This difference leads to room temperature formation of highly strained $MAPbI_3$ in MA(Ac) areas and I^-/Cl^- exchange occurs in Cl-rich areas resulting in increased strain with increased $PbCl_2$ amount. The chemical gradient and the resulting strain gradient were observed via ToF-SIMS and XRD measurements, respectively. To observe the effect of the resulting ferroelastic twin domain configurations on the charge carrier dynamics, we conducted TRPL measurements. The presence of larger ferroelastic domains implies a reduction in the overall domain wall density, which leads to longer charge carrier lifetimes.[30]

Our work shows that the crystal strain and thereby the formation of ferroelastic twin domains can be chemically manipulated by simply changing the ratio of different precursors without the need to apply any external force. This strategy offers a simple and scalable route to achieve a favorable domain arrangement in $MAPbI_3$-based devices, enabling faster and more efficient charge extraction. Even beyond domain engineering in $MAPbI_3$, chemical strain engineering is a promising idea for strain engineering in many other other lead halide perovskite materials.

4. Experimental Section

Materials: Methylalmmonium iodide (MAI) was purchased from Greatcell Energy. Lead acetate ($Pb(Ac)_2$ for perovskite precursor, 98.0% purity) and lead chloride ($PbCl_2$, 99.999%) were purchased from Tokyo Chemical Industry and Sigma–Aldrich, respectively. Anhydrous dimethylformamide (DMF) was purchased from Sigma Aldrich.

Perovskite Film Preparation: Glass substrates were brushed with Hellmanex on both sides and washed with hot tap water and milliQ water followed by drying with an air gun. The cleaned substrates were subjected to UV-Ozone treatment (FHR UVOH 150 LAB, 250 W) for 30 min with oxygen feeding rate of 1 L min^{-1} right before spin coating.

Two precursor solutions were prepared for the film preparation. Precursor solution 1 was prepared with MAI (477.0 mg, 3 mol), $Pb(Ac)_2$ (325.3 mg, 1 mol), and DMF (1 mL) while precursor solution 2 was prepared with MAI (238.5 mg, 1.5 mol), $PbCl_2$ (137.0 mg, 0.5 mol), and DMF (500 µL). The precursor solutions 1 and 2 were mixed in 9:1, 8:2, 7:3, and 6:4 volume ratios before the fabrication. The perovskite film fabrication was carried out by static spin coating, which was performed at 4000 rpms (1000 rpm s^{-1}) for 1 min after smearing 100 µL solution over the substrate. After the spin coating, all the samples were dried at room temperature for 10 min. After drying, all samples were annealed in DMF vapor atmosphere at 100 °C for 10 min. Glass petri dishes were used to obtain the DMF vapor atmosphere. The DMF vapor media were prepared before the coating started. The films were first put on the hotplate outside of the petri dish until they turned black (≈3 seconds) then put under DMF vapor atmosphere. Number of samples per petri dish were changed from 1 to 4. However, the amount of DMF should be changed accordingly. 15 µL DMF per film was used for the annealing process. All processes were carried out in a nitrogen glovebox.

Piezoresponse Force Microscopy Measurements: Piezoresponse force microscopy (PFM) is an Atomic force microscopy (AFM) mode, which is used to detect electromechanical material properties on the nanometer scale. A conductive tip is used to detect the response of the sample to an AC voltage.

Lateral piezoresponse force microscopy (PFM) measurements were performed on an Asylum Research MFP-3D AFM from Oxford Instruments together with a Zürich Instruments HF2 lock-in amplifier in an argon filled glovebox (O_2 and H_2O < 1ppm). The measurements were carried out with platinum-iridium coated SCM PIT-V2 cantilevers from Bruker with a nominal resonance frequency of 70 kHz and a spring constant of ≈2.5 nN nm^{-1}. The measurement of the PFM signal was performed at an AC excitation voltage with a peak amplitude of 2 V at the lateral contact resonance at ≈700 kHz to take advantage of the resonance enhancement.

X-ray Diffraction Measurements: X-ray diffraction (XRD) patterns were taken with Rigaku SmartLab using Cu Kα radiation. Diffractograms had been recorded in "θ"–"θ" geometry, using a Göbel mirror and automatic sample alignment. The scanning rate was 2° min^{-1} in steps of 0.01°. The total beam exposure time was 30 min.

Time of Flight Secondary Ion Mass Spectroscopy: ToF-SIMS experiments were performed using a TOF.SIMS5 (NCS) instrument (IONTOF GmbH, Münster, Germany) with 30 keV Bi3 primary ions and 5 keV Ar1500 cluster ions for sputtering at a 45° angle. Surface imaging was facilitated using the ultimate imaging mode at a current of 0.05 pA at a cycle time of 100 µs. Dual beam depth profiling was conducted on an analysis area of 200×200 µm^2 with a sputter area of 500×500 µm^2 at a sputter current of 2.5 nA.

Optical Measurements: Absorption data was collected using a Cary5000 UV–vis-NIR spectrometer by Agilent equipped with an integrating sphere. Time-resolved photoluminescence was conducted via time-correlated single photon counting on a FluoTime300 spectrometer by PicoQuant at an emission wavelength of 770 nm, following pulsed 485 nm excitation at a repetition rate of 500 kHz.

Supporting Information

Supporting Information is available from the Wiley Online Library or from the author.

Conflict of Interest

The authors declare no conflict of interest.

Data Availability Statement

The data that support the findings of this study are available from the corresponding author upon reasonable request.

[1] A. Kojima, K. Teshima, Y. Shirai, T. Miyasaka, *J. Am. Chem. Soc.* **2009**, *131*, 6050.

[2] M. M. Lee, J. Teuscher, T. Miyasaka, T. N. Murakami, H. J. Snaith, *Science* **2012**, *338*, 643.

[3] H.-S. Kim, C.-R. Lee, J.-H. Im, K.-B. Lee, T. Moehl, A. Marchioro, S.-J. Moon, R. Humphry-Baker, J.-H. Yum, J. E. Moser, M. Grätzel, N.-G. Park, *Sci. Rep.* **2012**, *2*, 1.

[4] J. J. Yoo, S. Wieghold, M. C. Sponseller, M. R. Chua, S. N. Bertram, N. T. P. Hartono, J. S. Tresback, E. C. Hansen, J.-P. Correa-Baena, V. Bulović, T. Buonassisi, S. S. Shin, M. G. Bawendi, *Energy Environ. Sci.* **2019**, *12*, 2192.

[5] O. A. Jaramillo-Quintero, R. S. Sanchez, M. Rincon, I. Mora-Sero, *J. Phys. Chem. Lett.* **2015**, *6*, 1883.

[6] A. Ashar, N. Ganesh, K. Narayan, *Adv. Electron. Mater.* **2018**, *4*, 1870012.

[7] L. Protesescu, S. Yakunin, M. I. Bodnarchuk, F. Krieg, R. Caputo, C. H. Hendon, R. X. Yang, A. Walsh, M. V. Kovalenko, *Nano Lett.* **2015**, *15*, 3692.

[8] C. C. Stoumpos, C. D. Malliakas, M. G. Kanatzidis, *Inorg. Chem.* **2013**, *52*, 9019.

[9] T. J. Jacobsson, J.-P. Correa-Baena, M. Pazoki, M. Saliba, K. Schenk, M. Grätzel, A. Hagfeldt, *Energy Environ. Sci.* **2016**, *9*, 1706.

[10] K. X. Steirer, P. Schulz, G. Teeter, V. Stevanovic, M. Yang, K. Zhu, J. J. Berry, *ACS Energy Lett.* **2016**, *1*, 360.

[11] M. B. Johnston, L. M. Herz, *Acc. Chem. Res.* **2016**, *49*, 146.

[12] S. D. Stranks, G. E. Eperon, G. Grancini, C. Menelaou, M. J. Alcocer, T. Leijtens, L. M. Herz, A. Petrozza, H. J. Snaith, *Science* **2013**, *342*, 341.

[13] D. Shi, V. Adinolfi, R. Comin, M. Yuan, E. Alarousu, A. Buin, Y. Chen, S. Hoogland, A. Rothenberger, K. Katsiev, Y. Losovyj, X. Zhang, P. A. Dowben, O. F. Mohammed, E. H. Sargent, O. M. Bakr, *Science* **2015**, *347*, 519.

[14] E. G. Moloney, V. Yeddu, M. I. Saidaminov, *ACS Mater. Lett.* **2020**, *2*, 1495.

[15] H. Yuce, C. A. Perini, J. Hidalgo, A.-F. Castro-Méndez, C. Evans, P. F. Betancur, J. N. Vagott, Y. An, K. Bairley, M. M. Demir, J.-P. Correa-Baena, *Opt. Mater.* **2021**, 111806.

[16] C. Zhu, X. Niu, Y. Fu, N. Li, C. Hu, Y. Chen, X. He, G. Na, P. Liu, H. Zai, Y. Ge, Y. Lu, X. Ke, Y. Bai, S. Yang, P. Chen, Y. Li, M. Sui, L. Zhang, H. Zhou, Q. Chen, *Nat. Commun.* **2019**, *10*, 1.

[17] G. Kim, H. Min, K. S. Lee, D. Y. Lee, S. M. Yoon, S. I. Seok, *Science* **2020**, *370*, 108.

[18] J. Zhao, Y. Deng, H. Wei, X. Zheng, Z. Yu, Y. Shao, J. E. Shield, J. Huang, *Sci. Adv.* **2017**, *3*, eaao5616.

[19] J. A. Steele, H. Jin, I. Dovgaliuk, R. F. Berger, T. Braeckevelt, H. Yuan, C. Martin, E. Solano, K. Lejaeghere, S. M. Rogge, C. Notebaert, W. Vandezande, K. P. F. Janssen, B. Goderis, E. Debroye, Y.-K. Wang, Y. Dong, D. Ma, M. Saidaminov, H. Tan, Z. Lu, V. Dyadkin, D. Chernyshov, V. V. Speybroeck, E. H. Sargent, J. Hofkens, M. B. J. Roeffaers, *Science* **2019**, *365*, 679.

[20] Y. Chen, Y. Lei, Y. Li, Y. Yu, J. Cai, M.-H. Chiu, R. Rao, Y. Gu, C. Wang, W. Choi, H. Hu, C. Wang, Y. Li, J. Song, J. Zhang, B. Qi, M. Lin, Z. Zhang, A. E. Islam, B. Maruyama, S. Dayeh, L.-J. Li, K. Yang, Y.-H. Lo, S. Xu, *Nature* **2020**, *577*, 209.

[21] I. M. Hermes, S. A. Bretschneider, V. W. Bergmann, D. Li, A. Klasen, J. Mars, W. Tremel, F. Laquai, H.-J. Butt, M. Mezger, R. Berger, B. J. Rodriguez, S. A. L. Weber, *J. Phys. Chem. C* **2016**, *120*, 5724.

[22] B. Huang, G. Kong, E. N. Esfahani, S. Chen, Q. Li, J. Yu, N. Xu, Y. Zhang, S. Xie, H. Wen, P. Gao, J. Zhao, J. Li, *npj Quantum Mater.* **2018**, *3*, 1.

[23] H. Röhm, T. Leonhard, M. J. Hoffmann, A. Colsmann, *Energy Environ. Sci.* **2017**, *10*, 950.

[24] M. U. Rothmann, W. Li, Y. Zhu, U. Bach, L. Spiccia, J. Etheridge, Y.-B. Cheng, *Nat. Commun.* **2017**, *8*, 1.

[25] Y. Liu, L. Collins, R. Proksch, S. Kim, B. R. Watson, B. Doughty, T. R. Calhoun, M. Ahmadi, A. V. Ievlev, S. Jesse, S. T. Retterer, A. Belianinov, K. Xiao Huang, B. G. Sumpter, S. V. Kalinin, B. Hu, O. S. Ovchinnikova, *Nat. Mater.* **2018**, *17*, 1013.

[26] E. Strelcov, Q. Dong, T. Li, J. Chae, Y. Shao, Y. Deng, A. Gruverman, J. Huang, A. Centrone, *Sci. Adv.* **2017**, *3*, e1602165.

[27] A. A. Medjahed, P. Dally, T. Zhou, N. Lemaitre, D. Djurado, P. Reiss, S. Pouget, *Chem. Mater.* **2020**, *32*, 3346.

[28] J. Breternitz, M. Tovar, S. Schorr, *Sci. Rep.* **2020**, *10*, 1.

[29] X. Xiao, W. Li, Y. Fang, Y. Liu, Y. Shao, S. Yang, J. Zhao, X. Dai, R. Zia, J. Huang, *Nat. Commun.* **2020**, *11*, 1.

[30] I. M. Hermes, A. Best, L. Winkelmann, J. Mars, S. M. Vorpahl, M. Mezger, L. Collins, H.-J. Butt, D. S. Ginger, K. Koynov, S. A. L. Weber, *Energy Environ. Sci.* **2020**, *13*, 4168.

[31] S. M. Vorpahl, R. Giridharagopal, G. E. Eperon, I. M. Hermes, S. A. Weber, D. S. Ginger, *ACS Appl. Energy Mater.* **2018**, *1*, 1534.

[32] H. Röhm, T. Leonhard, M. J. Hoffmann, A. Colsmann, *Adv. Funct. Mater.* **2020**, *30*, 1908657.

[33] W. Zhang, M. Saliba, D. T. Moore, S. K. Pathak, M. T. Hörantner, T. Stergiopoulos, S. D. Stranks, G. E. Eperon, J. A. Alexander-Webber, A. Abate, A. Sadhanala, S. Yao, Y. Chen, R. H. Friend, L. A. Estroff, U. Wiesner, H. J. Snaith, *Nat. Commun.* **2015**, *6*, 1.

[34] D.-K. Lee, D.-N. Jeong, T. K. Ahn, N.-G. Park, *ACS Energy Lett.* **2019**, *4*, 2393.

[35] Y. Dang, Y. Liu, Y. Sun, D. Yuan, X. Liu, W. Lu, G. Liu, H. Xia, X. Tao, *CrystEngComm* **2015**, *17*, 665.

[36] T. Leonhard, H. Röhm, F. J. Altermann, M. J. Hoffmann, A. Colsmann, *J. Mater. Chem. A* **2021**, *9*, 21845.

[37] E. L. Unger, A. R. Bowring, C. J. Tassone, V. L. Pool, A. Gold-Parker, R. Cheacharoen, K. H. Stone, E. T. Hoke, M. F. Toney, M. D. McGehee, *Chem. Mater.* **2014**, *26*, 7158.

[38] Y. Liu, A. V. Ievlev, L. Collins, A. Belianinov, J. K. Keum, M. Ahmadi, S. Jesse, S. T. Retterer, K. Xiao, J. Huang, B. G. Sumpter, S. V. Kalinin, B. Hu, O. S. Ovchinnikova, *Adv. Electron. Mater.* **2020**, *6*, 1901235.

[39] M. Coll, A. Gomez, O. Mas-Marza, O. Almora, G. Garcia-Belmonte, M. Campoy-Quiles, J. Bisquert, *J. Phys. Chem. Lett.* **2015**, *6*, 1408.

[40] J. Zhang, K. Wang, Q. Yao, Y. Yuan, J. Ding, W. Zhang, H. Sun, C. Shang, C. Li, T. Zhou, S. Pang, *ACS Appl. Mater. Interfaces* **2021**.

Supporting Information

Chemical Strain Engineering of MAPbI$_3$ Perovskite Films

*Yenal Yalcinkaya, Ilka M. Hermes, Tobias Seewald, Katrin Amann-Winkel, Lothar Veith, Lukas Schmidt-Mende, and Stefan A.L. Weber**

Chemical Strain Engineering of MAPbI₃ Perovskite Films

Yenal Yalcinkaya Ilka Maria Hermes Tobias Seewald Katrin Amann-Winkel Lothar Veith Lukas Schmidt-Mende Stefan A.L. Weber*

Y. Yalcinkaya, Prof. Dr. K. Amann-Winkel, Dr. L. Veith , Prof. Dr. S. A. L. Weber
Max Planck Institute for Polymer Research, Ackermannweg 10, 55128 Mainz, Germany
Email Address: webers@mpip-mainz.mpg.de
Dr. I. M. Hermes
Leibniz Institute for Polymer Research Dresden e.V. Institute of Physical Chemistry and Polymer Physics
Department Polymer Interfaces Hohe Str. 6 01069 Dresden, Germany
Y. Yalcinkaya, Prof. Dr. K. Amann-Winkel, Prof. Dr. Stefan A. L. Weber
Institute of Physics, Johannes Gutenberg University Mainz, Duesbergweg 10-14, 55128 Mainz, Germany
T. Seewald, Prof. Dr. L. Schmidt-Mende
Department of Physics, University of Konstanz, Universitätsstr. 10, 78464, Germany
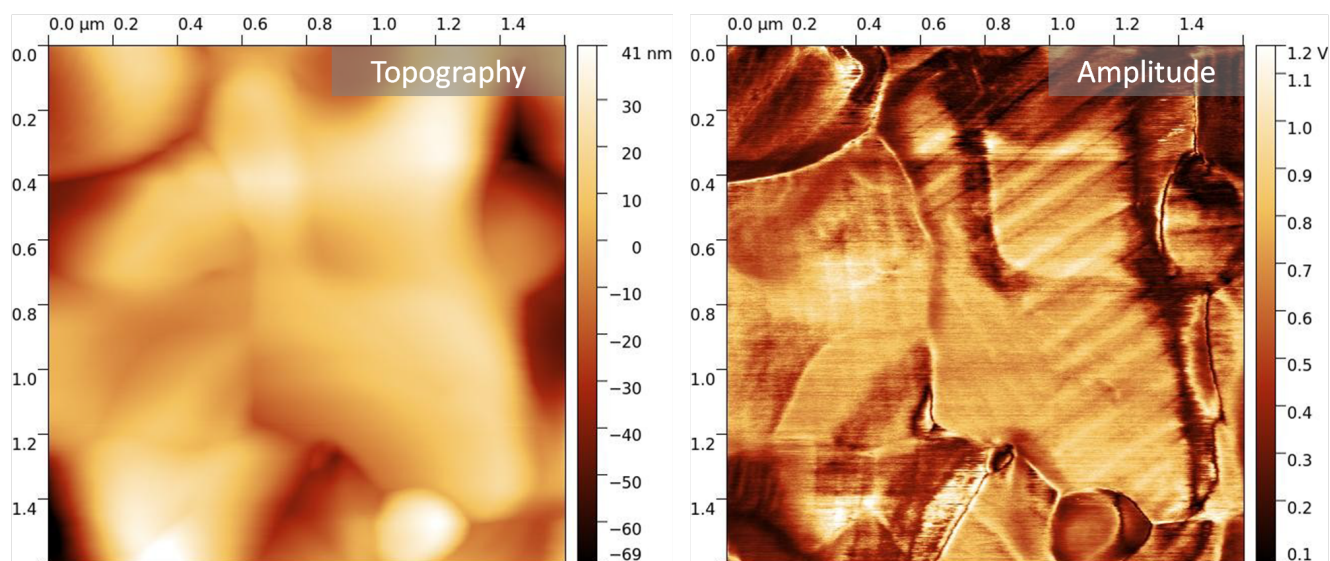
Figure S1: Topography and lateral PFM images of MAPbI₃ film made with only MAI and Pb(Ac)₂.
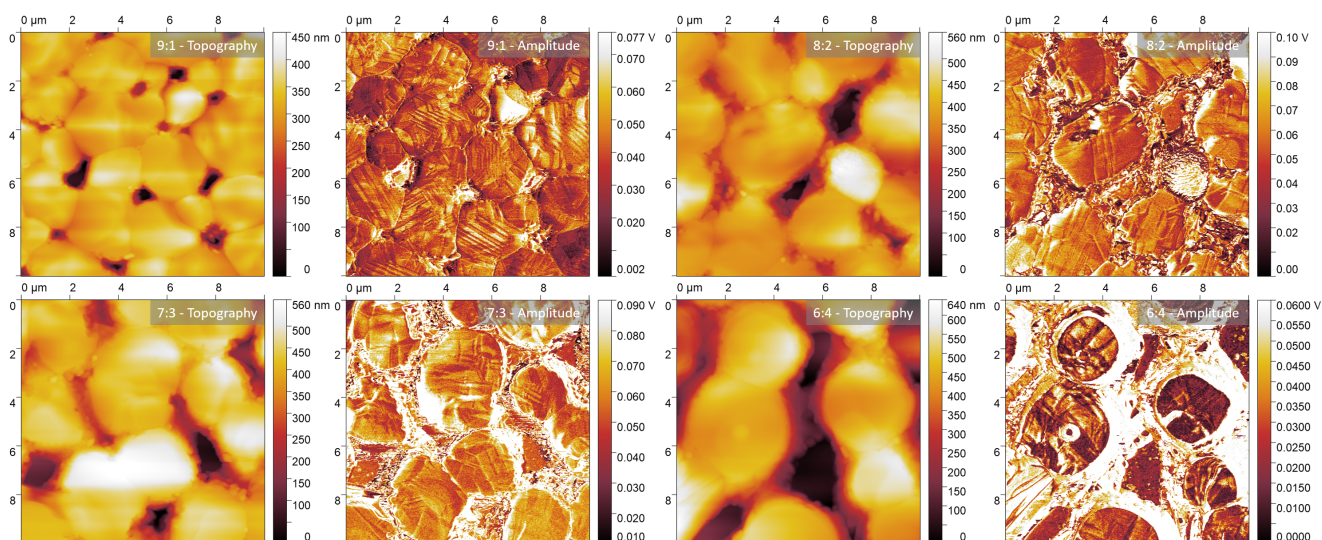
Figure S2: Topography and lateral PFM images of MAPbI$_3$ films with Pb(Ac)$_2$ / PbCl$_2$ ratios of 9:1, 8:2, 7:3 and 6:4.

Bragg's Law

The Bragg's law gives the relation between the diffraction angle and the interplanar distance as follows:

$$n\lambda = 2dsin\theta \tag{1}$$

where λ, d, and θ denotes interplanar distance, and diffraction angles, respectively. Furthermore, the interplanar distance for the tetragonal lattice is given as

$$\frac{1}{d^2} = \frac{(h^2 + k^2)}{a^2} + \frac{l^2}{c^2} \tag{2}$$

where h,k, and l are the Miller indices and a and c are lattice parameters. When Equation S1 and S2 are combined, it can be seen that the reflection angles for hkl planes in XRD may give information on the lattice parameters. A shift to higher scattering angles would indicate lattice shrinkage whereas a shift to lower scattering angles would indicate lattice expansion. Therefore, the peak shift to lower scattering angles in Figure 2 can be interpreted as possible lattice expansion.

X-ray Diffraction Measurements

In order to gain insight on the twin formation, we carried out XRD measurements on MAPbI$_3$ films with different precursor ratios (Figure S5, Supporting Information) right after the spin coating without annealing. First notable observation here is the increasing intensity of MAPbCl$_3$ reflection upon increasing the PbCl$_2$ content in the precursor, which supports the I$^-$ / Cl$^-$ ion exchange theory. Even though the MAPbCl$_3$ reflection is present in all spectra in Figure S5, the intensity of the peaks is extremely low compared to a pure MAI/PbCl$_2$ film. This could be caused by the formation of a Cl-rich perovskite region at the interface to the substrate. Another important observation is the absence of twinning in MAI/PbCl$_2$ film while all other samples show (004)/(220) twinning. These results suggest the room temperature crystallization of tetragonal MAPbI$_3$ due to high volatility of MA(Ac) leads to high strain - ergo twinning. On the other hand, in case of twinning in MAPbI$_3$ film made from MAI/PbCl$_2$ precursors, the I$^-$ / Cl$^-$ ion exchange is the main reason for the strain. Therefore, we speculate that the increased strain in MAPbI$_3$ films from Pb(Ac)$_2$ / PbCl$_2$ precursors is the combined result of having highly strained MAPbI$_3$
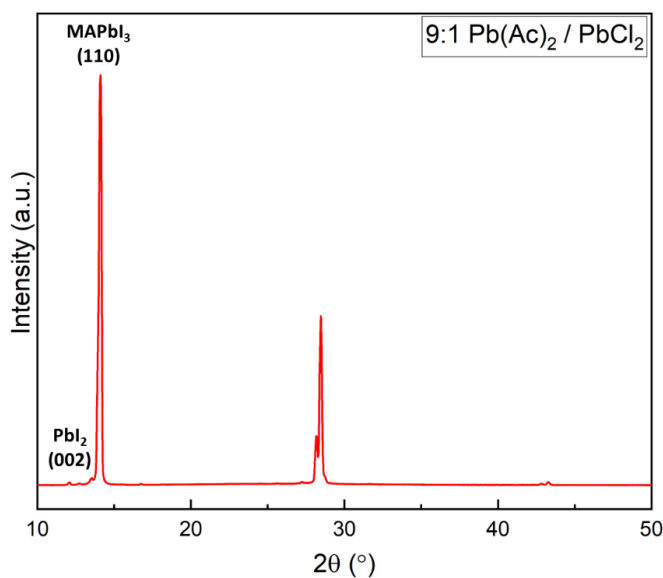
Figure S3: XRD pattern of MAPbI$_3$ film with 9:1 Pb(Ac)$_2$ / PbCl$_2$ ratio.
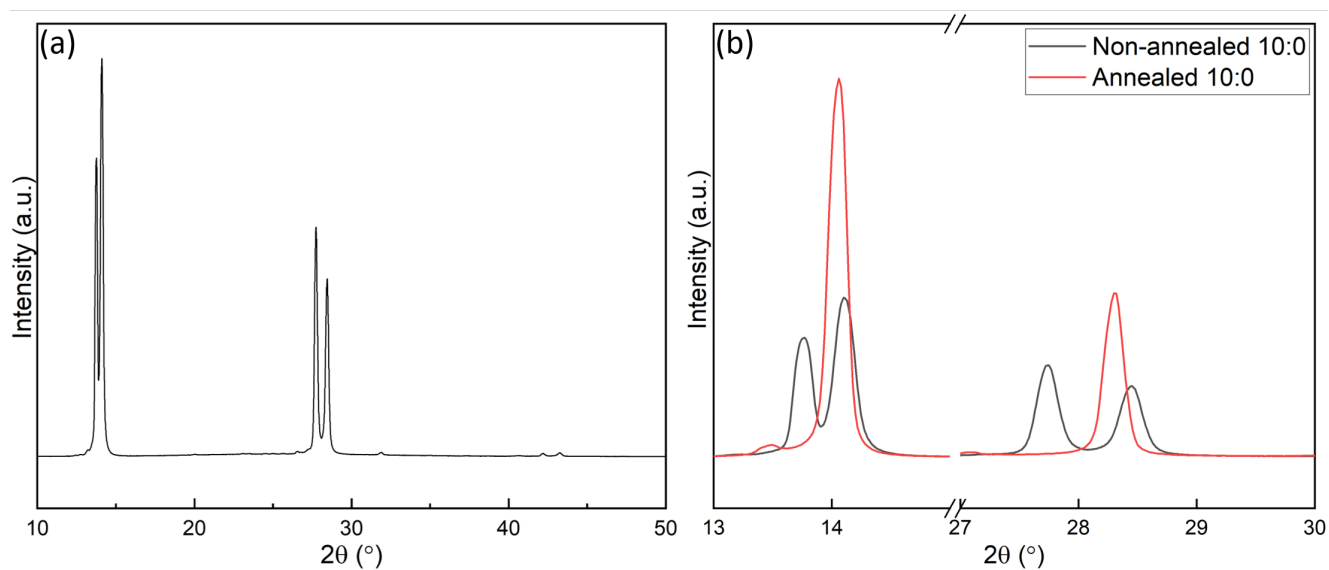
Figure S4: XRD pattern of MAPbI$_3$ film made with only MAI and Pb(Ac)$_2$ (a) without and (b) with annealing.

grains in Pb(Ac)$_2$-rich areas due to room temperature crystallization and I$^-$ / Cl$^-$ ion exchange in PbCl$_2$-rich areas during MAPbI$_3$ formation. The peak around 17° did not correspond to any perovskite phases, therefore was assumed to belong to an intermediate phase, as previously reported by Medjahed et al. [1].
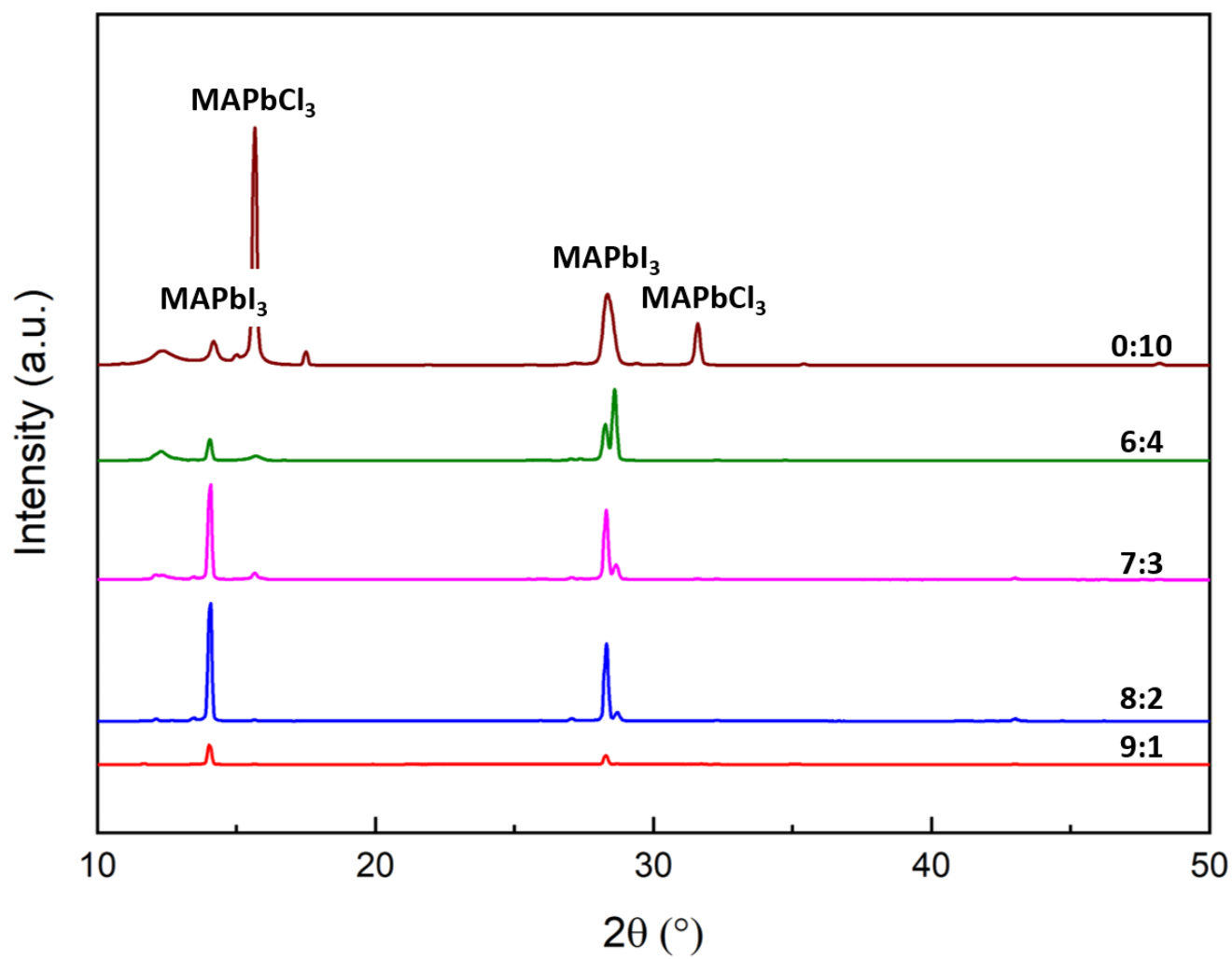
Figure S5: XRD pattern of non-annealed MAPbI$_3$ films with Pb(Ac)$_2$ / PbCl$_2$ ratios of 9:1, 8:2, 7:3, 6:4, and 0:10.

Grazing Incidence X-ray Diffraction
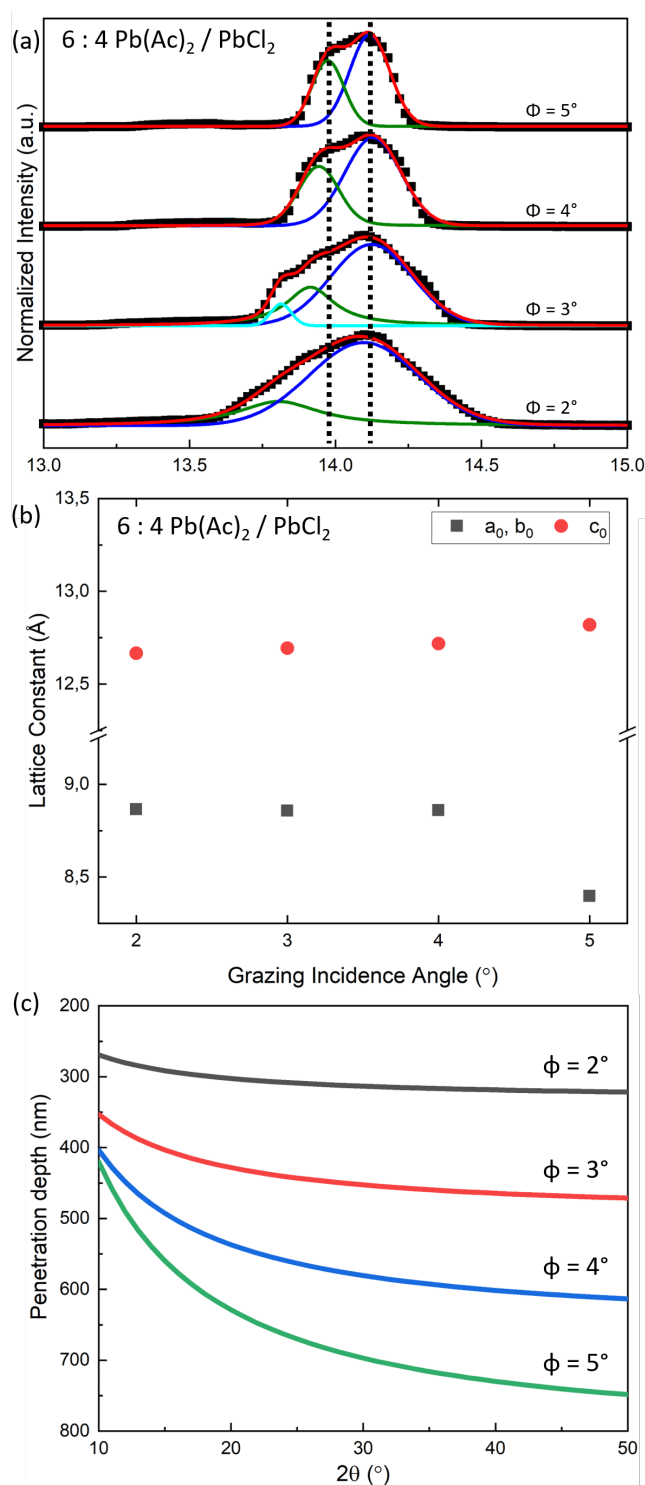
Figure S6: (a) Gracing incidence angle dependent XRD reflections of MAPbI$_3$ film made with 6:4 Pb(Ac)$_2$ / PbCl$_2$ ratio, (b) the lattice constants of MAPbI$_3$ depending on the grazing incidence angle, and (c) Estimated penetration depths for different grazing incidence angles for MAPbI$_3$ film. The shoulder appearing for 3° grazing incidence angle is not defined and could be related to non-90° domains.

We estimated the x-ray penetration depth (z) based on the following equation [2]:

$$z = a_L \left(\frac{1}{sin\alpha} + \frac{1}{sin(2\theta - \alpha)} \right)^{-1} \tag{3}$$

where a_L and α are attenuation length and grazing incidence angle, respectively. The x-ray penetration depth is conventionally defined as the depth where X-ray intensity reduced to 1/e of the initial intensity. The penetration depths values estimated from Equation S3 for incidence angles of 2°, 3°, 4°, and 5°are given in Figure S6c.

Time-of-Flight Secondary Ion Mass Spectroscopy

We obtained the ToF-SIMS results by bombarding the sample surface with Ar clusters and collecting the sputtered ions from the sample. With this process we were able to get vertical and lateral ion distribution of our perovskite films. However, obtaining the actual sample depth during ToF-SIMS is difficult due to differences in local sputtering rates. Therefore, we included Si signal as the indicator element for the glass substrate to mark the substrate position. The simultaneous appearance of the Si signal with a peak in the Cl signal is a clear indicator for a Cl-rich layer at the bottom of the film and the ion exchange interface within the film.
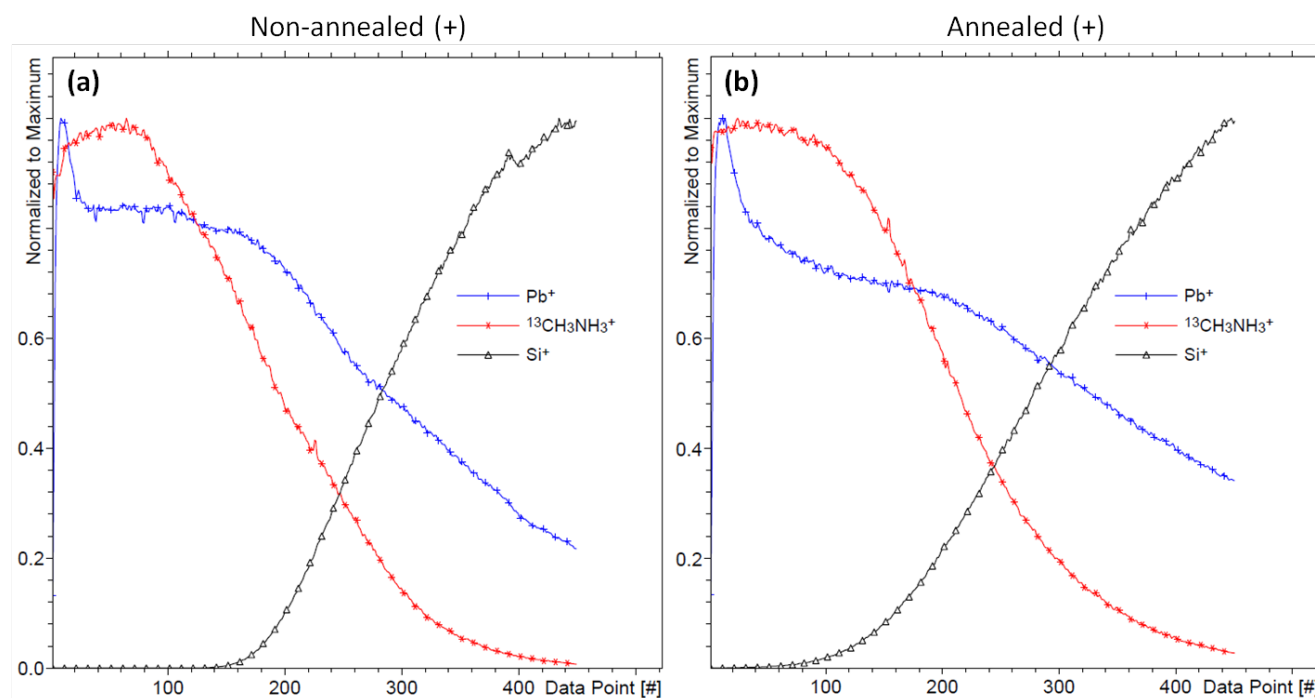
Figure S7: Depth profiles of positive ions in MAPbI$_3$ film made with 6:4 Pb(Ac)$_2$ / PbCl$_2$ ratio.
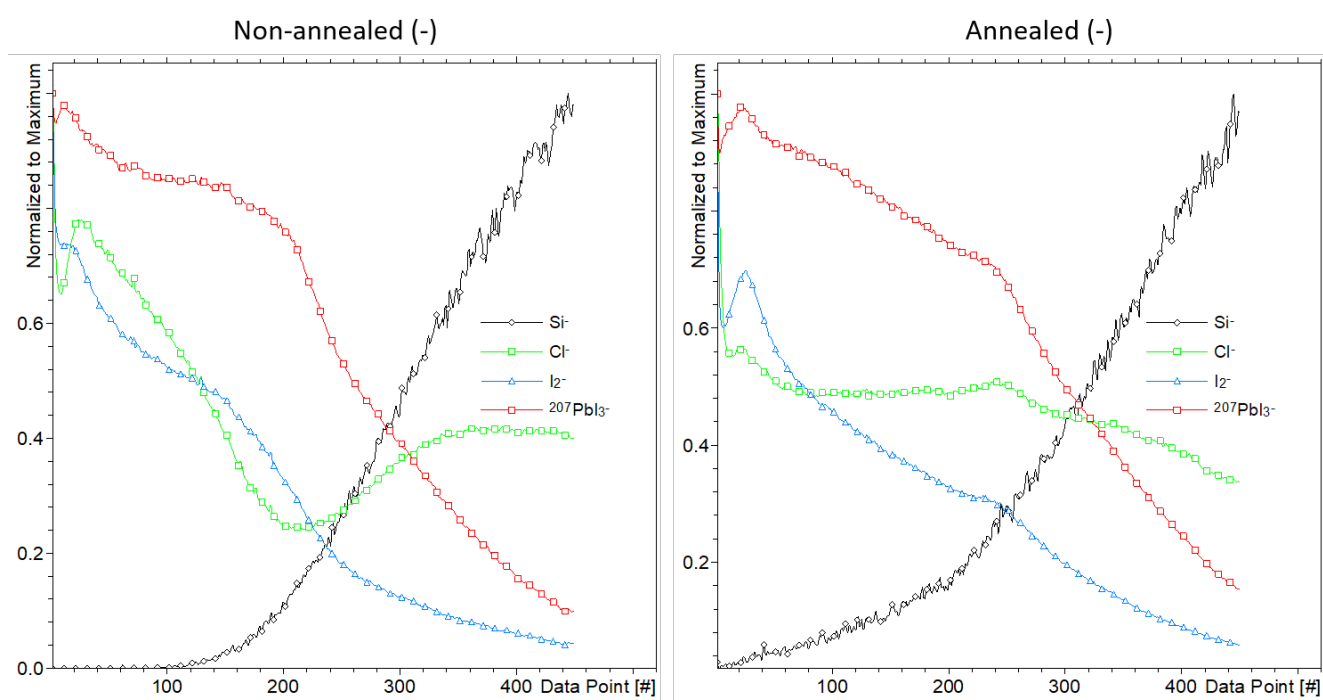
Figure S8: Depth profiles of negative ions in MAPbI$_3$ film made with 9:1 Pb(Ac)$_2$ / PbCl$_2$ ratio.
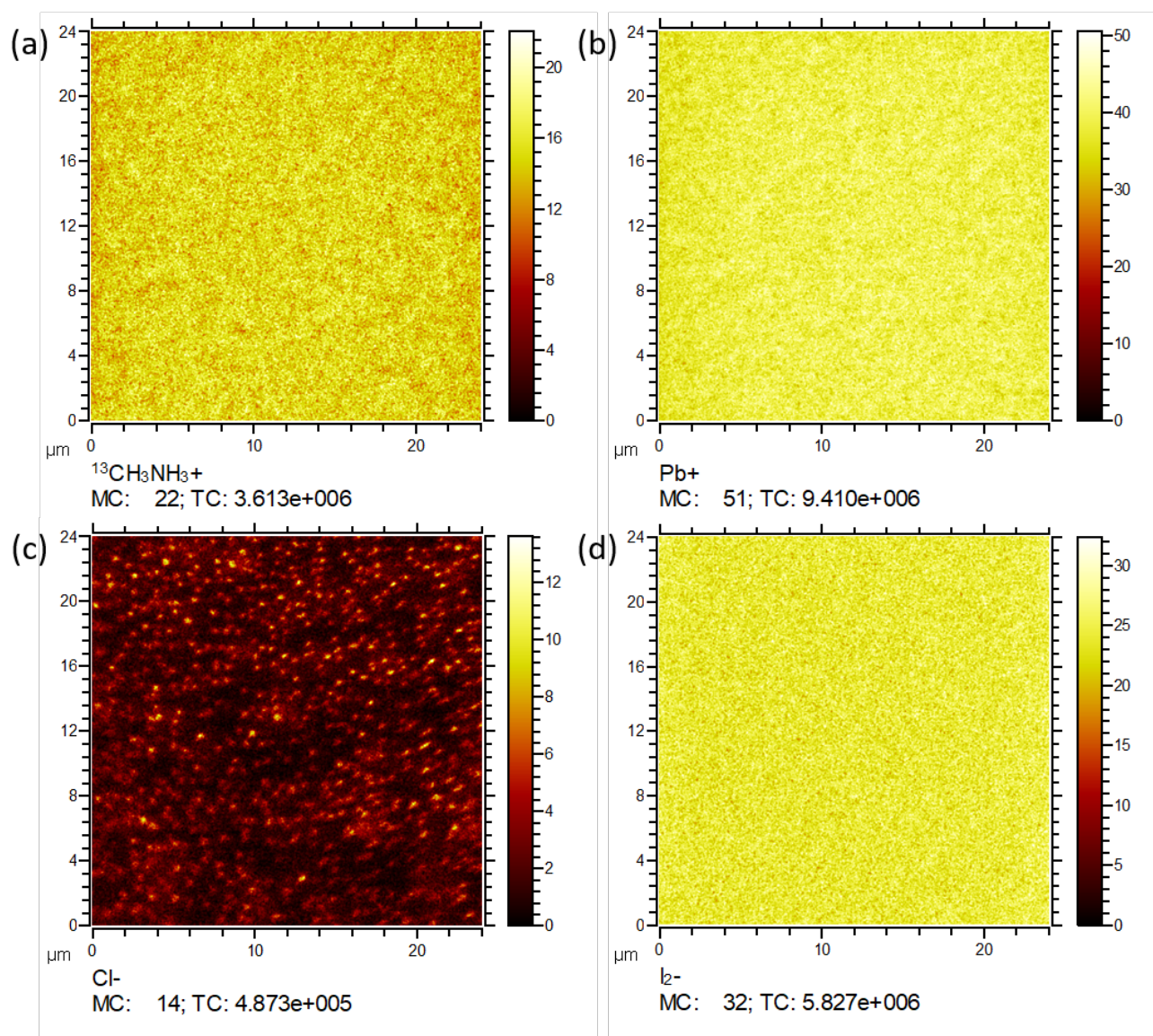
Figure S9: Lateral chemical cation distributions in non-annealed MAPbI$_3$ film made with 6:4 Pb(Ac)$_2$ / PbCl$_2$ ratio, 24 μm x 24 μm.
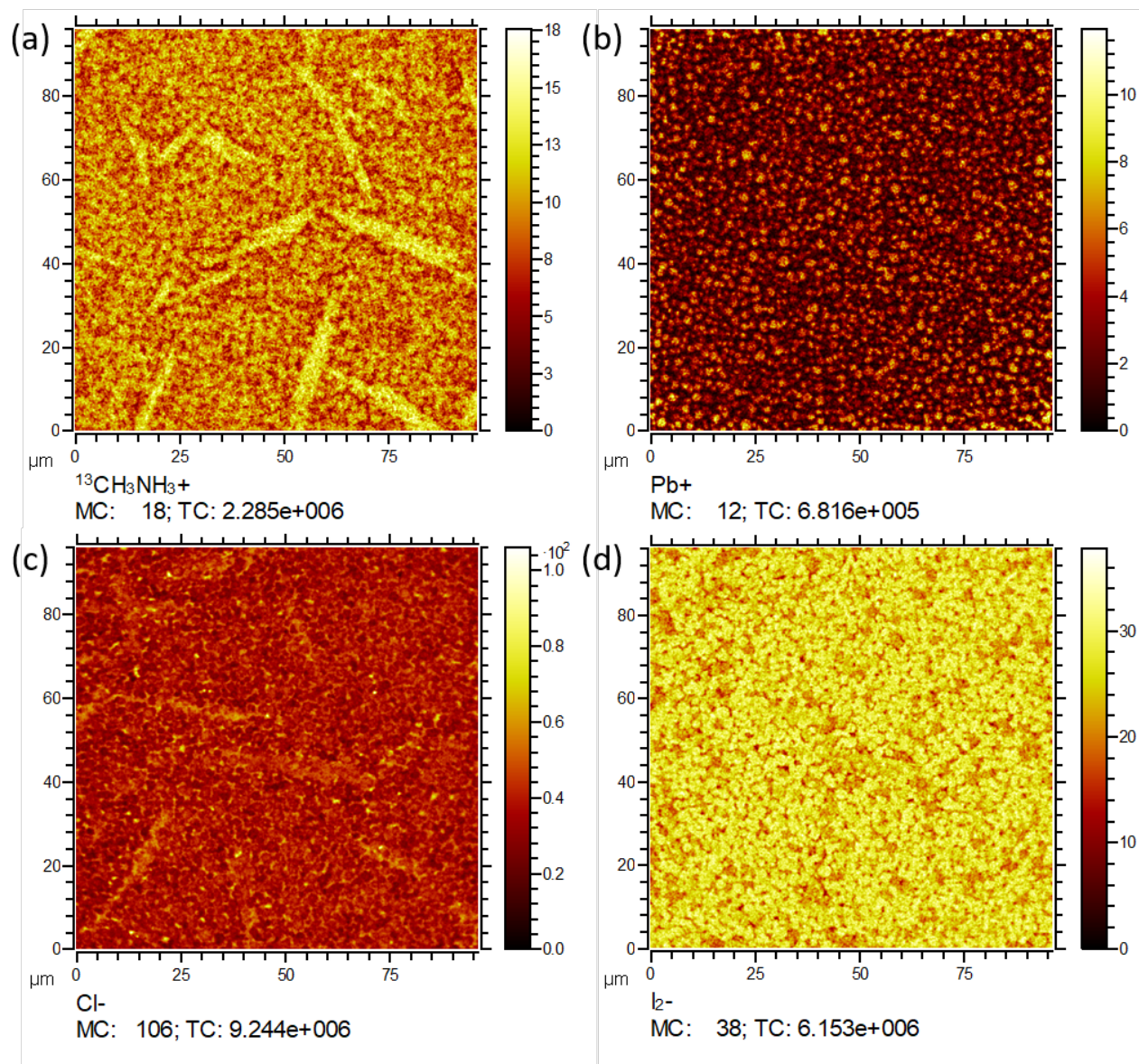
Figure S10: Lateral chemical ion distributions in annealed MAPbI$_3$ film made with 6:4 Pb(Ac)$_2$ / PbCl$_2$ ratio, 100 μm x 100 μm.

(a) Pb+
MC: 46; TC: 7.360e+006

(b) $^{13}CH_3NH_3+$
MC: 27; TC: 4.176e+006

(c) Cl-
MC: 113; TC: 4.698e+006

(d) I_2-
MC: 25; TC: 2.987e+006
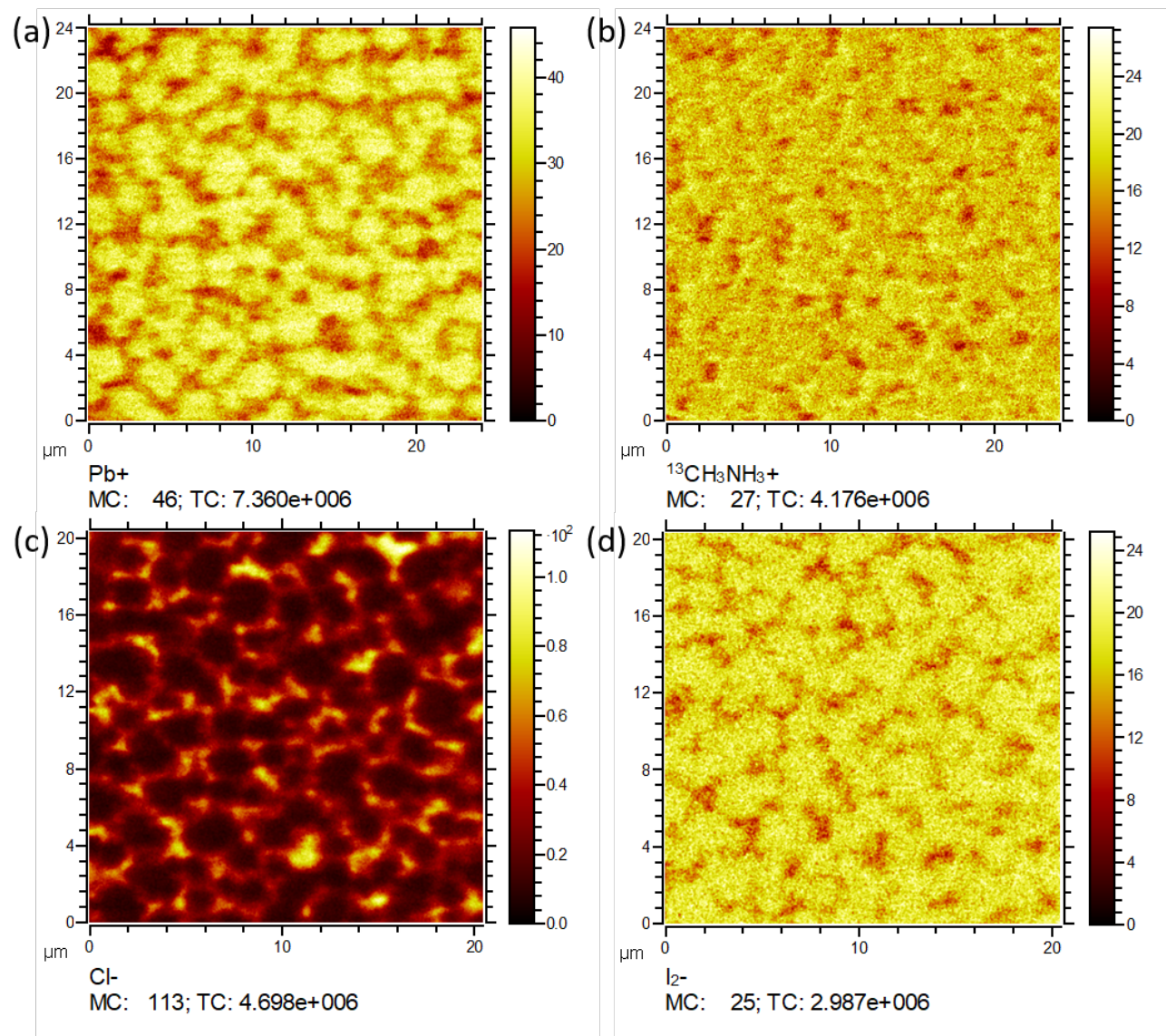
Figure S11: Lateral chemical ion distributions in annealed MAPbI$_3$ film made with 6:4 Pb(Ac)$_2$ / PbCl$_2$ ratio, 24 µm x 24 µm.

Bandgap and Time-resolved Photoluminescence Fit Results
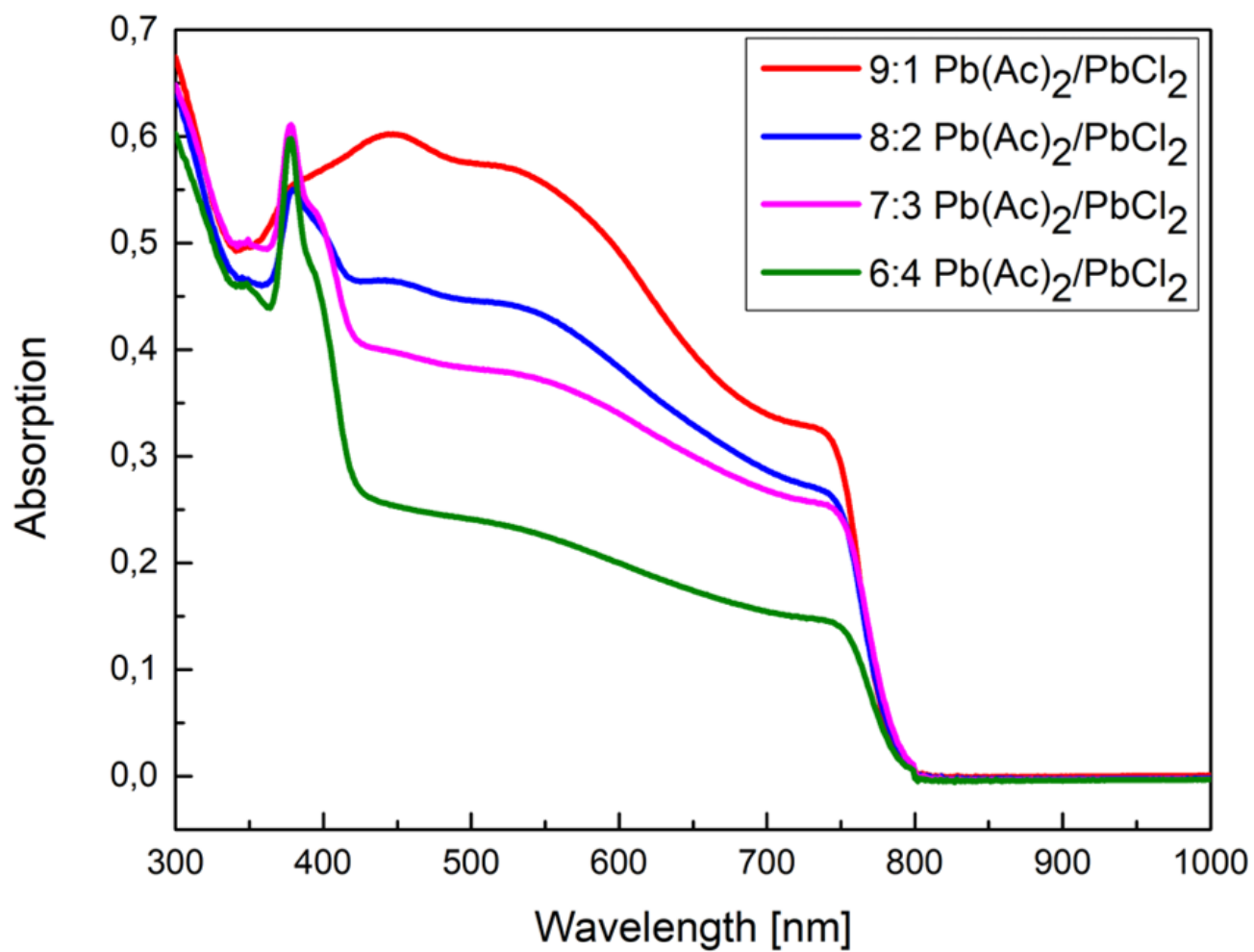
Figure S12: UV-Vis measurement results of MAPbI$_3$ thin films with Pb(Ac)$_2$ / PbCl$_2$ ratios of (a) 9:1, (b) 8:2, (c) 7:3 and (d) 6:4.
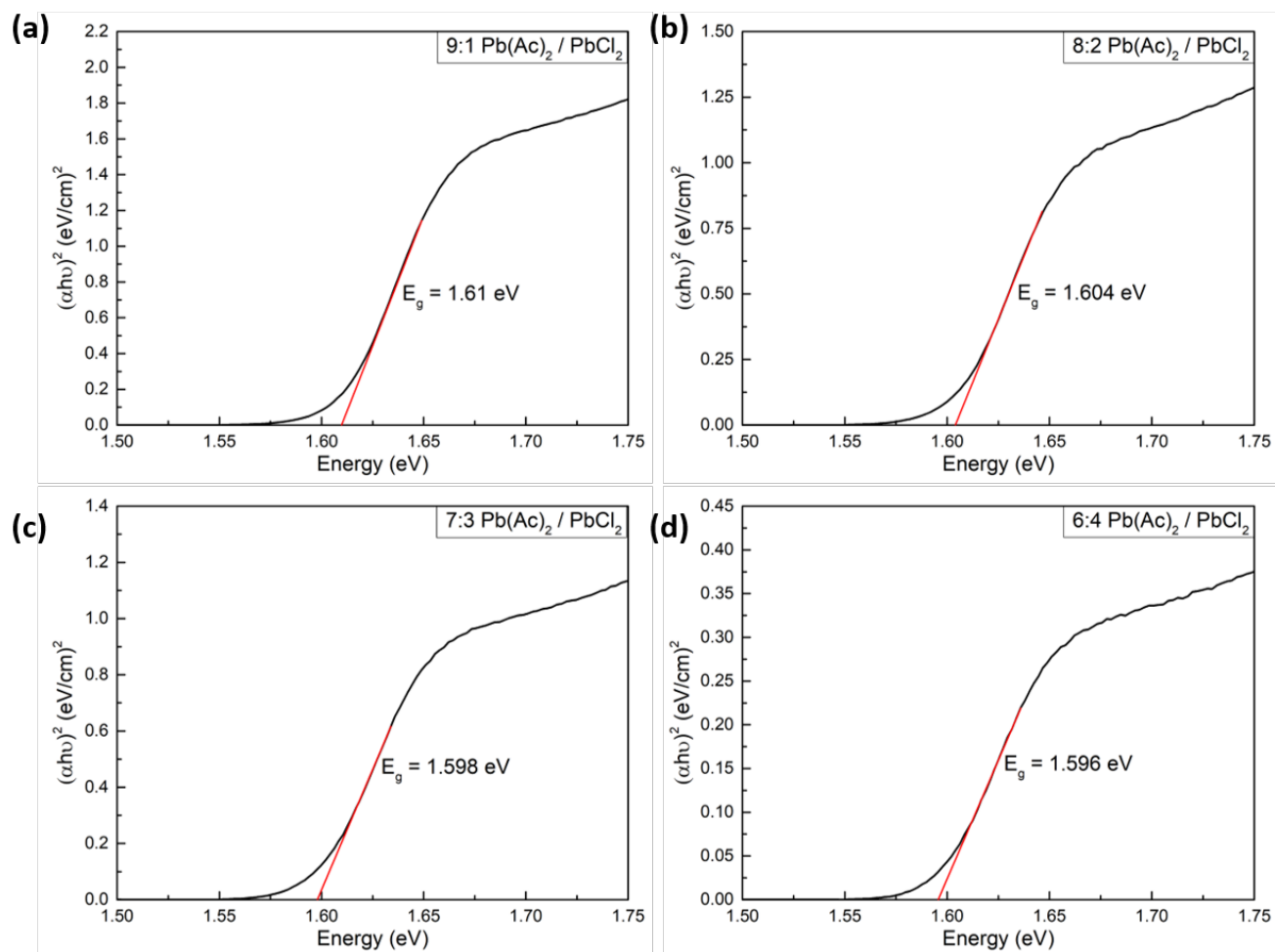
Figure S13: Tauc plots of MAPbI$_3$ thin films with Pb(Ac)$_2$ / PbCl$_2$ ratios of (a) 9:1, (b) 8:2, (c) 7:3 and (d) 6:4.
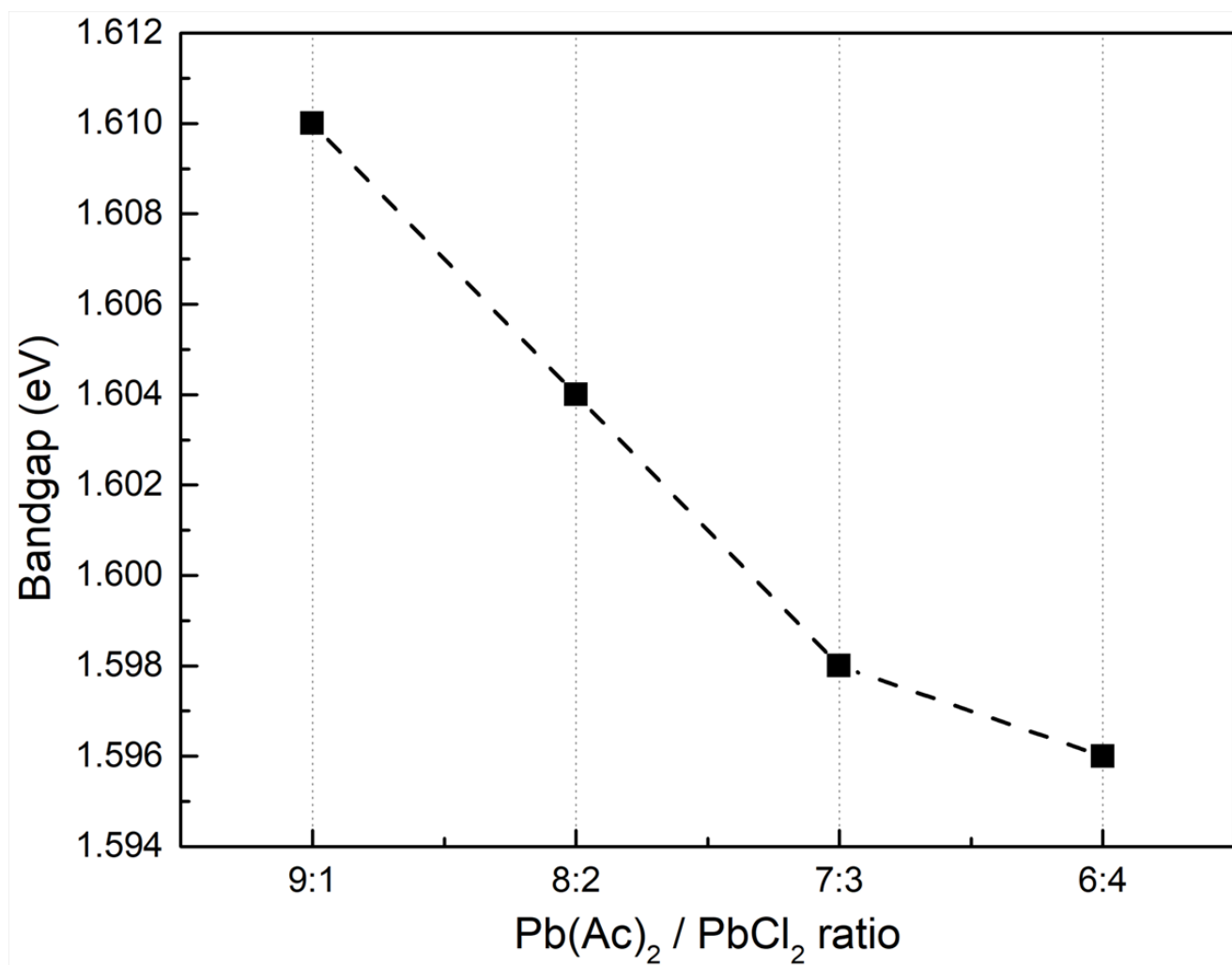
Figure S14: Pb(Ac)$_2$ / PbCl$_2$ ratio dependent bandgaps of MAPbI$_3$ films.

Table S1: TRPL fit results for MAPbI$_3$ thin films with Pb(Ac)$_2$ / PbCl$_2$ ratios of 10:0, 9:1, 8:2, 7:3 and 6:4.

Pb(Ac)$_2$ / PbCl$_2$ ratio	A1	τ_1 (ns)	A2	τ_2 (ns)	<τ> (ns)
9:1	2089.57 ± 5.37	17.39 ± 0.07	3570.17 ± 6.14	75.37 ± 0.08	68.47 ± 0.23
8:2	2607.27 ± 5.66	13.31 ± 0.05	5196.40 ± 3.90	90.27 ± 0.06	84.78 ± 0.15
7:3	6327.90 ± 5.17	106.16 ± 0.07	5196.40 ± 7.02	14.95 ± 0.04	96.71 ± 0.18
6:4	5758.97 ± 8.06	16.51 ± 0.04	6185.36 ± 6.22	115.99 ± 0.10	104.34 ± 0.24

SEM Images
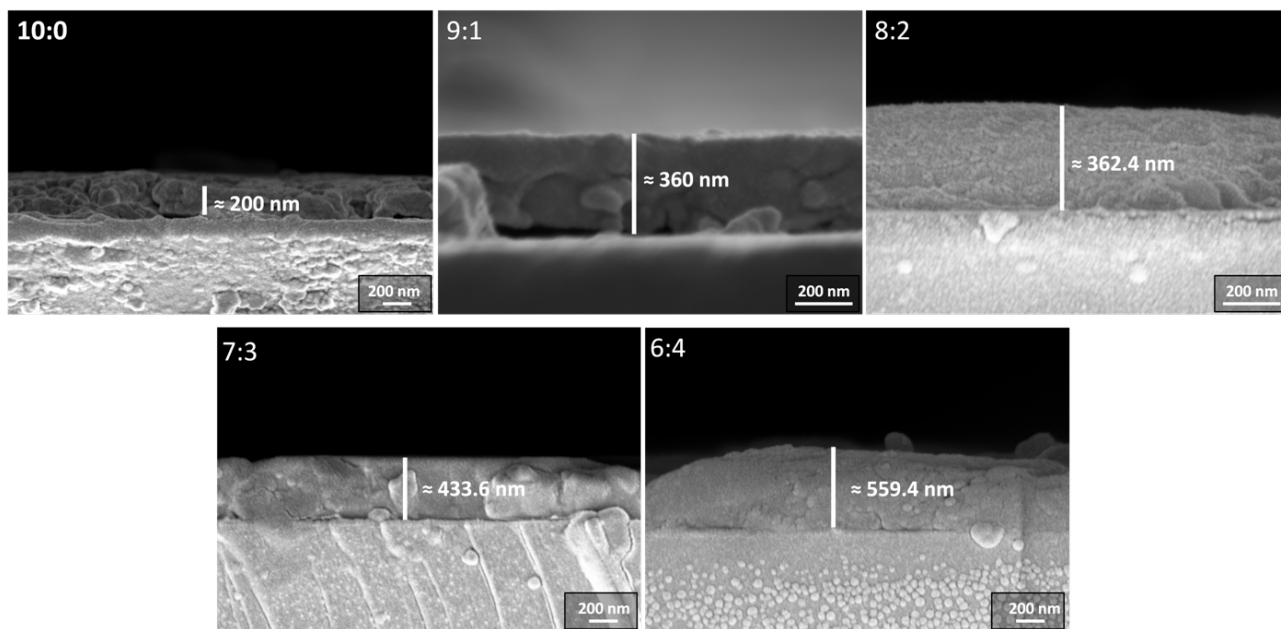
Figure S15: Cross-sectional SEM images of MAPbI$_3$ films with different Pb(Ac)$_2$ / PbCl$_2$ ratios.

References

[1] A. A. Medjahed, P. Dally, T. Zhou, N. Lemaitre, D. Djurado, P. Reiss, S. Pouget, *Chemistry of Materials* **2020**, *32*, 8 3346.

[2] M. Dimitrievska, A. Fairbrother, R. Gunder, G. Gurieva, H. Xie, E. Saucedo, A. Pérez-Rodríguez, V. Izquierdo-Roca, S. Schorr, *Physical Chemistry Chemical Physics* **2016**, *18*, 12 8692.

4 Nanoscale Surface Photovoltage Spectroscopy

Summary & Author Contributions

In this paper, we utilized time-resolved KPFM to investigate defect and free charge carrier dynamics within halide perovskites. To this end, we employed nanoscale surface photovoltage spectroscopy (nano-SPV) and nanoscale ideality factor mapping (nano-IFM) to map charge carrier recombination, ion migration, and defects in halide perovskite samples with different morphologies.

Mehmet Yenal Yalcinkaya and Pascal Rohrbeck are the first co-authors of this paper. Mehmet Yenal Yalcinkaya measured the reference sample (Figure 2) and methylamine treated sample (Figure 5) via nano-SPV and developed nano-IFM method as an alternative way to map defects in reference sample (Figure 6) and methylamine treated sample (Figure 7).

Nanoscale Surface Photovoltage Spectroscopy

Yenal Yalcinkaya, Pascal N. Rohrbeck, Emilia R. Schütz, Azhar Fakharuddin, Lukas Schmidt-Mende, and Stefan A.L. Weber*

Understanding electron and ion dynamics is an important task for improving modern energy materials, such as photovoltaic perovskites. These materials usually have delicate nano- and microstructures that influence the device parameters. To resolve detailed structure–function relationships on the relevant micro- and nanometer length scales, the current macroscopic and microscopic measurement techniques are often not sufficient. Here, nanoscale surface photovoltage spectroscopy (nano-SPV) and nanoscale ideality factor mapping (nano-IFM) via time-resolved Kelvin probe force microscopy are introduced. These methods can map nanoscale variations in charge carrier recombination, ion migration, and defects. To show the potential of nano-SPV and nano-IFM, these methods are applied to perovskite samples with different morphologies. The results clearly show an improved uniformity of the SPV and SPV decay distribution within the perovskite films upon passivation and increasing the grain size. Nevertheless, nano-SPV and nano-IFM can still detect local variations in the defect density on these optimized samples, guiding the way for further optimization.

1. Introduction

Lead halide perovskites are promising materials for optoelectronic applications due to their direct adjustable band gap,[1–3] high defect tolerance,[4] and long charge carrier lifetimes.[5–7] Unlike conventional semiconductors, lead halide perovskites do not possess a high density of deep trap states.[8] The trap states due to crystal defects within the halide perovskites appear

within or close to the energy bands. This defect tolerance allows high-quality perovskite films to be fabricated from simple solution processes. Nonetheless, energy losses still occur at areas with high defect density, such as grain boundaries (GB) of the halide perovskites or interfaces within perovskite solar cells (PSCs), increasing nonradiative recombination losses during device operations.[9]

Defects related to non-radiative recombination in perovskites mainly occur as 1D point defects such as interstitials, antisites, or vacancies; 2D defects such as GBs, interfaces, and surfaces; and 3D defects such as clusters of iodine or lead or defects at the contacts. Interfacial recombination may originate from energy alignment mismatch between layers, surface defects, and charge carrier back transfer.[10–14] Improving the perovskite film quality by means of passivation is a common strategy to improve device efficiency.[15,16] Common surface passivation methods use chemical agents that partially fill the vacancies on the perovskite film surface. Here, the active group (ammonium, for example) fills the A^+ cation vacancies, whereas other parts of the passivation agent can be used, for example, for increasing the hydrophobicity of the perovskite surface. A good example is phenylethylammonium ion (PEA^+), which contains an ammonium and a hydrophobic phenyl group.[15]

The main goal of defect passivation is to increase the efficiency of PSCs. The most common and straightforward way to characterize the perovskite film quality is therefore to measure the efficiency of PSC devices. To understand the mechanisms behind efficiency losses, however, it is helpful to characterize the perovskite layer itself. Commonly used methods aim at monitoring the charge carrier dynamics such as photoluminescence (PL)[17]; transient absorption[18]; Terahertz, microwave, or electrical impedance spectroscopy[19,20]; surface photovoltage (SPV)[21]; and surface photocurrent[22] measurements. These methods are usually conducted on macroscopic length scales and therefore yield measurements that are averaged over many different grains, GBs, and other interfaces. Local measurements such as PL microscopy[23] and fluorescence lifetime microscopy (FLIM)[24] can record and map the charge carrier dynamics. However, the lateral resolution of these optical methods is diffraction-limited and cannot fully resolve effects at the GBs. Alternatively, qualitative SPV mapping can be performed via scanning electron microscopy (SEM). Here, the electric fields generated by the local photovoltage modulate the secondary electron emission and

Y. Yalcinkaya, P. N. Rohrbeck, S. A. Weber
Max Planck Institute for Polymer Research
Ackermannweg 10, 55128 Mainz, Germany
E-mail: webers@mpip-mainz.mpg.de

Y. Yalcinkaya, S. A. Weber
Institute of Physics
Johannes Gutenberg University Mainz
Duesbergweg 10-14, 55128 Mainz, Germany

E. R. Schütz, A. Fakharuddin, L. Schmidt-Mende
Department of Physics
University of Konstanz
Universitätsstr. 10, 78464 Konstanz, Germany

ADVANCED
SCIENCE NEWS
www.advancedsciencenews.com

ADVANCED
OPTICAL
MATERIALS
www.advopticalmat.de

thereby the image contrast. Irde et al.[25] have demonstrated the SEM-based mapping of SPV dynamics on methylammonium lead iodide thin films within seconds to hours.[25] Pietralunga et al.[26] used SEM-based SPV spectroscopy to study charge transport dynamics, internal electric field configurations, and interface energetics of perovskite films under illumination.[26] Generally, the irradiation with high-energy electrons under high vacuum conditions can damage delicate perovskite samples,[27] even though electron beam damage can be reduced via the use of low-energy electron beams[28] or by reducing the electron dose,[29] limiting the spatial resolution and the signal-to-noise ratio.[25,30]

Here, atomic force microscopy (AFM) is a more gentle and versatile alternative. Next to the sample topography, AFM can detect many other surface properties and sub-granular structures.[31–33] Using conductive AFM (C-AFM), Shao et al.[34] measured the current values on the perovskite grains and the GBs in between. These measurements demonstrated that ion migration is faster at GBs compared to grain interiors. Conings et al.[35] used C-AFM to track the degradation of methylammonium lead iodide films after annealing. Recently, we showed via C-AFM that an increased grain size as a result of methylamine treatment resulted in a higher conductivity and a lower charge accumulation at the GBs, indicating more efficient charge dissociation and transport within the grains. Another important AFM method is Kelvin probe force microscopy (KPFM). KPFM maps the electrostatic surface potential and has been used to reveal interfacial charges within perovskite devices[36–38] and band bending behavior at the GBs.[15,39] KPFM is particularly powerful in combination with sample excitation, for example, using voltage or light.[38,40] Since the contact potential difference (CPD) is depending on the electrostatic landscape on the surface, sample excitation by means of voltage or light pulses adds a modulation to the measured CPD value. Thus, KPFM can track charge carrier dynamics with high spatial resolution. Collins et al. carried out dynamic KPFM measurements by using general-mode KPFM (G-Mode KPFM)[41,42] to do fast KPFM measurements in the time range of tens of microseconds.[41] Other methods such as pump-probe KPFM (pp-KPFM)[43–46] can even locally resolve processes down to 1 ps.[43] Nevertheless, these methods require short excitation pulses at high repetition rates, limiting the application to fast and ultrafast processes (<µms).

In this study, we demonstrate KPFM-based nanoscale surface photovoltage spectroscopy (nano-SPV) and nanoscale ideality factor mapping (nano-IFM) as a tool to map the nanoscale distribution of defects. Using these methods, we investigate triple cation $Cs_{0.05}FA_{0.8}MA_{0.15}PbI_3$ perovskite films with different morphologies and surface passivation. We use nano-SPV to visualize the charge carrier dynamics at grains and GBs on perovskite half-cells with an architecture of (ITO/TiO_2-SnO_2/perovskite) with small, large, and PEA-passivated perovskite grains. Our nano-SPV measurements offer two types of measurement: i) tracking the SPV dynamics during and after a light pulse to track the extraction and recombination time of photo-generated charge carriers (nano-SPV) and ii) tracking the SPV as a function of light illumination to obtain the local ideality factor, n_{id} (nano-IFM). The results show suppressed ion migration when the number of GBs is lower due to large grains. Furthermore, half-cells showed more uniform and lower defect densities when the perovskite films were PEA-passivated or had larger grains.

2. Theory

Here, we introduce some common macroscopic SPV-based measurement methods and how we implement them in nano-SPV operation mode using KPFM.

2.1. Surface Photovoltage and Surface Photovoltage Decay

Upon illumination of a photovoltaic sample, the electrostatic potential on the surface will change. This SPV is commonly measured by means of a macroscopic Kelvin Probe. Here, a millimeter-sized metal plate mechanically vibrates above the sample. In the presence of a voltage difference between the plate and the surface, the periodic variations in the plate distance will lead to a capacitive current. By compensating the voltage difference via an external voltage, the capacitive current can be minimized. Already without external voltage, there is an intrinsic voltage difference called the contact potential difference (CPD). The CPD corresponds to the difference in work functions or the position of the Fermi Level, E_F, of the probe and the sample material:

$$V_{CPD} = \frac{E_F^{tip} - E_F^{sample}}{e} \tag{1}$$

where e is the elemental charge. Any illumination-induced change in the measured CPD value corresponds to the SPV:

$$V_{SPV} = V_{CPD,\ illum.} - V_{CPD,\ dark} \tag{2}$$

The SPV signal can have different contributions: i) band flattening at the semiconductor surface and ii) charge separation at buried interfaces. At the surface, defect states lead to Fermi-level pinning and band bending. The increased charge carrier concentration during illumination screens the trapped surface charges, leading to band flattening[47] (Figure S1, Supporting Information). The resulting change in the surface potential can be observed as a SPV signal, where the polarity depends on the majority charge carriers as in n- or p-type doping (Figure S1, Supporting Information). Typically, n-type semiconductors yield positive SPV while the SPV values are negative for p-type semiconductors. Therefore, the doping status of the sample can be estimated by the sign of the SPV value.[48]

On photovoltaic device stacks, a SPV signal can be caused by band bending at buried interfaces, for example, between the absorber and a charge-selective contact (Figure S2, Supporting Information). Here, photo-generated charge carriers redistribute across the heterojunction depending on the characteristics of the charge-selective layer. If the layer is an electron transport layer (ETL), the electrons will be transported while the holes remain within the semiconductor film and the resulting SPV will be positive due to the imbalance of free charges in the film volume.[26] On the contrary, if the charge selective layer is a hole transport layer (HTL), the electrons will remain in the absorber while the holes are transferred, leading to a negative SPV because of an excess of electrons.[26]

Since the SPV signal depends on the Fermi level and the Fermi level change under illumination in the sample, it is influenced by band bending, doping,[49] and stoichiometry in the sample.[50]
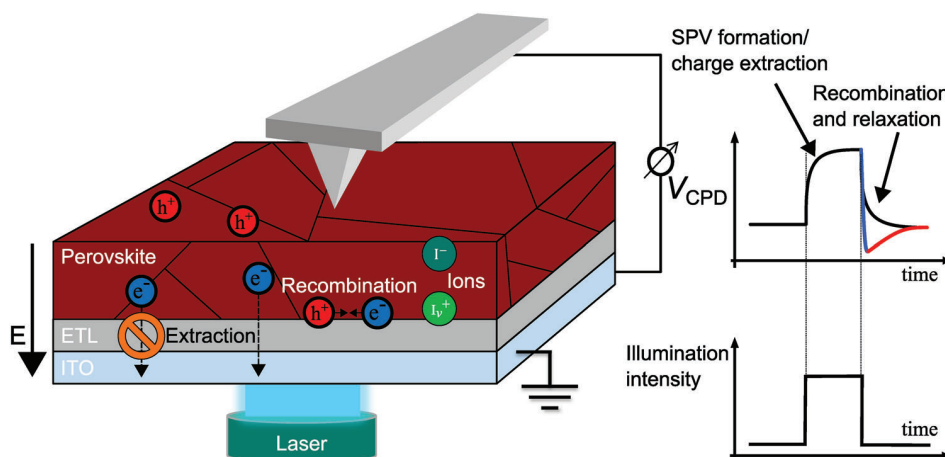
Figure 1. Schematic overview of the tr-KPFM setup. The laser intensity is either modulated in a pulse shape or a slow intensity increase with the tip engaged to the surface while the local CPD signal is recorded. The CPD traces contain information about local charge carrier extraction processes, which result in the formation of an electric field *E* (arrow on the left). After the light pulse, the CPD trace reveals information about recombination processes and the presence of defect states such as GBs and interfaces, which hinder the extraction of charges (blocking symbol).

To disentangle the different contributions to the SPV signal, we can track the SPV decay after an illumination pulse (SPV spectroscopy). The SPV transients contain information about recombination rates,[51] trap density,[52] and ion migration[40] effects. **Figure 1** shows the illustration of a SPV decay measurement result demonstrating the characteristic voltage decay following an illumination pulse. The decrease pattern gives information about the contributing charge carriers. The fast-decaying component (blue curve in Figure 1) is typically the electronic one whereas the slow-decaying one (red curve in Figure 1) is usually the ionic component.[40] The electronic decay is correlated to the electron–hole recombination mechanisms taking place at the perovskite bulk or the interface between the perovskite and the ETL after the illumination pulse. The more trap-assisted recombination occurs, the faster the SPV decay takes place. The ionic decay is correlated to the re-distribution of the ions from the surface which can be migrating from the crystal lattice or be adsorbed from the environment. Also, the electric field generated by the migration of electrons and the accumulation of holes at the surface influences the movement of ions within the film.

We further interpret the dynamics during the SPV formation at the beginning of a light pulse as the interfacial extraction of charge carriers. Other experimental studies using PL[53] or photoconductivity measurements came to a similar conclusion.[54] The results by Grill et al. suggest that only the ETL or HTL interface is the charge transport-limiting factor in the device and not the perovskite itself.[26,54] This means it is possible to see interfacial proprieties of the device by tracking the change of the SPV.[26]

2.2. Ideality Factor

The current–voltage (*I*–*V*) characteristics of semiconductor diodes such as solar cells can be described by the Shockley diode equation:

$$I = I_L - I_S \left(e^{\frac{V}{n_{id} k_B T/q}} - 1 \right) \tag{3}$$

where *I* is the overall current of the solar cell, I_L is the light-generated current, I_S is the reverse bias saturation current, *V* is the voltage across the solar cell, k_B is the Boltzmann constant, *T* is the temperature, and *q* is the elementary charge. Here, the ideality factor, n_{id}, is a measure of how close a photovoltaic device behaves to an ideal diode ($n_{id} = 1$). Deviations from the ideal diode behavior can be caused by charge carrier recombination mechanisms. Here, n_{id} can be estimated as the relation between the quasi-Fermi-level splitting, ΔE_F, and the recombination rate, R[55]:

$$n_{id,C} = \frac{1}{kT} \frac{d\Delta E_F}{dln(R)} \tag{4}$$

where $n_{id,\,C}$ is the conceptual ideality factor and kT is the thermal energy. Typically, a higher n_{id} suggests that the traps within the semiconductor contribute to the recombination process more.[56] Practically, it is hard to obtain values for the recombination rate and local quasi-Fermi level splitting values independently to obtain $n_{id,\,C}$. To work around this obstacle, an approximate value for n_{id} can be estimated from the current and voltage of the device. Here, the dark current, J_d, replaces the recombination rate, whereas the external voltage, V_e, replaces the local quasi-Fermi level splitting to obtain dark ideality factor, $n_{id,\,d}$, in Equation 5:

$$n_{id,d} = \frac{q}{kT} \frac{dV_e}{dln(J_d)} \tag{5}$$

This equation uses easily measurable quantities to obtain n_{id}. Nevertheless, this approach has the disadvantage that shunt or series resistances contribute to the ideality factor, as well as the recombination rates. Therefore, the $n_{id,\,d}$ can give misleading results.

At open circuit conditions under illumination, charge generation and recombination rates are equal, as the net charge extraction is zero. Here, the steady-state open-circuit voltage (V_{oc}) can be seen as an approximation of the quasi-Fermi level splitting.

**ADVANCED
SCIENCE NEWS**

www.advancedsciencenews.com

**ADVANCED
OPTICAL
MATERIALS**

www.advopticalmat.de

By measuring V_{oc} as a function of light intensity, ϕ, we can vary the recombination/generation rate within the device. Modifying Equation 6 yields

$$n_{id,l} = \frac{q}{kT}\frac{dV_{oc}}{dln(\phi)} \qquad (6)$$

which we refer to as the light ideality factor, $n_{id,l}$. This value gives information about the recombination mechanisms with a minimum contribution from series or shunt resistances. Thus, a comparison of the $n_{id,l}$ values between samples allows for determining the degree of trap-assisted recombination.[57] Nevertheless, there is an ongoing debate about the interpretation of n_{id} in PSC devices. Recently, Caprioglio et al.[58] reported on optical n_{id} measurements on half and full perovskite solar cells with different perovskite/transport layer interfaces and compared the n_{id} values. Their work suggests that the interfacial recombination dominates in n_{id} over the bulk recombination contribution.

2.3. Static and Time-Resolved Kelvin Probe Force Microscopy

The methods discussed so far rely on macroscopic measurements, for example, using a millimeter-sized Kelvin probe or an optical excitation spot.[59] KPFM is an AFM-based adaptation of the Kelvin probe measurement principle.[60–63] Instead of a capacitive current, KPFM detects the electrostatic force caused by the tip-sample potential to quantify the CPD. KPFM-based CPD maps can give information about facets,[64] band bending due to defects,[65] and energy level alignment in solar cells.[38]

To both map and record the nanoscale CPD and SPV dynamics with KPFM, the conventional scanning mode would be too slow. We recently introduced a point-wise time-resolved KPFM (tr-KPFM) data acquisition method where we record the sample response to a light or voltage pulse subsequently on every pixel of an image (Figure 1).[38,66] Here, we collect the CPD dynamics upon light or bias excitation subsequently at individual pixels within a designated area of the sample. Once the whole map is completed, we can either extract snapshots of the CPD distribution at defined positions in time or extract traces of CPD dynamics at defined positions in space (see also Experimental Section for more details). This method has the advantage that it is not limited in terms of the duration of the CPD traces. In particular, on PSC samples, where the full ionic relaxation can take several hundreds of milliseconds,[38] it is important to wait long enough to allow the sample to relax back to an equilibrium state. Other dynamic KPFM methods[41–46,67] require an excitation at high repetition rates, which might leave the sample effectively in an excited state. Thus, using only standard KPFM equipment (lock-in amplifier and feedback system), tr-KPFM can map the CPD and SPV distribution in the time scale of hundreds of microseconds to seconds. We call this operation mode nano-SPV.

Although flexible in terms of longer timescales, there are physical restrictions in terms of the shortest timescales that can be detected with tr-KPFM and nano-SPV. In the heterodyne KPFM detection mode used in this study,[68,69] signals are detected by means of an amplitude change on one of the cantilever's reso-

nances. Therefore, the smallest detectable time scale τ_{min} is determined by the damping or Q-factor on this resonance:

$$\tau_{min,n} = \frac{Q_n}{f_n \cdot \pi} \qquad (7)$$

where Q_n and f_n are the Q-factor and frequency of the n-th resonance of the AFM cantilever, respectively (see Experimental Section and Section S2, Supporting Information, for details). For a typical cantilever used in this study with second eigenmode frequency $f_2 = 977$ kHz and $Q_2 = 461$, the smallest timescale is, therefore, $\tau_{lim} = 150$ μs. This limit could be further pushed by using cantilevers with higher resonance frequency, or by using frequency modulation detection.

3. Results and Discussion

To investigate the correlation between sample structure, surface treatment, and defect distribution in perovskite thin films, we prepared triple cation perovskite films with 0.95:1.05 A^+/B^{2+} cation ratio with different structures (see Experimental Section for details). The topography images obtained via AFM are shown in Figure S3 in Section S4, Supporting Information. These include: i) a reference sample with small ($<d>_{Ref} = 200 \pm 60$ nm) grains (Ref), ii) a dimethyl sulfoxide (DMSO) vapor solvent annealed ($SA_{Pristine}$) ($<d>_{SA_{Pristine}} = 590 \pm 160$ nm), iii) solvent-annealed triple cation sample with PEA-I surface passivation (SA_{Pass}) ($<d>_{SA_{Pass}} = 670 \pm 210$ nm), and iv) a methylamine gas-treated triple cation sample with large ($<d>_{MA80} > 100$ μm) grains (MA80). By comparing the reference perovskite film to the solvent vapor-annealed and/or passivated perovskite films, we aim to identifying surface structures with locally higher or lower defect concentrations.

3.1. Reference Sample

The topography on the reference sample (**Figure 2**a) shows a structure of grains with a size of $<d>_{Ref} = 200 \pm 60$ nm. The correlated equilibrium CPD map before the voltage pulse (Figure 2b) mostly shows the contrast between the grains and the GBs due to band bending at the GBs,[15] where CPD increase and decrease correspond to downward and upward band bending, respectively. The CPD varies at the GBs within a range of 2 to 30 mV (Figure S4, Supporting Information). Furthermore, most GBs show higher CPD values compared to the grain interiors with minor exceptions (Figure S4e, Supporting Information). Since the band bending direction is determined by the type of defects, we argue that the minority GBs that show smaller CPD compared to the grains indicate different type of defects compared to the rest of the GBs within the film. Apart from that, some grains exhibited around 240 mV lower CPD value than the rest of the image (average value of 760 ± 90 mV). By subtracting the CPD values before illumination from the CPD values during illumination, we obtained a map of the SPV distribution (Figure 2c). The illumination pulse (0 ms $< t <$ 201.6 ms) resulted in an average photopotential of 280 ± 90 mV. Interestingly, grains with initially lower CPD exhibited about 190 mV higher SPV compared to the rest of the sample. The heterogeneous distribution of the SPV
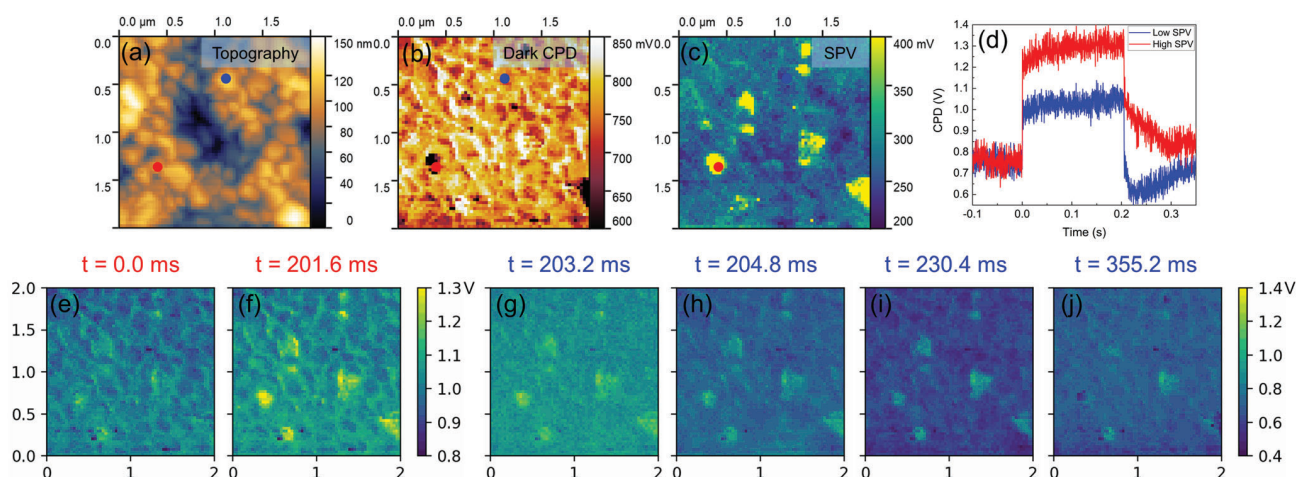
**ADVANCED
SCIENCE NEWS**

www.advancedsciencenews.com

**ADVANCED
OPTICAL
MATERIALS**

www.advopticalmat.de

Figure 2. a) Topography, b) CPD in dark, c) SPV, and d) SPV plots over time from marked areas of reference perovskite sample. Panels (e)–(j) show the CPD maps at different time frames. The maps have 150x150 pixels.

suggests either non-uniform defect distribution or non-uniform chemical stoichiometry within the reference perovskite film. The former possibility would be causing changes in the local Fermi levels, whereas the latter would change the Fermi level shift during illumination.[50]

When comparing the dynamics at high and low SPV areas (Figure 2d; red and blue markers in Figure 2c and Figure S5b, Supporting Information), the SPV decay at the high SPV grain shows a slower decay compared to SPV decay at the low SPV grain (Figure 2d). Furthermore, the SPV decay at the blue marker shows a rapid decrease to negative SPV values before returning to the equilibrium dark CPD value. This undershoot could be caused by ion migration as illustrated in Figure 1.[40] During illumination, the electric field caused by the SPV polarizes mobile ions within the perovskite layer. After the illumination, the electronic polarization rapidly decays, leaving behind the ionic field that generates a negative surface voltage. The slower SPV decays within the high SPV grain (red and orange markers) suggest that the defect density is lower at the high SPV areas of the reference sample. Furthermore, the absence of an SPV undershoot during decay also suggests that the ion migration is suppressed at the high SPV areas.

The snapshots of the CPD distribution of the reference perovskite film at different times during the nano-SPV measurement show the time-evolution of the SPV before (Figure 2b), during (Figure 2e,f), and after (Figure 2g–j) the illumination pulse (see also Video S1, Supporting Information). Directly after the laser was switched on, the CPD distribution remained rather uniform at 1030 ± 40 mV; 200 ms later, the contrast between the low and high SPV grains was clearly visible. Directly upon switching off the laser, the CPD values started to decrease due to the charge carrier recombination (Figure S6, Supporting Information). The electronic recombination for most of the image occurred within the first $\approx$30 ms after the laser was switched off (Figure 2i) at which the average CPD reached a minimum (Figure S6, Supporting Information). After reaching the minimum, the average CPD of the whole map increased again due to the slow decay of the ionic polarization that occurs in low SPV areas (blue plot in

Figure 2d), and most grains relaxed back to their original dark CPD values (Figure 2j). The high SPV grains, however, showed longer decay times without the ionic undershoot, as also shown in Figure 2d. The absence of ionic polarization and the longer SPV decay time suggest that the defect density is lower at the high SPV areas of the reference sample.

3.2. Solvent-Annealed Pristine Sample

To investigate the effect of solvent annealing on the defect density, we prepared triple cation perovskite films with a post-treatment of DMSO solvent annealing. This post-treatment should lead to a better crystallinity of larger grains and decreased GB density.[70] It also has been shown that the larger grain size reduces the defect density within the perovskite layer.[71] The topography of the $SA_{Pristine}$ sample (**Figure 3a**) showed larger perovskite grains ($<d>_{SA_{Pristine}} = 590 \pm 160$ nm) compared to the reference ($<d>_{Ref} = 200 \pm 60$ nm) due to the solvent annealing.[72] The dark CPD picture of $SA_{Pristine}$ can be found in Figure S16 in Section S6, Supporting Information. The distortions in the form of comb-like artifacts were caused by sample drift.

The nano-SPV map of the $SA_{Pristine}$ sample (Figure 3b) shows a pattern that matches some features in the topography map. The ETL of the reference sample and the $SA_{Pristine}$ are SnO_2 and c-TiO_2, respectively (see Experimental Section). Nevertheless, compared to the reference, the SPV value decreased slightly, from 280 ± 90 to 210 ± 50 mV on the $SA_{Pristine}$ sample. This lower SPV signal could be the result of a reduced band bending at the top surface due to the improved film quality[73,74] or a reduced charge transfer at the ETL interface, for example, due to energy barriers. Furthermore, at some of the GBs, we observed a stronger SPV contrast compared to the reference sample (SPV profiles in Figure S12b, Supporting Information). These profiles reveal a 73 ± 15 mV lower SPV at the GB compared to the grain interior. This value is in agreement with previous reports.[15] The lower SPV at the GBs could be caused by band bending at the GBs.[48] Furthermore, we see a SPV contrast of about 32 ± 5 mV between

**ADVANCED
SCIENCE NEWS**
www.advancedsciencenews.com

**ADVANCED
OPTICAL
MATERIALS**
www.advopticalmat.de
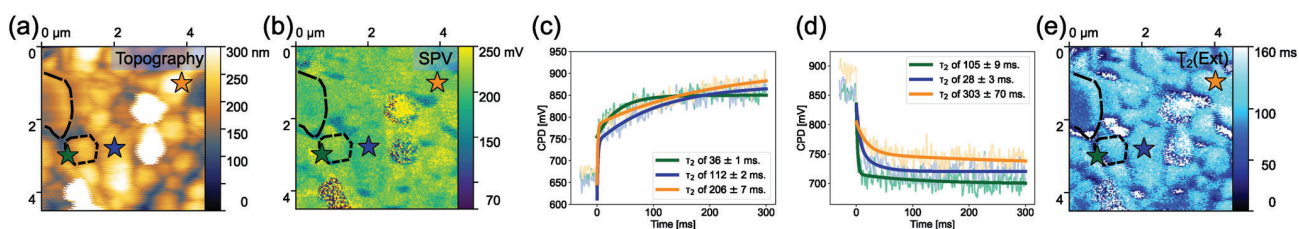
Figure 3. a) The topography; b) SPV map; c) CPD spectroscopy curves with 30 ms pre-zero data of spots marked in (a), (b), and (e) with a calculated slow timescale of electron extraction (τ_2(extraction)) in respect to turning on the laser; d) CPD spectroscopy curves with 30 ms pre-zero data of spots marked in (a), (b), and (e) with a calculated slow timescale of electron recombination (τ_2(recombination)) in respect to turning off the laser; and e) SPV rise time τ_2 (ext) map of $Cs_{0.05}FA_{0.8}MA_{0.15}PbI_3$ perovskite film with 0.95:1.05 A/B cation ratio ($SA_{Pristine}$). An extended version is available in Figures S7–S9, Supporting Information.

some individual grains and even within the same grain (see Figure S13b,c, Supporting Information). These differences could result from a facet dependency of the SPV,[75] stochiometry differences, or the defect distribution within the perovskite film. The elevated structures that are visible in the topography (Figure 3a) and the corresponding noisy SPV features in Figure 3b, together with a locally lower CPD (Figure S16, Supporting Information) could be caused by a locally higher PbI_2 concentration.[15]

We further analyzed the nano-SPV dynamics in different locations on the map with similar SPV values. One spot was chosen to be on a GB (green star) and two were placed within different grains (blue and orange stars in Figure 3a,b,e). Analyzing the SPV decay curves, it is obvious that the ionic undershoot that we observed on the reference sample disappeared on most grains in Figure 3d (some exceptions are shown in Figure S7 in Section S6, Supporting Information). The suppression of ion migration[40] is a result of the increased grain size and fewer GBs.[74,76] We want to point out that the increase in the grain size already had a massive impact on the ion migration. This means increasing the grain size alone already improves the defect density at the GBs. Although the grains marked with blue and orange stars exhibited a similar SPV value, the timescale until the SPV reached equilibrium varied from 112 ± 2 to 206 ± 7 ms, respectively. On the GBs, these timescales were even shorter $\sim 36 \pm 1$ ms ($< \tau_2$(ext) $>$(GB) $_{SA_{Pristine}} = 64 \pm 21$ ms; $< \tau_2$(ext) $>$(grain) $_{SA_{Pristine}} = 300 \pm 30$ ms; see also Video S2, Supporting Information). Changes of SPV in the time range of seconds have been reported before by tr-SEM measurements[25] and by earlier tr-KPFM measurements on device cross sections.[77,78]

Since ion migration is suppressed in solvent-annealed samples, the SPV decay is dominated by electron–hole recombination. Therefore, the shorter decay at the GBs can be attributed to faster electron–hole recombination, which points out higher defect density at the GBs. We interpret the equilibration time of the SPV as a local capacitive charging or extraction time, where the photogenerated charges fill up the capacitor between the bottom contact and the perovskite surface. Here, a faster equilibration time is indicative of a higher generation rate or a lower capacitance of the perovskite material. Moreover, the recombination or discharging traces and, therefore, the time in Figure 3d also show a wide variation of τ_2(rec) values between 28 ± 3 and 303 ± 70 ms. We did not observe a consistent correlation between the extraction and recombination times, indicating that the mechanisms of charge extraction and charge recombination are different. This is up to future research.

The fact that the nano-SPV measurements yield complete SPV traces for every position on the samples allows for generating maps of the equilibration timescales. We were able to fit most of the nano-SPV traces for excitation (ext) and recombination (rec) with a double exponential fit, indicating that two distinctly different timescales, τ_1 and τ_2, are involved in the dynamics. While all the other timescales showed no clear contrast, we found a distinct contrast between the grain interior and the GB in τ_2(ext) (see Figure 3e). Furthermore, there is a weak correlation between the SPV magnitude and the SPV extraction time that could be connected to different crystal facets. Generally, we observed higher SPV extraction times for lower SPV grains or grain facets, for example, the area in Figure 3b right to the long dotted line marked grain. This area had a lower SPV, but a higher extraction time in Figure 3e. This contrast trend could originate from stoichiometric differences or variations in defect density between grains in the triple cation perovskite film. The difference of τ_2(ext) between the grain interior and the GB is about 33 ± 6 ms (see Figure S14b, Supporting Information). This observation demonstrates that the extraction of charge carriers usually takes place much faster at GBs compared to the grain interior.

Although Regalado-Pérez et al. have suggested poor electronic transport due to local electric fields at GBs caused by an accumulation of negatively charged ionic defects,[74] Tainter et al. performed bulk measurements of photocurrent at excitation-junction separations much larger than topographical feature size and find that large fractions of excited carriers travel across multiple GBs.[79] These authors assumed that GBs do not prevent charge diffusion and GBs are not major impediments to charge motion in the polycrystalline films.[79–81] Moreover, Shao et al. saw that larger grains have GBs perpendicular to the substrate.[82] We, therefore, think that the overall increase in the grain size due to the DMSO vapor annealing has not only improved the crystallinity of the film but also made the GBs fast perpendicular pathways to the underlying substrate. Such a conductive pathway would explain the faster dynamics that we observed at the GBs with nano-SPV. Furthermore, Figure 3e shows not only a difference between the grain interior and the GB but also shows a facet dependence of the timescale of the nano-SPV response (e.g., the top left grain marked with a dashed line in Figure 3a,b,e and Figure S7a–d, Supporting Information).

Comparing the map of extraction/generation time constants (Figure 3e) to the map of the fast recombination/decay timescale in Figure S18, Supporting Information, we see a similar pattern. In particular, positions where the SPV stabilized fast were also
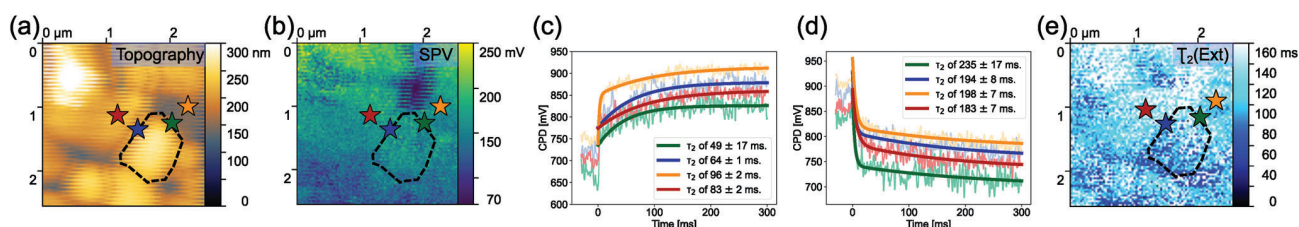
**ADVANCED
SCIENCE NEWS**

www.advancedsciencenews.com

**ADVANCED
OPTICAL
MATERIALS**

www.advopticalmat.de

Figure 4. a) The topography; b) SPV map; c) CPD spectroscopy curves with 30 ms pre-zero data of spots marked in (a), (b), and (e) with a calculated slow timescale of electron extraction (τ_2 (extraction)) in respect to turning on the laser; d) CPD spectroscopy curves with 30 ms pre-zero data of spots marked in (a), (b), and (e) with a calculated slow timescale of electron recombination (τ_2 (recombination)) in respect to turning off the laser; and e) SPV rise time τ_2 (ext) map of $Cs_{0.05}FA_{0.8}MA_{0.15}PbI_3$ perovskite film with 0.95:1.05 A/B cation ratio and surface passivation (SA_{Pass}). A combined figure of the CPD spectroscopy trajectory shown in (c) and (d) can be found in Figure S24, Supporting Information.

positions with fast SPV decay after the light was switched off. Interestingly, the second timescale obtained from the fits was very long, up to 1.5 s (see Figure S19, Supporting Information). Mapping the longer timescale, we observed a much more homogeneous contrast. Nevertheless, the exact meaning of this second timescale remains unclear and will be subject to future studies.

3.3. Solvent-Annealed and Passivated Sample

The topography of the SA_{Pass} sample **Figure 4**a shows slightly larger perovskite grains ($<d>_{SA_{Pass}} = 670 \pm 210$ nm) compared to the $SA_{Pristine}$ sample (Figure 3a). Again, the comb artifacts are caused by sample drift and should not affect the interpretation of the results. The dark CPD picture of SA_{Pass} can be found in Figure S28 in Section S7, Supporting Information.

The nano-SPV image (Figure 4b) shows a more uniform distribution compared to the SPV image of the $SA_{Pristine}$ sample (Figure 3b). Overall, the SPV value decreased from 210 mV with an RMS variation of 50 mV on the reference sample to 160 mV with an RMS deviation of 30 mV on the passivated sample. The decrease of the SPV could be the result of less band bending (shown in Figure S1, Supporting Information) due to the passivation of surface defect states. Furthermore, the grain–GB contrast decreased as a result of the passivation. The dark CPD decreased probably due to the site-specific passivation of the GBs by forming a 2D perovskite.[15] The lower defect density due to the passivation specifically at the GBs may lead to decreased band bending (see Figure S1, Supporting Information). This causes the SPV to be lower since there is less energy needed to flatten the bands.

To further support the homogeneous distribution of the passivation agent, we analyzed again four spots on the SA_{Pass} sample with similar SPV values (see spots in Figure 4b) on GBs and within grains. Figure 4c shows that the curves appear much more similar compared to the $SA_{Pristine}$ (Figure 3c,d). The values of τ_2 (ext) are only separated by about ≈23 %. The SPV extraction time map of SA_{Pass} given in Figure 4e shows an overall improved SPV extraction time uniformity compared to the $SA_{Pristine}$ sample (see Figure 3e and Video S3, Supporting Information). There is a medium intergranular difference of τ_2 (ext) of ≈20 ms between the grains shown in Figure 4e. Similar to the pristine perovskite film, the fast recombination time map (see Figure S30, Supporting Information) shows a uniform distribution (Figure 4a). Some non-uniformity could be caused by the non-homogeneous distribution of PEA-ions on the surface

during preparation. Nevertheless, the distribution is much more homogeneous compared to the pristine one (Figure S18, Supporting Information). Slower SPV recombination times usually indicate slower recombination[83] due to the passivation. Therefore, our results show that surface passivation with PEA leads to a more uniform SPV distribution and SPV extraction time behavior on GBs and within grains due to the homogenized defect density within the perovskite film and/or the formation of 2D-perovskite phases shown in a previous study.[15]

3.4. Methylamine-Treated Sample

The topography image of the MA80 sample (**Figure 5**a) shows a structure where the grain size exceeds 100 μm. Due to the limited scan size of the AFM, we were not able to investigate areas with several grains and therefore focused on one particular GB (diagonal line from top left to bottom right in Figure 5a). The CPD map before the illumination (Figure 5b) shows grain–GB contrast without any contrast within grains with no topographical features. The average dark CPD was 960 ± 50 mV within the grains with and about 65 mV higher at the GBs. The SPV map (Figure 5c) obtained during the illumination pulse (0 ms $<t<$ 201.6 ms) shows an average SPV of 200 ± 40 mV with an ≈60 mV lower value at the GB. The fact that the CPD and SPV contrast are almost identical at the GBs supports the notion of band bending at the GBs that we suggested previously. Apart from the GBs, MA80 shows uniform behavior considering both CPD and SPV distribution. Therefore, we suggest that methylamine treatment heals the perovskite grains and homogenizes the stoichiometry, leading to a more uniform CPD and SPV distribution.

To investigate the nano-SPV dynamics at high and low SPV areas (Figure 5c, blue and red markers, respectively), we looked at the SPV traces located at the grain interiors and a GB, respectively (Figure 5d, blue and red markers in c, respectively). The SPV dynamics upon excitation were comparable to those of the previous samples. Surprisingly, we observed a spike (inset of Figure 5d) in CPD about 3 ms after the light was switched off. Such a V_{OC} overshooting effect has also been reported by Herterich et al. during solar cell device measurements.[84] These authors suggested that due to the presence of mobile ions in the perovskite layer, a space charge layer forms between the perovskite and the contact layer. This space charge layer decreases the conductivity of the majority charge carriers, leading to a gradient of the quasi-Fermi level splitting at the contact interface. When the light is switched

**ADVANCED
SCIENCE NEWS**

www.advancedsciencenews.com

**ADVANCED
OPTICAL
MATERIALS**

www.advopticalmat.de
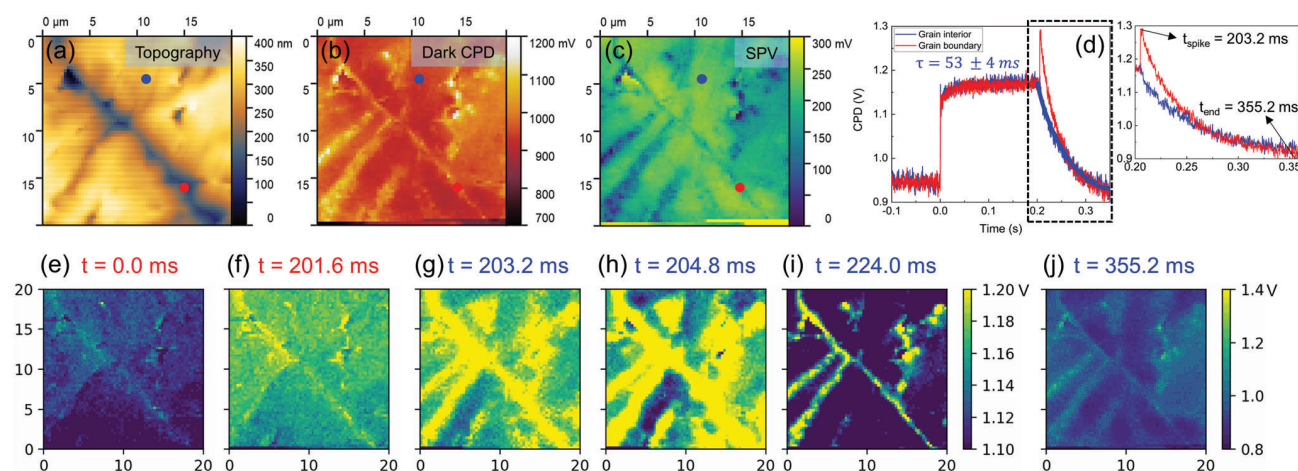
Figure 5. a) Topography, b) CPD in dark, c) SPV, and d) SPV plots over time from marked areas of the MA80 sample. Panels (e)−(j) show the CPD maps at different time frames. The maps have 150x150 pixels.

off, this gradient at the interface decreases faster compared to the bulk quasi-Fermi level splitting, resulting in V_{OC} overshoot.

When we examine a nano-SPV trace within a grain, we see a SPV decay without any overshoot. Furthermore, in both grain and GBs, the decay shows longer SPV decay times compared to the reference sample. The SPV decay given in Figure 5e decays with a characteristic time of 53 ± 4 ms according to the double exponential fit of the signal. This result is also backed by our previous observations on MA gas-treated samples.[85] The longer charge recombination times in both tr-PL (Figure S38, Supporting Information) and SPV decay (Figure 5d) indicate reduced defect density of the MA80 film due to the healing effect of methylamine treatment and fewer GBs. The increased crystallinity and grain orientation that we observed from the XRD patterns (Figure S36, Supporting Information) is possibly a contributing factor that leads to increased charge recombination times. The PL spectra given in Figure S37a, Supporting Information, also support the improvements that we see in SPV and XRD results, since the PL full-width half maximum is narrower after the methylamine treatment. The absence of a SPV undershoot further supports our earlier conclusion that decreasing the number of GBs further suppresses ion migration within the perovskite.

The SPV time frames gathered from the MA80 film during the nano-SPV experiment show the CPD distribution before (Figure 5b), during (Figure 5e,f), and after (Figure 5g–j) light illumination (see also Video S4, Supporting Information). When the laser was first switched on, the CPD had an average value of 1130 ± 50 mV, while it evolved to an average of 1160 ± 20 mV within 200 ms (Figure 5e,f). After switching off the laser, the CPD within the grains started to relax back to the original values due to charge carrier recombination. The SPV maps revealed that the SPV overshoot within the first 3 ms after the light pulse had a magnitude of up to 120 mV in the vicinity of the GB. This overshoot leads to a SPV decay contrast between the perovskite grains and the GBs, comparable to the dark CPD distribution. The SPV overshoot contrast between the GB and the grains suggests that the ion accumulation at the interface is higher at GBs. At the end of the nano-SPV recording at $t = 355.2$ ms, we see that the CPD

image is almost identical to the dark CPD image. This suggests a more uniform SPV decay behavior within the grains of the MA80 film compared to the reference film. Moreover, the absence of CPD contrast within the grains suggests that the methylamine treatment could be working as a passivation treatment by healing the A+-cation site defects or causing uniform chemical stoichiometry distribution throughout the film.

3.5. Nanoscale Ideality Factor Mapping

As we have shown, CPD and SPV measurements can be used to map sample heterogeneity in terms of Fermi level contrast and SPV decay times, which are mainly related to defects. However, the changes in these parameters could be linked to local stoichiometry changes[50] as well as they could be linked to the presence of defects within the perovskite layer or at the interfaces. Furthermore, the time resolution of tr-KPFM during SPV decay is determined by the use of our cantilevers and is in the order of 0.-1-1 ms. This limitation makes it difficult to obtain quantitative results from samples with shorter SPV decay times (Figure 2j). Therefore, we introduce a new KPFM-based technique where we locally measure the recombination behavior in the semiconductor film by measuring the $n_{id, l}$ of our perovskite half-cells named nano-IFM. To use the concept of $n_{id, l}$ to our advantage, we used our AFM tip as a nanoscale probe for each pixel and measured the SPV as a function of illumination intensity. By doing so, we are able to map the $n_{id, l}$ in the scan area of the sample (see Section S10, Supporting Information).

The topography image (**Figure 6**a) shows the granular structure of the same reference perovskite film given in Figure 2. The grain size varied between 100 and 400 nm. The SPV map shows an average SPV of 110 ± 20 mV (Figure 6b). Some grains show higher SPV values up to 200 mV compared to the rest of the sample. Furthermore, SPV values decreased between 10 and 20 mV at the GBs. As we suggested previously, the SPV contrast could be related to the stoichiometry or defect density distribution within the reference perovskite film. The $n_{id, l}$ distribution within the grains shows the same trend as the SPV distribution, where the

2301318 (8 of 12)

**ADVANCED
SCIENCE NEWS**

www.advancedsciencenews.com

**ADVANCED
OPTICAL
MATERIALS**

www.advopticalmat.de
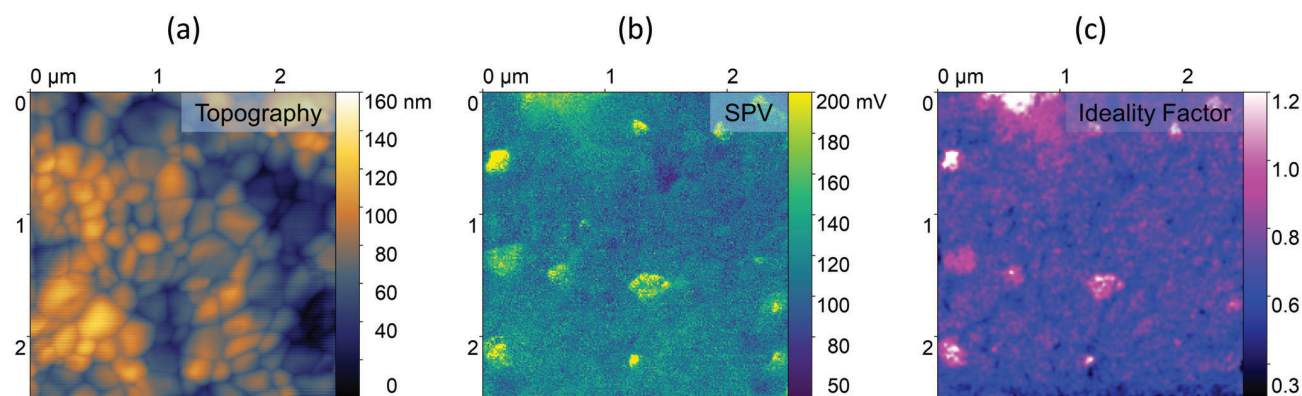
Figure 6. a) Topography, b) SPV, and c) $n_{id, l}$ maps of reference perovskite film. The map contains 200x200 pixels. The nano-IFM map was 1x1 pixel Gaussian filtered.

average $n_{id, l}$ value is 0.69 ± 0.11, with up to 0.3 higher $n_{id, l}$ values within the grains with higher SPV in Figure 6b, suggesting that these grains exhibit a lower defect density (Figure 6c). Thus, we conclude that the defect density at the grain interiors is not uniform within the perovskite film, in agreement with the earlier interpretation of the SPV decay (Figure 2a–f) and SPV distribution (Figure 2h). Moreover, this result also suggests a direct correlation between the quasi-Fermi level splitting and the $n_{id, l}$, which demonstrates the dominance of interfacial recombination in our perovskite half-cells.[58,59] The GBs in Figure 6d show lower $n_{id, l}$ values between 15 and 20 compared to the grain interiors, which points out the higher defect density at the GBs.

On the MA80 sample, we again focused on a region with a GB (Figure 5g). Here, we observed two GBs: the crack-like boundary on the left and the more subtle boundary on the right (**Figure 7**a). Apart from these boundaries, the topography was smooth with 36 nm RMS roughness (Figure 7a). The SPV map (Figure 7b) shows a uniform distribution within the grains with an average value of 370 ± 50 mV and about 20 mV lower SPV values at the GB. However, SPV values of the grains near the GB were about 50 mV higher compared to the average SPV. The features appearing in these areas in the dark CPD map (Figure S42b, Supporting Information) suggest that this effect could be related to a stoichiometric change. The $n_{id, l}$ map, like the SPV map, shows uniform

distribution within the MA80 film with an average value of 0.92 ± 0.28 (Figure 7c). Some areas within the grains show an about 0.4 lower n_{id}, value compared to the average value. This decrease could be related to the topographical features (Figure 7a). The grain–GB contrast in Figure 7d exhibits a $n_{id, l}$ drop of around 0.1 at the GB. This shows that the GBs still possess higher defect density, even after the methylamine treatment. Interestingly, the SPV contrast (Figure 7b) and the $n_{id, l}$ contrast (Figure 7c) do not exactly overlap. This supports our previous notion that SPV increases near the GBs are caused by the chemical stoichiometry changes. Therefore, a comparison of the SPV and the $n_{id, l}$ maps can give us stoichiometry and defect contrasts within the same film after a single nano-IFM measurement.

Comparing the overall $n_{id, l}$ values of the measured films, we see that the average $n_{id, l}$ increased after the methylamine treatment from 0.69 ± 0.18 to 0.92 ± 0.28. Therefore, our nano-IFM results suggest that the methylamine treatment increases the grain sizes and decreases the defect density inside the grains. The non-conventional $n_{id, l}$ values below 1 could be related to the fact that the measurements are carried out on perovskite half-cells with ITO/ETL/perovskite structure in which there is a charge carrier imbalance due to the absence of an HTL layer. Previously, $n_{id, l}$ values below 1 have been reported to be caused by energy misalignment between the absorber layer and the HTL in organic
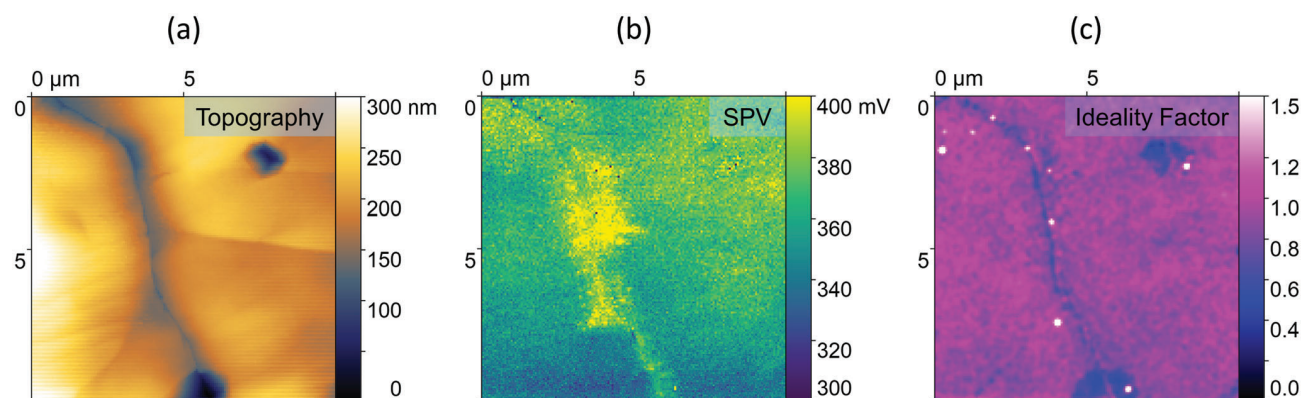
Figure 7. a) Topography, b) SPV, and c) $n_{id, l}$ maps of MA80 film. The map contains 150x150 pixels. The $n_{id, l}$ map was 1x1 pixel Gaussian filtered.

solar cells.[86] Also, the effect of ion migration and the possible space charge layers at the interfaces on $n_{id, l}$ is not entirely clear in the classical diode theory.[87] The quantities obtained via nano-IFM could be the subject of future research.

4. Conclusion

Using nano-SPV and nano-IFM, we demonstrate the effect of GBs on the lateral defect distribution in triple-cation perovskite films. Using pulsed and ramped laser illumination during tr-KPFM measurements, we showed the occurring changes within the perovskite films with small grains, large grains, and passivated grains. These measurements enabled us to experimentally demonstrate the effect of chemical processing on the nanostructures and charge carrier dynamics within the halide perovskite devices. Fewer GBs within the perovskite film lead to longer SPV lifetimes, which agrees with longer electron–hole lifetimes as observed in tr-PL. Furthermore, the ion migrations within the perovskite films were suppressed in solvent-annealed ($SA_{Pristine}$ and SA_{Pass}) and MA80 films due to a lower density of GBs and higher crystallinity. The nano-SPV and SPV decay maps showed more uniformity when defects were passivated via PEA coating. Also, the nano-SPV map showed that the MA80 film shows a more uniform SPV distribution compared to the reference perovskite film. We furthermore showed the different recombination behavior of reference and MA80 perovskite films by nano-IFM. Our $n_{id, l}$ mapping results show that different GBs can show varying recombination mechanisms but they are still the main locations for trap-assisted recombination within the perovskite films. According to our results, the negative effects of GBs are suppressed by surface passivation. On top of that, the grain interiors are also positively affected by the passivation agent coating as the higher SPV decay values measured in the grains suggest. Nevertheless, even the optimized films still exhibited some lateral variations in the defect density, thus guiding the way for targeted optimization of perovskite solar cells. Our results highlight the potential of nano-SPV and nano-IFM for the investigation of nanoscale structure–function relationships in optoelectronic materials beyond perovskites.

5. Experimental Section

Preparation of Perovskite Films: The planar ETL/perovskite half solar cells had the architecture of $ITO/c\text{-}TiO_2/Cs_{0.05}FA_{0.8}MA_{0.15}PbI_3$.

The triple-cation perovskites ($Cs_{0.05}FA_{0.8}MA_{0.15}PbI_3$) used for the tr-KPFM measurements were prepared on Ossila ITO-coated glass substrates with a conductivity of 20 Ω. After being brushed with Hellmanex III (Hellma), the ITO substrates were washed with hot tap water and milliQ water and then dried with an air gun. Afterward, the ITO substrates were treated with UV–ozone for 30 min freshly before the preparation of the compact TiO_2 ($c\text{-}TiO_2$) and once more before the perovskite layer. The $c\text{-}TiO_2$ layer was prepared by spin coating 80 µL of a 0.75 mol L^{-1} aqueous $TiCl_{4(aq)}$ solution on the ITO glass. The substrates were dried for 5 min @ 100 °C and then heated for 30 min on a high-temperature hot plate at a temperature of 500 °C. The perovskite precursor solution of 1.0:1.0, 0.9:1.1, and 0.8:1.2 A^+:B^{2+} cation ratio were prepared each with the concentration of 1.3 mol L^{-1} for PbI_2 in DMSO: *N,N*-dimethylformamide (DMF) (both anhydrous, Sigma-Aldrich) in a 1:4 volume ratio (v:v). For spin coating, 100 µL of the perovskite precursor solution was placed on the substrate and spin coated for 10 s @ 1000 rpm followed by 20 s @ 6000 rpm. 5 s before the end of the second step, 200 µL of chlorobenzene (CB) was used as an antisolvent. The substrate was then put on a hot plate with a temperature of 100 °C first until the substrate turned black and the film dried completely (≈10 s) and then for 15 min in an atmosphere of DMSO under a petri dish for solvent annealing. For each six samples, one petri dish was used with 90 µL of DMSO. The solvent annealing step was followed by a step of thermal annealing at 100 °C for another 15 min without DMSO for drying.

The passivated films were prepared by letting the samples cool after the thermal annealing step and then using a 10 mM solution of PEA-I solution in dry 2-propanol (IPA). 100 µL of the passivation solution was put on the perovskite substrates and spin-coated for 20 s @ 3000 rpm. The samples were then dried by thermal annealing for 10 min @ 100 °C on the hot plate. In addition, the samples were put in a dry and dark atmosphere for at least 11 days; some were left in there for 36 days.

The samples for grain size effect investigation were prepared on Lumtec ITO-coated glass substrates. The ITO substrates were ultrasonicated for 30 min in detergent solution in deionized water, acetone, and isopropanol. After cleaning, the ITO substrates were treated with oxygen plasma for 7 min. The SnO_2 precursor was prepared by the reflux method,[88] which involved preparing a 0.1 M solution of tin(II) chloride dihydrate ($SnCl_2 \cdot H_2O$, Alfa Aesar) in a 1:19 butanol (Sigma-Aldrich)/deionized water mixture and heating it at 110 °C for 4 h. Then, the solution was spin-coated at 2000 rpm for 30 s and annealed at 130 °C for 60 min to obtain the SnO_2 layer. The perovskite precursor solution was prepared by dissolving 507.1 mg PbI_2, 73.4 mg $PbBr_2$ (Sigma-Aldrich), 22.4 mg methylammonium bromide (Sigma-Aldrich), and 172 mg formamidinium iodide (Greatcell Solar) in 1:4 DMSO:DMF. Then, 53 µL of 389.7 mg mL^{-1} cesium iodide (Sigma-Aldrich) in DMSO solution was added to the perovskite precursor solution. The perovskite precursor solution was then spin-coated at 1000 rpm for 10 s and then at 6000 rpm for 20 s. 250 µL of CB (anhydrous, Sigma-Aldrich) was dropped onto the sample roughly 5 s before the end of the program. After the coating, the films were annealed at 100 °C for 60 min on a hot plate.

The perovskite films with extremely large grains were obtained via a methylamine treatment.[85] The methylamine treatment was carried out with 230 mbar of methylamine partial pressure. The perovskite film was kept under this methylamine atmosphere for 10 s before the pressure was pumped up to 600 mbar, decreasing the methylamine partial pressure to ≈170 mbar during recrystallization.

Kelvin Probe Force Microscopy Measurements: KPFM was measured on an Oxford Instruments/Asylum Research MFP-3D Infinity AFM in a nitrogen glovebox (level of humidity below 0.3 %, level of oxygen below 0.1 %) for all experiments. The Pt/Ir-coated conductive cantilevers (Bruker Model: SCM-PIT-V2) had a typical resonance frequency of ≈75 kHz, a spring constant of 2 N m^{-1}, a tip radius of 25 nm, and a tip height of 10 to 15 µm. The topography feedback was performed with amplitude modulation (AM) on the first eigenmode, and the oscillation amplitude was kept to ≈20–30 nm for all measurements. A Zurich Instruments HF2 Lock-In amplifier was used for all heterodyne KPFM experiments,[68,69] to perform the KPFM feedback. The electric drive amplitude of the ω_E signal varied between 2 and 5 V depending on the obtained signal from the sample. The sample was grounded via the sample holder with an external wire to the ground level of the Zürich Lock-In Amplifier. The compensating V_{DC} was applied to the tip, minimizing the electrostatic tip–sample interactions. For SPV measurements, the sample was illuminated from below by a pulsed laser (Cobolt 06-01 Series) at 488 nm. The laser power was controlled by a custom-written code within the MFP3D's control software by the AFM controller (Asylum Research ARC2), which provided analog voltage to activate the illumination.

Optical Measurements: PL and tr-PL measurements were performed on a PicoQuant FluoTime300 fluorescence spectrometer with an excitation wavelength of 405 nm. The repetition rate was set as 40 and 1 MHz for steady-state and time-resolved measurements, respectively. A 455 nm longpass filter was placed between the sample and the detector to block the stray laser light.

UV–vis absorbance spectroscopy was carried out with a CARY 5000 UV-Vis spectrometer by Agilent Technologies.

2301318 (10 of 12)

X-ray Diffraction Measurements: The XRD measurements were performed on a Bruker D8 X-ray diffractometer with a Cu anode using the K(alpha) emission line between 5° and 70°. The measurements were made with a step resolution of 0.02° and a 192 s integration time per step.

Supporting Information

Supporting Information is available from the Wiley Online Library or from the author.

Acknowledgements

Conflict of Interest

The authors declare no conflict of interest.

Data Availability Statement

The data that support the findings of this study are available from the corresponding author upon reasonable request.

Keywords

[1] L. Protesescu, S. Yakunin, M. I. Bodnarchuk, F. Krieg, R. Caputo, C. H. Hendon, R. X. Yang, A. Walsh, M. V. Kovalenko, *Nano Lett.* **2015**, *15*, 3692.

[2] C. C. Stoumpos, C. D. Malliakas, M. G. Kanatzidis, *Inorg. Chem.* **2013**, *52*, 9019.

[3] T. J. Jacobsson, J.-P. Correa-Baena, M. Pazoki, M. Saliba, K. Schenk, M. Grätzel, A. Hagfeldt, *Energy Environ. Sci.* **2016**, *9*, 1706.

[4] K. X. Steirer, P. Schulz, G. Teeter, V. Stevanovic, M. Yang, K. Zhu, J. J. Berry, *ACS Energy Lett.* **2016**, *1*, 360.

[5] M. B. Johnston, L. M. Herz, *Acc. Chem. Res.* **2016**, *49*, 146.

[6] S. D. Stranks, G. E. Eperon, G. Grancini, C. Menelaou, M. J. Alcocer, T. Leijtens, L. M. Herz, A. Petrozza, H. J. Snaith, *Science* **2013**, *342*, 341.

[7] D. Shi, V. Adinolfi, R. Comin, M. Yuan, E. Alarousu, A. Buin, Y. Chen, S. Hoogland, A. Rothenberger, K. Katsiev, Y. Losovyj, X. Zhang, P. A. Dowben, O. F. Mohammed, E. H. Sargent, O. M. Bakr, *Science* **2015**, *347*, 519.

[8] R. E. Brandt, J. R. Poindexter, P. Gorai, R. C. Kurchin, R. L. Hoye, L. Nienhaus, M. W. Wilson, J. A. Polizzotti, R. Sereika, R. Zaltauskas, L. C. Lee, J. L. MacManus-Driscoll, M. Bawendi, V. Stevanovic, T. Buonassisi, *Chem. Mater.* **2017**, *29*, 4667.

[9] Y. Lei, Y. Xu, M. Wang, G. Zhu, Z. Jin, *Small* **2021**, *17*, 2005495.

[10] C. Aranda, A. Guerrero, J. Bisquert, *ACS Energy Lett.* **2019**, *4*, 741.

[11] D. Yang, X. Zhang, K. Wang, C. Wu, R. Yang, Y. Hou, Y. Jiang, S. Liu, S. Priya, *Nano Lett.* **2019**, *19*, 3313.

[12] M. Abdi-Jalebi, M. Ibrahim Dar, S. P. Senanayak, A. Sadhanala, Z. Andaji-Garmaroudi, L. M. Pazos-Outón, J. M. Richter, A. J. Pearson, H. Sirringhaus, M. Grätzel, R. H. Friend, *Sci. Adv.* **2019**, *5*, eaav2012.

[13] E. Halvani Anaraki, A. Kermanpur, M. T. Mayer, L. Steier, T. Ahmed, S.-H. Turren-Cruz, J. Seo, J. Luo, S. M. Zakeeruddin, W. R. Tress, T. Edvinsson, M. Grätzel, A. Hagfeldt, J.-P. Correa-Baena, *ACS Energy Lett.* **2018**, *3*, 773.

[14] N. Arora, M. I. Dar, A. Hinderhofer, N. Pellet, F. Schreiber, S. M. Zakeeruddin, M. Grätzel, *Science* **2017**, *358*, 768.

[15] S. Gharibzadeh, P. Fassl, I. M. Hossain, P. N. Rohrbeck, M. Frericks, M. Schmidt, T. Duong, M. R. Khan, T. Abzieher, B. A. Nejand, F. Schackmar, O. Almora, T. Feeney, R. Singh, D. Fuchs, U. Lemmer, J. P. Hofmann, S. A. L. Weber, U. W. Paetzold, *Energy Environ. Sci.* **2021**, *14*, 5875.

[16] C. Ma, N.-G. Park, *ACS Energy Lett.* **2020**, *5*, 3268.

[17] M. Stolterfoht, V. M. Le Corre, M. Feuerstein, P. Caprioglio, L. J. A. Koster, D. Neher, *ACS Energy Lett.* **2019**, *4*, 2887.

[18] E. Serpetzoglou, I. Konidakis, G. Kakavelakis, T. Maksudov, E. Kymakis, E. Stratakis, *ACS Appl. Mater. Interfaces* **2017**, *9*, 43910.

[19] H. Hempel, T. J. Savenije, M. Stolterfoht, J. Neu, M. Failla, V. C. Paingad, P. Kužel, E. J. Heilweil, J. A. Spies, M. Schleuning, J. Zhao, D. Friedrich, K. Schwarzburg, L. D. A. Siebbeles, P. Dörflinger, V. Dyakonov, R. Katoh, M. J. Hong, J. G. Labram, M. Monti, E. Butler-Caddle, J. Lloyd-Hughes, M. M. Taheri, J. B. Baxter, T. J. Magnanelli, S. Luo, J. M. Cardon, S. Ardo, T. Unold, *Adv. Energy Mater.* **2022**, *12*, 2102776.

[20] E. Von Hauff, D. Klotz, *J. Mater. Chem. C* **2022**, *10*, 742.

[21] Y.-C. Chin, M. Daboczi, C. Henderson, J. Luke, J.-S. Kim, *ACS Energy Lett.* **2022**, *7*, 560.

[22] N. Li, A. Feng, X. Guo, J. Wu, S. Xie, Q. Lin, X. Jiang, Y. Liu, Z. Chen, X. Tao, *Adv. Energy Mater.* **2022**, *12*, 2103241.

[23] S. Zouhair, S.-M. Yoo, D. Bogachuk, J. P. Herterich, J. Lim, H. Kanda, B. Son, H. J. Yun, U. Würfel, A. Chahboun, M. K. Nazeeruddin, A. Hinsch, L. Wagner, H. Kim, *Adv. Energy Mater.* **2022**, *12*, 2200837.

[24] Y. Zhang, Y. Zhu, M. Hu, N. Pai, T. Qin, Y.-B. Cheng, U. Bach, A. N. Simonov, J. Lu, *J. Phys. Chem. Lett.* **2022**, *13*, 2792.

[25] G. Irde, S. M. Pietralunga, V. Sala, M. Zani, J. M. Ball, A. J. Barker, A. Petrozza, G. Lanzani, A. Tagliaferri, *Micron* **2019**, *121*, 53.

[26] S. M. Pietralunga, G. Irde, A. J. Barker, J. M. Ball, A. Petrozza, V. Sala, M. Zani, G. Lanzani, A. Tagliaferri, *Adv. Mater. Interfaces* **2020**, *7*, 2000297.

[27] S. K. Yadavalli, M. Chen, M. Hu, Z. Dai, Y. Zhou, N. P. Padture, *Scr. Mater.* **2020**, *187*, 88.

[28] D. Zhang, Y. Zhu, L. Liu, X. Ying, C.-E. Hsiung, R. Sougrat, K. Li, Y. Han, *Science* **2018**, *359*, 675.

[29] R. Egerton, P. Li, M. Malac, *Micron* **2004**, *35*, 399.

[30] J. Ran, O. Dyck, X. Wang, B. Yang, D. B. Geohegan, K. Xiao, *Adv. Energy Mater.* **2020**, *10*, 1903191.

[31] I. M. Hermes, S. A. Bretschneider, V. W. Bergmann, D. Li, A. Klasen, J. Mars, W. Tremel, F. Laquai, H.-J. Butt, M. Mezger, R. Berger, B. J. Rodriguez, S. A. L. Weber, *J. Phys. Chem. C* **2016**, *120*, 5724.

[32] I. M. Hermes, A. Best, L. Winkelmann, J. Mars, S. M. Vorpahl, M. Mezger, L. Collins, H.-J. Butt, D. S. Ginger, K. Koynov, S. A. L. Weber, *Energy Environ. Sci.* **2020**, *13*, 4168.

[33] Y. Yalcinkaya, I. M. Hermes, T. Seewald, K. Amann-Winkel, L. Veith, L. Schmidt-Mende, S. A. Weber, *Adv. Energy Mater.* **2022**, 2202442.

[34] Y. Shao, Y. Fang, T. Li, Q. Wang, Q. Dong, Y. Deng, Y. Yuan, H. Wei, M. Wang, A. Gruverman, J. Shielda, J. Huang, *Energy Environ. Sci.* **2016**, *9*, 1752.

ADVANCED
SCIENCE NEWS

www.advancedsciencenews.com

ADVANCED
OPTICAL
MATERIALS

www.advopticalmat.de

[35] B. Conings, J. Drijkoningen, N. Gauquelin, A. Babayigit, J. D'Haen, L. D'Olieslaeger, A. Ethirajan, J. Verbeeck, J. Manca, E. Mosconi, F. De Angelis, H.-G. Boyen, *Adv. Energy Mater.* **2015**, *5*, 1500477.

[36] V. W. Bergmann, S. A. Weber, F. Javier Ramos, M. K. Nazeeruddin, M. Grätzel, D. Li, A. L. Domanski, I. Lieberwirth, S. Ahmad, R. Berger, *Nat. Commun.* **2014**, *5*, 5001.

[37] I. M. Hermes, Y. Hou, V. W. Bergmann, C. J. Brabec, S. A. Weber, *J. Phys. Chem. Lett.* **2018**, *9*, 6249.

[38] S. A. Weber, I. M. Hermes, S.-H. Turren-Cruz, C. Gort, V. W. Bergmann, L. Gilson, A. Hagfeldt, M. Graetzel, W. Tress, R. Berger, *Energy Environ. Sci.* **2018**, *11*, 2404.

[39] E. M. Lanzoni, T. Gallet, C. Spindler, O. Ramirez, C. K. Boumenou, S. Siebentritt, A. Redinger, *Nano Energy* **2021**, *88*, 106270.

[40] E. Strelcov, S. Jesse, Y.-L. Huang, Y.-C. Teng, I. I. Kravchenko, Y.-H. Chu, S. V. Kalinin, *ACS Nano* **2013**, *7*, 6806.

[41] L. Collins, A. Belianinov, S. Somnath, N. Balke, S. V. Kalinin, S. Jesse, *Sci. Rep.* **2016**, *6*, 30557.

[42] L. Collins, M. Ahmadi, J. Qin, Y. Liu, O. S. Ovchinnikova, B. Hu, S. Jesse, S. V. Kalinin, *Nanotechnology* **2018**, *29*, 44.

[43] Z. Schumacher, A. Spielhofer, Y. Miyahara, P. Grutter, *Appl. Phys. Lett.* **2017**, *110*, 5.

[44] B. Grévin, O. Bardagot, R. Demadrille, *Beilstein J. Nanotechnol.* **2020**, *11*, 323.

[45] V. Aubriet, K. Courouble, O. Bardagot, R. Demadrille, Ł. Borowik, B. Grévin, *Nanotechnology* **2022**, *33*, 225401.

[46] J. Murawski, T. Graupner, P. Milde, R. Raupach, U. Zerweck-Trogisch, L. Eng, *J. Appl. Phys.* **2015**, *118*, 15.

[47] E. Johnson, *Phys. Rev.* **1958**, *111*, 153.

[48] D. Cavalcoli, A. Cavallini, *Phys. Status Solidi c* **2010**, *7*, 1293.

[49] J. T.-W. Wang, Z. Wang, S. Pathak, W. Zhang, D. W. deQuilettes, F. Wisnivesky-Rocca-Rivarola, J. Huang, P. K. Nayak, J. B. Patel, H. A. M. Yusof, Y. Vaynzof, R. Zhu, I. Ramirez, J. Zhang, C. Ducati, C. Grovenor, M. B. Johnston, D. S. Ginger, R. J. Nicholas, H. J. Snaith, *Energy Environ. Sci.* **2016**, *9*, 2892.

[50] G. Alkhalifah, A. D. Marshall, F. Rudayni, S. Wanigasekara, J. Z. Wu, W.-L. Chan, *J. Phys. Chem. Lett.* **2022**, *13*, 6711.

[51] S. Wood, D. O'Connor, C. W. Jones, J. D. Claverley, J. C. Blakesley, C. Giusca, F. A. Castro, *Sol. Energy Mater. Sol. Cells* **2017**, *161*, 89.

[52] L. Kronik, Y. Shapira, *Surf. Sci. Rep.* **1999**, *37*, 1.

[53] Q. Zhou, B. Wang, R. Meng, J. Zhou, S. Xie, X. Zhang, J. Wang, S. Yue, B. Qin, H. Zhou, Y. Zhang, *Adv. Funct. Mater.* **2020**, *30*, 2000550.

[54] I. Grill, M. F. Aygüler, T. Bein, P. Docampo, N. F. Hartmann, M. Handloser, A. Hartschuh, *ACS Appl. Mater. Interfaces* **2017**, *9*, 37655.

[55] T. Kirchartz, F. Deledalle, P. S. Tuladhar, J. R. Durrant, J. Nelson, *J. Phys. Chem. Lett.* **2013**, *4*, 2371.

[56] C. Van Berkel, M. Powell, A. Franklin, I. French, *J. Appl. Phys.* **1993**, *73*, 5264.

[57] D. Prochowicz, R. Runjhun, M. M. Tavakoli, P. Yadav, M. Saski, A. Q. Alanazi, D. J. Kubicki, Z. Kaszkur, S. M. Zakeeruddin, J. Lewiński, M. Grätzel, *Chem. Mater.* **2019**, *31*, 1620.

[58] P. Caprioglio, C. M. Wolff, O. J. Sandberg, A. Armin, B. Rech, S. Albrecht, D. Neher, M. Stolterfoht, *Adv. Energy Mater.* **2020**, *10*, 2000502.

[59] A. Dasgupta, S. Mahesh, P. Caprioglio, Y.-H. Lin, K.-A. Zaininger, R. D. Oliver, P. Holzhey, S. Zhou, M. M. McCarthy, J. A. Smith, M. Frenzel, M. G. Christoforo, J. M. Ball, B. Wenger, H. J. Snaith, *ACS Energy Lett.* **2022**, *7*, 2311.

[60] M. Nonnenmacher, M. o'Boyle, H. K. Wickramasinghe, *Appl. Phys. Lett.* **1991**, *58*, 2921.

[61] L. Kelvin, *Lond. Edinb. Dublin Philos. Mag. J. Sci.* **1898**, *46*, 82.

[62] J. Weaver, D. W. Abraham, *J. Vac. Sci. Technol. B Microelectron. Nanometer Struct. Process. Meas. Phenom.* **1991**, *9*, 1559.

[63] Y. Martin, D. W. Abraham, H. K. Wickramasinghe, *Appl. Phys. Lett.* **1988**, *52*, 1103.

[64] U. J. Bahnmüller, H. Kuper, T. Seewald, Y. Yalcinkaya, J. A. Becker, L. Schmidt-Mende, S. A. Weber, S. Polarz, *Nanomaterials* **2021**, *11*, 3057.

[65] W. Zhang, S. Pathak, N. Sakai, T. Stergiopoulos, P. K. Nayak, N. K. Noel, A. A. Haghighirad, V. M. Burlakov, D. W. DeQuilettes, A. Sadhanala, W. Li, L. Wang, D. S. Ginger, R. H. Friend, H. J. Snaith, *Nat. Commun.* **2015**, *6*, 10030.

[66] P. Rohrbeck, *Master thesis*, Johannes Gutenberg University Mainz, **2021**.

[67] D. Toth, B. Hailegnaw, F. Richheimer, F. A. Castro, F. Kienberger, M. C. Scharber, S. Wood, G. Gramse, *ACS Appl. Mater. Interfaces* **2020**, *12*, 48057.

[68] J. L. Garrett, J. N. Munday, *Nanotechnology* **2016**, *27*, 24.

[69] A. Axt, I. M. Hermes, V. W. Bergmann, N. Tausendpfund, S. A. L. Weber, *Beilstein J. Nanotechnol.* **2018**, *9*, 1809.

[70] Z. Xiao, Q. Dong, C. Bi, Y. Shao, Y. Yuan, J. Huang, *Adv. Mater.* **2014**, *26*, 6503.

[71] X. Yang, Y. Wei, F. Huang, S. Jin, D. Luo, Y. Fang, Y. Zhao, Q. Guo, Y. Huang, L. Fan, J. Wu, *Sol. Energy* **2019**, *177*, 299.

[72] J. Bing, S. Huang, A. W. Y. Ho-Baillie, *Energy Technol.* **2020**, *8*, 1901114.

[73] Y. Guo, S. Yuan, D. Zhu, M. Yu, H.-Y. Wang, J. Lin, Y. Wang, Y. Qin, J.-P. Zhang, X.-C. Ai, *Phys. Chem. Chem. Phys.* **2021**, *23*, 6162.

[74] E. Regalado-Pérez, E. B. Díaz-Cruz, J. Landa-Bautista, N. R. Mathews, X. Mathew, *ACS Appl. Mater. Interfaces* **2021**, *13*, 11833.

[75] S. Y. Leblebici, L. Leppert, Y. Li, S. E. Reyes-Lillo, S. Wickenburg, E. Wong, J. Lee, M. Melli, D. Ziegler, D. K. Angell, D. F. Ogletree, P. D. Ashby, F. M. Toma, J. B. Neaton, I. D. Sharp, A. Weber-Bargioni, *Nat. Energy* **2016**, *1*, 16093.

[76] D. Prochowicz, R. Runjhun, M. M. Tavakoli, P. Yadav, M. Saski, A. Q. Alanazi, D. J. Kubicki, Z. Kaszkur, S. M. Zakeeruddin, J. Lewiński, M. Grätzel, *Chem. Mater.* **2019**, *31*, 1620.

[77] V. W. Bergmann, S. A. L. Weber, F. Javier Ramos, M. K. Nazeeruddin, M. Grätzel, D. Li, A. L. Domanski, I. Lieberwirth, S. Ahmad, R. Berger, *Nat. Commun.* **2014**, *5*, 5001.

[78] V. W. Bergmann, Y. Guo, H. Tanaka, I. M. Hermes, D. Li, A. Klasen, S. A. Bretschneider, E. Nakamura, R. Berger, S. A. Weber, *ACS Appl. Mater. Interfaces* **2016**, *8*, 19402.

[79] G. D. Tainter, M. T. Hörantner, L. M. Pazos-Outón, R. D. Lamboll, H. Āboliņš, T. Leijtens, S. Mahesh, R. H. Friend, H. J. Snaith, H. J. Joyce, F. Deschler, *Joule* **2019**, *3*, 1301.

[80] R. Ciesielski, F. Schäfer, N. F. Hartmann, N. Giesbrecht, T. Bein, P. Docampo, A. Hartschuh, *ACS Appl. Mater. Interfaces* **2018**, *10*, 7974.

[81] D. W. DeQuilettes, S. Jariwala, S. Burke, M. E. Ziffer, J. T.-W. Wang, H. J. Snaith, D. S. Ginger, *ACS Nano* **2017**, *11*, 11488.

[82] Y. Shao, Y. Fang, T. Li, Q. Wang, Q. Dong, Y. Deng, Y. Yuan, H. Wei, M. Wang, A. Gruverman, J. Shield, J. Huang, *Energy Environ. Sci.* **2016**, *9*, 1752.

[83] K. Fu, C. T. Nelson, M. C. Scott, A. Minor, N. Mathews, L. H. Wong, *Nanoscale* **2016**, *8*, 4181.

[84] J. Herterich, M. Unmüssig, L. Wagner, G. Loukeris, J. Faisst, M. List, M. Kohlstädt, U. Würfel, *Energy Technol.* **2022**, *10*, 2100868.

[85] E. R. Schütz, A. Fakharuddin, Y. Yalcinkaya, E. Ochoa-Martinez, S. Bijani, A. R. b. Mohd Yusoff, M. Vasilopoulou, T. Seewald, U. Steiner, S. A. Weber, L. Schmidt-Mende, *APL Mater.* **2022**, *10*, 081110.

[86] S. Wheeler, F. Deledalle, N. Tokmoldin, T. Kirchartz, J. Nelson, J. R. Durrant, *Phys. Rev. Appl.* **2015**, *4*, 024020.

[87] N. Courtier, *Phys. Rev. Appl.* **2020**, *14*, 024031.

[88] C. Chen, Y. Jiang, J. Guo, X. Wu, W. Zhang, S. Wu, X. Gao, X. Hu, Q. Wang, G. Zhou, Y. Chen, J.-M. Liu, K. Kempa, J. Gao, *Adv. Funct. Mater.* **2019**, *29*, 1900557.

ADVANCED OPTICAL MATERIALS

Supporting Information

Nanoscale Surface Photovoltage Spectroscopy

Yenal Yalcinkaya, Pascal N. Rohrbeck, Emilia R. Schütz, Azhar Fakharuddin, Lukas Schmidt-Mende and Stefan A.L. Weber*

Supporting Information
Nanoscale Surface Photovoltage Spectroscopy

S1   Band bending at interfaces
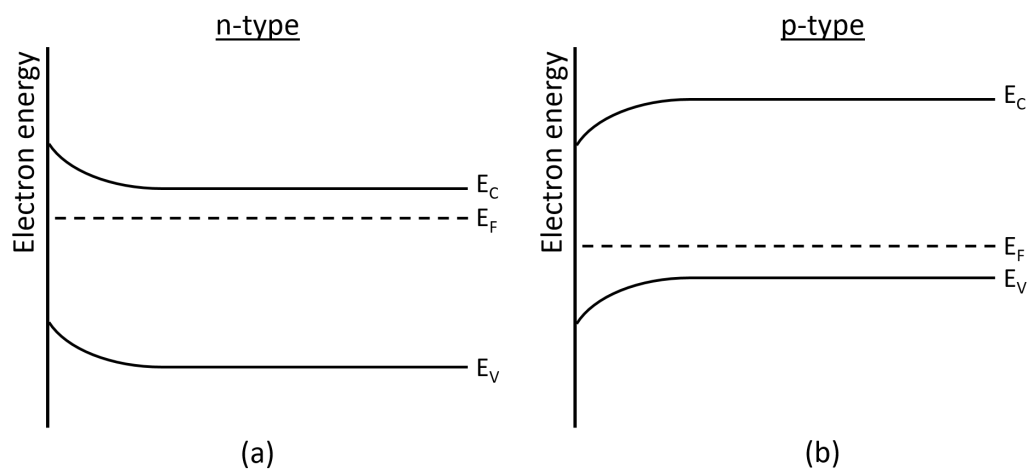
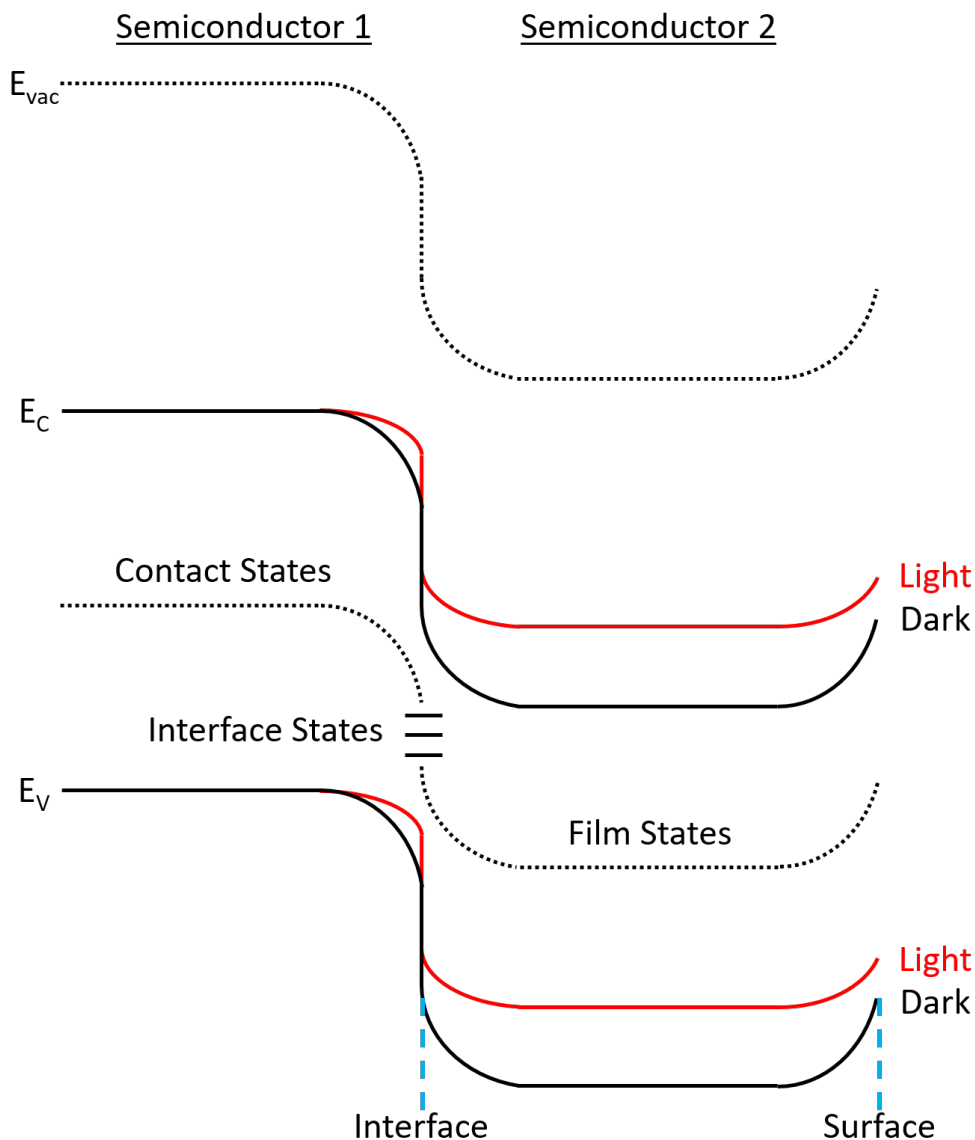Figure S1: Band bending of (a) n-type and (b) p-type semiconductors.

Figure S2: Band alignment illustration for two semiconductor heterojunction.

S2   Time limitation of the tr-KPFM method

tr-KPFM gives us the ability to map the charge carrier dynamics within the perovskite thin films and locate the defects. This method has a time resolution limit to detect fast changes due to the intrinsic amplitude modulation (AM) detection mode limit which is proportional to $\frac{Q}{f_0 \pi}$[1].. Q is the damping factor (also known as Q-factor) of the oscillation of the cantilever, and f_0 is the mechanical resonance frequency at which the cantilever oscillates.

The Q-factor of the detection of the electric signal can be calculated by Equation (S8) [2, 3]..

$$Q = \frac{f \cdot \sqrt{2}}{FWHM} \tag{S8}$$

$FWHM$ is the full width at half maximum of the resonance peak for the amplitude curve and f is the resonance frequency.

S3 Fit of tr-KPFM data

The CPD spectra was fitted with an exponential fit of the form seen in Equation (S9).

$$\mathrm{CPD}(t) = \mathrm{CPD_{eq.}} + A_1 \cdot \exp\left(\frac{x_0 - x}{\tau_1}\right) + A_2 \cdot \exp\left(\frac{x_0 - x}{\tau_2}\right) \tag{S9}$$

$\mathrm{CPD_{eq.}}$ is the equilibrium CPD value during light state or respectively dark state CPD. A_1 and A_2 are the values how much the CPD is changing with the respective time scales τ_1 or τ_2.

S4 Topography comparison
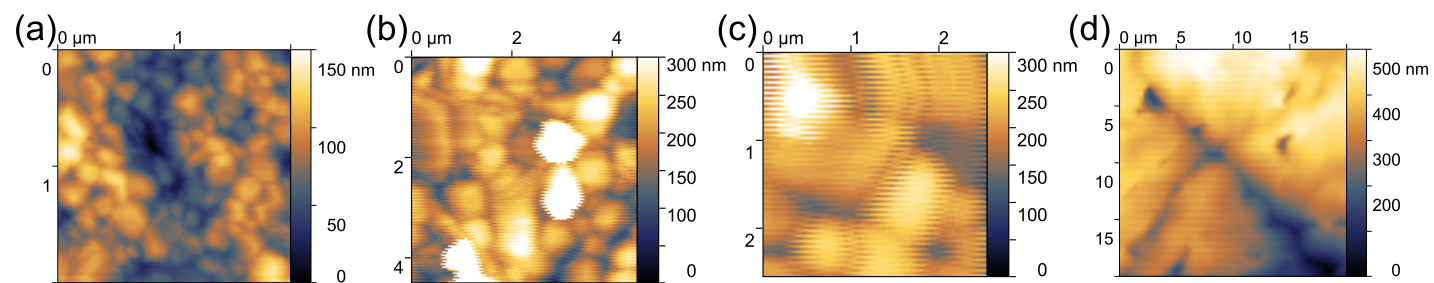
Figure S3: The topography of (a) Reference, (b) SA$_\text{Pristine}$, (c) SA$_\text{Pass}$, (d) MA80 sample.

S5   Further Analysis of the Reference sample
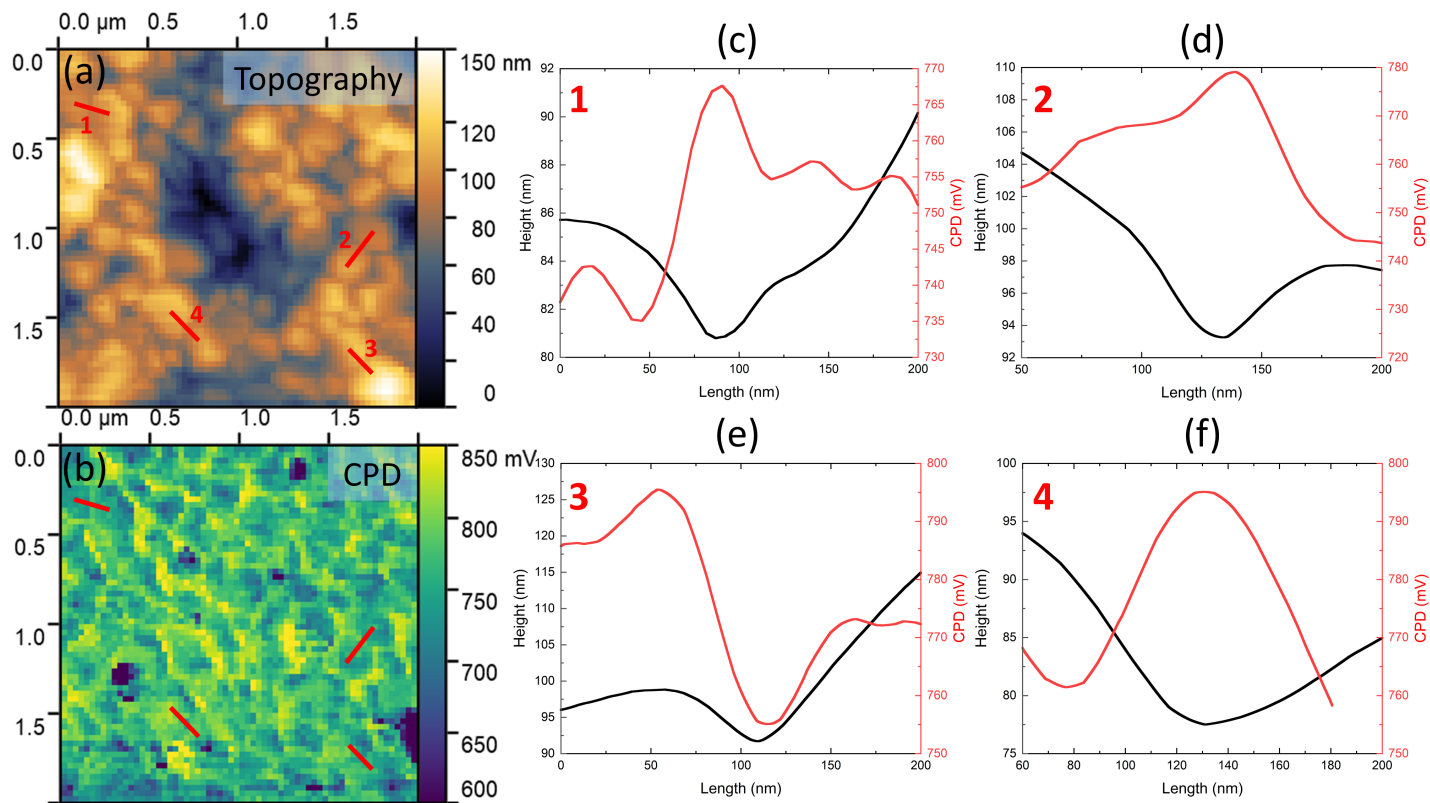
Figure S4: (a) Topography and (b) CPD of reference perovskite sample in dark conditions. (c-f) The profiles showing the changes of topography and CPD at GBs. The drawn profiles enable us to locate the CPD changes accurately.
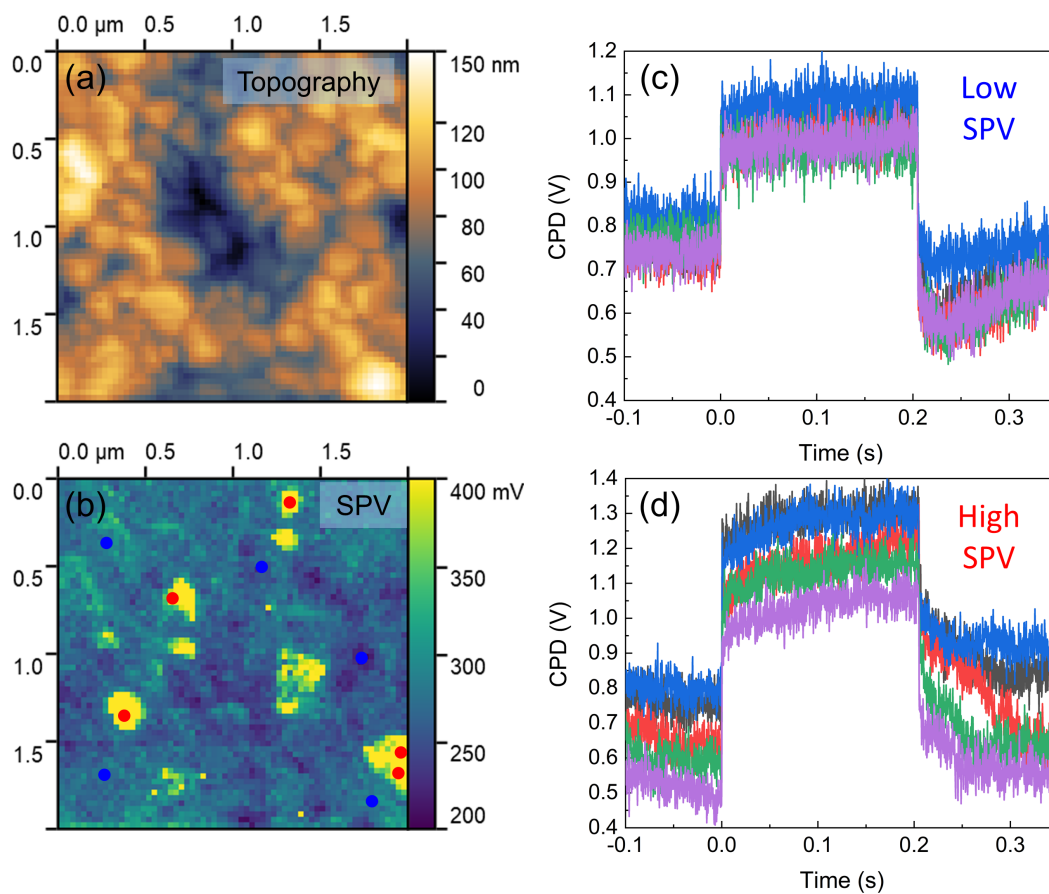
Figure S5: (a) Topography, (b) SPV, and further CPD profiles from (c) low SPV and (d) high SPV areas in the reference sample.
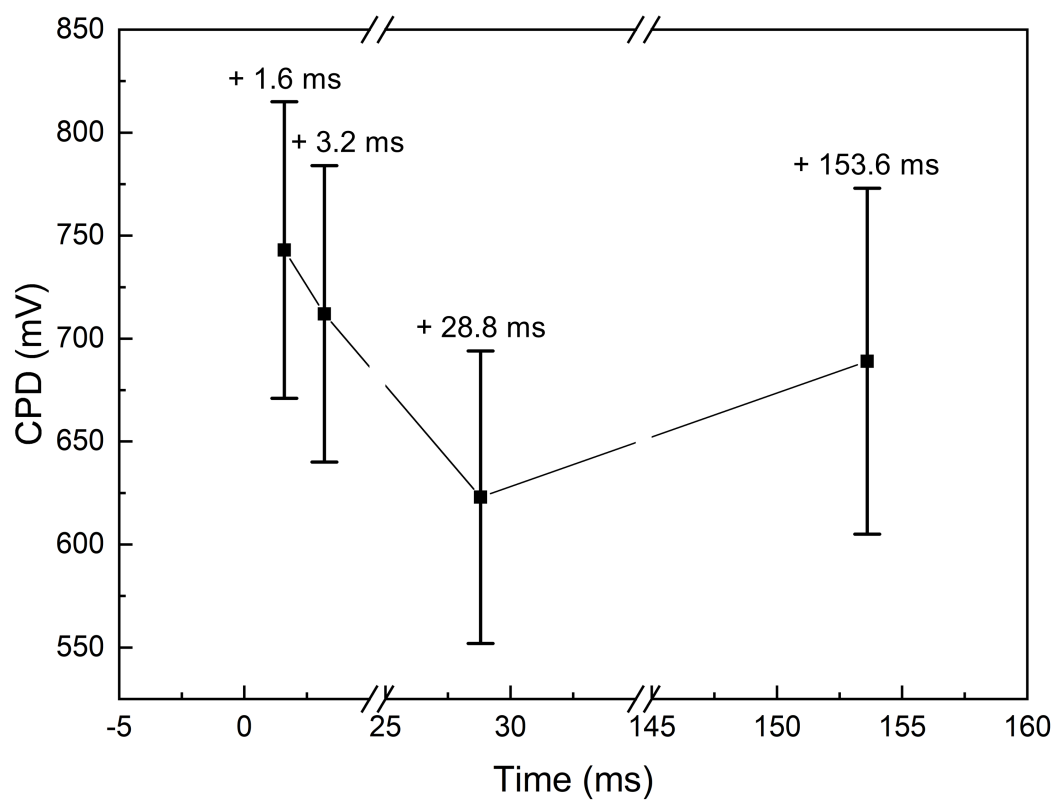
Figure S6: Time dependant CPD evolution of the reference perovskite film after laser was switched off. The average CPD values corresponds to the timeframes from Figure 2(g-j).

S6 Further Analysis of the pristine solvent annealed sample SA$_{\text{Pristine}}$
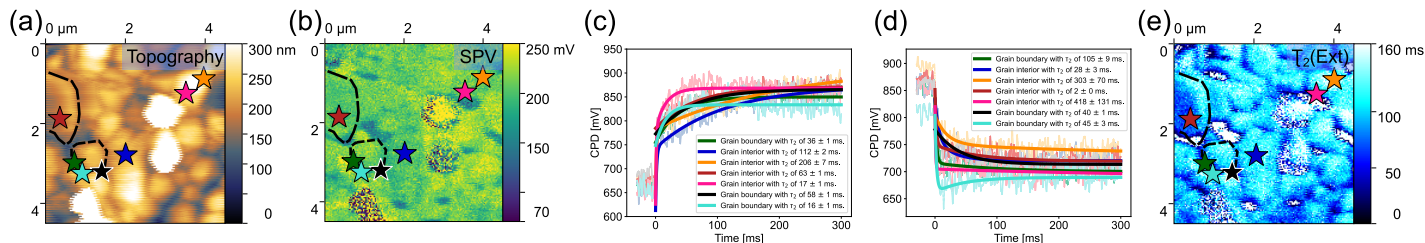
Figure S7: (a) The topography, (b) SPV map, (c) CPD spectroscopy curves of spots marked in (a), (b) and (e) with calculated slow time scale of electron extraction (τ_2(ext)) in respect to turning on the laser, (d) CPD spectroscopy curves with 30 ms pre-zero data of spots marked in (a), (b) and (e) with calculated slow time scale of electron recombination (τ_2(rec)) in respect to turning off the laser and (e) SPV rise time τ_2(ext) map of $Cs_{0.05}FA_{0.8}MA_{0.15}PbI_3$ perovskite film with 0.95:1.05 A/B cation ratio (SA$_{\text{Pristine}}$).
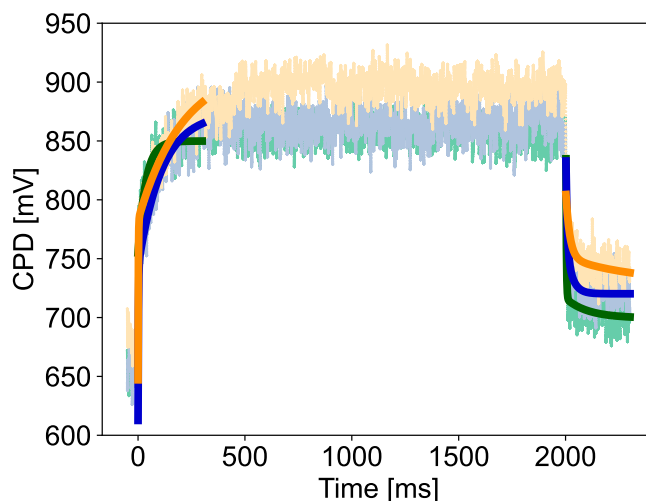
Figure S8: Whole CPD spectroscopy trajectory curves of spots marked in (a), (b) and (e) in Figure 3 with fitted slow time scale of electron extraction (τ_2(ext)) and electron recombination (τ_2(rec)) in respect to turning on the laser of $Cs_{0.05}FA_{0.8}MA_{0.15}PbI_3$ perovskite film with 0.95:1.05 A/B cation ratio (SA$_{\text{Pristine}}$).
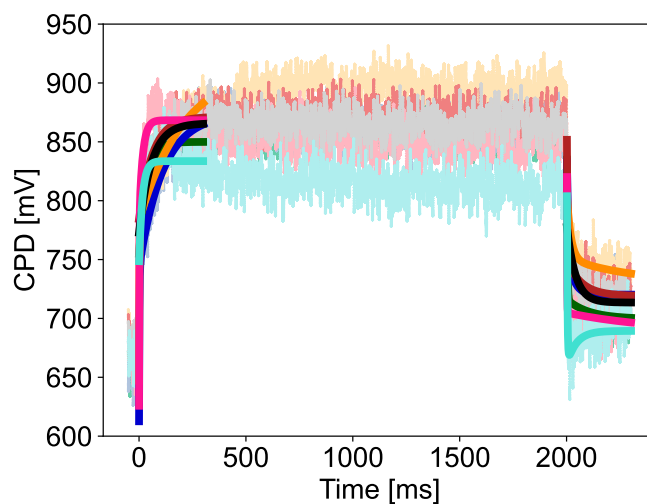
Figure S9: Whole CPD spectroscopy trajectory curves of spots marked in (a), (b) and (e) in Figure S7 with fitted slow time scale of electron extraction (τ_2(ext)) and electron recombination (τ_2(rec)) in respect to turning on the laser of $Cs_{0.05}FA_{0.8}MA_{0.15}PbI_3$ perovskite film with 0.95:1.05 A/B cation ratio ($SA_{Pristine}$).
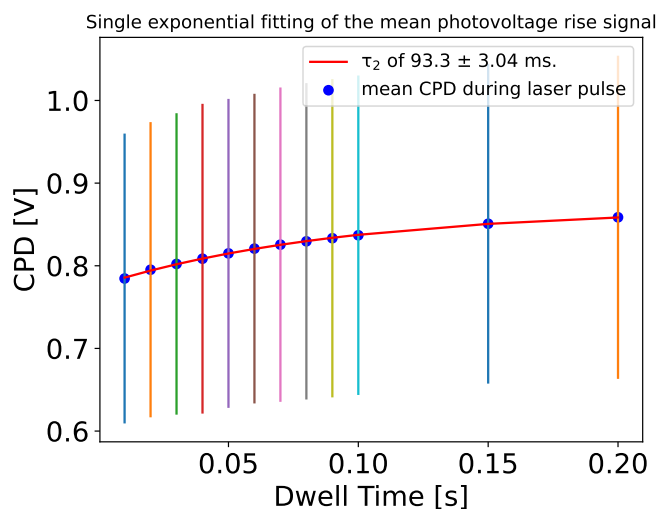
Figure S10: Time dependant CPD evolution of the overall $SA_{Pristine}$ film after laser was switched on. The average CPD values were calculated in $10\,ms$ steps away from each other compared to the switch on of the laser.
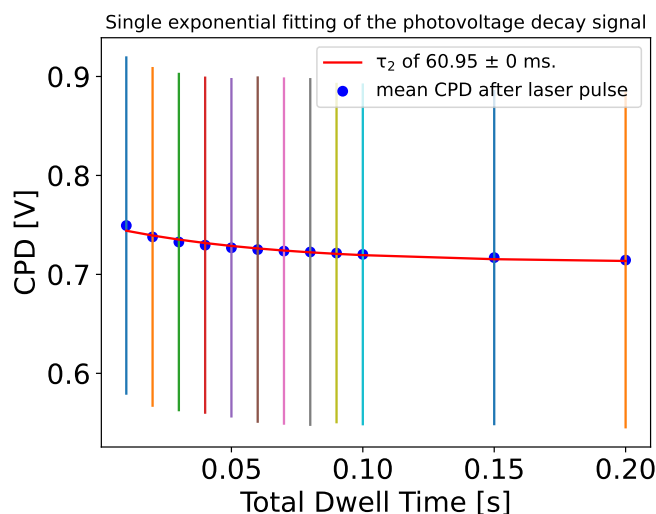
Figure S11: Time dependant CPD evolution of the overall $SA_{Pristine}$ film after laser was switched off. The average CPD values were calculated in 10 ms steps away from each other compared to the switch off of the laser.
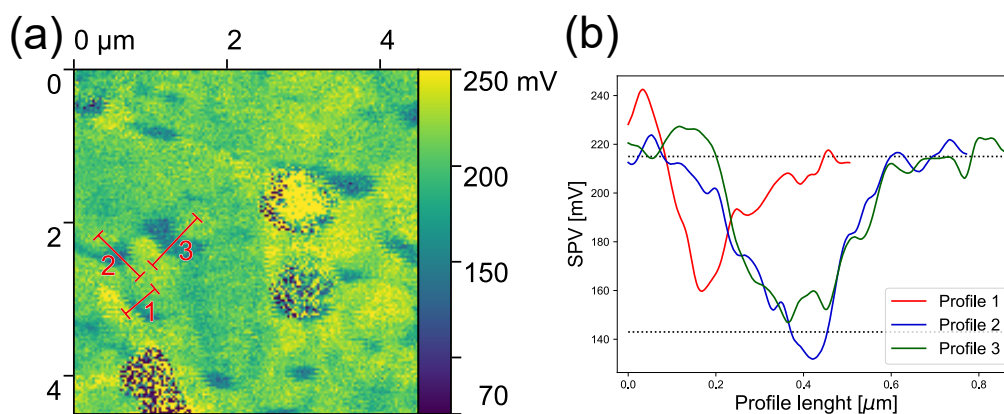
Figure S12: Profile analysis of the SPV picture shown in Figure 3(b). The profile lines averaged over 6 lines marked from 1 - 3 in (a) are shown in (b) with the dotted lines showing the average of SPV value of the grain interior and GB, respectively.
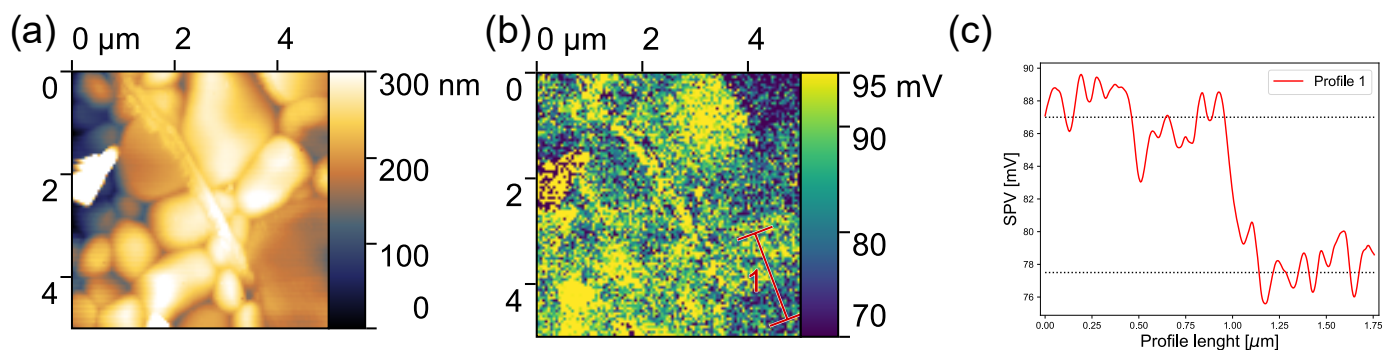
Figure S13: (a) Topography, (b) SPV map and (c) profile analysis of the SPV cahnge within a grain marked in (b) of $Cs_{0.05}FA_{0.8}MA_{0.15}PbI_3$ perovskite film with 1:1 A/B cation ratio. The profile lines averaged over 14 lines marked in (b) are shown in (c) with the dotted lines showing the average of SPV value along the grain interior of 87 ± 2 mV and 78 ± 2 mV which leads to intragranular difference of 9 ± 2 mV.

(a)

(b)
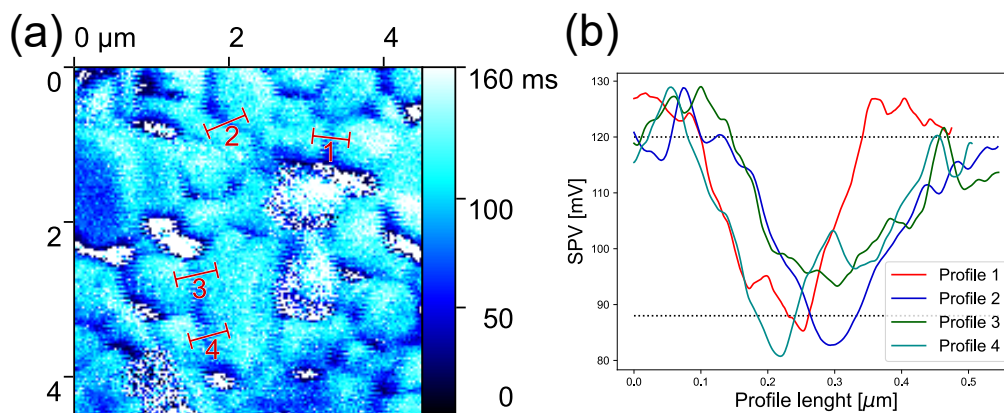
Figure S14: Profile analysis of the τ_2(ext) map shown in Figure 3(e). The profile lines averaged over 7 lines marked from 1 - 4 in (a) are shown in (b) with the dotted lines showing the average of τ_2(ext) value of 122 ± 6 ms and 88 ± 6 ms the grain interior and grain boundary, respectively. This leads to difference between grain interior and grain boundary of 32 ± 6 ms.
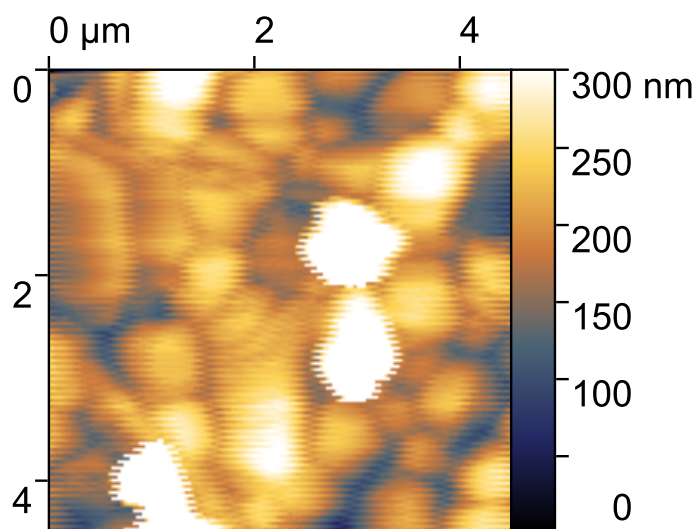
Figure S15: Topography map of $Cs_{0.05}FA_{0.8}MA_{0.15}PbI_3$ perovskite film with 0.95:1.05 A/B cation ratio.
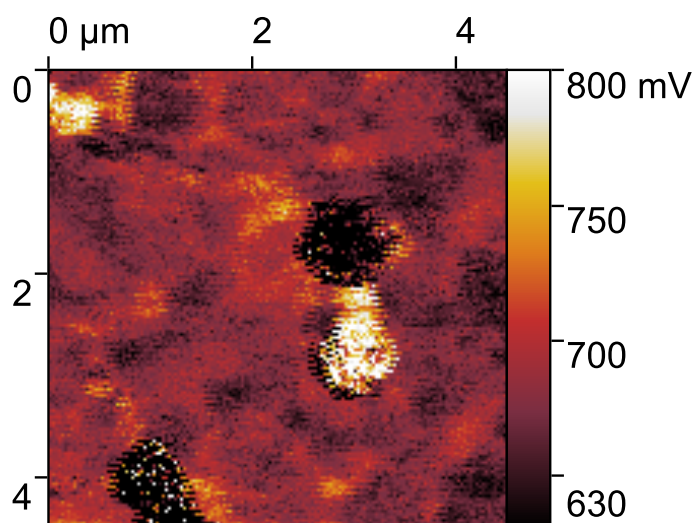
Figure S16: Dark CPD map of $Cs_{0.05}FA_{0.8}MA_{0.15}PbI_3$ perovskite film with 0.95:1.05 A/B cation ratio.
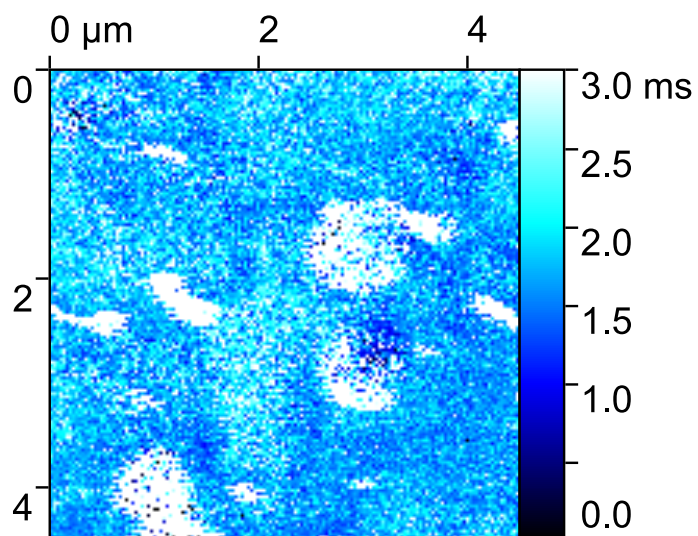
Figure S17: SPV rise time (τ_1(ext)) map of $Cs_{0.05}FA_{0.8}MA_{0.15}PbI_3$ perovskite film with 0.95:1.05 A/B cation ratio.
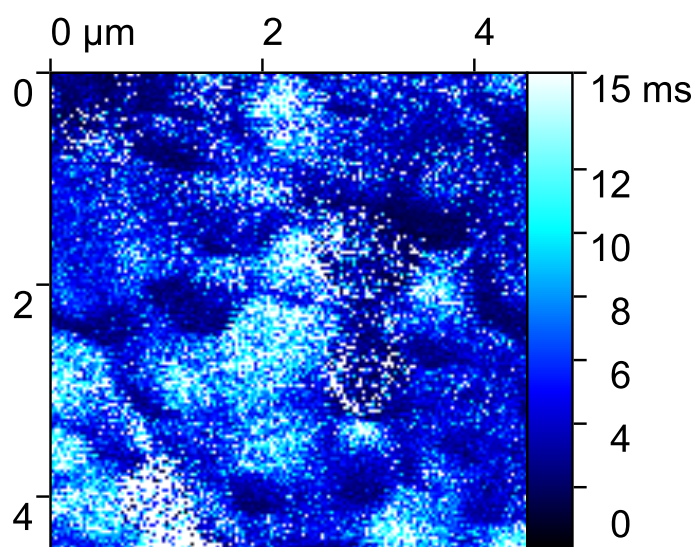
Figure S18: SPV decay time (τ_1(rec)) map of $Cs_{0.05}FA_{0.8}MA_{0.15}PbI_3$ perovskite film with 0.95:1.05 A/B cation ratio.
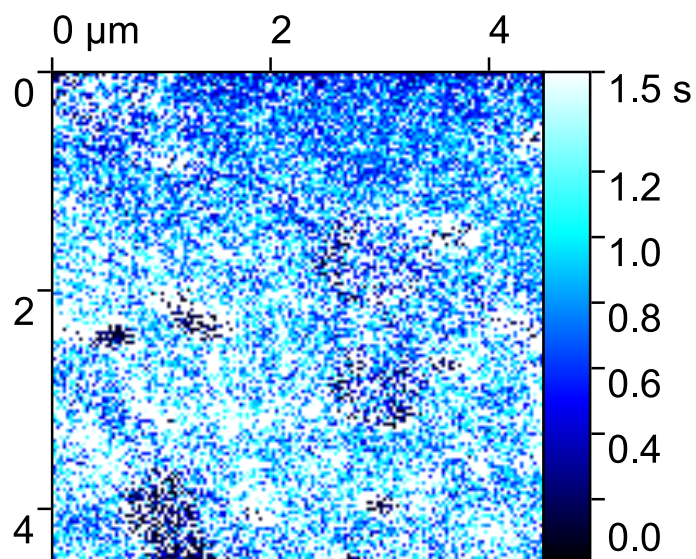
Figure S19: SPV decay time (τ_2(rec)) map of $Cs_{0.05}FA_{0.8}MA_{0.15}PbI_3$ perovskite film with 0.95:1.05 A/B cation ratio.
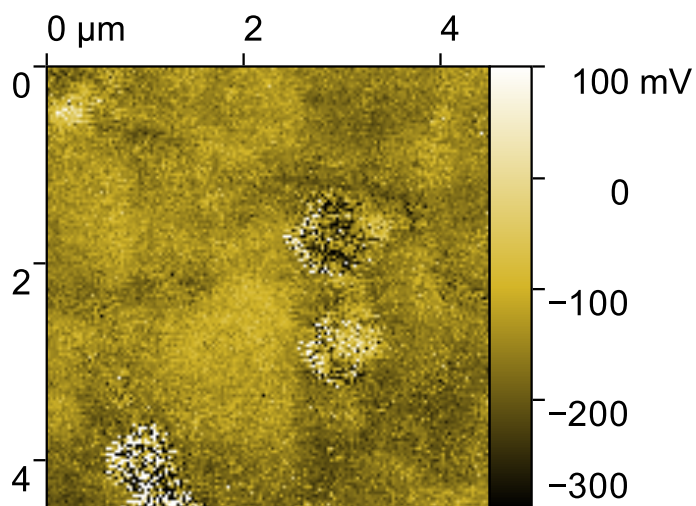
Figure S20: SPV rise amplitude (A_1(ext)) map of $Cs_{0.05}FA_{0.8}MA_{0.15}PbI_3$ perovskite film with 0.95:1.05 A/B cation ratio.
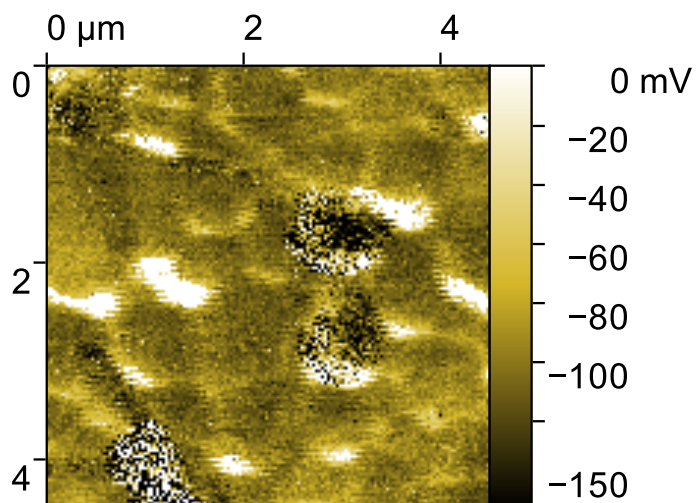
Figure S21: SPV rise amplitude (A_2(ext)) map of $Cs_{0.05}FA_{0.8}MA_{0.15}PbI_3$ perovskite film with 0.95:1.05 A/B cation ratio.
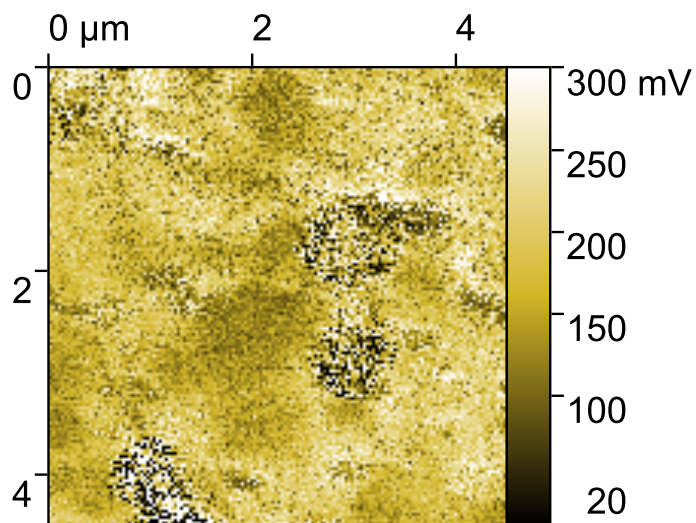
Figure S22: SPV decay amplitude (A_1(rec)) map of $Cs_{0.05}FA_{0.8}MA_{0.15}PbI_3$ perovskite film with 0.95:1.05 A/B cation ratio.
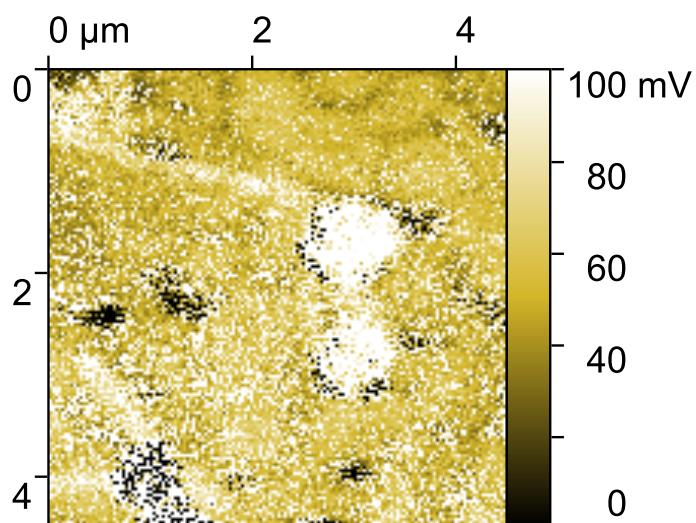
Figure S23: SPV decay amplitude (A_2(rec)) map of $Cs_{0.05}FA_{0.8}MA_{0.15}PbI_3$ perovskite film with 0.95:1.05 A/B cation ratio.

S7 Further Analysis of the passivated solvent annealed sample SA$_{\text{Pass}}$
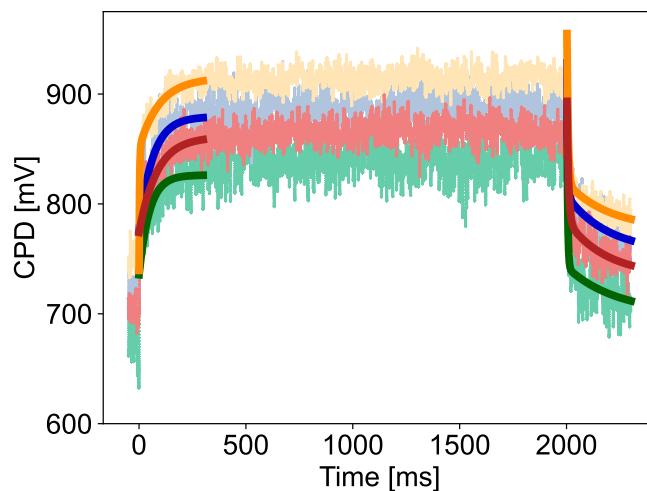
Figure S24: Whole CPD spectroscopy trajectory curves of spots marked in (a), (b) and (e) in Figure 4 with fitted slow time scale of electron extraction (τ_2(ext)) and electron recombination (τ_2(rec)) in respect to turning on the laser of Cs$_{0.05}$FA$_{0.8}$MA$_{0.15}$PbI$_3$ perovskite film with surface passivation and 0.95:1.05 A/B cation ratio (SA$_{\text{Pass}}$).
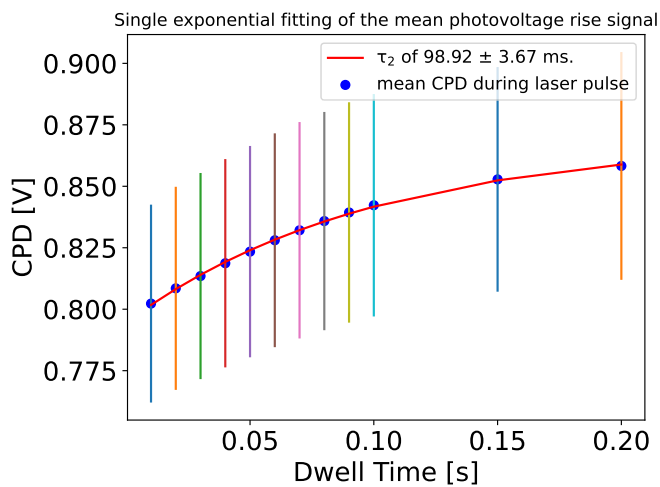
Figure S25: Time dependant CPD evolution of the overall SA$_{\text{Pass}}$ film after laser was switched on. The average CPD values were calculated in 10 ms steps away from each other compared to the switch on of the laser.
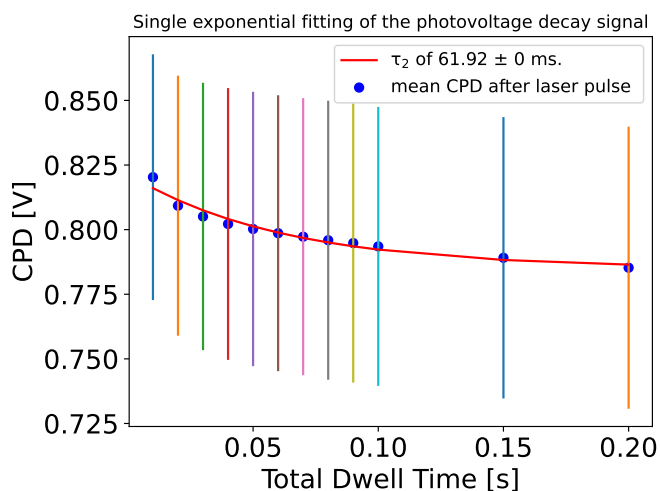
Figure S26: Time dependant CPD evolution of the overall SA$_{\text{Pass}}$ film after laser was switched off. The average CPD values were calculated in $10\,\text{ms}$ steps away from each other compared to the switch off of the laser.
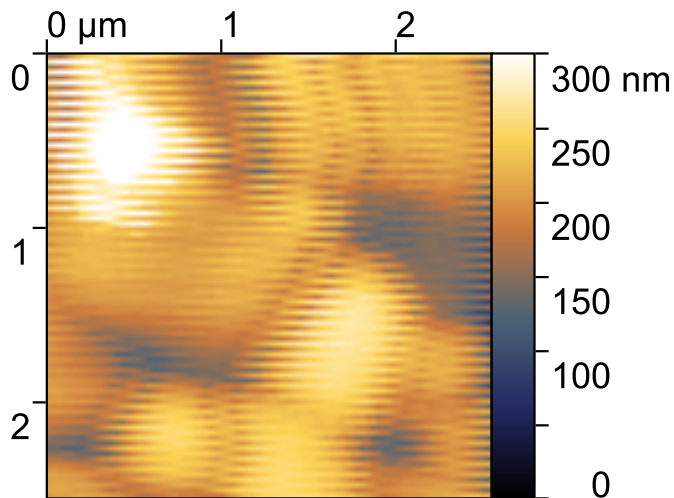
Figure S27: Topography map of PEA-passivated $\text{Cs}_{0.05}\text{FA}_{0.8}\text{MA}_{0.15}\text{PbI}_3$ perovskite film with 0.95:1.05 A/B cation ratio.
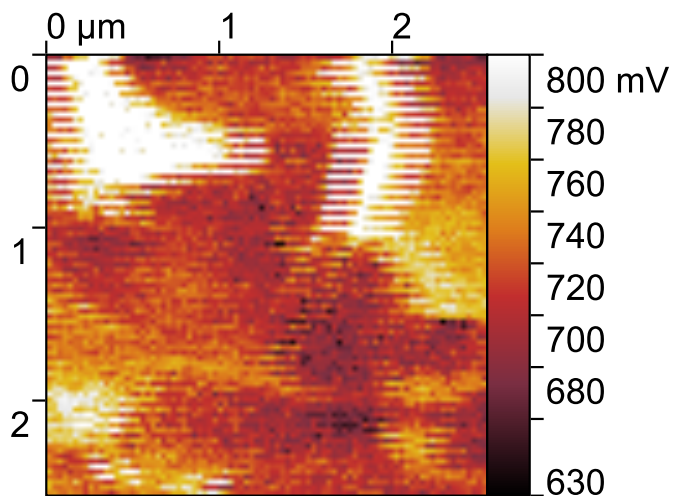
Figure S28: Dark CPD map of PEA-passivated $\text{Cs}_{0.05}\text{FA}_{0.8}\text{MA}_{0.15}\text{PbI}_3$ perovskite film with 0.95:1.05 A/B cation ratio.
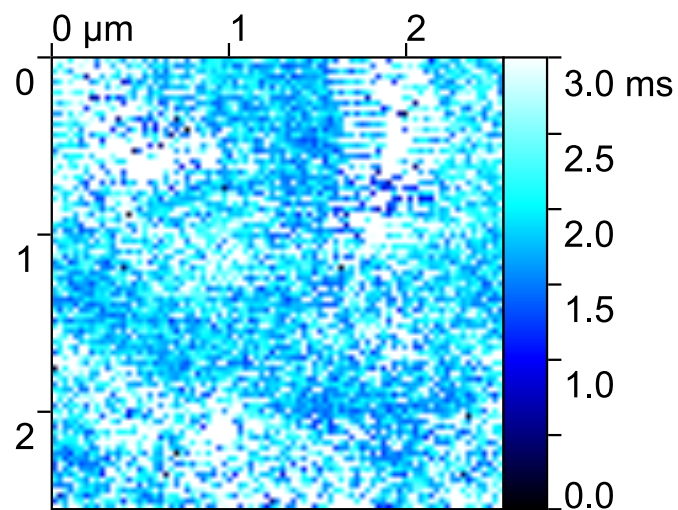
Figure S29: SPV rise time (τ_1(ext)) map of PEA-passivated $Cs_{0.05}FA_{0.8}MA_{0.15}PbI_3$ perovskite film with 0.95:1.05 A/B cation ratio.
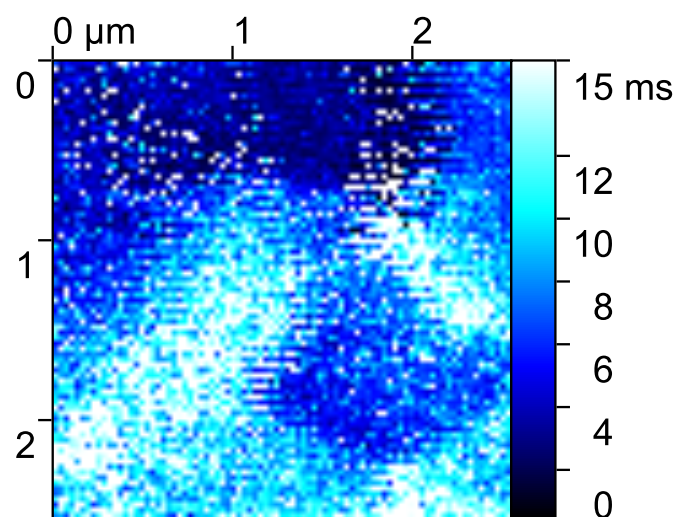
Figure S30: SPV decay time (τ_1(rec)) map of PEA-passivated $Cs_{0.05}FA_{0.8}MA_{0.15}PbI_3$ perovskite film with 0.95:1.05 A/B cation ratio.
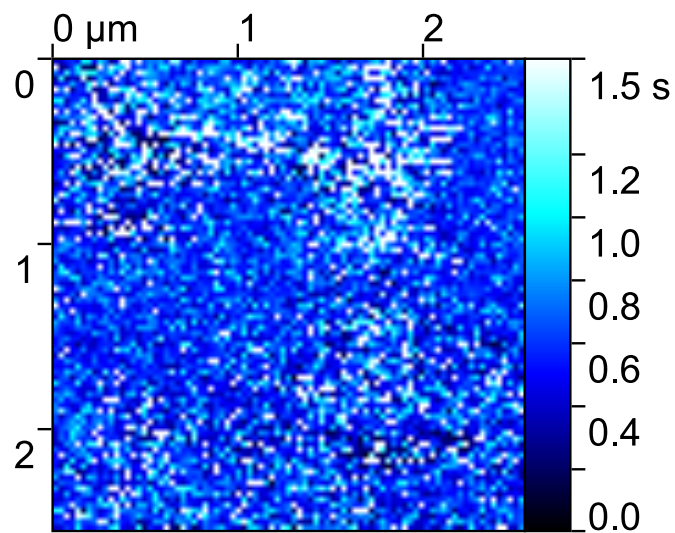
Figure S31: SPV decay time (τ_2(rec)) map of PEA-passivated $Cs_{0.05}FA_{0.8}MA_{0.15}PbI_3$ perovskite film with 0.95:1.05 A/B cation ratio.
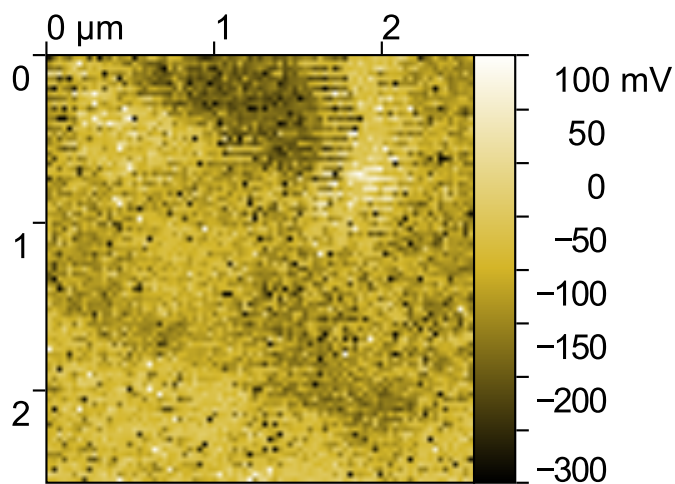
Figure S32: SPV rise amplitude (A_1(ext)) map of PEA-passivated $Cs_{0.05}FA_{0.8}MA_{0.15}PbI_3$ perovskite film with 0.95:1.05 A/B cation ratio.
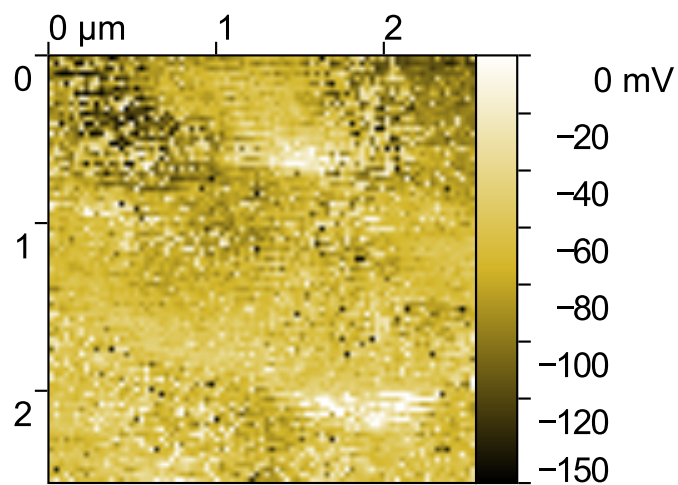
Figure S33: SPV rise amplitude ($A_2(\text{ext})$) map of PEA-passivated $Cs_{0.05}FA_{0.8}MA_{0.15}PbI_3$ perovskite film with 0.95:1.05 A/B cation ratio.
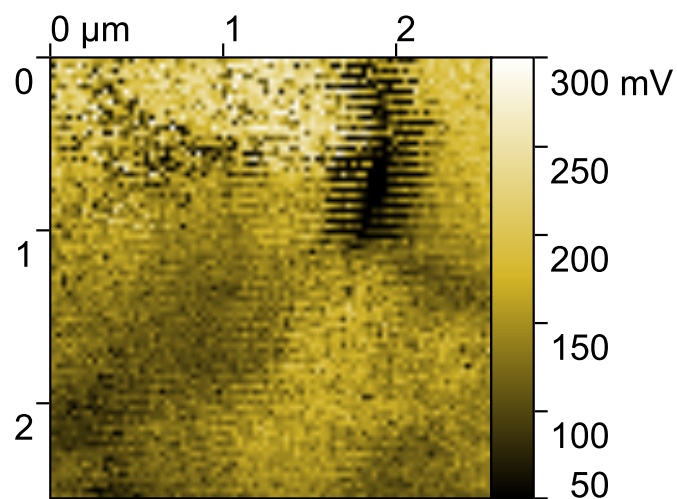
Figure S34: SPV decay amplitude ($A_1(\text{rec})$) map of PEA-passivated $Cs_{0.05}FA_{0.8}MA_{0.15}PbI_3$ perovskite film with 0.95:1.05 A/B cation ratio.
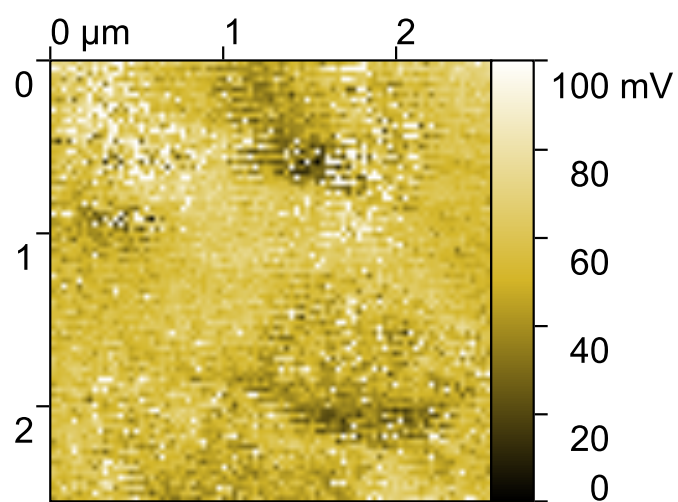
Figure S35: SPV decay amplitude (A_2(rec)) map of PEA-passivated $Cs_{0.05}FA_{0.8}MA_{0.15}PbI_3$ perovskite film with 0.95:1.05 A/B cation ratio.

S8 Further Analysis of the MA80 sample
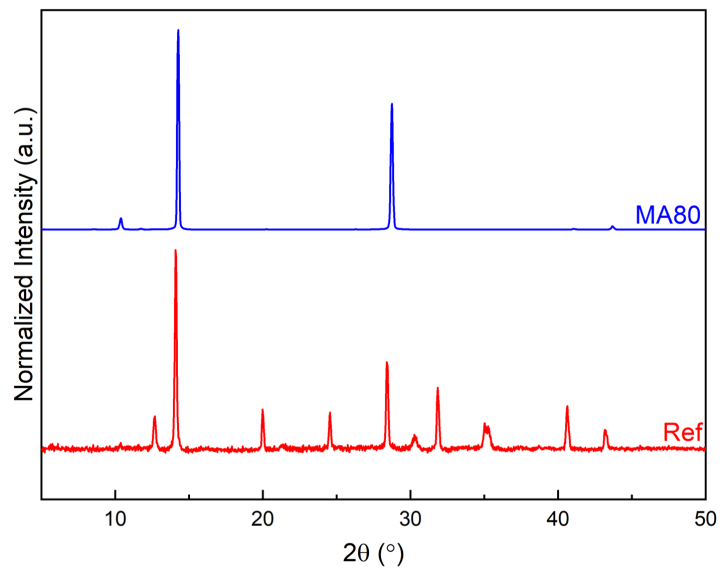
Figure S36: XRD patterns of reference and MA80 perovskite films.
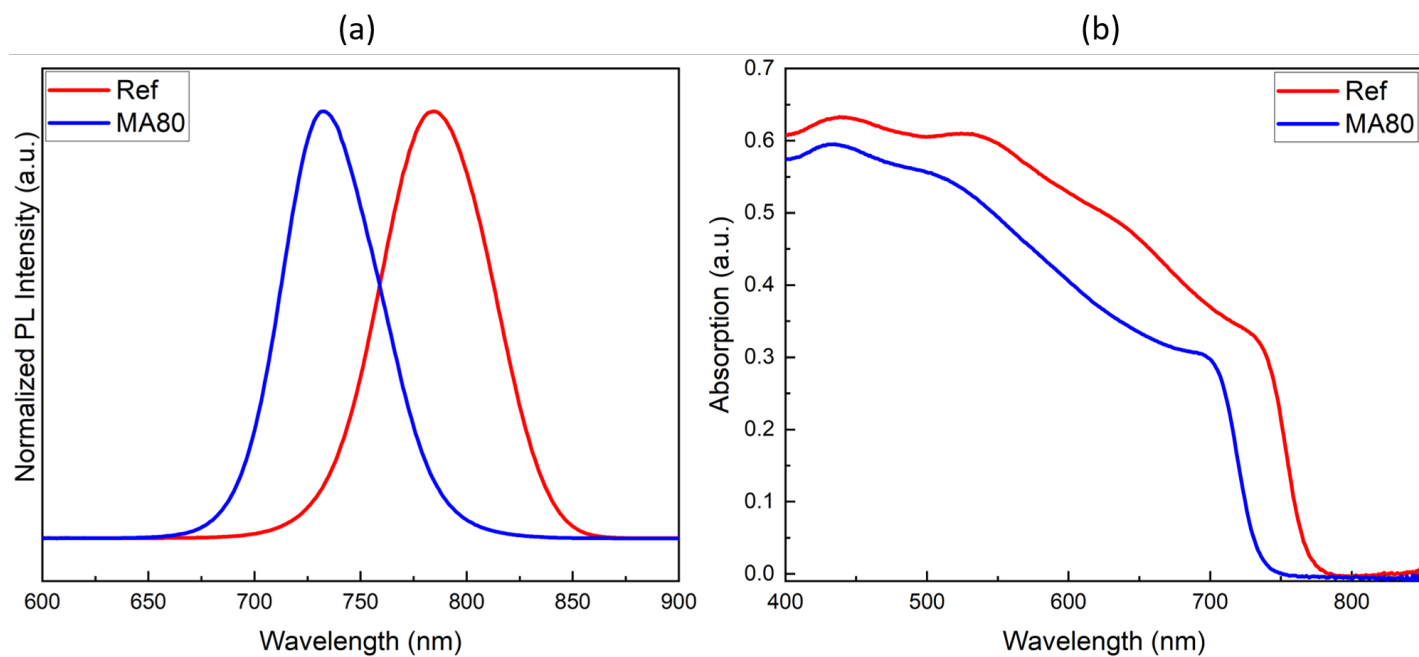
Figure S37: Photoluminescence and absorption spectra of reference and MA80 perovskite films.
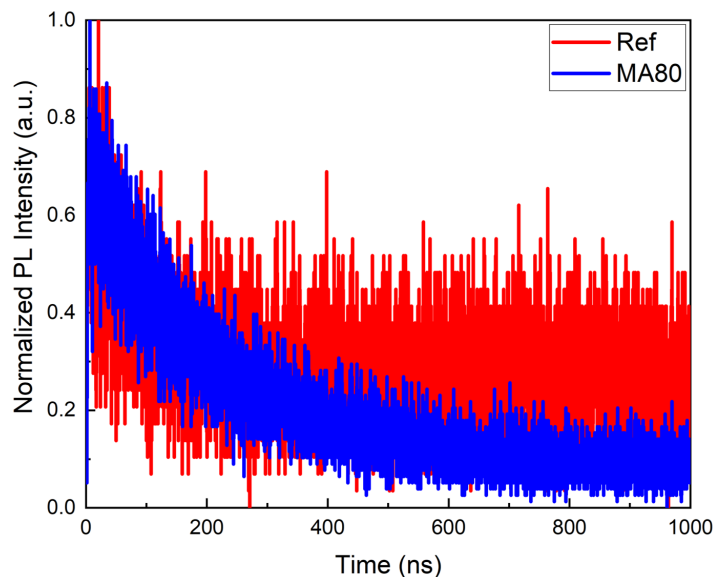
Figure S38: Time-resolved photoluminescence spectra of reference and MA80 perovskite films.

S9 Long-time measurements

Long-time measurements of the trajectroy is shown in **Figure S39**.
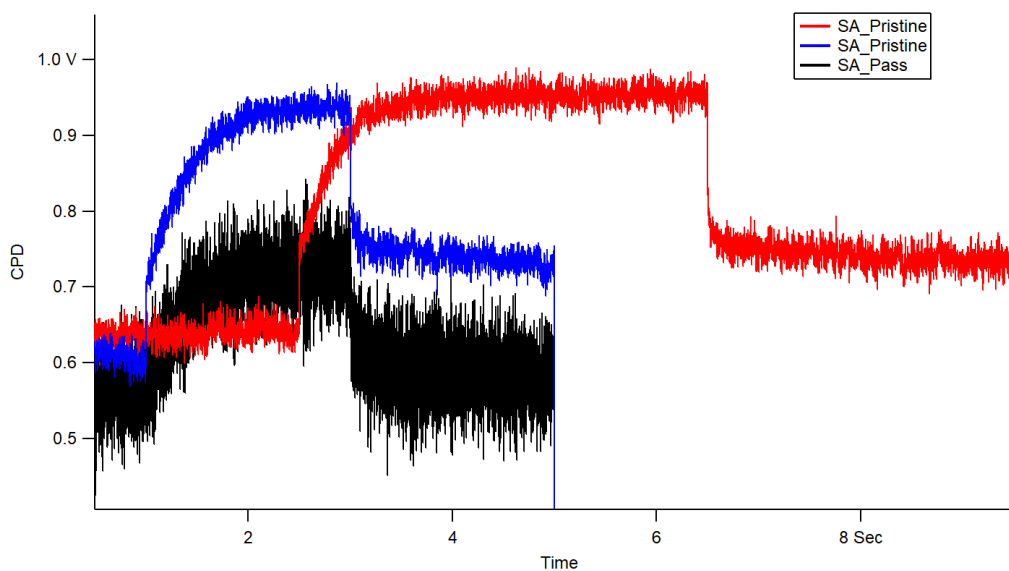
Figure S39: Whole CPD spectroscopy trajectory curves before the respective force maps of $SA_{Pristine}$ (red and blue curve) and SA_{Pass}(black curve) of $Cs_{0.05}FA_{0.8}MA_{0.15}PbI_3$ perovskite films with 0.95:1.05 A/B cation ratio.

In Figure S39 the long-time CPD change due to the illumination according to Figure 1 shows that the CPD_{dark} is not the same compared to the CPD value directly after the light pulse. Interestingly, this is independent of the dwell time (see red and blue curve in Figure S39). Moreover, the red and blue curve was measured right after each other. So, after applying the erase pulse to the red curve the CPD_{dark} value of the blue curve is very comparable to the CPD_{dark} value of the red curve. This difference of the CPD value is not visible in the SA_{Pass} sample (see black curve in Figure S39).

S10 Nanoscale Ideality Factor Mapping

The intensity of the laser is controlled by the analog voltage that is provided by the controller of our AFM and the analog voltage dependence of the laser intensity is measured to be linear. This relation gives us the ramp up parameters of the laser intensity. By using this we can plot the SPV against the logarithmic light intensity and obtain the $n_{id,l}$ which reveals the information about the recombination behavior of the sample. Since the recombination mechanisms are closely related to the trap density within the perovskite films, mapping $n_{id,l}$ this way enables us to map the defects on a nanoscale.
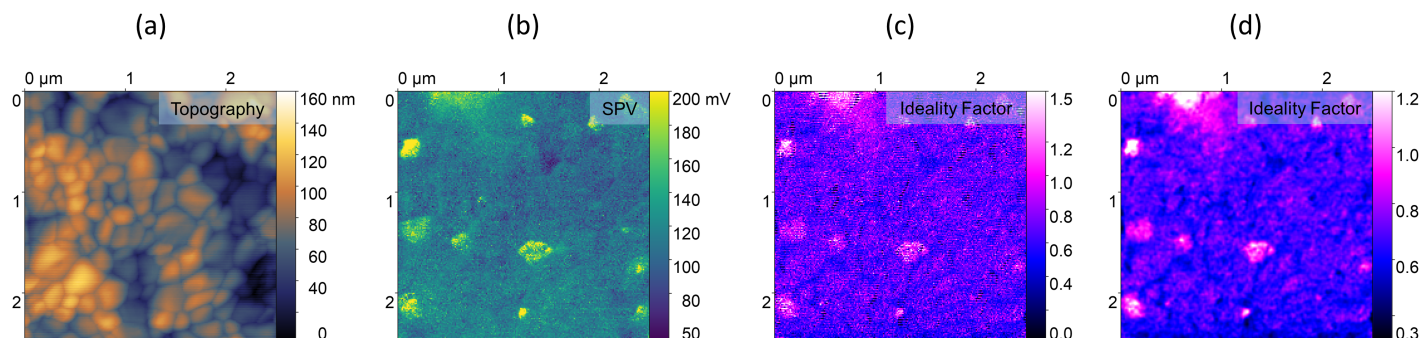
Figure S40: (a) Topography, (b) SPV, (c) $n_{id,l}$, and (d) 1x1 pixel Gaussian filtered $n_{id,l}$ maps of reference perovskite film. The map contains 200x200 pixels.
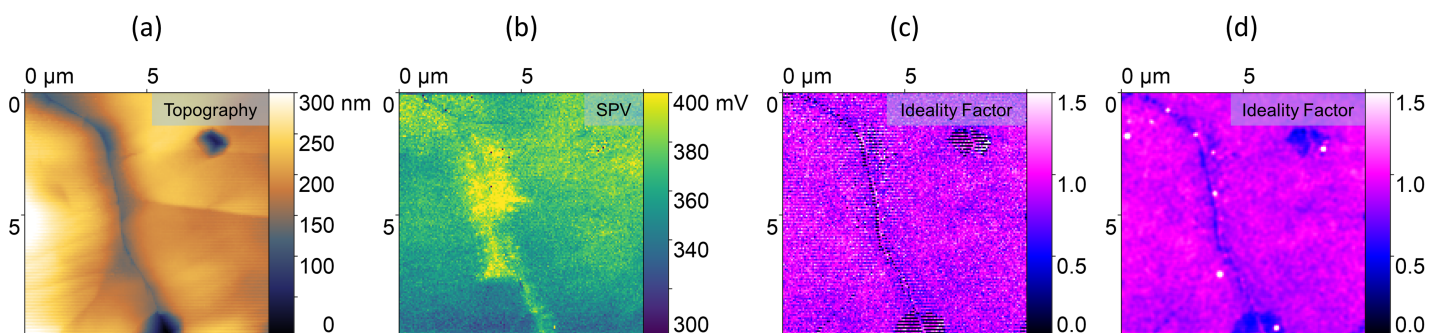
Figure S41: (a) Topography, (b) SPV, (c) $n_{id,l}$, and (d) 1x1 pixel Gaussian filtered $n_{id,l}$ maps of MA80 film. The map contains 150x150 pixels.
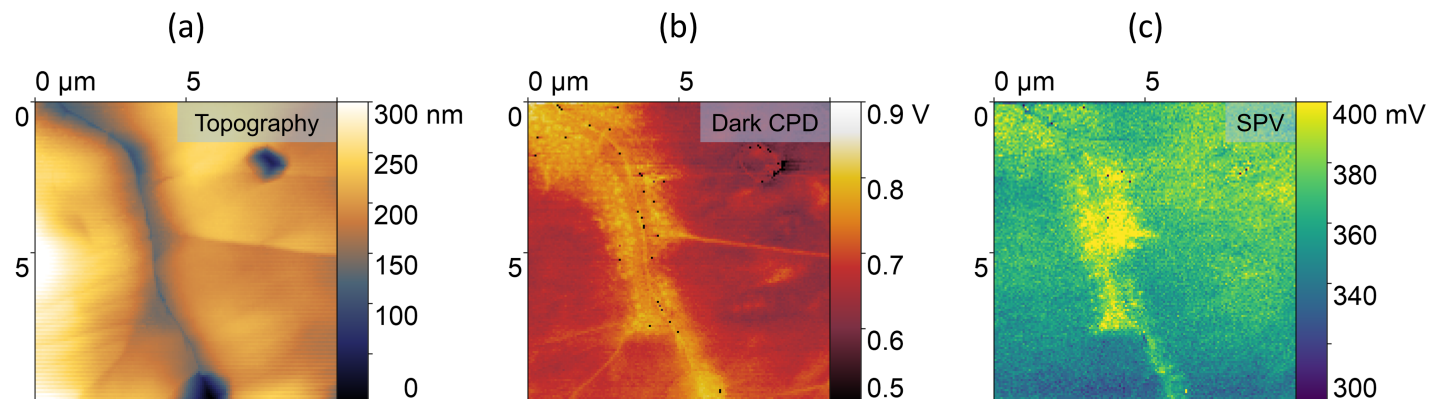
Figure S42: (a) Topography, (b) dark CPD, and (c) SPV maps of MA80 film.

Bibliography

[1] B. Voigtländer, *Scanning Probe Microscopy*, NanoScience and Technology. Springer Berlin Heidelberg, Berlin, Heidelberg, **2015**.

[2] A. Varol, I. Gunev, B. Orun, C. Basdogan, *Nanotechnology* **2008**, *19*, 7 075503.

[3] A. Perez-Cruz, A. Dominguez-Gonzalez, I. Stiharu, R. A. Osornio-Rios, *Ultramicroscopy* **2012**, *115* 61.

5 Reduced Defect Density in Crystalline Halide Perovskite Films via Methylamine Treatment for the Application in Photodetectors

Summary & Author Contributions

In this paper, we show the effect of methylamine assisted heat treatment on morphology and the electrical properties of halide perovskites. We show the morphology via SEM, the changes in cristallinity via XRD, and the changes in the optical properties by PL measurements. Then we investigated the electronic properties of methylamine treated films via space-charge limited current and C-AFM. Finally, we showed the performance increase of photodetectors that use methylamine treated halide perovskites.

Mehmet Yenal Yalcinkaya conducted the C-AFM measurements to measure local conductivity under dark and illuminated conditions to understand the changes at the grain bounderies.

Reduced defect density in crystalline halide perovskite films via methylamine treatment for the application in photodetectors

Emilia R. Schütz,[1] (iD) Azhar Fakharuddin,[1] (iD) Yenal Yalcinkaya,[2,3] Efrain Ochoa-Martinez,[4] (iD) Shanti Bijani,[5] (iD)
Abd. Rashid bin Mohd Yusoff,[6] (iD) Maria Vasilopoulou,[7] Tobias Seewald,[1] (iD) Ullrich Steiner,[4] (iD)
Stefan A. L. Weber,[2,3] and Lukas Schmidt-Mende[1,a)] (iD)

AFFILIATIONS

[1] Department of Physics, University of Konstanz, D-78457 Konstanz, Germany
[2] Max Planck Institute for Polymer Research, Ackermannweg 10, 55128 Mainz, Germany
[3] Institute of Physics, Johannes Gutenberg University Mainz, Duesbergweg 10-14, 55128 Mainz, Germany
[4] Adolphe Merkle Institute, University of Fribourg, Chemin des Verdiers 4, 1700 Fribourg, Switzerland
[5] Unidad de Nanotecnología, Centro de Supercomputador y Bioinnovación SCBI, Universidad de Málaga, Calle Severo Ochoa 34, 29590 Campanillas (Málaga), Spain
[6] Department of Chemical Engineering, Pohang University of Science and Technology (POSTECH) 77 Cheongam-Ro, Nam-Gu, Pohang 37673, Republic of Korea
[7] Institute of Nanoscience and Nanotechnology, National Center for Scientific Research "Demokritos," 15341 Agia Paraskevi, Attica, Greece

[a)]Author to whom correspondence should be addressed: Lukas.Schmidt-Mende@uni-konstanz.de

ABSTRACT

Considerable efforts have been devoted to optimizing and controlling the morphology and electronic properties of lead halide perovskites. The defect density of a perovskite layer strongly depends on the processing conditions. Consequently, the fabrication process of high-quality films is often complex, and reproducibility is a challenge. In this work, we present a methylamine gas-based method to recrystallize perovskite layers of any given quality in a controlled way, leading to millimeter-sized domains. Crystallinity significantly increases upon methylamine treatment, and crystal growth follows a preferred orientation. Photoluminescence- and space-charge limited current measurements show that the trap density halves after recrystallization. Conductive atomic force microscopy measurements show a higher surface conductivity and an improved spatial homogeneity after methylamine treatment. When applied in photodetectors, the improved film quality of the recrystallized films leads to increased detectivities of $\approx 4 \times 10^{11}$ Jones compared to 3×10^9 Jones of a reference device. The response time falls from 0.1 to 10^{-5} s upon methylamine treatment. Our work, thus, presents a promising route to fabricating reproducible, high-quality perovskite films through well-controllable recrystallization.

I. INTRODUCTION

Organic–inorganic hybrid perovskite materials are currently achieving breakthroughs in a range of optoelectronic devices due to their unique properties.[1–4] These include their low defect density and high defect tolerance,[5–7] the facile bandgap[8–10] and nanocrystal size[11] tuning, and high charge carrier mobilities in the range of 1–30 cm^2/Vs.[12–14] As these materials are commonly processed from solution and their crystallization completes within time spans of several seconds up to a few minutes, the fabrication process is very delicate.[15,16] Extreme care is necessary for developing high-quality perovskite films. Uncontrolled growth of perovskite crystals

leads to the formation of defects due to compositional and structural disorder, which significantly limit device performance.[17,18] Surface defects in perovskite films, including those at grain boundaries (GBs), are well-known,[18] and high-efficiency devices often employ surface passivation techniques to reduce the defect density.[17,19]

Since the emergence of halide perovskites, efforts have, therefore, been dedicated to engineering their film morphology. Irrespective of the ongoing debate whether large or small grains are desirable for high-efficiency devices, the GBs, if not effectively passivated, act as defect sites leading to a non-radiative recombination.[20] GBs have also shown to be sites of moisture ingress and are, thus, among the primary sources of device instability.[21] This is why several strategies to fabricate large perovskite grains have been introduced. Some notable methods include hot casting,[22,23] optimizing the reaction temperature of perovskite annealing,[24] template-assisted growth,[25–27] thermal and solvent treatments,[28,29] and the effect of substrate layers.[30,31] Note that these methods add complexity to the device fabrication process and that not all of them are compatible with large-area processing.

Methylamine (MA^0) gas-based post-treatments present a different approach to improving the morphology and crystallinity of perovskite films.[32] They are based on the interaction between MA^0 and hybrid organic–inorganic perovskites first reported by Zhou *et al.*[33] When exposed to the MA^0 gas, the perovskite phase readily collapses into a liquid intermediate phase,[34]

$$ABX_3(s) + x\,MA^0(g) \longleftrightarrow ABX_3 \cdot xMA^0(l). \qquad (1)$$
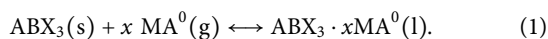
The causes of this interaction are thought to be the disruption of the bonds in the PbI_6 octahedral lattice due to bonding of the MA^0 with lead (Pb^{2+}) and methylammonium (MA^+) ions.[35,36]

In principle, two different routes to recrystallization have been explored. When the MA^0 atmosphere is removed, the film recrystallizes and forms a smooth, fine-grained film. Improved surface coverage, crystallinity, and vastly improved solar cell performance compared to raw films have been achieved this way.[33,37] The other method, first shown by Jacobs and Zang,[38] relies on heating the sample without removing the MA^0 gas. At elevated temperatures, crystal seeds form and grow outward, forming large domains. Such films exhibit increased crystallinities[38,39] and have successfully been implemented in high-performing solar cells by Fan *et al.*[39] Irrespective of the recrystallization method, the crystal phase reforms during the treatments, its properties depending only on the atmospheric conditions. In consequence, these post-deposition treatments could provide the means to decouple the film quality from the initial deposition process and, therefore, are promising to improve reproducibility, facilitate upscaling, and lower production costs. As they open up the opportunity to reduce or even eliminate the influence of GBs in film degradation due to the increased grain size, such MA^0-gas treatments also show great promise regarding the stability of fabricated devices.

We herein present a new MA^0-based treatment protocol and setup with which we can obtain mixed triple cation perovskite films with near-millimeter domain size. We show drastically improved crystallinities, as evidenced by x-ray diffraction (XRD) intensities increasing by orders of magnitude in the recrystallized films. In addition, space-charge limited current (SCLC) measurements show a reduction of the trap densities from 8×10^{16} to 4×10^{16} cm^{-3}

after MA^0 treatment, resulting in strongly improved photodetection devices, with the specific detectivities increasing from $\approx 3 \times 10^9$ to 4×10^{11} Jones.

II. RECRYSTALLIZING PEROVSKITE FILMS IN A METHYLAMINE ATMOSPHERE

Precise control over the amount of MA^0 gas to which the samples are exposed as well as over the temperature and exposure times, allowing us to systematically vary and optimize all parameters during exposure and recrystallization. The setup and processing conditions are described in further detail in the supplementary material (see Fig. S1).

We found that at a given MA^0 partial pressure p_{MA}, the perovskite film only collapses into a liquid state when below a temperature T_{rec}. Above this transition temperature, the material is solid in equilibrium despite a persisting MA^0 atmosphere. Determining these temperatures, T_{rec} for different p_{MA} gives a rough phase p–V diagram shown in Fig. 1(a). Note that these values were determined for a mixed triple-cation perovskite $[Cs_{0.1}(MA_{0.17}FA_{0.83})_{0.9}Pb(I_{0.83}Br_{0.17})_3]$, but an equivalent behavior is observed in $MAPbI_3$.

Taking advantage of this knowledge, we have developed a MA^0 treatment protocol that reliably yields large grains grown in a controlled fashion. In contrast to previous studies,[38,39] we choose to keep the temperature constant throughout the entire process and instead lower the partial pressure to initialize recrystallization. As the heating process often takes minutes, during which the film may or may not start crystallizing, and the heating rate varies with external conditions, the MA^0 treatment becomes faster and more predictable this way.

We start with the sample at an elevated temperature T, which is kept constant. After establishing an inert nitrogen atmosphere, a certain amount of MA^0 gas is led into the chamber up to a MA^0 partial pressure p_{MA}. If T is smaller than the recrystallization temperature $T_{rec}(p_{MA})$ at this initial partial pressure, the film collapses into the liquid phase. To initialize recrystallization, the partial pressure inside the reaction chamber is then lowered by gradually evacuating the chamber. As the transition is crossed as indicated by the arrow in Fig. 1(a), recrystallization starts in the form of seed nuclei. These crystals slowly grow until the entire substrate is covered with large grains.

By choosing a combination of pressures and temperatures where we move to a point in the phase diagram just barely above the recrystallization temperature after evacuation, we can achieve very slow nucleation and grain growth, resulting in nearly millimeter-sized grains. The higher the temperature difference $T - T_{rec,\,new}$ (i.e., the greater the vertical distance from the transition line in the phase diagram), the faster the crystallization process becomes and the smaller the resulting grains (see Fig. S2). We, thus, also gain control over the mean grain size by controlling the recrystallization temperature.

Figure 1(b) shows the top-view optical microscopy images of the nucleation and growth of individual grains. It is clearly visible how individual grains nucleate and symmetrically grow outward. The growth process itself takes several minutes and ends when neighboring grains meet to form a continuous film.
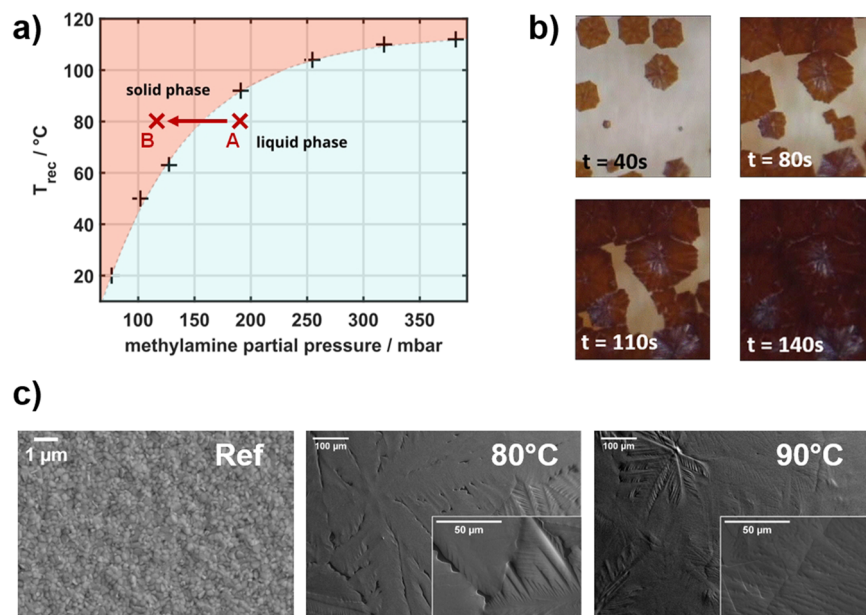
FIG. 1. (a) Transition temperatures T_{rec} for different MA^0 partial pressures inside the chamber. The dotted line guides the eye along the transition line between the solid and the liquid state. During the process, the MA^0 partial pressure is lowered along the red arrow from the exemplary point A to point B. As the transition line is crossed during this process, recrystallization is induced. (b) The recrystallization process after nucleation, as observed through a microscope camera from above. (c) Scanning electron microscopy (SEM) topographies of the anti-solvent reference and the MA^0 treated 80 °C and 90 °C films.

We have applied this process to a mixed triple-cation perovskite to investigate the resulting film properties. The perovskite layer was deposited on indium tin oxide (ITO)/tin(II) oxide (SnO_2) substrates. An untreated reference film was compared to the recrystallized samples throughout this work. We used a MA^0 partial pressure of ~230 mbar, which was then reduced to 170 mbar through pumping. We found that for these pressures, the samples can be liquefied and recrystallized if the sample temperature T lies between roughly 80 and 100 °C. At the lower end of this range, the resulting recrystallization process is slow and takes up to 30 min. While the recrystallization process is much faster at higher temperatures, the liquefaction is only very brief or partial above 100 °C, leading to an incomplete film transformation. We have chosen two temperatures T within this range, 80 and 90 °C, and have characterized the resulting film properties, which we discuss below.

III. FILM MORPHOLOGY, CRYSTALLINITY, AND COMPOSITION

Figure 1(c) shows scanning electron microscopy (SEM) images of an as-deposited reference film and the recrystallized films after MA^0 treatment at 80 and 90 °C. The surface of the reference film is very uniform and smooth, and individual grains with diameters on the order of tens of nanometers are visible. In contrast, domains of several hundred micrometers in diameter are visible after MA^0 treatment. For these slowly grown grains, one can clearly discern their point of origin, where nucleation in the liquid phase first occurred, and structures that radiate outward in the direction of crystal growth. The main difference between the samples at 80 and 90 °C lies in how different grains meet at their edges to form boundaries. In the 80 °C films, gaps and holes are apparent at the domain boundaries, whereas in the 90 °C films, the individual domains meet almost seamlessly.

One possible explanation for this observation is the long crystallization times at 80 °C. Similar to observations made in conventional perovskite film fabrication from solvent-based precursors,[40,41] the liquid phase on the substrate tends to de-wet from the surface. In the moment of liquefaction, when the solid phase collapses, the substrate is still fully covered. As recrystallization starts, however, crystals partially replace the liquid areas. At the edges of the growing grains, holes in the films start to become energetically favorable. If the recrystallization process is too slow and the film has enough time to de-wet, gaps may form between different grains. At a higher recrystallization temperature, the crystals grow much faster and meet at their boundaries before the liquid has had time to locally de-wet.

It is worth noting that no substructures comparable to the grains in the reference are resolved in the MA^0 treated films. The visible planes appear to be perfectly flat in the SEM images (see Fig. S3). Atomic force microscopy (AFM) topographies [see Figs. 5(b) and 5(d)] do show a smaller substructure on the order of tens of micrometers, which are still orders of magnitude larger than the reference grain size. In addition, electron backscattering diffraction studies (see Fig. S4) show that the recrystallized film is oriented in one crystallographic direction within individual domains. We, therefore, conclude that the slow growth from the liquid intermediary resembles the growth of single crystals from solution and leads to large crystalline domains.

To corroborate these observations, we obtained XRD spectra of the films [Fig. 2(a)]. The peak intensities of the (110)-peak have been extracted and are shown in Fig. 2(b).

The results, indeed, show that the MA^0 treatment produces highly crystalline films with a (110) out-of-plane orientation. In contrast, the reference sample shows orders of magnitude lower XRD peak intensities and differently oriented phases, indicating a distribution of small and randomly oriented crystallites. A careful analysis of the (110) diffraction peak in Fig. 2(c) shows a shift to
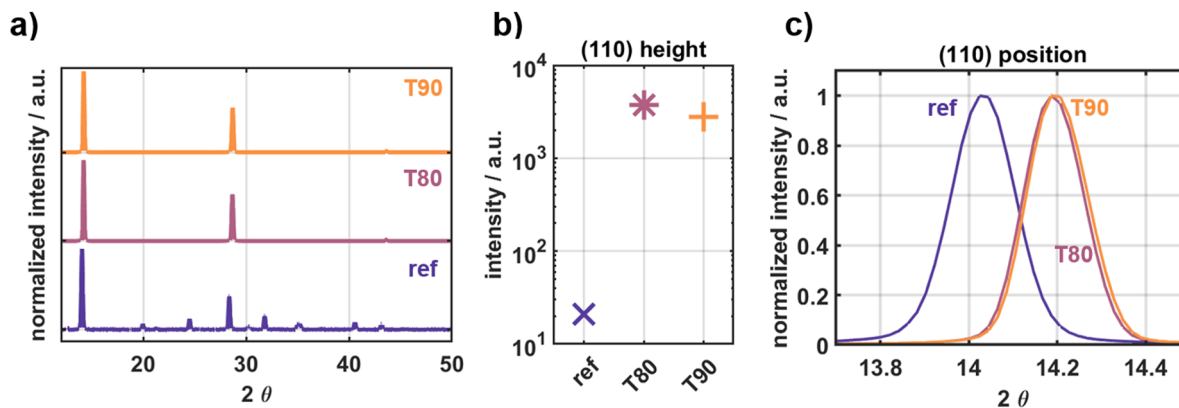
FIG. 2. (a) XRD patterns obtained for reference and MA^0 treated samples, recrystallized at different temperatures. (b) Comparison of (110) peak intensity for the different samples. (c) Normalized intensity for the (110) diffraction peak.

larger diffraction angles upon MA^0 treatment. This phenomenon is accompanied by a substantial shift in the photoluminescence (PL) peak position to smaller wavelengths of around 30 nm from 760 to 732 nm after MA^0 treatment (see Fig. S5). Equivalent observations of a shift in the optical bandgap were made by ultraviolet–visible (UV–vis) spectroscopy measurements (see Figs. S6 and S7 and Table SI). There are two possible explanations for this behavior: an increase in macrostrain[42] or compositional changes. A partial exchange of formamidinium (FA^+) for MA^+ in the perovskite lattice could explain the peak shifts[43,44] and is plausible, considering the exposure of the film to MA^0 gas. Similar gas-induced compositional transformations have been demonstrated before.[45–47] The hypothesis of a compositional change is supported by x-ray photoelectron spectroscopy (XPS) measurements showing a decreased relative amount of nitrogen in the films after MA^0 treatment (see the supplementary material, Tables SII and SIII as well as Figs. S8 and S9, for more details). The Williamson–Hall analysis of our data (see Fig. S10 and Table SIV), on the other hand, shows that there is, indeed, increased microstrain in the film. The shifts in the XRD peak position and bandgap are, thus, likely caused by a combination of both effects. The Williamson–Hall analysis also shows an increase in calculated crystallite size after MA^0 treatment, proving a qualitative improvement in crystallite packing after recrystallization. For a more detailed discussion, see the supplementary material (Fig. S10 and Table SIV).

IV. PHOTOLUMINESCENCE AND QUANTIFICATION OF DEFECT DENSITIES

To further characterize our films, we performed PL measurements. The samples are excited with a pulsed 405 nm laser source. As mentioned above, the emission peak shifts from 760 to 734 nm and 732 nm after MA^0 treatment at 80 and 90 °C, respectively, likely primarily due to changes in film composition and strain. We performed time-resolved PL measurements under continuous illumination to track the changes of the emission behavior during light-soaking over 20 min.

Figure 3(a) shows the PL spectra of an exemplary reference sample. We observe a slow rise in intensity, which is steep at first and later flattens. This increase is accompanied by a shift of the emission peak to larger wavelengths with prolonged illumination. This behavior is observed consistently across all spots and samples, with variations in the exact magnitude of the increase.

Individual measurements are less consistent after MA^0 treatment. While, generally, the MA^0 treated samples exhibit an increase in intensity and a shift to larger wavelengths, the shape and magnitude of these trends vary between different spots. To illustrate this behavior, multiple measurements are shown in Fig. S11. The observed variations can be explained by comparing the laser spot size (around 300 μm) with the perovskite domain sizes. The reference films are very fine-grained, and individual domains are several orders of magnitude smaller than the illuminated spot. The measured PL is the collective signal of multiple grains across boundaries and bulk areas alike. Structural inhomogeneity within the films is, therefore, not resolved. The resulting measurement represents the average across the entire illuminated area. In contrast, the hundreds of micrometer-sized domains of the MA^0 treated samples are on the same scale as the laser spot size. When measuring different, randomly chosen spots on the film, the difference between growth centers, bulk areas, and boundaries will be represented in the resulting data.

Nonetheless, comparisons between the reference and MA^0 treated samples can be made when looking at the statistics of multiple measurements. Boxplots of the PL intensity increase relative to the initial value and the total peak shift are shown in Figs. 3(b) and 3(c).

It is apparent that the total increase in intensity is much less pronounced after MA^0 treatment. While the peak height increased 2.1-fold in the median measurement of the reference films, the median only increased 1.1-fold and 1.4-fold in the 80 and 90 °C samples, respectively. In addition, the total peak shift is less distinct and considerably less consistent after MA^0 treatment.

The observed slow increase in PL intensity has previously been attributed to different effects: Ion migration, facilitated by the photoexcitation of the material,[48,49] leading to a "curing" of defect states
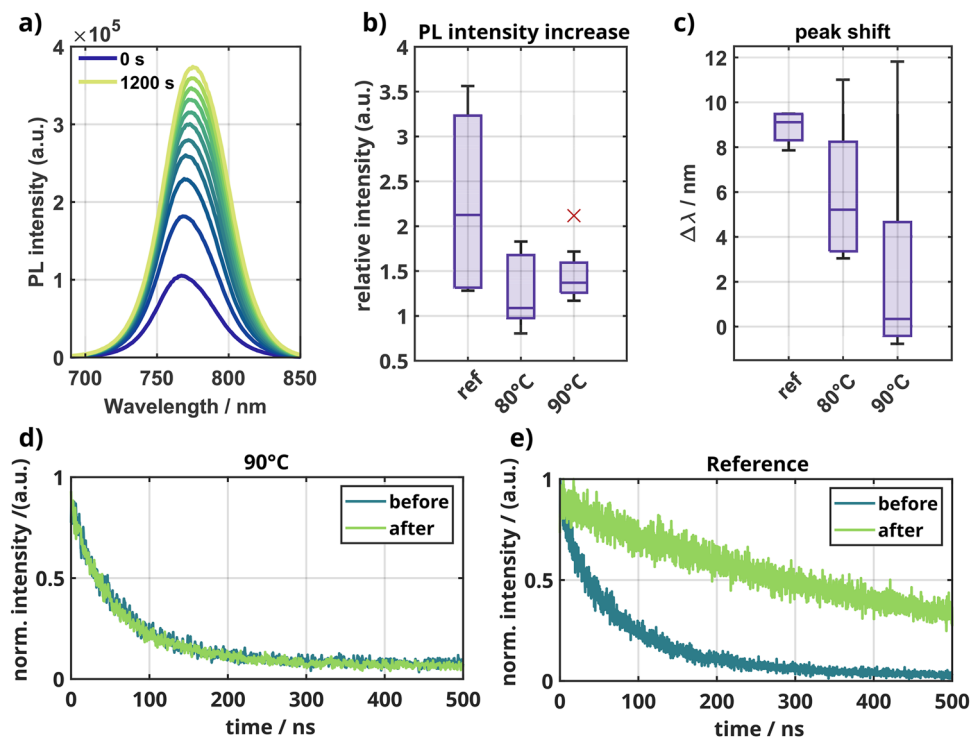
FIG. 3. (a) Exemplary PL spectra of a reference sample under continuous illumination between 0 and 1200 s. (b) Total relative intensity increase after 1200 s compared to the initial peak intensity for the reference samples and the MA^0 treated samples after recrystallization at 80 and 90 °C. (c) Total shift of the peak position after 1200 s of continuous illumination. (d) and (e) Time-resolved photoluminescence (TRPL) of the reference and MA^0 treated films, before and after 1200 s of continuous illumination.

upon illumination. Iodine ions, in particular, have been shown to migrate away from the site of illumination, removing defects and, thus, defect states on their way.[50] This reduces trap-assisted non-radiative recombination channels and the PL intensity increases. Furthermore, it has been shown that defect states are deactivated by photoexcited carriers more effectively in the presence of oxygen.[51–53]

Both mechanisms have in common that pre-existing defect states in the film are deactivated through illumination. The extent of this effect is, therefore, inherently coupled to the number of trap states present in the material previous to illumination. We can thus conclude that the reduced light-soaking induced increase in PL intensity indicates a lower trap density after MA^0 treatment. This finding is consistent with the drastically increased XRD intensity, indicating a higher degree of order in the film, and the reduced amount of boundaries and boundary defects, due to the increased grain size.

The observed shift in peak position is not commonly observed in light-soaking experiments.[50,51,53,54] This indicates that chemical changes, such as phase segregation, are induced upon illumination in this particular mixed perovskite. As this behavior is less pronounced after MA^0 treatment, the chemical phase stability is likely improved during the recrystallization process.

We further conducted time-resolved photoluminescence (TRPL) measurements of our ITO/SnO_2/perovskite samples before and after 1200 s of continuous illumination. Note that the fabrication of identical films on a different, non-conducting substrate would severely limit comparability due to the strong influence of the substrate material on the resulting film properties during recrystallization. The resulting decay curves are shown in Figs. 3(d)

and 3(e) for a reference and a 90 °C sample. The 80 °C samples show the same behavior as the 90 °C sample, as shown in Fig. S12. The effective lifetimes τ have been extracted from biexponential fits to the data (see the supplementary material, Table SV). It is apparent that the carrier lifetime of the reference film increases drastically from 40 to 240 ns after prolonged illumination, while the decay time remains virtually unchanged in the MA^0 treated samples.

This increase in lifetime is usually observed after light-soaking[50,51,54] and is attributed to the same mechanism as the increase in intensity. Defect states are deactivated, leading to reduced trap-assisted recombination, increasing the total charge carrier lifetime. In our samples, we assume both the PL quenching due to charge transfer at the SnO_2 interface and trap-mediated nonradiative recombination to impact the carrier lifetime.

In the MA^0 treated samples, the light-soaking induced changes in the trap density evidently do not affect the effective lifetime. Efficient quenching at the SnO_2/perovskite interface is the dominant process before and after light-soaking. In contrast, the lifetimes increased sixfold after illumination in the reference sample. The light-induced reduction in trap states notably affects recombination dynamics, implying that trap-assisted recombination plays a substantial role in the recombination dynamics in these films. In addition, the long lifetime after illumination, which is not reduced by quenching at the SnO_2 interface, suggests inferior charge transfer into the electron transport layer before MA^0 treatment. Overall, the TRPL measurements, thus, indicate lower trap densities and improved charge extraction at the SnO_2 interface after MA^0 treatment.

To further corroborate our hypothesis of fewer defects in the films after MA^0 treatment, we performed SCLC measurements and extracted the trap densities. For this purpose, we prepared electron-only devices in the configuration ITO/SnO$_2$/perovskite/[6,6]-phenyl-C$_{61}$-butyric acid methyl ester (PCBM)/2,9-dimethyl-4,7-diphenyl-1,10-phenanthroline (BCP)/silver (Ag), as sketched in Fig. 4(a).

The theory of SCLC measurements suggests that the current J through the device is proportional to the voltage V for low voltages, $J \propto V$. Once the bias reaches the trap-filled limit at V_{TFL}, i.e., when enough charges are injected into the layer to fill the traps that are limiting the transport, the current rises sharply. Above V_{TFL}, in the space-charge limited region, the current follows a square law ($J \propto V^2$).[55,56] The trap density is given by[55]

$$N_T = V_{TFL} \cdot \frac{2\varepsilon\varepsilon_0}{ed^2} \qquad (2)$$

using the measured values for V_{TFL}, the vacuum permittivity ε_0, the perovskite dielectric constant ε, the films thickness d, and the elementary charge e. A film thickness $d = 370$ nm was measured in cross-sectional SEM (see Fig. S13). The dielectric constant was taken as $\varepsilon = 65$, a value within the range reported for perovskites.[57,58]

Note that we have only extracted the electron trap density here, as the fabrication of hole-only devices would require the deposition and MA^0 treatment of equivalent perovskite films on a different p-type substrate layer. As mentioned above, the underlying surface sensitively impacts the resulting perovskite morphologies, especially after the MA^0 treatment, compromising comparability between both approaches.

Exemplary SCLC curves are shown in Fig. 4(b). Evidently, the transition voltage V_{TFL} shifts to lower values in the MA^0 treated films.

Note that the current density measured for the 80 °C sample is approximately two orders of magnitude higher below V_{TFL}. Considering the differences in film morphology in the SEM images from Fig. 1, we may explain this observation as follows: The 80 °C films tend to exhibit holes and gaps at the GBs. In these areas, the PCBM layer directly contacts SnO$_2$, resulting in a locally shorted circuit. The SCLC measurements are performed with an active area of roughly 0.133 cm^2, effectively integrating over the entire device area. The current density contains contributions from the gaps, increasing the overall current density. The perovskite, however, does exhibit SCLC behavior, which leads to the abrupt current rise at V_{TFL}.

We extracted the V_{TFL} from multiple measurements and calculated the electron trap density according to Eq. (2). Boxplots of the resulting values are shown in Fig. 4(c), allowing the two following observations: First, the median trap density drops from 8.145×10^{16} to 4.309×10^{16} cm^{-3} and 4.151×10^{16} cm^{-3} after MA^0 treatment at 80 and 90 °C, respectively, confirming our previous hypothesis.

Second, the distribution is much wider for the reference films than the recrystallized ones. The liquefaction and recrystallization steps effectively reset the film formation. Consequently, the new film properties depend only on this step, in contrast to the multiple steps and factors that influence the formation of the reference films during deposition. One can therefore infer that the MA^0 treatment leads to an improvement in reproducibility.

From the conjunction of PL and SCLC measurements, we conclude that the trap density decreases after recrystallization as the improved crystallinity and the enlarged grains lead to fewer defects in the bulk and at the GBs.

V. SPATIALLY RESOLVED CONDUCTIVITY

To further understand the defects and spatially resolved electronic properties, we measured the local current by conductive atomic force microscopy (c-AFM). Figures 5(a)–5(c) show the topology of the non-treated and MA^0 treated perovskite films. While the reference perovskite film features the typical small crystallites with grain sizes in the range of a few hundred nanometers, the MA^0 treated films exhibit domains with sizes exceeding several tens of micrometers. The MA^0 treated perovskite films also show a smaller root mean square roughness (16 nm for both 80 and 90 °C samples) than the non-treated counterparts (18.21 nm).

c-AFM maps of the three perovskite films [Figs. 5(d)–5(f)] show clear differences in the local electronic properties. A comparison of spatial surface current maps of perovskite films measured in the dark and under illumination (Figs. S14–S21) shows a manifold increase in current upon illumination. Note that the light intensity that was applied to the reference perovskite films saturates the current value when illuminating the MA^0 treated perovskite films. Therefore, lower intensities were used in the measurements of the
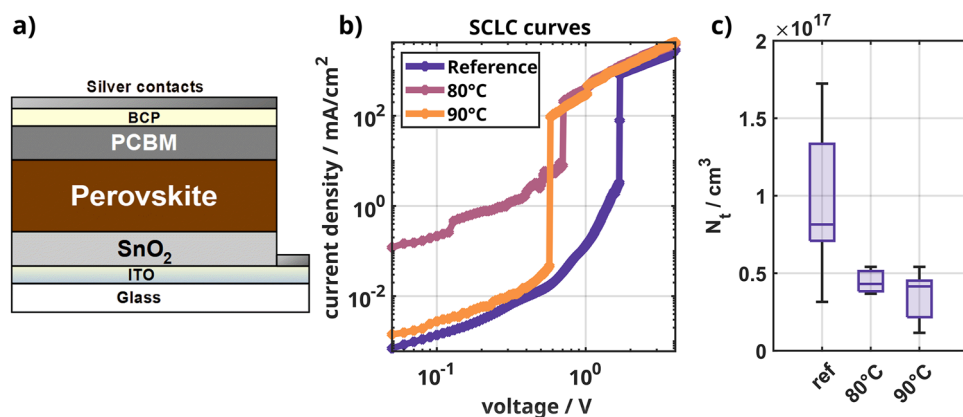

FIG. 4. (a) Architecture of the electron-only devices used for SCLC measurements. (b) Exemplary SCLC J–V curves of the reference device and MA^0 treated devices after recrystallization at 80 and 90 °C. It is apparent that the V_{TFL} shifts to lower voltages in the MA^0 treated films. (c) Extracted electron trap densities for the three types of devices.
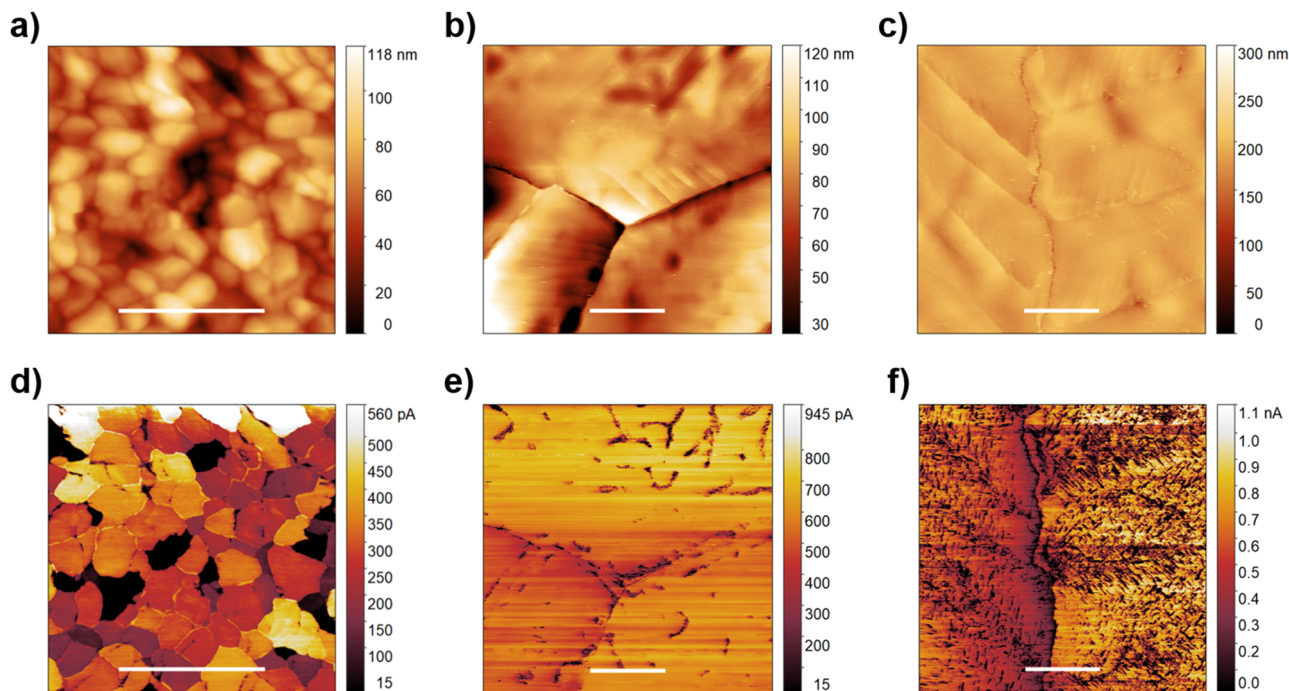
FIG. 5. (a)–(c) AFM topographies of the reference sample (scale bar 1 μm) as well as the 80 and 90 °C MA^0 treated samples (scale bars 5 μm), respectively. (d)–(f) Corresponding c-AFM maps under illumination of the reference sample as well as the 80 and 90 °C MA^0 treated samples.

recrystallized films. Clearly, the MA^0 treated perovskite films show a significantly higher local current than their non-treated reference counterpart, despite much lower illumination intensities. After recrystallization, the films exhibit a lower defect density, leading to a less recombination and, thus, a higher current. The 90 °C perovskite film shows the highest spatial current, which is indicative of the highest surface conductivity.

Another notable feature in the c-AFM maps of three films is the presence of distinct dark regions in the reference perovskite film, which is attributed to non-perovskite lead(II) iodide (PbI$_2$) phases that can be formed during the annealing process.[59,60] These features are absent in the recrystallized films, suggesting an improved spatial homogeneity.

Both the 80 and 90 °C perovskite films show a drop in current at the GBs. Notably, the current in the 90 °C sample drops at the distinct crack-like GB, but not at the line-like features within the large perovskite domains (see Fig. S22, profiles 3 and 4). This suggests that not all visible boundaries are equivalent and only some of them are detrimental for charge transport across the perovskite film.

In contrast to the MA^0 treated films, we note a *higher* current at the GBs in the reference perovskite film (Fig. S20). The c-AFM image of the same sample in the dark does not show this trend, suggesting that this effect is related to charge accumulation. Similar observations of higher currents at the GBs have been made in several publications.[61–63] It was suggested that the GBs act as effective charge dissociation centers when an applied bias overcomes the barrier height created by the boundary. A higher spatial current at the GB

compared to within the grain has also been experimentally demonstrated in a previous report,[64] suggesting that the defects formed were shallow in nature and play a beneficial role in charge transport. The different spatial surface current profiles of non-treated vs MA^0 treated perovskite films suggest that charge carriers dissociate at the GBs in the former, while efficient charge dissociation and transport take place within the grains in the latter.

VI. APPLICATION IN PHOTODETECTORS

To investigate how these improvements in the film structure translate to the performance of non-treated vs MA^0 treated perovskite films in device applications, photodetectors were fabricated in the configuration ITO/SnO$_2$/perovskite/molybdenum trioxide (MoO$_3$) (10 nm)/gold (Au) (100 nm). Figures 6(a)–6(c) show the current–voltage (I–V) curves of the three devices at various illumination intensities. It is evident that the photocurrent increases with the illumination intensity. The maximum values at 350 mW cm^{-2} and a bias of 2 V are 82 and 75 nA for the 80 and 90 °C samples, respectively. The current passing through the reference device is much smaller (2 nA) under the same measurement conditions. We further note that the magnitudes of the current increase under illumination (on/off ratio) are 18, 260, and 230 for the reference, 80, and 90 °C samples, respectively. It is, therefore, an order of magnitude higher for the MA^0 treated samples, with the 80 °C samples showing the most pronounced increase. We attribute the higher currents and on/off ratios of the MA^0 treated samples to the lower defect density.
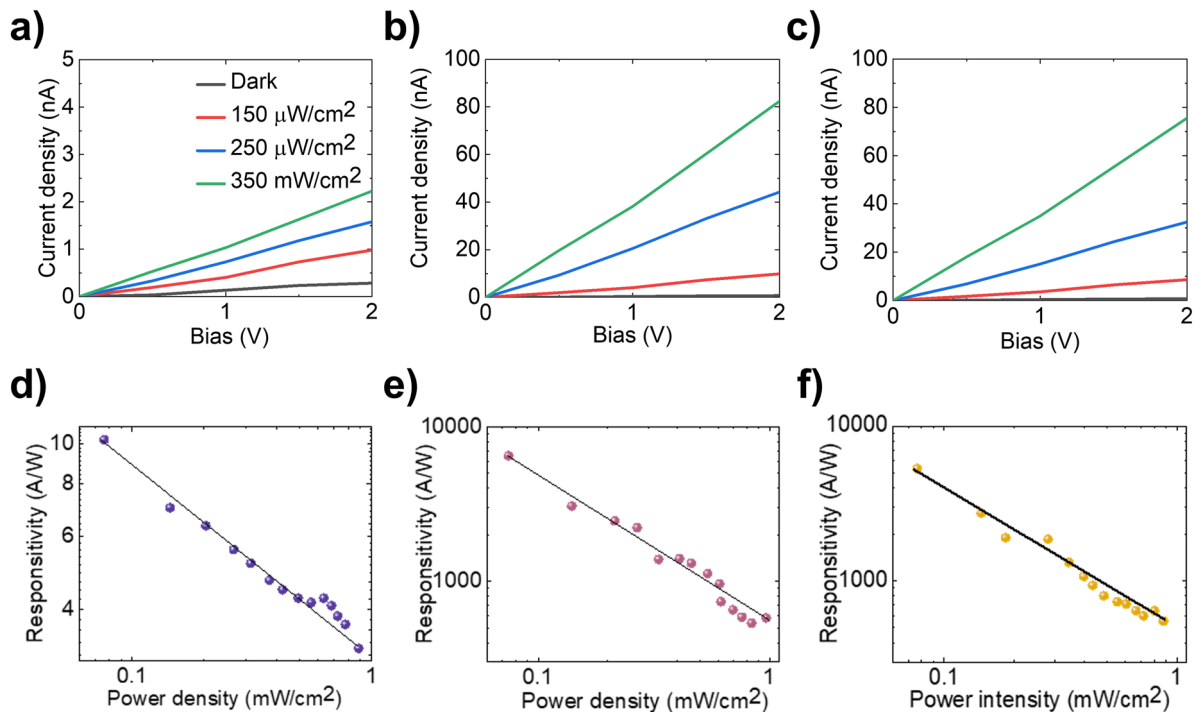
FIG. 6. (a)–(c) Photocurrent response of the three devices [reference in (a), 80 °C in (b), and 90 °C in (b)] at various excitation power densities and applied biases under 515 nm laser irradiation. (d)–(f) Responsivity as a function of power density of the reference in (d), 80 °C in (e), and 90 °C in (f) at 1 V.

In Figs. 6(d)–6(f), the responsivities are plotted over the power density, with the best performing device (MA^0 treated at 80 °C) demonstrating a responsivity of about 580 A W^{-1} at 1 mW cm^{-2}, which is nearly 200 times higher than the reference device (3 A W^{-1} at 1 mW cm^{-2}). The device MA^0 treated at 90 °C also demonstrated a similar responsivity value of 551 A W^{-1} at 1 mW cm^{-2} (under 515 nm laser illumination). The detectivity is a further important parameter to characterize the performance of photodetectors. The specific detectivity is given by[4]

$$D^* = A^{1/2} \cdot \frac{R}{(2 \cdot e \cdot I_{dark})^{1/2}}, \tag{3}$$

where A corresponds to the device area, R is the responsivity, e denotes the elementary charge, and I_{dark} refers to the dark current passing through the device. The specific detectivities of both MA^0 treated devices at 80 and 90 °C are 4.19×10^{11} and 3.94×10^{11} Jones, respectively, which are about two orders of magnitude higher than that of the non-treated reference device ($D^* = 3.36 \times 10^9$ Jones). Further important characteristics of photodetectors are the rise and fall times, which are directly related to the trap distribution in the perovskite films (in the bulk or at the surface). The rise time refers to the time required for the photodetector to rise from 10% to 90% of its full photocurrent value upon illumination. Analogously, the fall time is the time it takes for the photocurrent to drop from 90% to 10% when the laser is switched off. As shown in Figs. 7(a)–7(c), the rise and fall times for the MA^0 treated devices are in the range of a few

microseconds. In contrast, the response times of the reference films are several orders of magnitude longer (≈0.1 s). Such a significant increase in the response time of the MA^0 treated perovskite films, despite the similar device architecture, shows the beneficial effect of the reduced defect density after MA^0 treatment. The possibility of electron trapping and de-trapping at the defect sites is lowered, increasing the rise/fall times drastically.

Finally, Figs. 7(d)–7(f) show the normalized responsivity as a function of the laser modulation frequency. These figures illustrate that the 3 dB bandwidth for the MA^0 treated perovskite film-based photodetectors is above 450 kHz, which is significantly higher than the reference device (0.25 kHz). Notably, the 90 °C device shows a higher speed compared to the 80 °C device despite the lower sensitivity of the former, which could be beneficial for low-power, high-bandwidth on-chip interconnects in integrated electronics. Note that although only selected devices are shown here, the results have proven to be very reproducible across multiple films and devices.

In conclusion, the photodetectors employing MA^0 treated perovskite films show significantly better device performances than the non-treated reference devices. We believe this enhanced performance is due to two reasons: First, the larger grain size and low trap density (calculated from the SCLC measurement) of the MA^0 treated perovskite morphologies, and second, a lower trap filling effect in the MA^0 treated films as compared to a reference non-treated perovskite film, as evidenced in our TRPL data and the comparison of the rise/fall times.
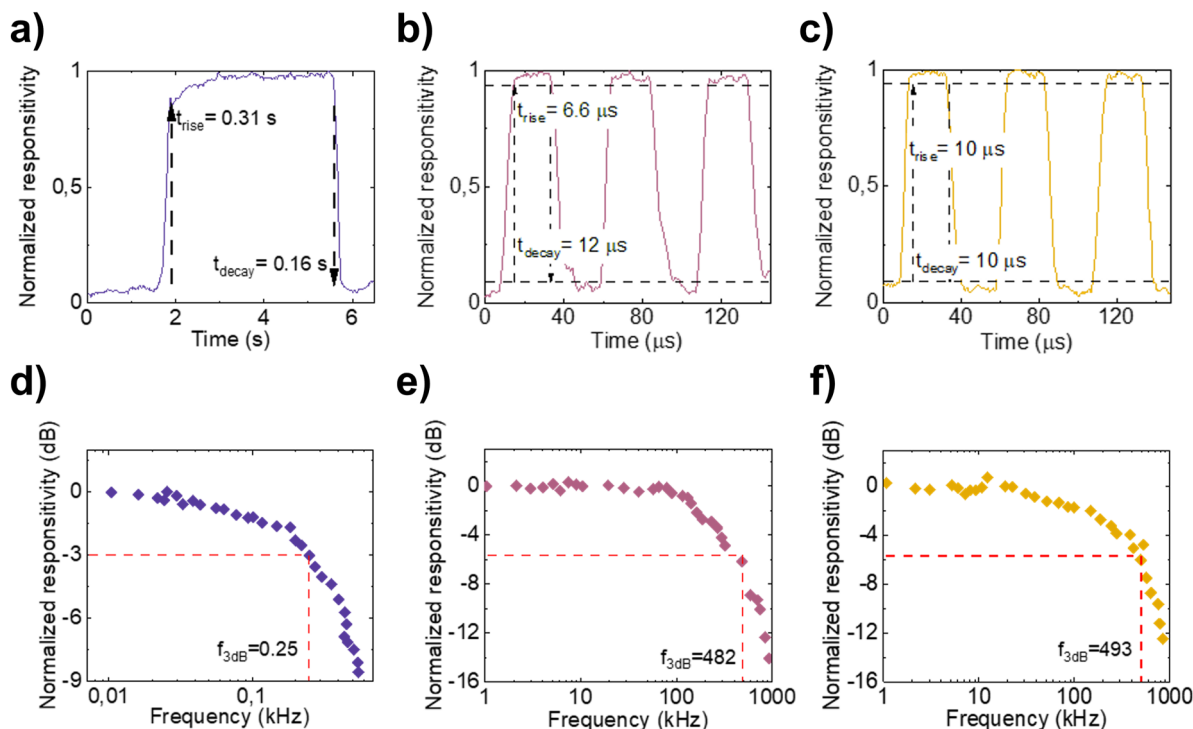
FIG. 7. (a)–(c) The rise and fall times of the three perovskite photodetectors [reference in (a), 80 °C in (b), and 90 °C in (c)] at 2 V. The incident laser light was switched on and off with a frequency of 0.125 and 15 kHz for the reference and MA^0 treated devices, respectively. (d)–(f) The normalized responsivity as a function of frequency at 2 V for the reference sample in (d), the 80 °C in (e), and 90 °C in (f) samples.

VII. CONCLUSION

In this work, we present a MA^0 treatment protocol for the reliable and adaptable fabrication of highly crystalline perovskite films. By recrystallizing samples under MA^0 atmosphere at elevated temperatures, we achieve large domains of uniform orientation. In consequence, the MA^0 treatment results in significantly increased crystallinities. XRD studies also show a peak shift, which we attribute to the exchange of FA^+ for MA^+ in the lattice of the mixed-cation perovskite with an additional strain-induced component. The implications of this change in compositions are unclear, but it could be prevented by replacing MA^0 with another amine, such as ammonia,[65] which cannot be permanently integrated into the perovskite structure. PL studies show that light-soaking induced defect-curing is reduced after MA^0 treatment, indicating a decreased trap density, which was confirmed by SCLC measurements. Through c-AFM measurements, we show that this improvement results in a higher conductivity and a lower charge accumulation at the grain boundaries, indicating efficient charge dissociation and transport within the grains.

Finally, we demonstrate that these properties translate into strongly improved detectivities and response times when applied in photodetection devices. The use of such MA^0 treatments could be highly beneficial for future applications, e.g., for the further development of perovskite-based photodetectors and perovskite solar cells,

where a low trap density is a prerequisite to achieving highly efficient and stable devices.

VIII. METHODS

Sample fabrication. All samples were prepared on *Lumtec* ITO glass sheets. Prior to layer deposition, the substrates were cleaned in an ultrasonic bath for 30 min each in deionized (DI) water with detergent, DI water, acetone and isopropanol, respectively. This was followed by 7 min oxygen plasma treatment. The SnO_2 precursor was prepared via the reflux method,[66] which involves heating a 0.1M solution of tin(II) chloride dihydrate ($SnCl_2 \cdot 2H_2O$) (*Alfa Aesar*) in a 1:19 mixture of butanol (*Sigma-Aldrich*) and DI water at 110 °C for 4 h. SnO_2 layers were obtained via spin-coating the mixture solution at 2000 rpm for 30 s and annealing for 60 min at 130 °C. For the perovskite precursor, 507.1 mg of PbI_2 (*TCI*) and 73.4 mg lead(II) bromide ($PbBr_2$) (*Sigma-Aldrich*) were dissolved in in 1 ml 1:4 dimethyl sulfoxide (DMSO):*N,N*-dimethylformamide (DMF) (both anhydrous, *Sigma-Aldrich*). This solution was used to additionally dissolve 22.4 mg methylammonium bromide (MaBr) (*Sigma-Aldrich*) and 172 mg formamidinium iodide (FAI) (*Greatcell Solar*). Finally, 53 μl of 389.7 mg ml^{-1} cesium iodide (CsI) (*Sigma-Aldrich*) in DMSO was added. The precursor was spin-coated at 1000 rpm for 10 s and then at 6000 rpm for 20 s.

250 μl of chlorobenzene (CB) (anhydrous, *Sigma-Aldrich*) was dropped onto the sample roughly 5 s before the end of the program as anti-solvent, and the sample was transferred onto a hotplate at 100 °C for 60 min annealing.

The MA^0 treatment was performed with a MA^0 partial pressure of 230 mbar during exposure. The film was kept under this atmosphere for 10 s before pumping to $p_0 = 600$ mbar, thus reducing the MA^0 partial pressure to roughly 170 mbar during recrystallization. See the supplementary material for more details. The process was observed from above with a *DinoLite AF4915ZTL* microscope camera. To measure the recrystallization temperatures shown in Fig. 1(a), untreated triple-cation perovskite films were exposed to a fixed MA^0 partial pressure p_{MA} at different temperatures, until the highest temperature at which the film still turned into the transparent liquid was found and determined to be T_{rec}.

The electron-only devices for SCLC measurements were finalized by spin-coating 20 mg ml^{-1} [60]-PCBM (99% purity, *Ossila*) in CB (*Sigma-Aldrich*) at 2000 rpm for 90 s, annealing at 70 °C for 10 min, and spin-coating 0.5 mg ml^{-1} BCP in ethanol (anhydrous, *Sigma-Aldrich*) for 30 s at 5000 rpm. Finally, a 100 nm thick Ag contact layer was evaporated. For photodetectors, 10 nm of MoO_3 followed by 100 nm of Au was evaporated on top of the perovskite layers. All film deposition steps (except the initial SnO_2 layer), contact evaporation, and the SCLC characterization were performed in inert nitrogen atmosphere.

Characterization. SEM imaging and electron backscatter diffraction (EBSD) studies were performed on a Zeiss Gemini 500 electron microscope. XRD measurements were performed on a *Bruker D8* x-ray diffractometer. The XPS analyses were carried out in a Thermo Scientific Multilab 2000 spectrometer fitted with a dual-anode x-ray source (Mg K alpha and Al K alpha with photon energies 1253.6 and 1486.7 eV, respectively) and a 110 mm hemispherical sector analyzer. Survey spectra and high resolution core level spectra were measured using the Mg k-alpha x-ray source at 400 W and 15 eV pass energy. Each sample was supported on a sample stub using a copper double adhesive tape before entering to FEAL chamber. All the measurements were made on as-received samples and no surface sputtering with Ar ions was done. The core level spectra were fitted and deconvoluted using the CASA XPS software package. PL and TRPL were measured on a *PicoQuant FluoTime300* fluorescence spectrometer using a 405 nm excitation laser. The repetition rate was set to 40 MHz for steady state- and 1 MHz for time-resolved measurements. To block stray laser light, a 455 nm longpass filter was placed between the sample and the detector. For long-term illumination, the steady state settings were used. UV–vis absorbance spectroscopy was performed with a CARY 5000 UV/Vis spectrometer by Agilent Technologies. The conductive AFM measurements were carried out using a MFP-3D infinity atomic force microscope from Asylum Research (Oxford Instruments) in a nitrogen filled glovebox where the humidity and the oxygen levels are below 0.4% and 0.1%, respectively. The conductive AFM was performed with the platinum–iridium coated SCM PIT-V2 cantilevers (Bruker) with spring constants of 3 mN nm^{-1} and a free resonance of 75 kHz. The cantilever holder for the conductive AFM measurement was an ORCA cantilever holder from Asylum Research with 2 nA N^{-1} current amplification factor. The applied voltage was 750 mV for each sample. The photocurrent measurements were performed via an external light source with an adjustable light intensity. Photodetector

characterization was performed using a probe station under ambient condition. A red light-emitting diode (LED) (*OVLBx4C7 Series, OPTEK Technology, Inc.*, main wavelength: 514 nm) was mounted above the photodetector, which was controlled by a *Keysight B2902A* precision source/measure unit in the current source mode. The optical power density that reached the sample surface was determined by measuring a commercial reference photodiode (*PDB-C154SM, Luna Optoelectronics*) with a responsivity of ≈0.3 A W^{-1} at 514 nm.

SUPPLEMENTARY MATERIAL

See the supplementary material for more details on the MA^0 treatment process and process pressures, further structural characterization, further PL and UV–vis absorbance measurements, the Williamson–Hall analysis, XPS measurements, and more detailed AFM and c-AFM maps.

ACKNOWLEDGMENTS

AUTHOR DECLARATIONS

Conflict of Interest

The authors have no conflicts to disclose.

Author Contributions

Emilia R. Schütz: Conceptualization (equal); Data curation (lead); Investigation (equal). **Azhar Fakharuddin**: Conceptualization (equal); Investigation (equal); Supervision (equal). **Yenal Yalcinkaya**: Data curation (supporting). **Efrain Ochoa-Martinez**: Data curation (supporting). **Shanti Bijani**: Data curation (supporting). **Abd. Rashid bin Mohd Yusoff**: Data curation (supporting). **Maria Vasilopoulou**: Data curation (supporting). **Tobias Seewald**: Data curation (equal); Investigation (equal). **Ullrich Steiner**: Project administration (supporting). **Stefan A. L. Weber**: Project administration (supporting); Supervision (supporting). **Lukas Schmidt-Mende**: Conceptualization (equal); Project administration (equal); Resources (lead); Supervision (lead).

DATA AVAILABILITY

The data that support the findings of this study are available from the corresponding author upon reasonable request.

REFERENCES

[1] P. Roy, N. Kumar Sinha, S. Tiwari, and A. Khare, Solar Energy **198**, 665 (2020).
[2] X.-K. Liu, W. Xu, S. Bai, Y. Jin, J. Wang, R. H. Friend, and F. Gao, Nat. Mater. **20**, 10 (2021).

[3] L. Basiricò, A. Ciavatti, and B. Fraboni, Adv. Mater. Technol. 6, 2000475 (2021).

[4] C. Xie, C. K. Liu, H. L. Loi, and F. Yan, Adv. Funct. Mater. 30, 1903907 (2020).

[5] K. X. Steirer, P. Schulz, G. Teeter, V. Stevanovic, M. Yang, K. Zhu, and J. J. Berry, ACS Energy Lett. 1, 360 (2016).

[6] D. Meggiolaro, S. G. Motti, E. Mosconi, A. J. Barker, J. Ball, C. Andrea Riccardo Perini, F. Deschler, A. Petrozza, and F. De Angelis, Energy Environ. Sci. 11, 702 (2018).

[7] X. Zhang, M. E. Turiansky, and C. G. Van de Walle, J. Phys. Chem. C 124, 6022 (2020).

[8] J. H. Noh, S. H. Im, J. H. Heo, T. N. Mandal, and S. I. Seok, Nano Lett. 13, 1764 (2013).

[9] A. Amat, E. Mosconi, E. Ronca, C. Quarti, P. Umari, M. K. Nazeeruddin, M. Grätzel, and F. De Angelis, Nano Lett. 14, 3608 (2014).

[10] G. E. Eperon, S. D. Stranks, C. Menelaou, M. B. Johnston, L. M. Herz, and H. J. Snaith, Energy Environ. Sci. 7, 982 (2014).

[11] A. Ummadisingu, S. Meloni, A. Mattoni, W. Tress, and M. Grätzel, Angew. Chem., Int. Ed. 60, 21368 (2021).

[12] C. Wehrenfennig, G. E. Eperon, M. B. Johnston, H. J. Snaith, and L. M. Herz, Adv. Mater. 26, 1584 (2014).

[13] H. Oga, A. Saeki, Y. Ogomi, S. Hayase, and S. Seki, J. Am. Chem. Soc. 136, 13818 (2014).

[14] Z. Fan, K. Sun, and J. Wang, J. Mater. Chem. A 3, 18809 (2015).

[15] A. Dubey, N. Adhikari, S. Mabrouk, F. Wu, K. Chen, S. Yang, and Q. Qiao, J. Mater. Chem. A 6, 2406 (2018).

[16] S. Sánchez, L. Pfeifer, N. Vlachopoulos, and A. Hagfeldt, Chem. Soc. Rev. 50, 7108 (2021).

[17] F. Wang, S. Bai, W. Tress, A. Hagfeldt, and F. Gao, npj Flexible Electron. 2, 22 (2018).

[18] Y. Lei, Y. Xu, M. Wang, G. Zhu, and Z. Jin, Small 17, 2005495 (2021).

[19] E. Aydin, M. De Bastiani, and S. De Wolf, Adv. Mater. 31, 1900428 (2019).

[20] A.-F. Castro-Méndez, J. Hidalgo, and J.-P. Correa-Baena, Adv. Energy Mater. 9, 1901489 (2019).

[21] N. Phung and A. Abate, Small 14, 1802573 (2018).

[22] W. Nie, H. Tsai, R. Asadpour, J.-C. Blancon, A. J. Neukirch, G. Gupta, J. J. Crochet, M. Chhowalla, S. Tretiak, M. A. Alam, H.-L. Wang, and A. D. Mohite, Science 347, 522 (2015).

[23] K. Liao, C. Li, L. Xie, Y. Yuan, S. Wang, Z. Cao, L. Ding, and F. Hao, Nano-Micro Lett. 12, 156 (2020).

[24] X. Ren, Z. Yang, D. Yang, X. Zhang, D. Cui, Y. Liu, Q. Wei, H. Fan, and S. F. Liu, Nanoscale 8, 3816 (2016).

[25] Z. Yang, Z. Deng, X. Zhang, S. Wang, H. Chen, S. Yang, J. Khurgin, N. X. Fang, X. Zhang, and R. Ma, Adv. Mater. 30, 1704333 (2018).

[26] Z. Li, X. Liu, C. Zuo, W. Yang, and X. Fang, Adv. Mater. 33, 2103010 (2021).

[27] P. Shi, Y. Ding, Y. Ren, X. Shi, Z. Arain, C. Liu, X. Liu, M. Cai, G. Cao, M. K. Nazeeruddin, and S. Dai, Adv. Sci. 6, 1901591 (2019).

[28] Z. Yang, Q. Xu, X. Wang, J. Lu, H. Wang, F. Li, L. Zhang, G. Hu, and C. Pan, Adv. Mater. 30, 1802110 (2018).

[29] F. Zhang, J. Song, L. Zhang, F. Niu, Y. Hao, P. Zeng, H. Niu, J. Huang, and J. Lian, J. Mater. Chem. A 4, 8554 (2016).

[30] M. Hu, C. Bi, Y. Yuan, Y. Bai, and J. Huang, Adv. Sci. 3, 1500301 (2016).

[31] Q. Lian, M. Z. Mokhtar, D. Lu, M. Zhu, J. Jacobs, A. B. Foster, A. G. Thomas, B. F. Spencer, S. Wu, C. Liu, N. W. Hodson, B. Smith, A. Alkaltham, O. M. Alkhudhari, T. Watson, and B. R. Saunders, ACS Appl. Mater. Interfaces 12, 18578 (2020).

[32] T. Seewald, E. R. Schütz, C. Ebenhoch, and L. Schmidt-Mende, J. Phys.: Energy 2, 021001 (2020).

[33] Z. Zhou, Z. Wang, Y. Zhou, S. Pang, D. Wang, H. Xu, Z. Liu, N. P. Padture, and G. Cui, Angew. Chem., Int. Ed. 54, 9705 (2015).

[34] S. R. Raga, Y. Jiang, L. K. Ono, and Y. Qi, Energy Technol. 5, 1750 (2017).

[35] D. Bogachuk, L. Wagner, S. Mastroianni, M. Daub, H. Hillebrecht, and A. Hinsch, J. Mater. Chem. A 8, 9788 (2020).

[36] X. Huang, R. Chen, G. Deng, F. Han, P. Ruan, F. Cheng, J. Yin, B. Wu, and N. Zheng, J. Am. Chem. Soc. 142, 6149 (2020).

[37] Y. Jiang, E. J. Juarez-Perez, Q. Ge, S. Wang, M. R. Leyden, L. K. Ono, S. R. Raga, J. Hu, and Y. Qi, Mater. Horiz. 3, 548 (2016).

[38] D. L. Jacobs and L. Zang, Chem. Commun. 52, 10743 (2016).

[39] H. Fan, F. Li, P. Wang, Z. Gu, J.-H. Huang, K.-J. Jiang, B. Guan, L.-M. Yang, X. Zhou, and Y. Song, Nat. Commun. 11, 5402 (2020).

[40] A. Günzler, E. Bermúdez-Ureña, L. A. Muscarella, M. Ochoa, E. Ochoa-Martínez, B. Ehrler, M. Saliba, and U. Steiner, ACS Appl. Mater. Interfaces 13, 6854 (2021).

[41] G. E. Eperon, V. M. Burlakov, P. Docampo, A. Goriely, and H. J. Snaith, Adv. Funct. Mater. 24, 151 (2014).

[42] C. Zhu, X. Niu, Y. Fu, N. Li, C. Hu, Y. Chen, X. He, G. Na, P. Liu, H. Zai, Y. Ge, Y. Lu, X. Ke, Y. Bai, S. Yang, P. Chen, Y. Li, M. Sui, L. Zhang, H. Zhou, and Q. Chen, Nat. Commun. 10, 815 (2019).

[43] G. E. Eperon, D. Bryant, J. Troughton, S. D. Stranks, M. B. Johnston, T. Watson, D. A. Worsley, and H. J. Snaith, J. Phys. Chem. Lett. 6, 129 (2015).

[44] Z. Zhao, F. Gu, Y. Li, W. Sun, S. Ye, H. Rao, Z. Liu, Z. Bian, and C. Huang, Adv. Sci. 4, 1700204 (2017).

[45] Y. Zong, Y. Zhou, M. Ju, H. F. Garces, A. R. Krause, F. Ji, G. Cui, X. C. Zeng, N. P. Padture, and S. Pang, Angew. Chem., Int. Ed. 55, 14723 (2016).

[46] Y. Zhou, M. Yang, S. Pang, K. Zhu, and N. P. Padture, J. Am. Chem. Soc. 138, 5535 (2016).

[47] S. Pang, Y. Zhou, Z. Wang, M. Yang, A. R. Krause, Z. Zhou, K. Zhu, N. P. Padture, and G. Cui, J. Am. Chem. Soc. 138, 750 (2016).

[48] C. Li, Y. Zhong, C. A. M. Luna, T. Unger, K. Deichsel, A. Gräser, J. Köhler, A. Köhler, R. Hildner, and S. Huettner, Molecules 21, 1081 (2016).

[49] S. Ghosh, S. K. Pal, K. J. Karki, and T. Pullerits, ACS Energy Lett. 2, 2133 (2017).

[50] D. W. deQuilettes, W. Zhang, V. M. Burlakov, D. J. Graham, T. Leijtens, A. Osherov, V. Bulović, H. J. Snaith, D. S. Ginger, and S. D. Stranks, Nat. Commun. 7, 11683 (2016).

[51] Y. Tian, M. Peter, E. Unger, M. Abdellah, K. Zheng, T. Pullerits, A. Yartsev, V. Sundström, and I. G. Scheblykin, Phys. Chem. Chem. Phys. 17, 24978 (2015).

[52] Y. Tian, A. Merdasa, E. Unger, M. Abdellah, K. Zheng, S. McKibbin, A. Mikkelsen, T. Pullerits, A. Yartsev, V. Sundström, and I. G. Scheblykin, J. Phys. Chem. Lett. 6, 4171 (2015).

[53] X. Fu, D. A. Jacobs, F. J. Beck, T. Duong, H. Shen, K. R. Catchpole, and T. P. White, Phys. Chem. Chem. Phys. 18, 22557 (2016).

[54] K. Handloser, N. Giesbrecht, T. Bein, P. Docampo, M. Handloser, and A. Hartschuh, ACS Photonics 3, 255 (2016).

[55] M. A. Lampert, Phys. Rev. 103, 1648 (1956).

[56] M. A. Lampert and P. Mark, Current Injection in Solids (Academic Press, 1970).

[57] Q. Lin, A. Armin, R. C. R. Nagiri, P. L. Burn, and P. Meredith, Nat. Photonics 9, 106 (2015).

[58] H. S. Jung and N.-G. Park, Small 11, 10 (2015).

[59] Q. Chen, H. Zhou, T.-B. Song, S. Luo, Z. Hong, H.-S. Duan, L. Dou, Y. Liu, and Y. Yang, Nano Lett. 14, 4158 (2014).

[60] S. Gharibzadeh, P. Fassl, I. M. Hossain, P. Rohrbeck, M. Frericks, M. Schmidt, T. Duong, M. R. Khan, T. Abzieher, B. A. Nejand, F. Schackmar, O. Almora, T. Feeney, R. Singh, D. Fuchs, U. Lemmer, J. P. Hofmann, S. A. L. Weber, and U. W. Paetzold, Energy Environ. Sci. 14, 5875 (2021).

[61] J.-J. Li, J.-Y. Ma, Q.-Q. Ge, J.-S. Hu, D. Wang, and L.-J. Wan, ACS Appl. Mater. Interfaces 7, 28518 (2015).

[62] J. S. Yun, A. Ho-Baillie, S. Huang, S. H. Woo, Y. Heo, J. Seidel, F. Huang, Y.-B. Cheng, and M. A. Green, J. Phys. Chem. Lett. 6, 875 (2015).

[63] Y. Kutes, Y. Zhou, J. L. Bosse, J. Steffes, N. P. Padture, and B. D. Huey, Nano Lett. 16, 3434 (2016).

[64] J. Song, Y. Zhou, N. P. Padture, and B. D. Huey, Nat. Commun. 11, 3308 (2020).

[65] X. Y. Feng, K. W. Ng, S. P. Wang, W. Z. Chen, Z. Z. Zhang, W. Chen, Y. Y. Zhao, B. Tu, Z. K. Tang, H. Pan, and Z. B. He, J. Mater. Chem. A 8, 13585 (2020).

[66] C. Chen, Y. Jiang, J. Guo, X. Wu, W. Zhang, S. Wu, X. Gao, X. Hu, Q. Wang, G. Zhou, Y. Chen, J. M. Liu, K. Kempa, and J. Gao, Adv. Funct. Mater. 29, 1900557 (2019).

Supporting Information

Reduced defect density in crystalline halide perovskite films via methylamine
treatment for the application in photodetectors

Emilia R. Schütz,[1] Azhar Fakharuddin,[1] Yenal Yalcinkaya,[2,3] Efrain Ochoa-Martinez,[4]
Shanti Bijani,[5] Abd. Rashid bin Mohd Yusoff,[6] Maria Vasilopoulou,[7] Tobias Seewald,[1]
Ullrich Steiner,[4] Stefan A. L. Weber,[2,3] and Lukas Schmidt-Mende[1]

[1]*Department of Physics, University of Konstanz, D-78457 Konstanz,*
Germany

[2]*Max Planck Institute for Polymer Research, Ackermannweg 10, 55128 Mainz,*
Germany

[3]*Institute of Physics, Johannes Gutenberg University Mainz, Duesbergweg 10-14,*
55128 Mainz, Germany

[4]*Adolphe Merkle Institute, University of Fribourg, Chemin des Verdiers 4, 1700 Fribourg,*
Switzerland

[5]*Unidad de Nanotecnología, Centro de Supercomputador y Bioinnovación SCBI,*
Universidad de Málaga, Calle Severo Ochoa 34, 29590 Campanillas (Málaga),
Spain

[6]*Department of Chemical Engineering, Pohang University of Science*
and Technology (POSTECH) 77 Cheongam-Ro, Nam-Gu, Pohang 37673,
Republic of Korea

[7]*Institute of Nanoscience and Nanotechnology, National Center for*
Scientific Research "Demokritos", 15341, Agia Paraskevi, Attica,
Greece

SETUP AND TREATMENT PROCESS
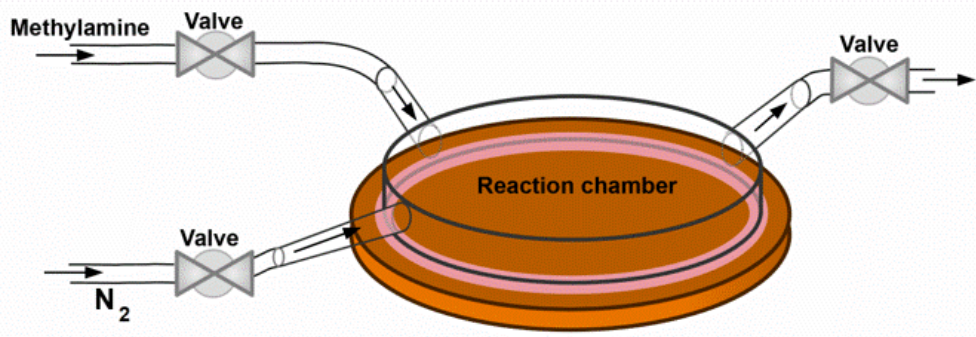
FIG. S1. Schematic of reaction chamber. It can be flushed with controlled amounts of MA0 and N2 and be pumped from the other side. The base is heatable, and optical observation is possible through the top.

Fig. S1 shows a schematic of the central reaction chamber. It consists of a cylindrical glass dome placed directly on a temperature-controlled hotplate. Through the glass top of the chamber, a microscope camera optically tracks the process. The samples rest on a hotplate of temperature T and are, heated from below. Both Methylamine and Nitrogen gas can be let into the chamber via automated valves and Mass Flow Controllers (MFCs). Because the volume V of the chamber is constant, the methylamine partial pressure p_{MA} only depends on the amount of gas let through the MFC and the current temperature. It can, thus, be precisely determined and controlled. Using the gas equation, the methylamine partial pressure can be calculated via:

$$p_{MA} = \frac{nRT}{V} \tag{1}$$

with the temperature T, the chamber volume V, the total amount of MA that is let into the chamber with the MFC in mol, and the gas constant R.

The gas outlet is located opposite the inlets and is also controlled with a valve. It connects to a regulated vacuum pump. The chamber can be pumped to a pre-defined, controlled pressure $p_{vac} < p_0$ lower than atmospheric pressure p_0. Before the treatment process, the chamber filled with nitrogen at this p_0. After the MA^0 gas is let into the chamber, the total pressure is then $p_tot = p_0 + p_{MA}$. To initialize recrystallization, the chamber is once again pumped to p_0. The total remaining MA^0 partial pressure $p_{MA,new}$ during recrystallization is:

$$p_{MA,new} = p_{MA} \cdot \frac{p_0}{p_0 + p_{MA}} \tag{2}$$

119
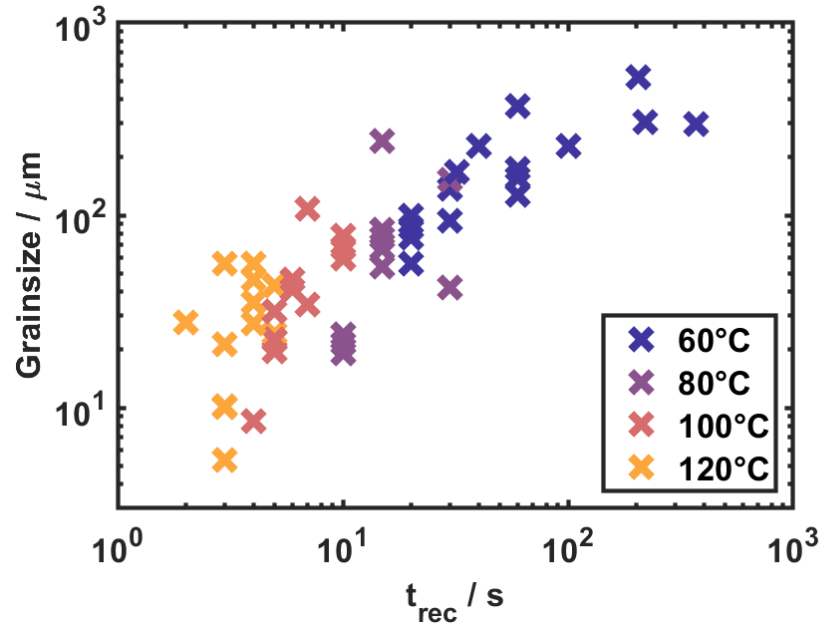
FIG. S2. Mean grain diameters of different MAPbI$_3$ films in dependence of the recrystallization time, i.e., the time it took for the growing domains to cover the entire film. The higher the temperature, the quicker grain growth and the smaller the resulting domains. Note that equivalent behavior is observed for triple-cation films, though the exact recrystallizaiton temperatures vary with composition.
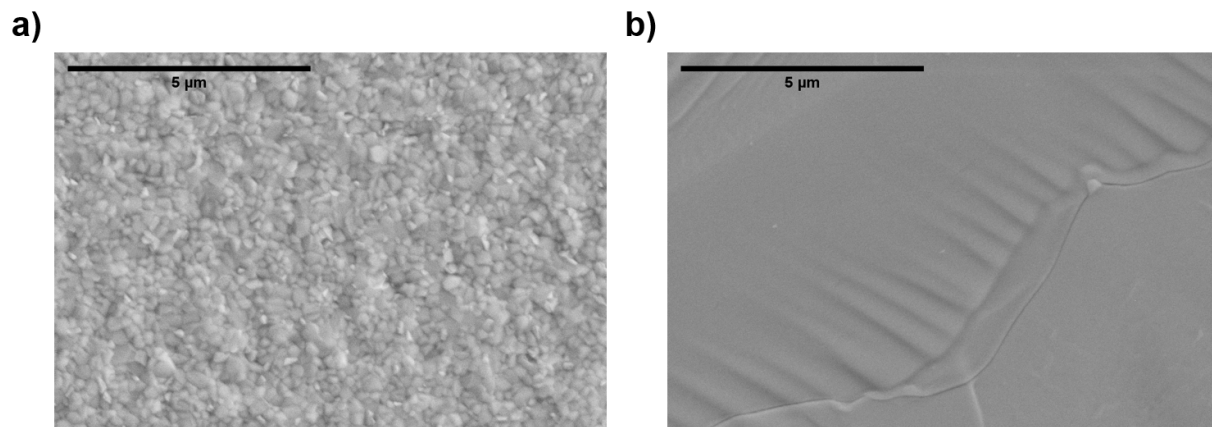
FIG. S3. SEM images of a) a reference film, and b) a 90 °C treated perovskite film. The planes in the samples after treatment appear quite smooth and do not exhibit any substructure comparable to the individual grains of the reference samples.

a) FSD Mixed Image 4

b) IPF Z Color 1

c) IPF Y Color 1

d) IPF X Color 1
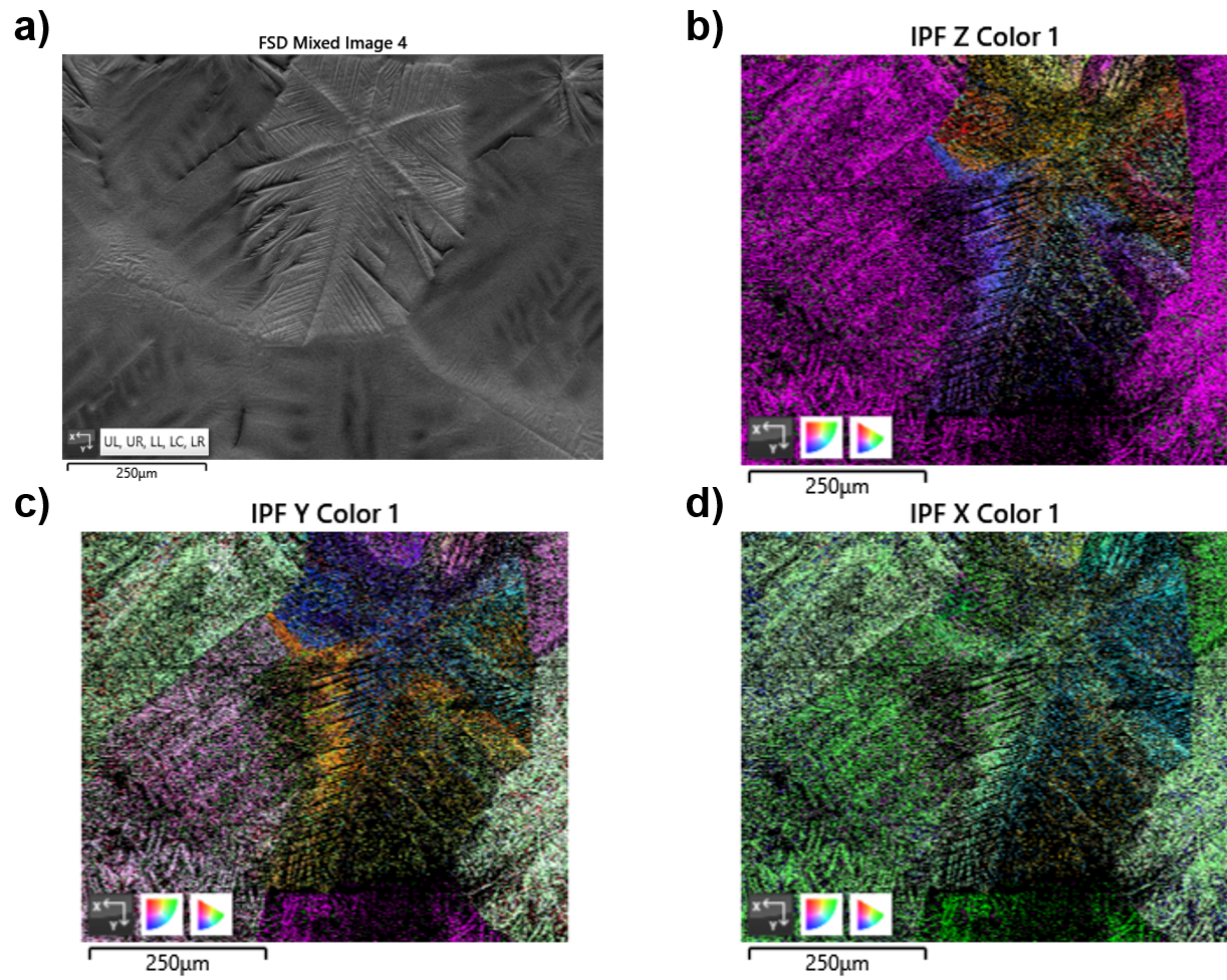
FIG. S4. EBSD maps of a treated perovskite film.
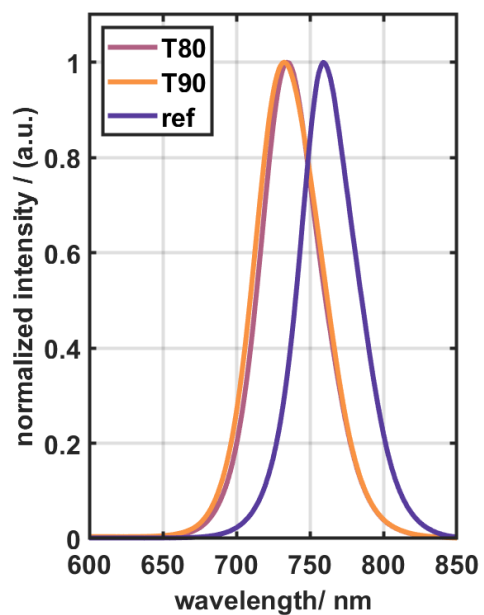
FIG. S5. Normalized PL spectra of the reference, 80 °C, and 90 °C treated samples. The peak position shifts from 760 nm to 734 nm and 732 nm after treatment at 80 °C and 90 °C, respectively.
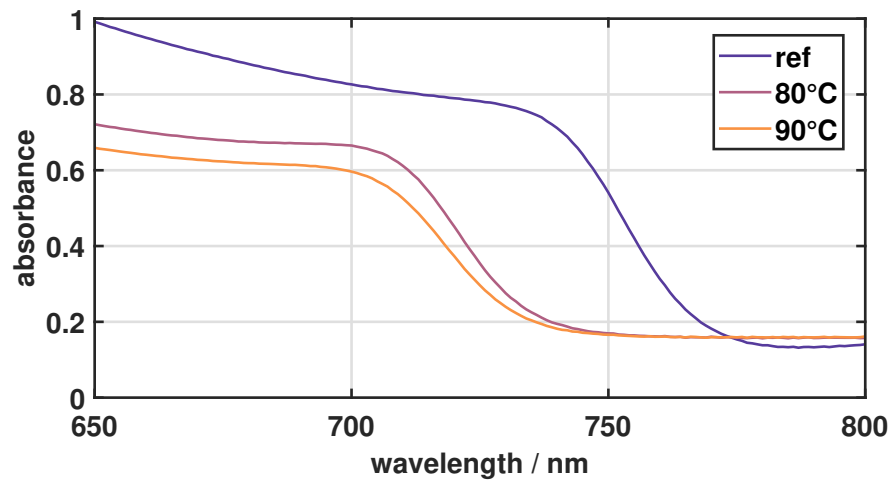
FIG. S6. UV-Vis absorbance measurements on all three groups. The shift in bandgap is clearly visible.

TAUC-PLOTS FOR THE DETERMINATION OF THE OPTICAL BANDGAP
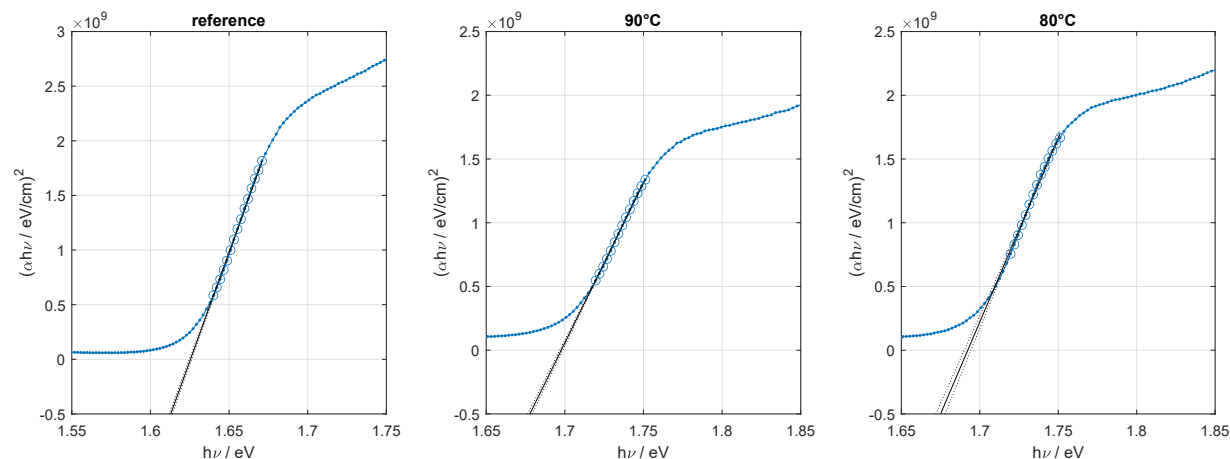
FIG. S7. TAUC-Plot for the determination of the optical bandgap from the UV-Vis measurements on all three groups. The optical bandgaps were calculated from absorbance measurementsusing TAUC plots[1–3]. For this purpose, $(\alpha h v)^2$ was plotted over the photon energy $h v$ in the region of the bandgap, where absorption coefficient α was calculated from the total absorbance assuming a film thickness of 370 nm. A linear fit was applied in this region, where the x-intercept is the calculated value for the optical bandgap.

TABLE SI. Calculated optical bandgaps from TAUC-fits, as well as values for R-squared for the perovskite films before treatment (Reference) and after recrystallization at different temperatures (80 °C and 90 °C).

Sample	bandgap / eV	absorption edge / nm	R-Squared of fit in Fig. S7
Reference	1.625	763	0.9986
80 °C	1.692	733	0.9946
90 °C	1.697	730	0.9985

XPS MEASUREMENTS

XPS analysis of 3 samples: One triple cation perovskite reference sample, and two samples analysed after methylamine treatment at 80 °C and 90 °C. Fast survey scans and high-resolution (HR) scans of specific elements have been performed on all samples. The elements analysed are C, N, O, Br, I, Cs and Pb; the elemental components (along with H_2) of a triple cation perovskite. The survey scans are shown in Fig. S8. For each of them, the atomic concentration has been included as an inset. High resolution scans for the C 1s, N 1s, and O 1s signals are shown in Fig. S9. Table SII summarizes the results for the atomic concentration extracted for all samples from high resolution scans, Table SIII shows relevant stoichometric relationships.

The survey analyses (Fig. S8) show, as expected, that Pb and I are the main components of the samples. There is no significant presence of any foreign element (apart from oxygen), that is not be expected in the composition of the samples.

The atomic concentrations deduced (Table SII) are within the compositions to be expected for a triple cation perovskite. There is, however, the already mentioned presence of oxygen and a larger than expected presence of carbon. In the case of carbon, in all samples there is a significant signal at 284.8 – 285 eV signalling adventitious carbon. Fig. S9b) shows also how there is an exchange of FA^+ for MA^+ for both treated samples, indeed at surface level, no remaining signal at 288.3 eV[4] is detected after treatment. This exchange is consistent with the compositional changes observed in PL signal and XRD. There is a sharp decrease in the nitrogen content in the treated samples Fig. S9b). Particularly the FA^+ signal for nitrogen close to 401 eV is replaced by a weaker signal at higher energies, coinciding with the position of MA^+ at 402.5 eV[4,5].

Oxygen increases with the treatment and temperature. As already reported, oxygen is an indicative of sample degradation due to light exposure[6], we observe the progression from a weak and broad peak at 532.5 – 533 eV that can include contributions of C=O and H_2O[6], and the appearance and increase of an O_2 signal at around 531.3 eV, consistent with the presence of Pb oxide. The increase in the presence of metallic Pb with temperature and treatment (Fig. S9d)) also suggests that part of this lead could be in an oxidised estate. The stoichiometric relation of halides (I+Br)/Pb, approaching the theoretical value of 3 for the sample treated at 80 °C is in agreement with the XRD measurements, indicating the highest crystallinity. The increase in iodide for the sample treated at 90 °C suggests a more advanced degradation state and the presence of surface PbI_2, in agreement with the higher presence of metallic lead.
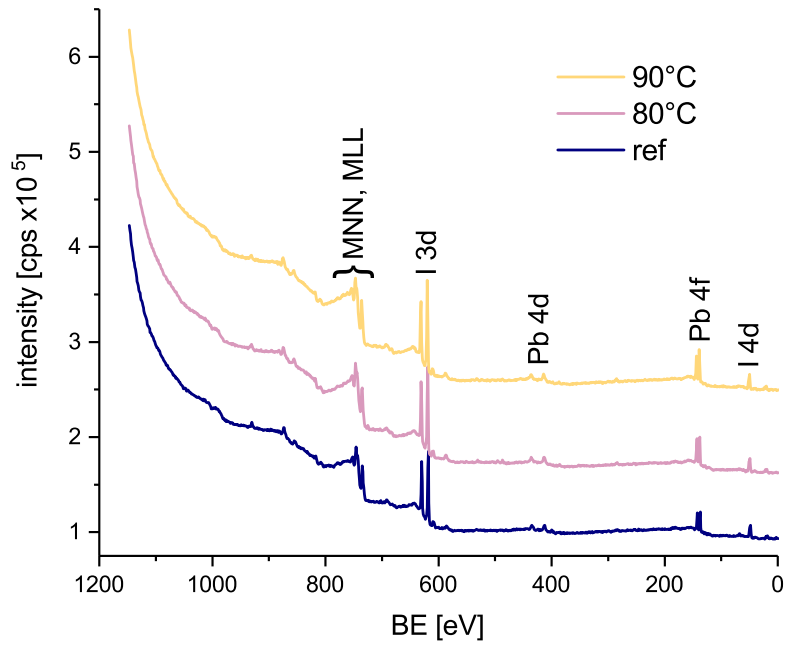
FIG. S8. Survey XPS scan for reference triple cation perovskite and films after methylamine treatment at 80 °C and 90 °C.

TABLE SII. Atomic concentrations extracted from XPS surface analysis.

	ref	80 °C	90 °C
Br 3d / %	4.4	3.9	2.6
C 1s / %	30.8	29.2	27.6
Cs 3d / %	0.1	0.8	0.4
I 3d / %	27.9	33.9	41.2
N 1s / %	23.4	11.3	9.4
O 1s / %	4.7	9.5	9.3
Pb 4f / %	8.7	11.4	9.4
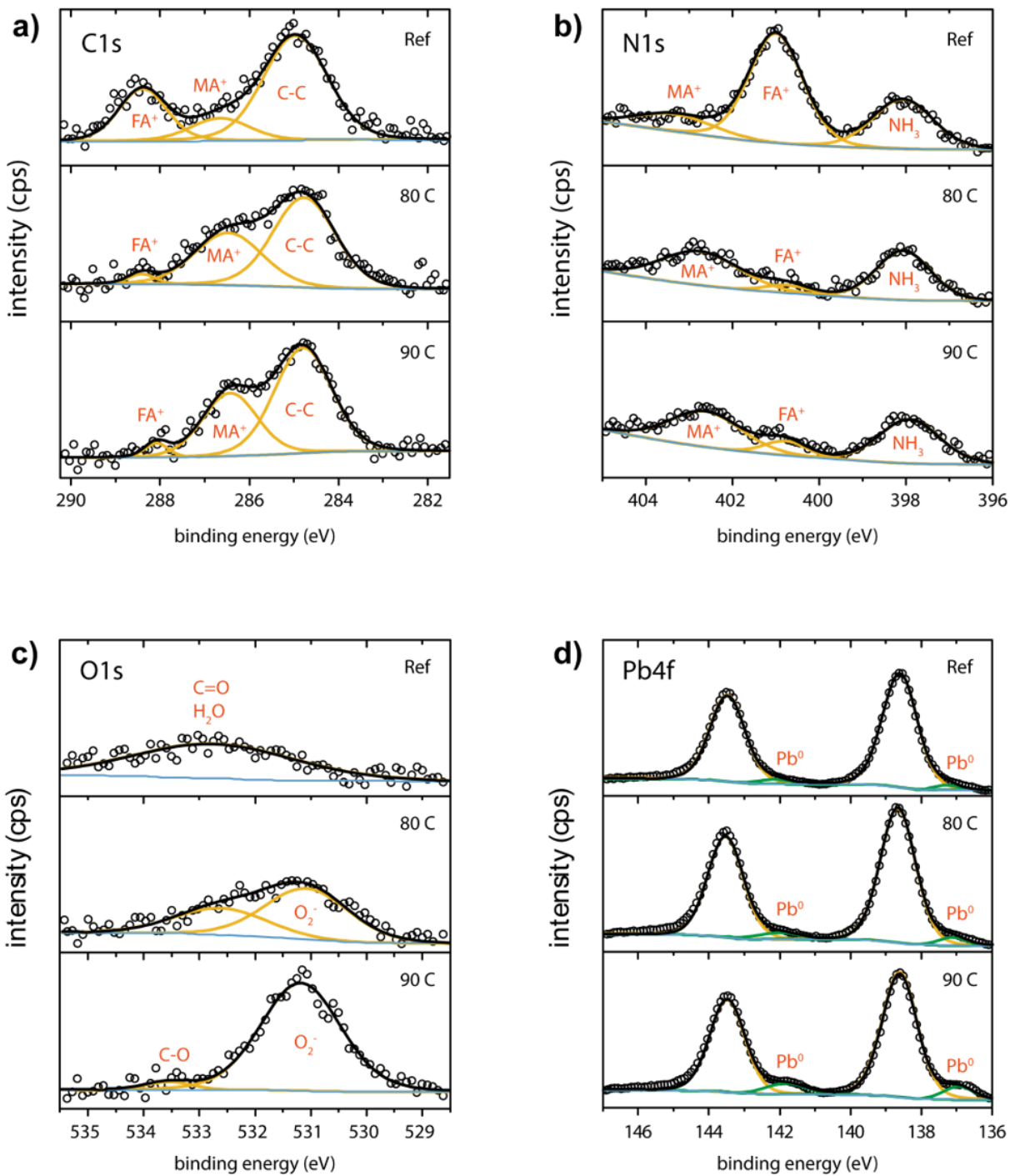
FIG. S9. High resolution XPS scans for a) C 1s, b) N 1s, c) O 1s, and d) Pb 4f, for the reference sample (red), and the samples treated at 80 °C (green) and 90 °C (blue).

TABLE SIII. Stoichometric relationships extracted from XPS surface analysis.

	Br/I	(I+Br)/Pb	N/C
ref	0.16	3.7	0.76
80 °C	0.11	3.30	0.39
90 °C	0.06	4.66	0.34

WILLIAMSON-HALL ANALYSIS
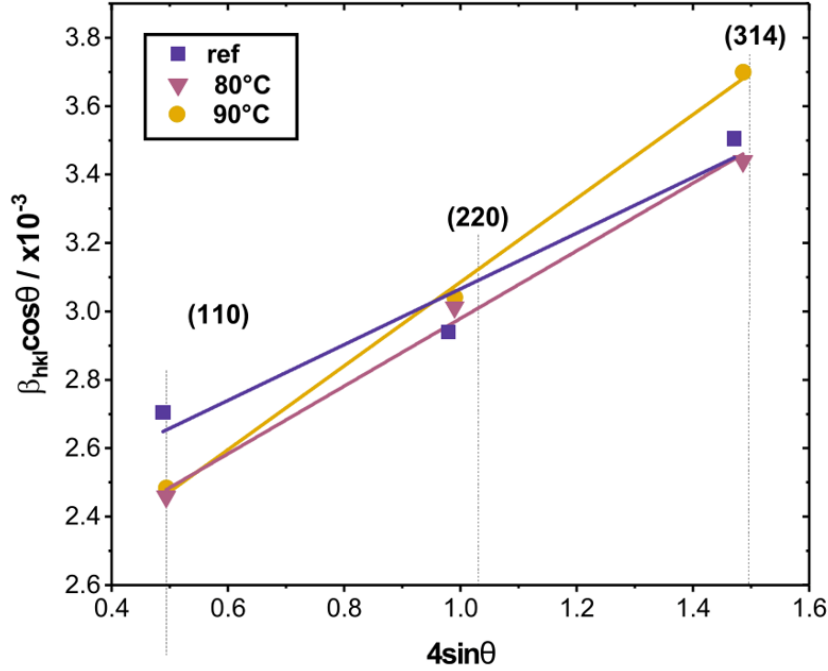
FIG. S10. Williamson-Hall plot derived from our XRD spectra

The Williamson-Hall plot is shown in Fig. S10. It relates the microstrain and the crystallite size with the XRD peak broadening[7]. For this purpose, Gaussian functions have been fitted to the diffraction spectra to extract the precise position and –broadening of the dominant peaks. These values are plotted according to the following equation:

$$\beta_{hkl} \cdot cos(\vartheta) = \frac{K\lambda}{D} + 4\varepsilon \cdot sin(\vartheta), \tag{3}$$

where β_{hkl} corresponds to the broadening observed in the analyzed peak at position ϑ, K is a proportionality constant equal to 0.94 for spherical microcrystallites, λ is the X-ray wavelength, D the microcrystallite dimension, and ε the microstrain. The intercept of the ordinate axis with the linear regression is, therefore, inversely proportional to the crystallite size. The slope is proportional to the residual microstrain in the film.

130

TABLE SIV. Average crystallite size and microstrain obtained according to equation 3 after the Williamson-Hall analysis for the perovskite films before treatment (Reference) and after recrystallization at different temperatures (80 °C and 90 °C). Both microstrain and crystallite sizes increase after treatment. The highest values are obtained for the higher recrystallization temperature of 90 °C.

Sample	Crystallite size / nm	Microstrain ε / 1×10^{-3}	R-Squared of fit in Fig. S10
Reference	64.4	0.82	0.94708
80 °C	72.8	0.99	0.99432
90 °C	77.9	1.22	0.99767
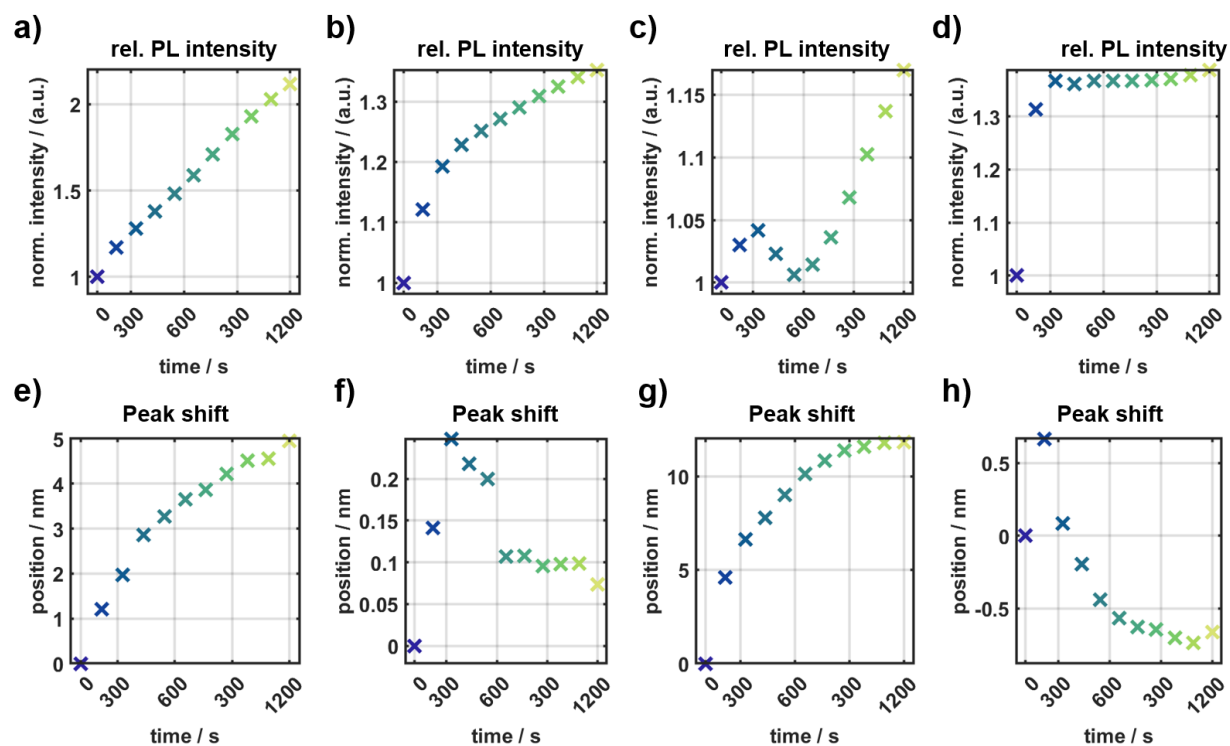
FIG. S11. a)-d) PL intensities during continuous illumination relative to the initial intensity for different spots on the 90 °C samples. e)-h) Position shift compared to the original peak position for the same spots on the 90 °C samples. The behavior varies wildly.
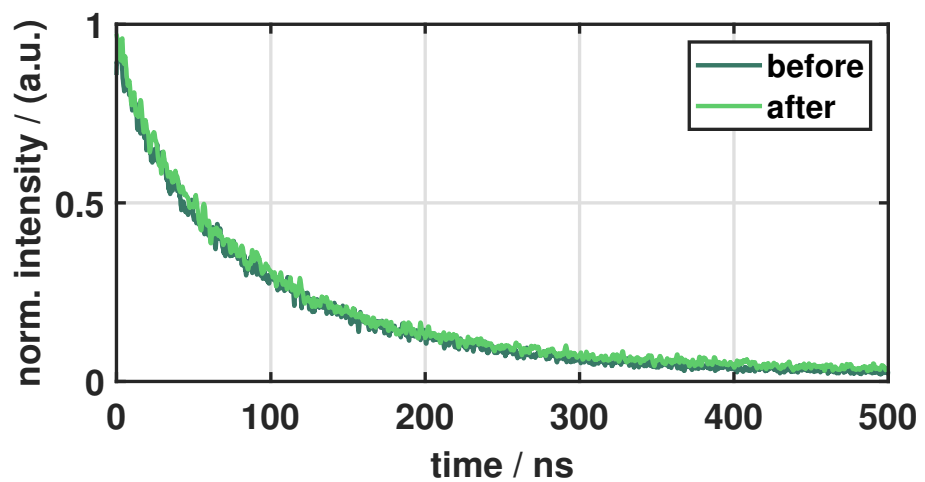
FIG. S12. TRPL of a 80 °C sample before- and after 1200 s of continuous illumination at 405 nm

BIEXPONENTIAL FITS OF TRPL DECAYS

The TRPL decays were fitted with a biexponential of the form:

$$f(t) = A_1 \cdot e^{-\frac{1}{\tau_1}} + A_2 \cdot e^{-\frac{1}{\tau_2}} + B \tag{4}$$

With the short and long lifetimes τ_1 and τ_2 and their respective amplitudes A_1 and A_2, and a constant background B. The resulting fit parameters and R-Squared values are shown in Table SV. From A_1, A_2, τ_1, and τ_2, an effective lifetime τ_{eff} was derived via[8]:

$$\tau_{eff} = \frac{\tau_1 A_1 + \tau_2 A2}{A_1 + A_2}. \tag{5}$$

τ_{eff} is also shown in Table SV.

TABLE SV. Fit parameters of biexponential fits to the TRPL decay measurements on our perovskite films. The longer and shorter lifetimes τ_1 and τ_2, the relative amplitude of the shorter decay compared to the longer $A_2/(A_1 + A_2)$, the effective lifetime τ_{eff} according to 5, and the R-squared values of the fits.

Sample	τ_1 / ns	τ_2 / ns	$A_2/(A_1 + A_2)$	τ_{eff} / ns	R-Squared of fit
Reference, before	203.16	30.13	0.95	39.45	0.9888
Reference, after	303.01	0.0124	$5e-11$	303.06	0.9941
80 °C, before	229.68	26.83	0.94	39.74	0.9892
80 °C, after	134.29	27.79	0.904	37.64	0.9959
90 °C, before	70.42	0.0069	$35e-6$	70.42	0.9207
90 °C, after	45.11	36.14	0.8810	37.20	0.9900
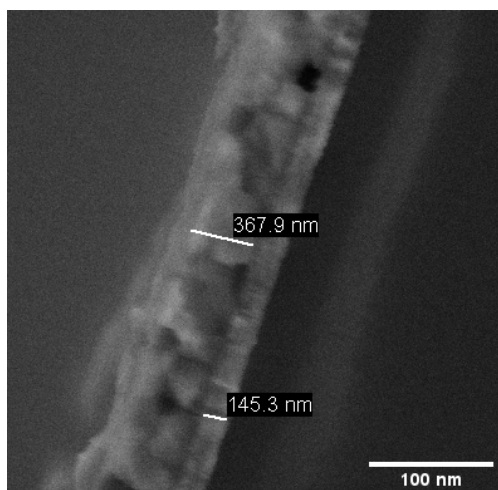
FIG. S13. cross section SEM image of a reference mixed perovskite film on glass/ITO/SnO$_2$, with the approximate SnO$_2$ and perovskite layer thicknesses.
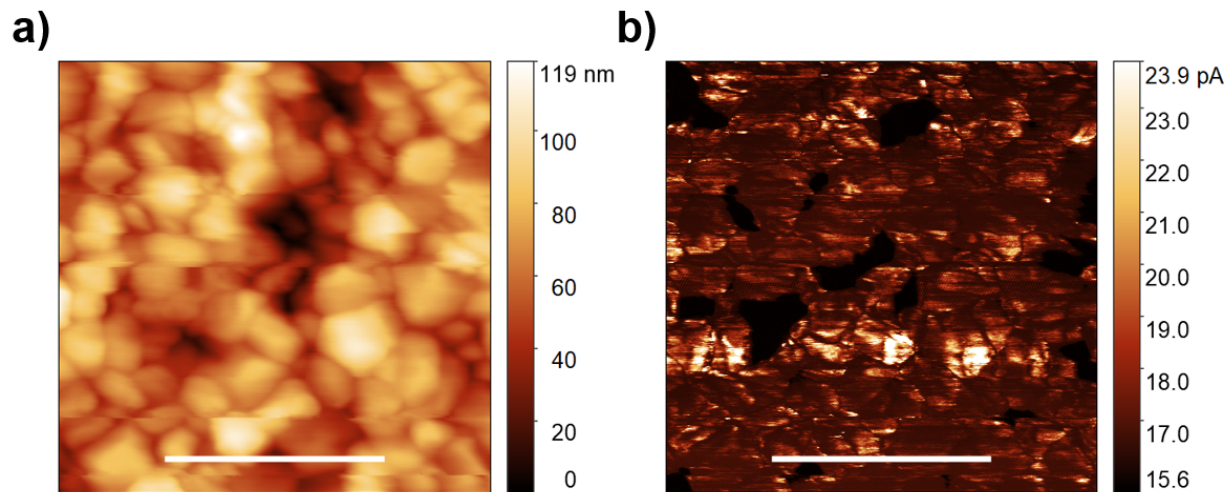
FIG. S14. AFM (a) and c-AFM (b) topographies of the reference sample measured in the dark.

a)

172 nm
160
140
120
100
80
60
23

b)

25 pA
23
22
21
20
19
18
17
16
15
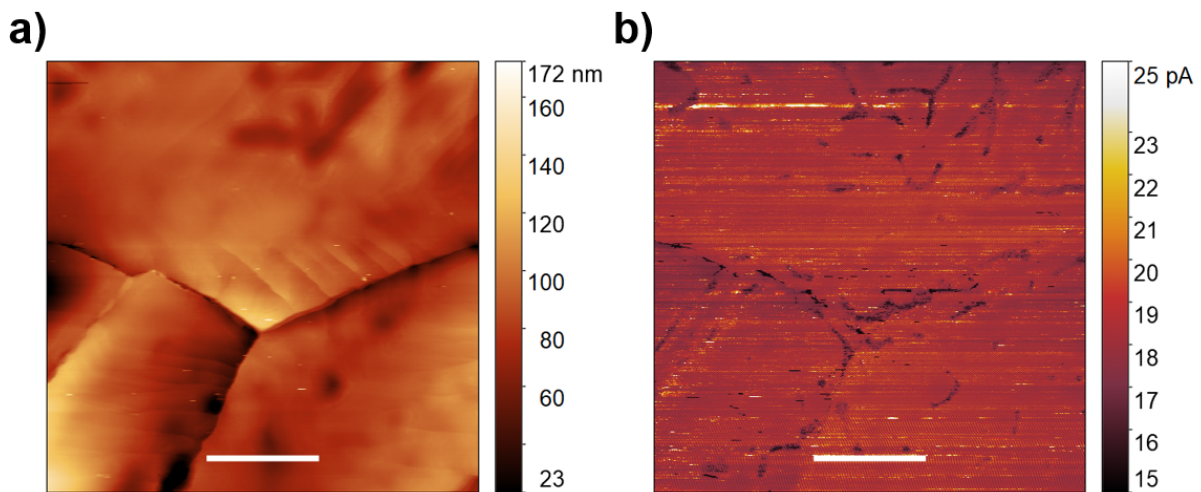
FIG. S15. AFM (a) and c-AFM (b) topographies of a 80 °C-treated sample measured in the dark.
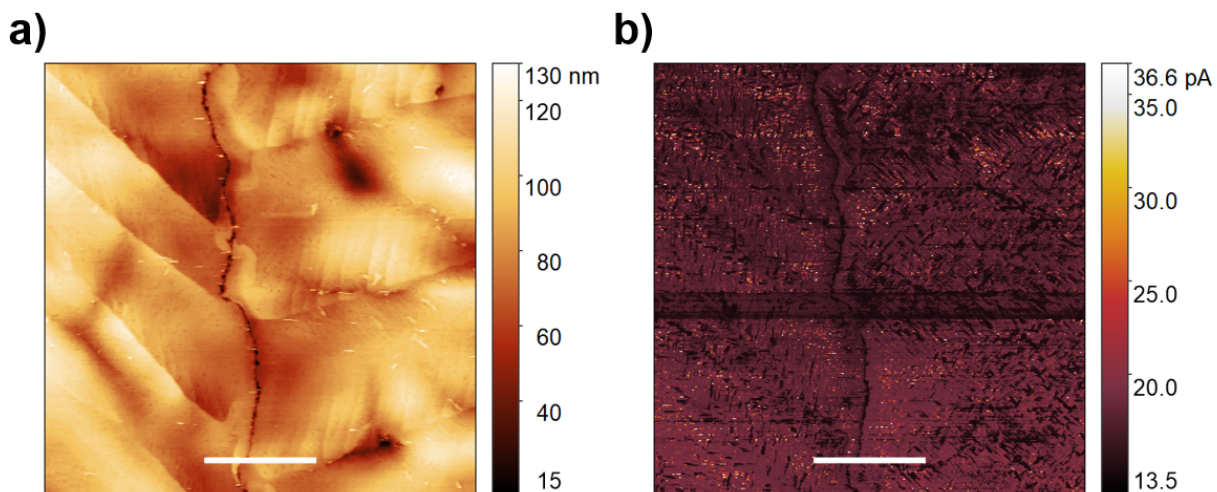
FIG. S16. AFM (a) and c-AFM (b) topographies of a 90 °C-treated sample measured in the dark.
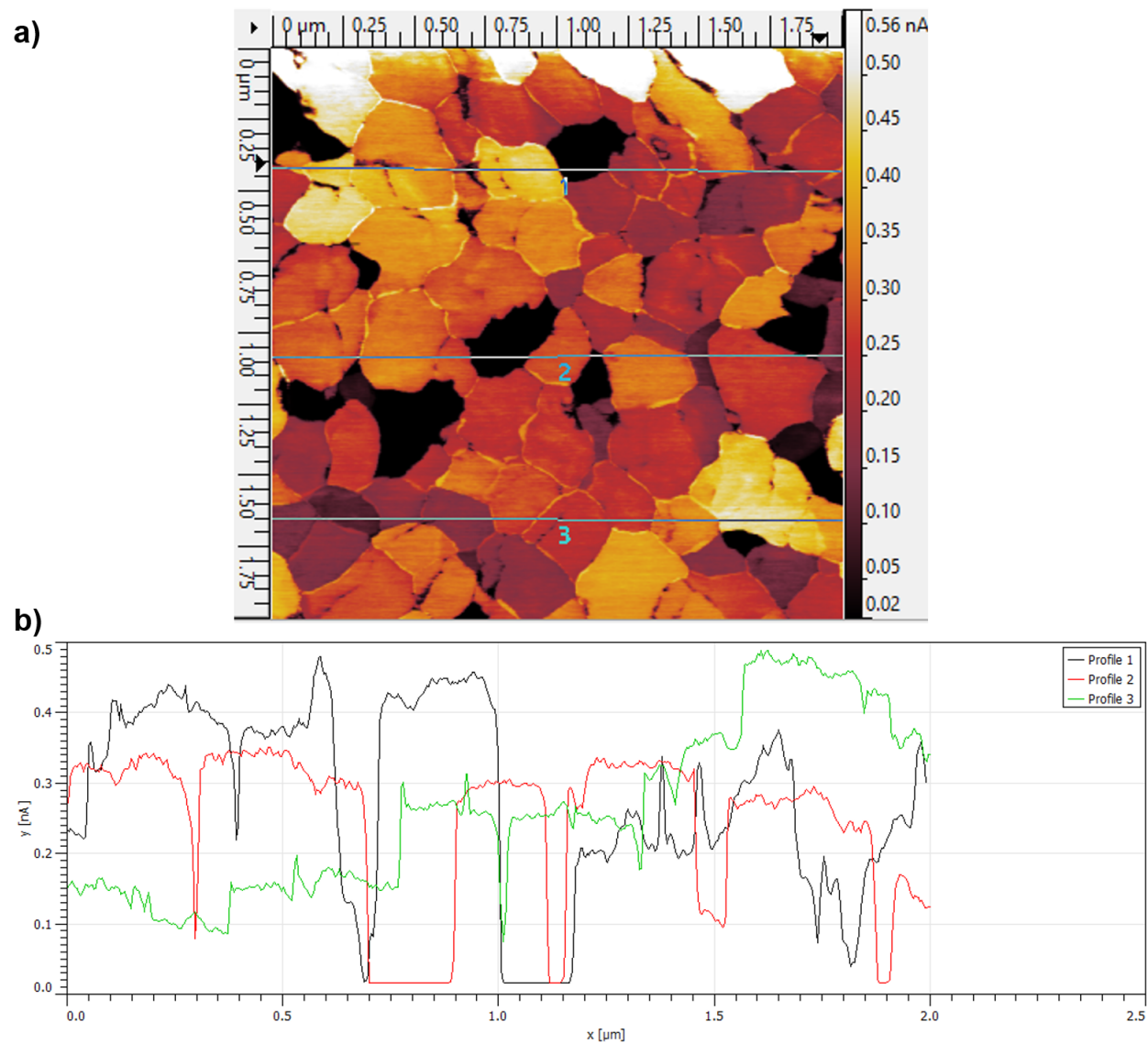
FIG. S17. a) c-AFM image of a reference sample under illumination. b) Current profiles of the lines indicated in Figure a).
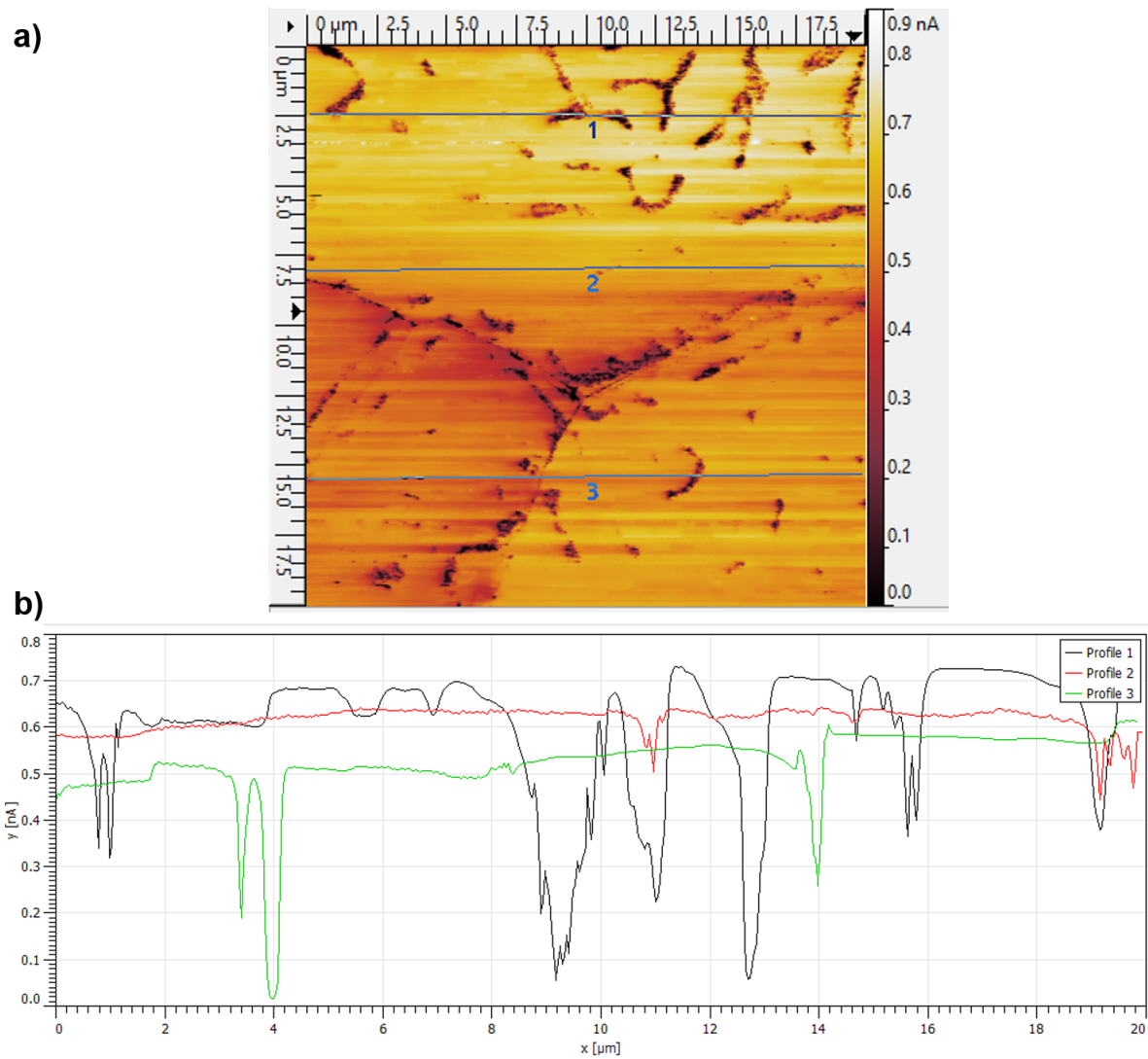
FIG. S18. a) c-AFM image of a 80 °C-treated sample under illumination. b) Current profiles of the lines indicated in Figure a).
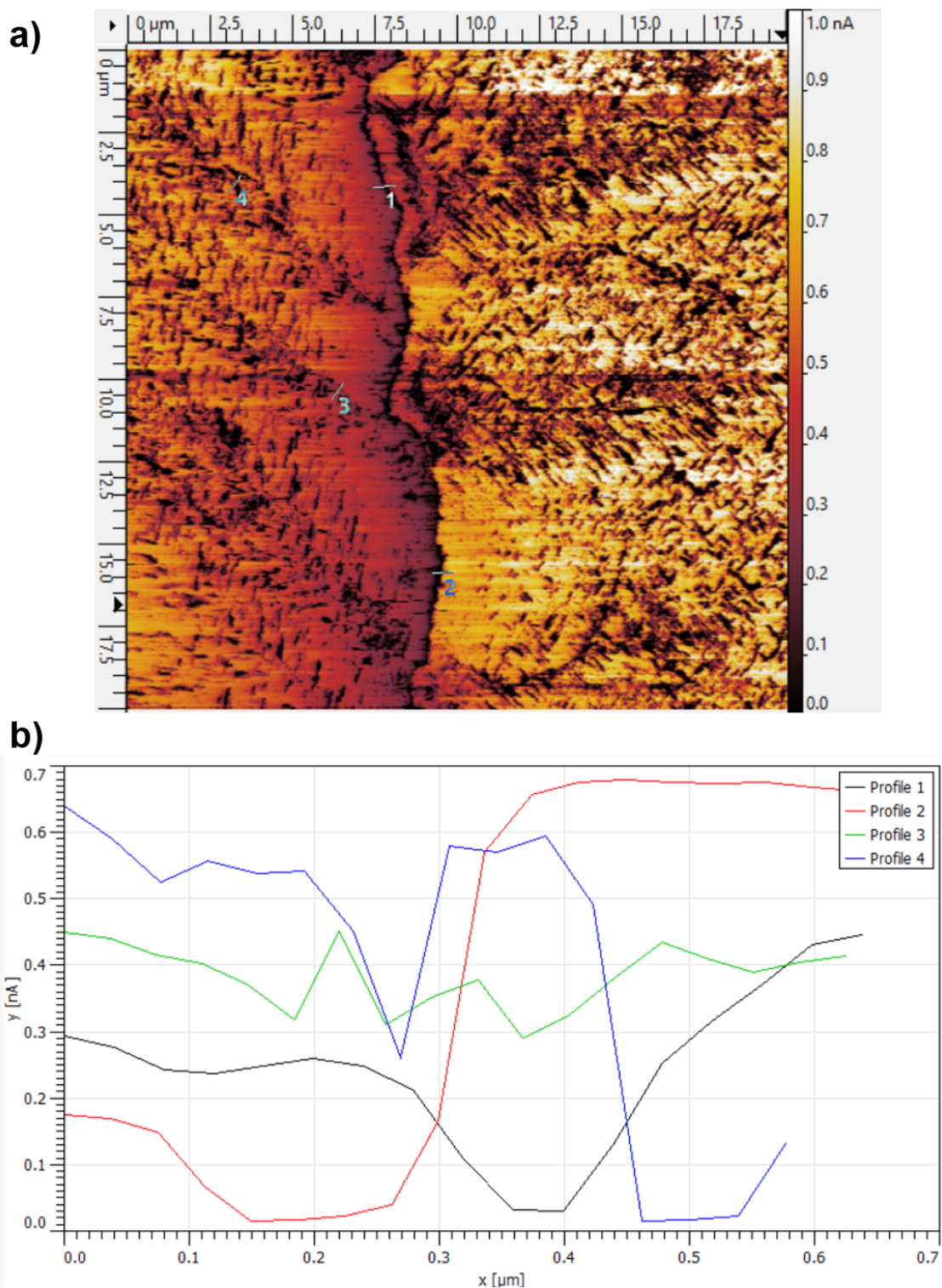
a)

b)
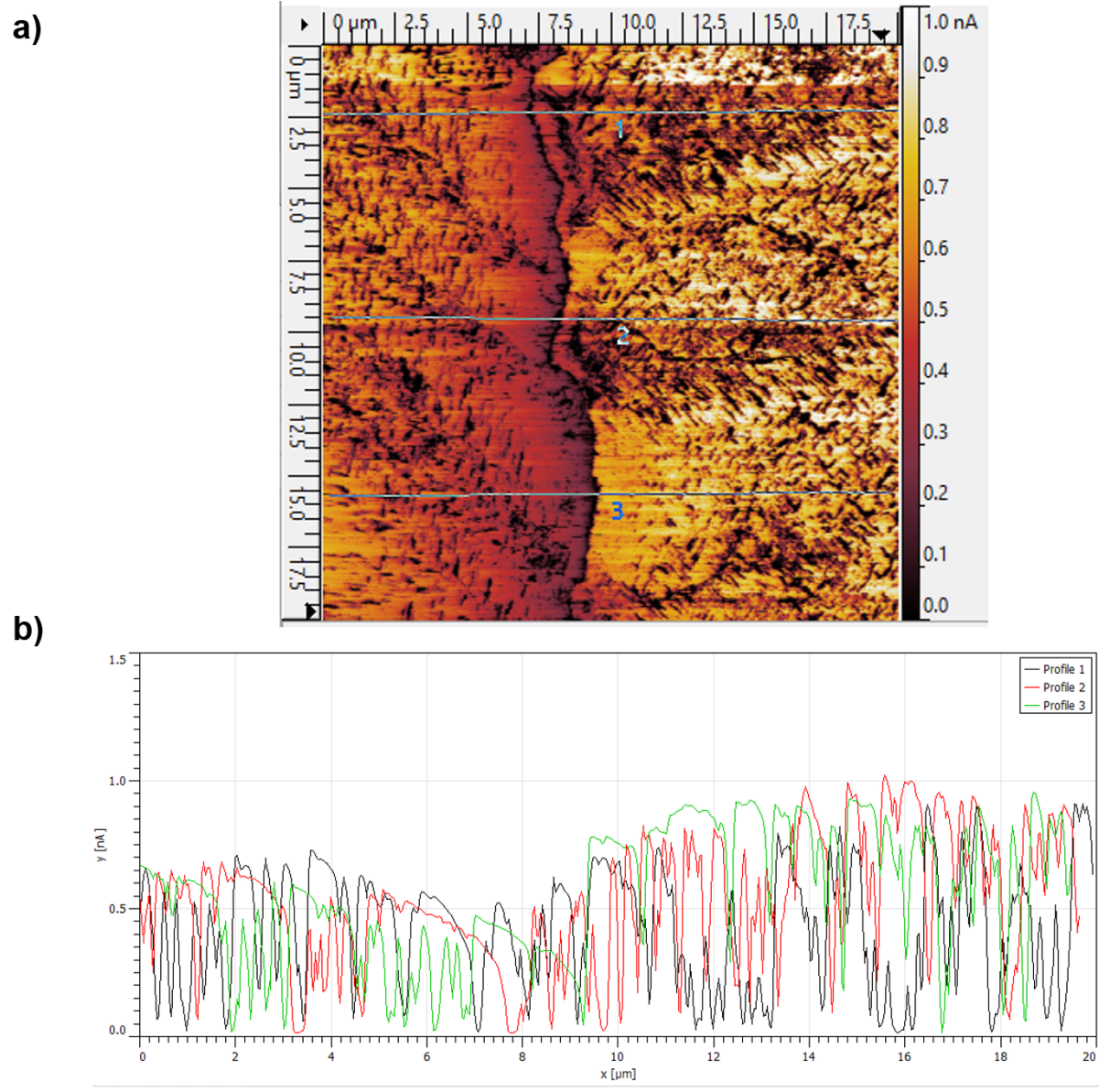
FIG. S19. a) c-AFM image of a 90 °C-treated sample under illumination. b) Current profiles of the lines indicated in Figure a).
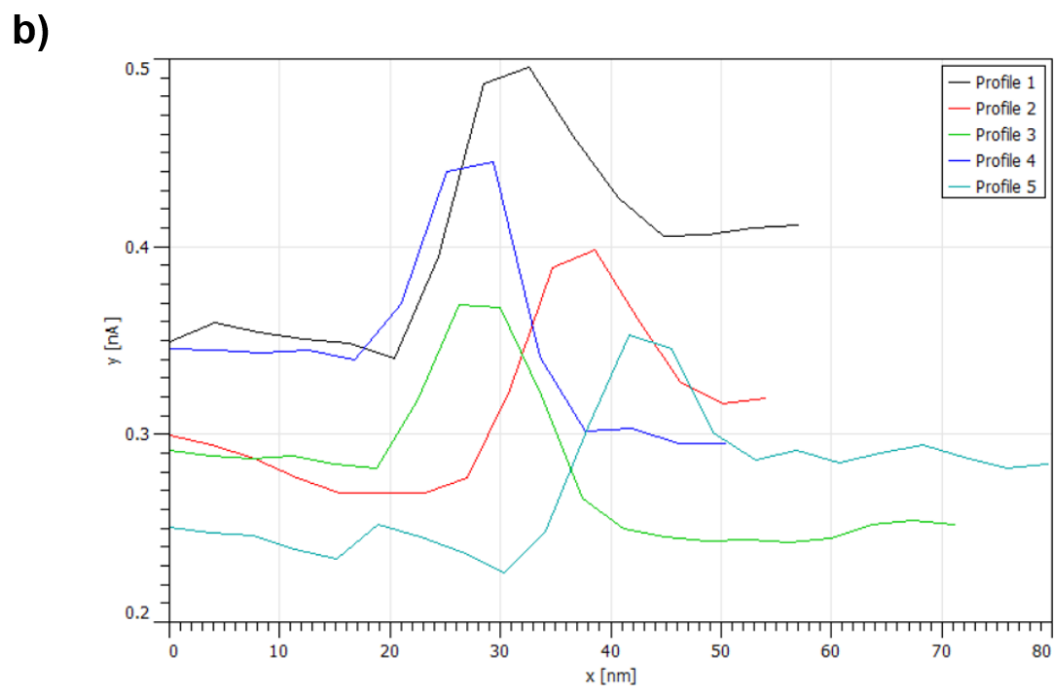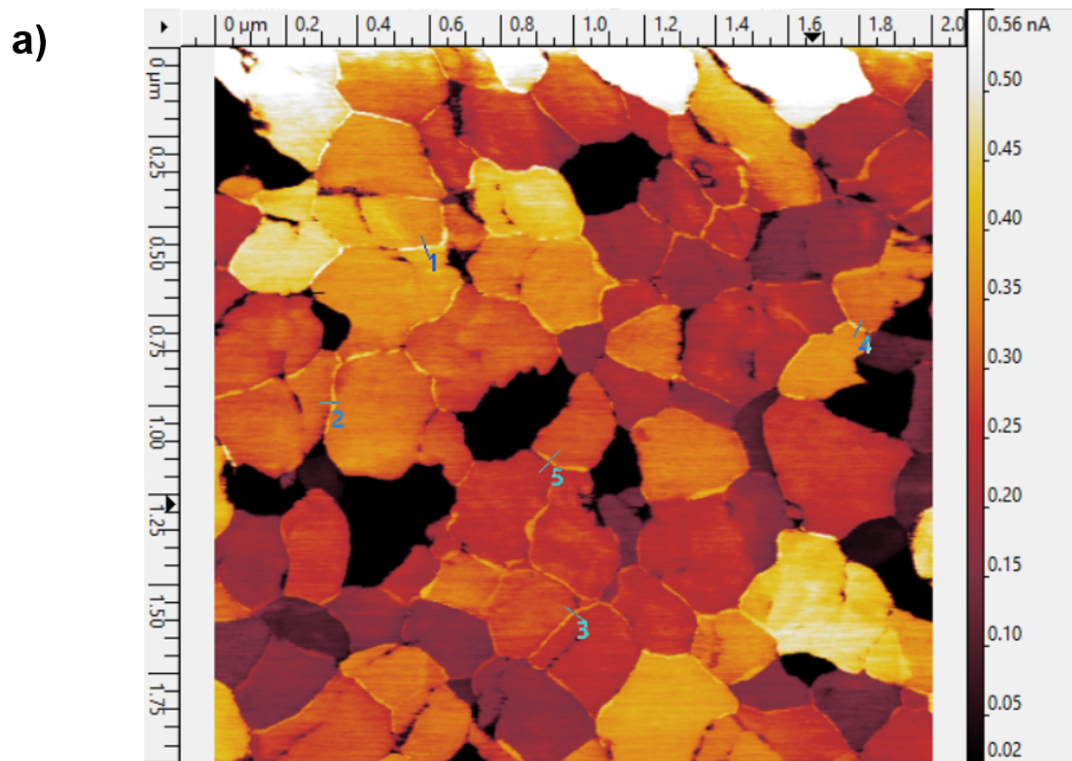
FIG. S20. a) c-AFM image of a reference sample under illumination. b) Current profiles of the lines indicated in Figure a).
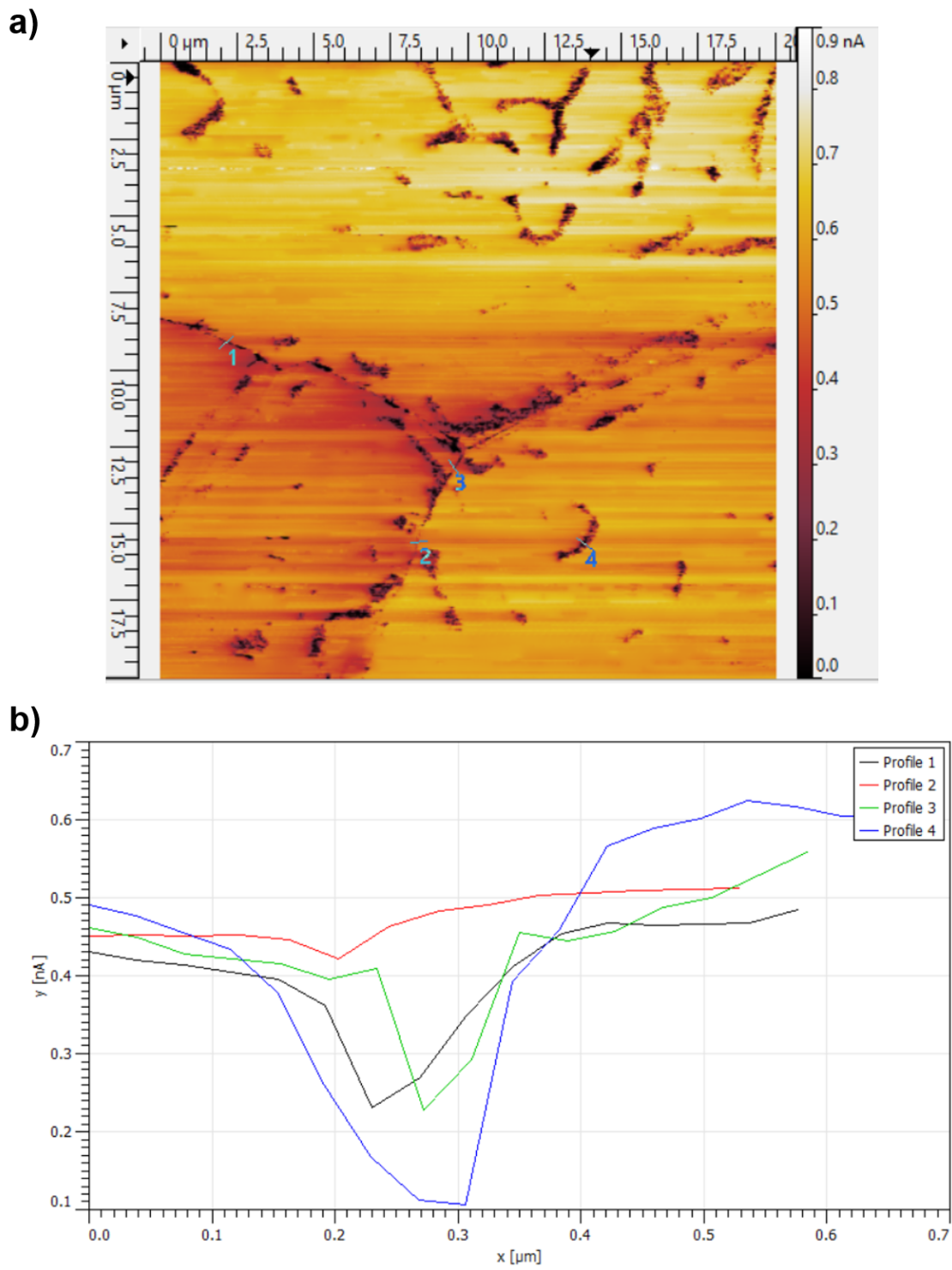
FIG. S21. a) c-AFM image of a 80 °C-treated sample under illumination. b) Current profiles of the lines indicated in Figure a).

FIG. S22. a) c-AFM image of a 90 °C-treated sample under illumination. b) Current profiles of the lines indicated in Figure a).

144

REFERENCES

[1] J. Tauc, "Optical properties and electronic structure of amorphous ge and si," Materials Research Bulletin **3**, 37–46 (1968).

[2] D. L. Wood and J. Tauc, "Weak absorption tails in amorphous semiconductors," Physical Review B **5**, 3144–3151 (1972).

[3] B. D. Viezbicke, S. Patel, B. E. Davis, and D. P. Birnie III, "Evaluation of the tauc method for optical absorption edge determination: Zno thin films as a model system," physica status solidi (b) **252**, 1700–1710 (2015).

[4] S. Cacovich, D. Messou, A. Bercegol, S. Béchu, A. Yaiche, H. Shafique, J. Rousset, P. Schulz, M. Bouttemy, and L. Lombez, "Light-induced passivation in triple cation mixed halide perovskites: Interplay between transport properties and surface chemistry," ACS Applied Materials & Interfaces **12**, 34784–34794 (2020).

[5] Q. Zhou, L. Liang, J. Hu, B. Cao, L. Yang, T. Wu, X. Li, B. Zhang, and P. Gao, "High-performance perovskite solar cells with enhanced environmental stability based on a (p-fc6h4c2h4nh3)2[pbi4] capping layer," Advanced Energy Materials **9**, 1802595 (2019).

[6] M. Anaya, J. F. Galisteo-López, M. E. Calvo, J. P. Espinós, and H. Míguez, "Origin of light-induced photophysical effects in organic metal halide perovskites in the presence of oxygen," The Journal of Physical Chemistry Letters **9**, 3891–3896 (2018).

[7] G. Williamson and W. Hall, "X-ray line broadening from filed aluminium and wolfram," Acta Metallurgica **1**, 22–31 (1953).

[8] G. Zatryb and M. Klak, "On the choice of proper average lifetime formula for an ensemble of emitters showing non-single exponential photoluminescence decay," Journal of Physics: Condensed Matter **32** (2020), 10.1088/1361-648X/ab9bcc.

6 Conclusion & Outlook

In summary, I focused on understanding sub-granular structures, such as ferroelastic twin domains and grain boundaries, and their relations to free charge carrier dynamics, defects, and ion migration. My investigation revealed that strain within halide perovskites can be chemically engineered, leading to changes in optical and electrical properties. Therefore, chemical strain engineering can be applied to perovskites regardless of the presence of ferroelastic twin domains.The second outcome of my research is that, although halide perovskites are tolerant to defects, grain boundaries are still high-defect-density areas and play a major role in charge carrier recombination and ion migration. Therefore, further optimization of grain boundaries and interfaces in halide perovskite will be needed for commercialized usage.

7   Acknowledgements

Curriculum Vitae

Mehmet Yenal Yalcinkaya
Turkish citizen, born 5 October 1993

EDUCATION

Ph.D. 2022 – (Ongoing)	**Chemistry, Johannes Gutenberg University Mainz** Mainz / Germany
Ph.D. 2018 – 2020 (Unfinished)	**Materials Science and Engineering, İzmir Institute of Technology** İzmir / Turkey
M.Sc. 2015 - 2018	**Materials Science and Engineering, Gebze Technical University** Kocaeli / Turkey

- **Thesis Title:** Growing Anatase Phase on Titanium Disks by Hydrothermal Process

B.Sc. 2011 - 2015	**Metallurgy and Materials Engineering Kocaeli University** Kocaeli / Turkey

- **Thesis Title:** Understanding the mechanism of tungsten based electrochromic glass coatings.

RESEARCH & PROJECTS

February 2020 – (Ongoing)	**Max Planck Institute for Polymer Research, Physics at Interfaces Department** Researcher
May 2018 – February 2020	**İzmir Institute of Technology (IZTECH), Materials Science and Engineering Department, İzmir / Turkey** Research Assistant
March 2018 – May 2018	**Italian Institute of Technology (IIT), Nanochemistry Department, Genoa / Italy** Visiting Student (Erasmus+)
July 2013 – September 2013	**Ilmenau University of Technology, Technical Physics Department, Ilmenau / Germany** Visiting Student (The International Association for the Exchange of Students for Technical Experience – IAESTE)

WORK EXPERIENCE

March 2017 - May 2017   **HAZERFEN Chemistry, Kocaeli / Turkey**
                             R&D Assistant

PUBLICATIONS

1. **Yalcinkaya, Y**., Rohrbeck, P. N., Schütz, E. R., Fakharuddin, A., Schmidt-Mende, L., & Weber, S. A. (2023). Nanoscale Surface Photovoltage Spectroscopy. Advanced Optical Materials, 2301318.

2. Schütz, E. R., Fakharuddin, A., **Yalcinkaya, Y**., Ochoa-Martinez, E., Bijani, S., Yusoff, M., & Schmidt-Mende, L. (2022). Reduced defect density in crystalline halide perovskite films via methylamine treatment for the application in photodetectors. *APL Materials*, *10*(8).

3. **Yalcinkaya, Y**., Hermes, I. M., Seewald, T., Amann-Winkel, K., Veith, L., Schmidt-Mende, L., & Weber, S. A. (2022). Chemical Strain Engineering of MAPbI3 Perovskite Films. *Advanced Energy Materials*, *12*(37), 2202442.

4. Yuce, H., Mandal, M., **Yalcinkaya, Y**., Andrienko, D., & Demir, M. M. (2022). Improvement of Photophysical Properties of CsPbBr3 and Mn2+: CsPb (Br, Cl) 3 Perovskite Nanocrystals by Sr2+ Doping for White Light-Emitting Diodes. *The Journal of Physical Chemistry C*, *126*(27), 11277-11284.

5. Bahnmüller, U. J., Kuper, H., Seewald, T., **Yalçinkaya, Y**., Becker, J. A., Schmidt-Mende, L., ... & Polarz, S. (2021). On the Shape-Selected, Ligand-Free Preparation of Hybrid Perovskite (CH3NH3PbBr3) Microcrystals and Their Suitability as Model-System for Single-Crystal Studies of Optoelectronic Properties. *Nanomaterials*, *11*(11), 3057.

6. Guvenc, C. M., **Yalcinkaya, Y**., Ozen, S., Sahin, H., & Demir, M. M. (2019). Gd3+-doped α-CsPbI3 nanocrystals with better phase stability and optical properties. *The journal of physical chemistry C*, *123*(40), 24865-24872.

CONFERENCE PRESENTATIONS

1. **Yenal Yalcinkaya,** "Passivation and Defect Mapping in Lead Halide Perovskites", MRS Fall Meeting 2022, Poster Presentation.

2. **Yenal Yalcinkaya,** "Chemical Engineering of Strain in MAPbI$_3$ Thin Films", MRS Fall Meeting 2022, Poster Presentation.

3. **Yenal Yalcinkaya,** "Chemical Engineering of Ferroelastic Twin Domains in MAPbI3 Films", NanoGe Fall Meeting 2021, Oral Presentation.

4. **Yenal Yalcinkaya,** "Tracking Ferroelastic Twin Domains in MAPbI3 Structure", NanoGe Fall Meeting 2021, Oral Presentation.

5. **Yenal Yalcinkaya,** "Enhanced Stability and Optical Properties of Gd^{3+} doped $CsPbI_3$ Nanocrystals", NanoGe Fall Meeting 2019, Oral Presentation.

6. **Yenal Yalcinkaya**, "Perovskite-based White LED Fabrication and Characterization", Şişecam Glass Symposium, İstanbul / Turkey, 2018, Oral Presentation.

7. **Yenal Yalcinkaya**, "Growing Anatase Phase on Titanium Disks by Hydrothermal Process", ElectroceramicTR, Kocaeli / Turkey, 2017, Poster Presentation.

8. **Yenal Yalcinkaya**, "Growing Anatase Phase on Titanium Disks by Hydrothermal Process" Gebze Technical University Postgraduate Research Symposium, Kocaeli / Turkey, 2016, Poster Presentation.